SYNTHESIS OF POROUS METAL PHOSPHONATE FRAMEWORKS FOR APPLICATIONS IN GAS SEPARATION AND STORAGE

Michael Thomas Wharmby

A Thesis Submitted for the Degree of PhD
at the
University of St Andrews

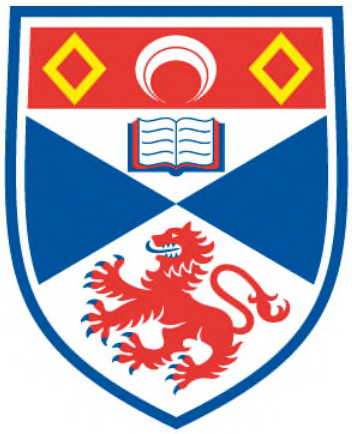

2012

Synthesis of Porous Metal Phosphonate Frameworks for Applications in Gas Separation and Storage

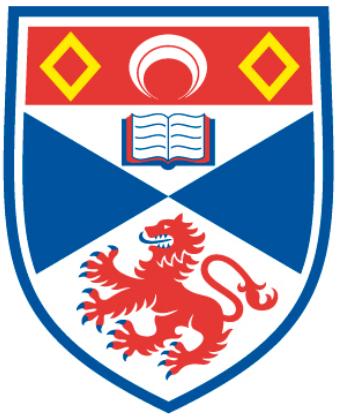

Michael Thomas Wharmby

This thesis is submitted in partial fulfilment for the degree of
Doctor of Philosophy
to the
University of St Andrews

May 2012

Declaration

1. Candidate's declarations:

I, Michael Thomas Wharmby, hereby certify that this thesis, which is approximately 72500 words in length, has been written by me, that it is the record of work carried out by me and that it has not been submitted in any previous application for a higher degree.

I was admitted as a research student in January, 2008 and as a candidate for the degree of Doctor of Philosophy in January, 2012; the higher study for which this is a record was carried out in the University of St Andrews between 2008 and 2012.

Signature of candidate: ..... Date: May 14, 2012

2. Supervisor's declaration:

I hereby certify that the candidate has fulfilled the conditions of the Resolution and Regulations appropriate for the degree of Doctor of Philosophy in the University of St Andrews and that the candidate is qualified to submit this thesis in application for that degree.

Signature of supervisor: ..... Date: May 14, 2012

3. Permission for electronic publication:

In submitting this thesis to the University of St Andrews I understand that I am giving permission for it to be made available for use in accordance with the regulations of the University Library for the time being in force, subject to any copyright vested in the work not being affected thereby. I also understand that the title and the abstract will be published, and that a copy of the work may be made and supplied to any bona fide library or research worker, that my thesis will be electronically accessible for personal or research use unless exempt by award of an embargo as requested below, and that the library has the right to migrate my thesis into new electronic forms as required to ensure continued access to the thesis. I have obtained any third-party copyright permissions that may be required in order to allow such access and migration, or have requested the appropriate embargo below.

The following is an agreed request by candidate and supervisor regarding the electronic publication of this thesis:

Embargo on both all of printed copy and electronic copy for the same fixed period of one year on the following ground(s): publication would preclude future publication;

Signature of candidate: ..... Signature of supervisor: .....
Date: May 14, 2012

Abstract

Porous metal phosphonate framework materials were synthesised by solvothermal reaction of bis(α-aminomethylenephosphonic acid) ligands with divalent and trivalent metal cations.

The syntheses and characterisation by NMR and, where possible, single crystal X-ray diffraction of seven bisphosphonic acid ligands, including N,N′-piperazine-bis(methylenephosphonic acid) ($H_4\mathbf{L}$), its racemic and enantiopure (R) 2-methyl ($H_4\mathbf{L}'$ and R-$H_4\mathbf{L}'$) and 2,5-dimethyl ($H_4\mathbf{L}''$) derivatives, and N,N′-4,4′-bipiperidine-bis(methylenephosphonic acid) ($H_4\mathbf{LL}$) are reported.

Syntheses of the known phase $Y_2(\mathbf{L}H_2)_3 \cdot 5H_2O$ and the new phases, STA-13(Y) (St Andrews microporous material No. 13) and $Y_2(R\text{-}\mathbf{L}'H_2)_3 \cdot 4H_2O$, from reactions of $Y(AcO)_3$ with $H_4\mathbf{L}$, $H_4\mathbf{L}'$ and R-$H_4\mathbf{L}'$ respectively are reported. The as-prepared and dehydrated structures of each phase have been determined from either laboratory or synchrotron powder X-ray diffraction data. Reaction of $Y(AcO)_3$ and $H_4\mathbf{L}''$ is shown to form a phase with a different structure. The features determining which structure crystallises are discussed. Syntheses of other rare-earth forms of STA-13 (Sc^{3+}, Gd^{3+}–Yb^{3+}) and the porosity of each phase to N_2 are reported. STA-13(Y) is the most porous form with loadings of ~ 3 mmol g^{-1} and ~ 4 mmol g^{-1} for N_2 and CO_2 respectively. MIL-91(Fe) was synthesised for the first time from reactions of Fe^{3+} cations with $H_4\mathbf{L}$. Its structure was confirmed by Rietveld refinement, but it was not porous. The first syntheses of $[Fe_4\mathbf{L}_{1.5}(AcO)_{1.5}(OH,H_2O)_3]\cdot 0.5NH_4 5.5H_2O$ ($\mathbf{L}$= $\mathbf{L}$ or $\mathbf{L}'$) are reported, from reactions of $H_4\mathbf{L}$ or $H_4\mathbf{L}'$ in the presence of an excess of Fe^{3+} cations. The phase is related to a previously reported Co phase.

The synthesis of divalent metal bisphosphonate STA-12(Mg) ($Mg_2(H_2O)_2\mathbf{L}\cdot 5.6H_2O$) was reported for the first time and its structure determined from single crystal X-ray diffraction. The dehydration behaviour of this material was compared with the known forms of STA-12. STA-12(Mg) is porous to both N_2 (~ 5.5 mmol g^{-1}) and

CO_2 ($\sim$ 8.5 mmol g^{-1}).

Reaction of H_4**LL** with Co^{2+} and Ni^{2+} gave two materials isoreticular with STA-12, labelled STA-16(Co) and STA-16(Ni). The structures of both materials were solved from synchrotron powder X-ray diffraction data. On dehydration, STA-16(Co) undergoes a reversible structural transition to an unknown structure. By contrast, STA-16(Ni) retains the same symmetry in the dehydrated form and its structure was determined from synchrotron powder X-ray diffraction data. Both materials are porous to N_2, with an uptake of up to 22.2 mmol g^{-1}, and CO_2 with maximum loading of 21.7 mmol g^{-1}. NLDFT analysis of N_2 adsorption data confirm the crystallographically determined pore radii. Syntheses of other frameworks with divalent cations and initial reactions of H_4**LL** with trivalent cations are also reported.

Publications

D. Fairen-Jimenez, A. Torrisi, R. Galvelis, M. T. Wharmby, A. Gellan, P. A. Wright, C. Mellot-Draznieks, T. Düren, **Swing Effect on the Adsorption of Energy-Related Gases on ZIF-8: a Combination of Experiments and Molecular Simulations**, in preparation.

M. T. Wharmby, G. M. Pearce, J. P. S. Mowat, J. M. Griffin, S. E. Ashbrook, P. A. Wright, L.-H. Schilling, A. Lieb, N. Stock, S. Chavin, S. Bordiga, E. Garcia, G. Pirngruber, M. Vreeke, L. Gora, **Synthesis and crystal chemistry of the STA-12 family of metal N,N′-piperazinebis(methylenephosphonates) and applications of STA-12(Ni) in the separation of gases**, Micropor. Mesopor. Mater., in press. (DOI: 10.1016/j.micromeso.2011.12.003)

M. J. Beir, W. Kleist, M. T. Wharmby, R. Kissner, B. Kimmerle, P. A. Wright, J.-D. Grunwaldt, A. Baiker, **Aerobic Epoxidation of Olefins Catalyzed by the Cobalt-Based Metal-Organic Framework STA-12(Co)**, Chem. Eur. J., 18 (2012), 887–898

M. T. Wharmby, P. A. Wright, **Open Framework and Microporous Metal Phosphonates MOFs with Piperazine-based Bisphosphonate Linkers**. In *Metal Phosphonate Chemistry: From Synthesis to Applications*; A. Clearfield, K. Demadis, Eds.; Royal Society of Chemistry, Cambridge, England, 2011; pp 317–343

D. Fairen-Jimenez, S. A. Moggach, M. T. Wharmby, P. A. Wright, S. Parsons, T. Düren, **Opening the Gate: Framework Flexibility in ZIF-8 Explored by Experiments and Simulations**, J. Am. Chem. Soc., 133 (2011), 8900–8902

M. T. Wharmby, J. P. S. Mowat, P. A. Wright, **Novel Large Pore Metal Organic Frameworks**, U.K. patent pending.

M. T. Wharmby, J. P. S. Mowat, S. P. Thompson, P. A. Wright, **Extending the Pore Size of Crystalline Metal Phosphonates toward the Mesoporous Regime by Isoreticular Synthesis**, J. Am. Chem. Soc., 133 (2011), 1266–1269

M. T. Wharmby, S. R. Miller, J. A. Groves, I. Margiolaki, S. E. Ashbrook, P. A. Wright, **Yttrium bisphosphonate STA-13: A racemic phosphonate metal organic framework with permanent microporosity**, Dalton Trans., 39 (2010), 6389–6391

J. P. S. Mowat, J. A. Groves, M. T. Wharmby, S. R. Miller, Y. Li, P. Lightfoot, P. A. Wright, **Lanthanide N,N′-piperazinebis(methylenephosphonates) (Ln = La, Ce, Nd) that display flexible frameworks, reversible hydration and cation exchange**, J. Solid State Chem., 182 (2009), 2769–2778

Acknowledgements

I have been supported throughout my PhD studies by many people, too many to name indiviually. Those not mentioned by name here, I owe you a debt of gratitude — thank you.

First I would like to thank my supervisor Prof. Paul Wright for giving me the opportunity to study for a PhD. Paul has been a constant source of support, enthusiasm, encouragement and a never ending supply of ideas over the last four year, all of which have made the project so diverse and interesting. I would like to thank him for allowing me the freedom to experiment with my own ideas as well as his. The EPSRC is thanks for providing funding for this project.

Within the School of Chemistry at St Andrews, I would like to thank past and present members of the Wright, Lightfoot and Ashbrook groups for their friendship, support and assistance with many aspects of this work, particularly Stuart Miller and Lorena Picone. Technical staff within the School of Chemistry are also thanked, particularly Sylvia Williamson for her tireless assistance with porosimetry, thermal and elemental analyses. I would also like to thank John Griffin for his assistance with solid state NMR, his friendship and general inquisitiveness about science. Charlotte Jones is thanked for numerous discussions over coffee and helping to keep me going. I am indebted to John Mowat who has been a great help throughout my four years with ideas, questions, coffee drinking, rock climbing and more. John has been a great support and friend.

I have collaborated in this work with several groups beyond St Andrews. Sachin Chavan, in the group of Prof. Sylvia Bordiga (Università di Torino, Turin, Italy) is thanked for collection of *in situ* IR and UV/Vis spectra. Wolfgang Kleist (K.I.T., Karlsruhe, Germany) is thanked for his enthusiasm for catalysis in STA-12. Prof. Norbert Stock (Christian-Albrechts-Universität zu Kiel, Kiel, Germany) is thanked for hosting me in his group to undertake high-throughput synthesis experiments

and for his seemingly boundless enthusiasm for understanding synthesis. Members of the Stock group are also thanked for their assistance with the work, and I am also indebted to Tim Ahnfeldt, for housing me, and Pala Maniam, Helge Reinsch and Stefan Bernt for keeping me entertained in Kiel. I would like to thank Tina Düren (University of Edinburgh, Edinburgh, UK) and members of her research group, particularly Ana Banu and Naomi Cessford, for teaching me how to simulate adsorption. I would like to say a big thank you to David Fairén-Jiménez for his assistance with adsorption simulation, his enthusiasm for understanding adsorption, his ideas for synthesising and studying adsorption in ZIFs and for his frienship and support throughout my studies.

Throughout my studies my family has been a great support. I would like to thank my parents and grandparents for their interest and enthusiasm in what I am studying — it has been a real help over the last four years. My parents' interest in science gave me a desire to understand the world around me and encouraged me to keep asking questions. This has led me to study for a PhD. There have been many difficult times and I would have struggled without their help. I really want to thank them for the love, support and encouragement that they have given me throughout my studies, not just my PhD.

Finally I would like to thank Julia Collins. Her love, boundless enthusiasm and seemingly endless positivity over the months have allowed me to write this thesis. Without this, writing would have been much more difficult. I cannot thank her enough for all the help and support she has given me. I look forward to what our future may bring.

MTW
Edinburgh, January 2012; Kiel, May 2012

Happy the man, and happy he alone,
He who can call today his own:
He who, secure within, can say,
Tomorrow do thy worst, for I have lived today.

Be fair or foul, or rain or shine
The joys I have possessed, in spite of fate, are mine.
Not Heaven itself, upon the past has power,
But what has been, has been, and I have had my hour.

Horace — Odes

Contents

List of Abbreviations

H_2BDC	Benzenedicarboxylic acid or terephthalic acid.
MIL	Matériaux de l'Institut Lavoisier, (framework) material reported by the research group of Prof. G. Férey, at Institut Lavoisier, Université de Versailles-St-Quentin en Yvelines, France.
PO_3C	Phosphonate or phosphonate group.
STA	St Andrews porous material, permanently porous framework material reported by the group of Prof. P. A . Wright, School of Chemsitry, University of St Andrews, UK.

Colour Scheme for Structural Diagrams

Purple	Generic alkali earth cation.
Blue	Mg
Mauve	Al
Dark pink	Cr
Dark green	V
Brown	Fe
Purple	Co
Green	Ni
Dark blue	Cu
Dark grey	Zn
Light pink	Generic lanthanide.
Orange	PO_3C group.

Chapter 1

Introduction

The separation of an individual gas species from a mixture of gases is an important step in many industrial processes. Examples include the separation of CO_2 and H_2 in a steam methane reformer; fractionation of air, specifically in the separation of O_2 and N_2; and the separation of CO_2 and CH_4 from landfill gas.[1] The increasing public awareness of climate change and the increasing problems of energy security have made finding efficient methods of separating H_2 and CO_2 a priority for government. Specifically, the separation and storage of clean H_2 would provide a cheap, widely available and, most importantly, clean energy source for transport.[2] The capture of CO_2 from sources such as power stations would help to mitigate the effect of climate change and the separation of CO_2 from a flue gas stream is the first step in this process.[3]

Industrial separations such as these are achieved by Pressure Swing Adsorption (PSA).[1] PSA relies on the ability of an adsorbent material, typically a porous solid such as a zeolite, to selectively adsorb one component of a gas mixture over another. A pressurised mixed gas stream is passed over a bed of adsorbent and one species is adsorbed more than the rest. Eventually the bed becomes saturated in this gas species and the flow of the stream is switched to another bed. Pressure is reduced in the first bed and the gas is desorbed as a pure phase (*Fig. 1.1*).

To improve the efficiency of separations of H_2 and CO_2 and for the development of new separations, new porous adsorbent materials must be prepared. The current work will focus on the synthesis of new porous solids for applications in PSA.

1.1 Porous Solids

A material may be described as a porous solid if it possesses cavities, channels or interstices,[4] a definition which includes materials with isolated void spaces (*closed*

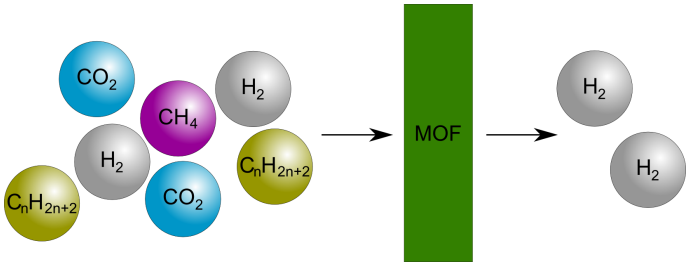

Figure 1.1: Schematic representation of the separation of H_2 from refinery gas using a porous adsorbent, in this case a Metal Organic Framework (MOF).

pores) or channels which are open at only one end (*blind pores*) (*Fig. 1.2*). A more appropriate, if restrictive, description of a porous solid is a material possessing pores with openings at external surfaces or continuous channel structures which may be accessible to an external fluid. Characterisation of pore size by adsorption of fluids has revealed a wide range of diameters which have been classified as:[4]

- Micropores: diameters less then 2 nm
- Mesopores: diameters between 2 and 50 nm
- Macropores: diameters greater than 50 nm

Porous solids have found a wide range of uses including gas storage, separation, catalysis and drug delivery[5, 6, 7] and encompass a wide range of material types from amorphous silicas and activated carbons to crystalline zeolites, zeotypes and, most recently, metal-organic frameworks. Of these materials, the most commercially important are the zeolites and zeotypes, whilst activated carbons have had some commercial success. Recent interest in metal-organic frameworks indicates that they too may be of industrial and/or commercial interest.[8, 9] This work will limit itself to the field of metal-organic frameworks, though it begins with a short review of the origins of zeolite and zeotype science.

1.2 Zeolites

Zeolites are a naturally occuring family of *tectosilicate* minerals, constructed from corner-sharing silicate or aluminate tetrahedra, which link together to form a framework of channels and pore spaces occupied by water molecules (*Fig. 1.3*). Silicon atoms are commonly exchanged to some degree with aluminium cations imparting a charge to the framework and requiring charge balancing alkali metal cations in the pore spaces, which may be exchanged for other cations.[10] The

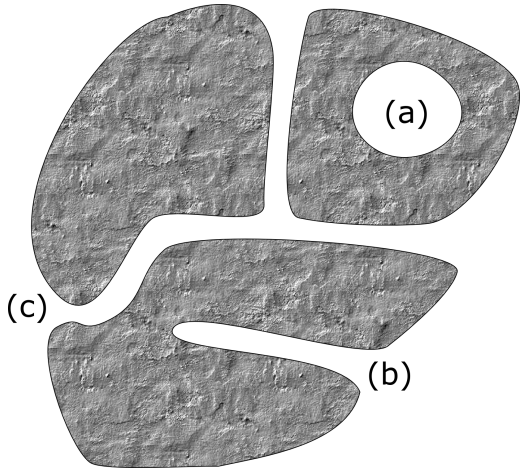

Figure 1.2: Schematic cross-section of a porous particle, showing different types of pore: a) closed pore; b) blind pore; c) through pore. *After Rouquerol et al.[4]*

minerals are commonly found in small deposits in vesicles (*Fig. 1.4*) or larger cavities in igneous and metamorphic geological terranes. The first zeolite mineral, stilbite, was described by A. F. Cronstedt in 1756, who also recognised this was a member of a new class of minerals.[11] Cronstedt observed that on heating a sample of stilbite the apparently dry material released large amounts of steam. Cronstedt named this new family "zeolite" from the Greek *zeo* (to boil) and *lithos* (a stone).

Over the following 200 years zeolites retained an academic interest leading to the observation of important features including adsorptive properties, ion exchange capacity and molecular sieving (of liquids).[12] In the mid to late 1940s R. M. Barrer reported a series of studies including the first reproducible synthesis of the zeolite mordenite,[13] reports of separations using zeolite minerals[14] and, of particular interest to industry, the separation of nitrogen and oxygen by adsorption.[15]

Following this early work, R. M. Milton and D. W. Breck working at Union Carbide discovered a number of important zeolites, including types A, X and Y.[16, 17, 18, 19] This led Union Carbide to commercialise production of zeolites for applications in the drying of refrigerant gas and natural gas. Although zeolite synthesis was possible, extensive commercialisation was hindered by the lack of mineable deposits, which would make large scale use cheaper. Geological discoveries from the late 1950s of large sedimentary deposits of zeolites in the western United States, however, permitted Union Carbide and others to expand the use of zeolites.[12] Early applications of zeolites include the separation of normal and isoparaffin (the so-called "IsoSiv" process);[20] application of zeolite X in catalytic cracking of oil by Mobil oil in the early 1960s; and the introduction in the mid-1970s (by Henkel) of zeolite A as a replacement for phosphates in detergents, following

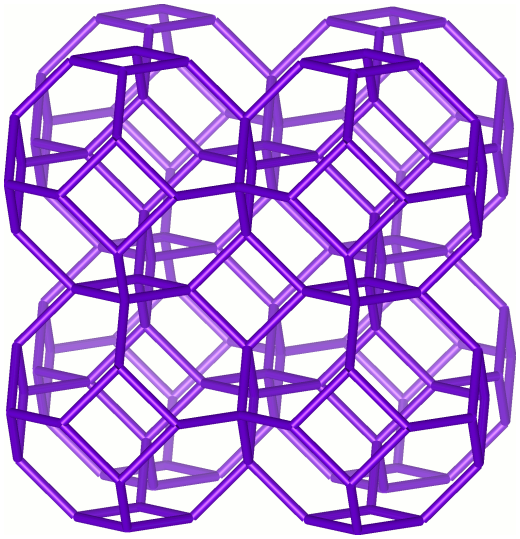

Figure 1.3: The sodalite zeolite network. Nodes are tetrahedra sites (T-sites, commonly Al^{3+} or Si^{4+} cations) within the framework. Edges represent T-O-T bonds.

Figure 1.4: Photograph of vesicular lava (Staffin, Skye, UK). Vesicles, formed by gas within the lava, are filled with zeolite (white crystals) crystallised from Al^{3+} or Si^{4+} fluids which flowed through the lava after cooling. One penny coin for scale.

concerns about over-use of phosphates resulting in eutrophication.[12]

The applications of zeolites have a strong dependence on their crystal structure[14] and on framework composition (i.e. the degree of aluminium substitution).[10] The inclusion of alkylammonium cations in synthesis was found to both control the Si/Al ratio of the resulting zeolite and direct the framework structure.[21, 22] A wide range of quaternary ammonium cations have since been developed to control the synthesis of zeolites and this has led to a growth in the number of known framework types. The online *Database of Zeolite Structures* includes 197 unique zeolite frameworks,[23] of which 38 are known natural zeolites.[24] Computational simulations have indicated, however, that there may be many more structures to find, with over five million frameworks (including some duplicates) in the *Atlas of Prospective Zeolite Structures*.[25]

1.2.1 Zeotypes

To increase the diversity of structure types, and thus applications, building blocks other than silicon and/or aluminium or other tetrahedral cations might be selected. Such materials, possessing zeolite like structures are termed "zeotypes". Aluminophosphates ($AlPO_4$s) reported by Flanigen and co-workers were the first example of such microporous framework materials synthesised without silica[26]. AlPO synthesis requires the presence of an organic amine or quaternary ammonium salt, otherwise dense $AlPO_4$ or $AlPO_4$ hydrates form. $AlPO_4$s consist of strictly

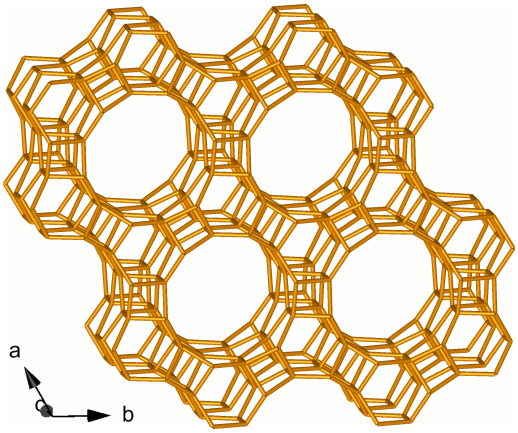

Figure 1.5: The AFI network, of which $AlPO_4$-5 is the type structure.[26] Large cylindrical channels parallel to the *c*-direction are templated by organic amines in the synthesis. In the absence of these templating molecules, dense $AlPO_4$ phases form.

alternating corner-sharing alumina and phosphate tetrahedra, with the most common structure type that of $AlPO_4$-5 (Fig. 1.5). Unlike aluminosilicate zeolites, $AlPO_4$s have a neutral framework. Substitution is however possible on both aluminium and phosphorus sites:[27] with silicon replacing phosphorus, leaving a proton in the framework to form a charge-balancing bridging hydroxyl group;[28] or di- or trivalent metals replacing aluminium, requring charge-balancing by residual alkylammonium cations.[29]

1.3 Metal Organic Frameworks

Metal Organic Frameworks (MOFs — or Porous Coordination Polymers) are hybrid framework materials consisting of rod-like organic molecules that bridge either individual or clusters of metal ions together through coordinative bonding to form a three dimensional network. MOFs contain large voids between the framework-forming units, which may or may not be accessible to adsorbate molecules. Without such pore spaces, the material might better be described as a Coordination Polymer. Exact nomenclature for this class of materials is, however, not rigorously defined[30] and is currently the subject of an IUPAC project.[31]

Kinoshita *et al.* report an early example of the use of organic bridging ligands in the preparation of a framework material constructed through coordinative bonding.[32] Although the structure of Bis(adiponitrilo)copper(I) nitrate is reported as consisting of a diamondoid network of Cu^+ cations linked together by adiponitrile ligands leaving large $\sim 6 \times 12$ Å rhombic channels, no porosity measurements were reported. Allison and Barrer report investigations into the porosity of

Werner complexes (β-M^{2+}(4-methylpyridine)$_4$(SCN)$_2$, M = Mn, Co, Ni), which were thought to demonstrate clathration and reversible guest exchange.[33] These compounds were shown not to be clathrates, as adsorption was reversible, but rather porous crystals with pores accessible to a wide range of adsorbates (including O_2, N_2, Ar, xylenes and C1-C6 alcohols). Werner complexes prepared with alkyl pyridines other than 4-methylpyridine, however, showed little or no porosity. Werner complexes, although porous crystals, are not framework materials as each ligand coordinates only one metal and no extended network is therefore present.

The first designed synthesis of a MOF was reported by Hoskins and Robson in the preparation of Cu^+ (4,4′,4″,4‴-tetracyanotetraphenylmethane) BF_4^-, which possesses a diamondoid network of tetrahedrally coordinated Cu^+ ions coordinated by four tetrahedral tetracyano-ligands (*Fig. 1.6*).[34] Pore-spaces are filled with liquid-like nitrobenzene and half the adamantane cavities are occupied by a BF_4^- counterion. In this seminal work, Hoskins and Robson considered many factors to ensure the preparation of a highly porous material: tetrahedral building units were selected to favour either a diamondoid or Lonsdaleite-like lattice with large pore spaces and windows between the rods; interpenetration/catenation of networks was prevented through selection of a bulky counterion; and the reversible nature of coordinative bonding involved in preparing the material allowed defects formed during crystallisation to be undone and orderly crystallisation continued. Although large pore-spaces are present in this material and the anion exchange of BF_4^- for the larger PF_6^- was observed, Hoskins and Robson do not report porosimetry measurements.

One of the first reported porous MOFs was Zn(BDC)·(DMF)(H_2O),[35] with a structure of H-bonded layers of binuclear Zn^{2+} paddlewheel clusters linked by BDC groups to give an array of rhombic channels parallel to the [2 0 1] direction (*Fig. 1.7*). The material is porous to both N_2 (2.5 mmol g^{-1}) and CO_2 (3.0 mmol g^{-1}), with a (Langmuir) surface area for N_2 of 270 m^2 g^{-1}. The following year the first highly porous MOFs, HKUST-1 and MOF-5 were reported with (Langmuir) surface areas of 918 m^2 g^{-1}[36] and 2900 m^2 g^{-1}[37] respectively. HKUST-1 contains Cu^{2+} cations in a binuclear paddlewheel arrangement, with each cluster linked to 8 others through four trimesate linkers (*Fig. 1.8a*). The structure is built up of octahedral *secondary building units* (*vide infra*) consisting of six paddlewheel clusters linked by four trimesate linkers. These secondary building units stack together to give a porous three dimensionally connected network of 1 nm channels. MOF-5 shows a similar stacking of octahedral units in the form of smaller tetrameric μ_4-oxo clusters of tetrahedrally coordinated Zn^{2+} cations (*Fig. 1.8b*). These are linked together by rod-like BDC units to give two cavities of 1.5 and 1.1 nm diameter linked by

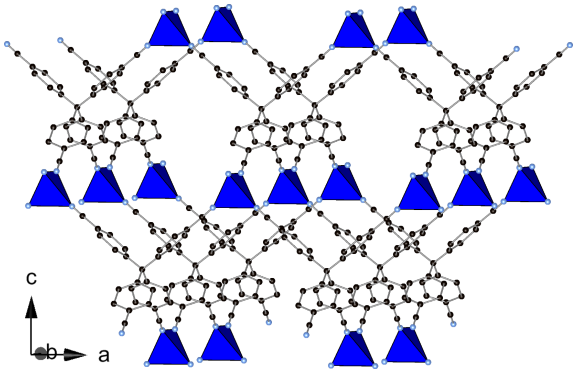

Figure 1.6: Cu^{+} (4,4′,4″,4‴-tetracyanotetraphenylmethane) BF_4^- viewed along the at an oblique angle to the *b*-direction.[34] BF_4^- anions omitted for clarity. The pore network of this structure is highly interconnected. The narrowest parts of the channels have free diameters of ~ 12 Å.

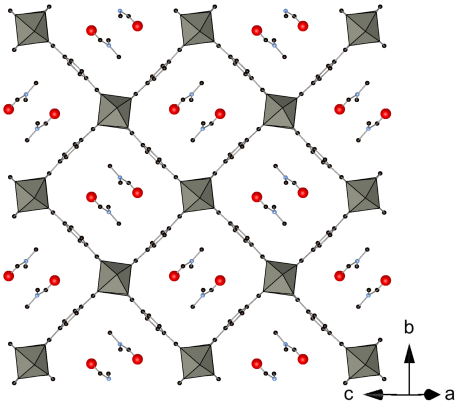

Figure 1.7: View of the first porous Zn-BDC MOF,[35] onto structural layer in the (2 0 1) plane, showing binuclear Zn paddlewheel clusters linked by BDC linkers. Rhombic channels are occupied by DMF molecules

windows of 0.8 nm diameter.

Eddaoudi *et al.* were able to increase the porosity of MOF-5 by increasing the length of the linker between the tetrameric $Zn^{(II)}$ clusters, whilst retaining the same network topology, reporting a series of *isoreticular* frameworks (IRMOF-1 — MOF-5 — to IRMOF-16) with either larger pores or functionalised linkers.[38] Yaghi *et al.* extended the idea of reticular synthesis by using topological ideas to describe the connectivity of any MOF network.[39] To describe a MOF network, the structure is broken down into *secondary building units* (SBUs) which may be individual ligands, clusters of metal cations or larger assemblies of ligands and metal cations (as in the case of HKUST-1). The tiling of these SBUs in space gives the 3-periodic net of the MOF. A searchable database — the Reticular Chemistry Structure Resource (RCSR) — of all known 3-periodic nets has been compiled by O'Keeffe *et al.*[40] which allows the classification of MOFs into families and also the construction of models for crystal structure determination.[41] In reticular synthesis, SBUs of the same topology but longer in length or with additional pendant functional groups are used to prepare materials with the same 3-periodic net, but with larger pores or decorated pore surfaces. The principle of reticular chemistry had, however, been postulated prior to Yaghi *et al.* by Férey who termed it *scale chemistry*.[42, 43] Férey's scale chemistry is not limited to the construction of MOF frameworks, but covers all inorganic materials, considering these materials to be made up from rigid polyhedral bricks which stack together to build the structure.

Serre *et al.* applied ideas of SBUs in the preparation of MIL-88 and MIL-89, using

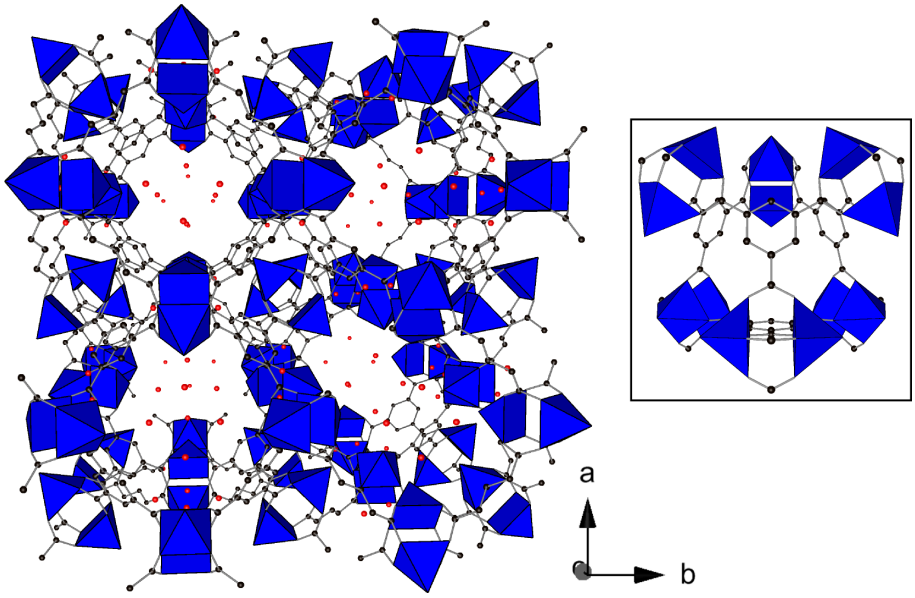

(a)

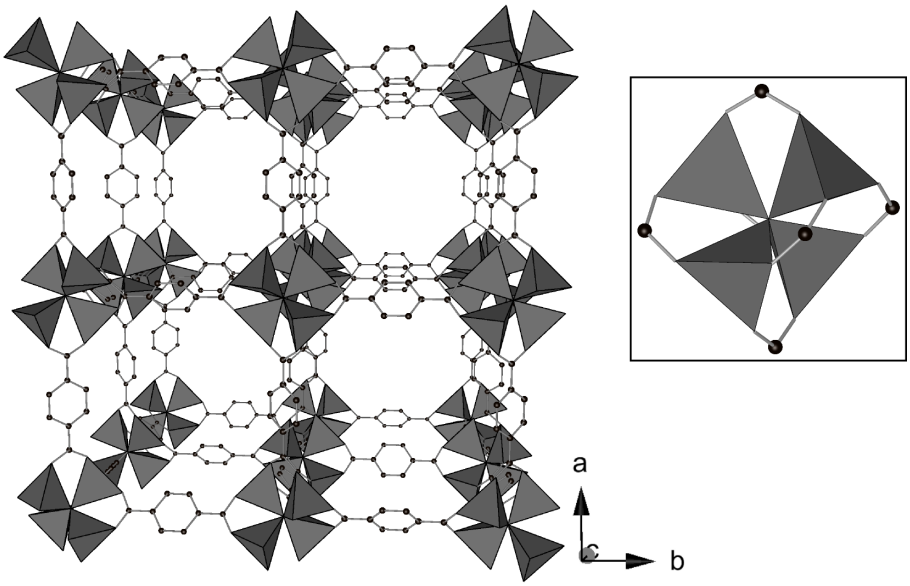

(b)

Figure 1.8: Structures of HKUST-1 (*top*)[36] and MOF-5 (*bottom*)[37] both viewed at oblique angles to the *c*-direction. Insets show the topologically octahedral SBUs forming the structures.

trimeric $Fe^{(III)}$ acetate, the structure of which is based on $Fe_3(\mu_3\text{-O})$ clusters, as the SBU to be linked together with fumaric or *trans,trans*-muconic acids respectively.[44] Applying scale chemistry to MIL-88 Surblé *et al.* were able to prepare an isoreticular family of MIL-88 structures with fumaric acid (MIL-88A), H_2BDC (MIL-88B) (*Fig. 1.9*), 2,6-napthalenedicarboxylic acid (MIL-88C) and 4,4'-biphenyldicarboxylic acid (MIL-88D) with increasingly large unit cell and pore volume.[45] Although non-porous to gas molecules, both MIL-88(A-D) and MIL-89 will exchange solvent with a solution and experience large changes in unit cell volume on solvent exchange or dehydration.[46, 47] In addition to MIL-88B, reaction of H_2BDC with trivalent metals has led to two other important structures: MIL-53[48] and MIL-101[49]. Related to MIL-101, MIL-100 is prepared by reaction of M^{3+} cations and trimesic acid.[50]

MIL-53 has a structure of infinite chains of $MO_4(\mu_2\text{-OH})_2$ (M = Al,[51] Sc,[52] Cr,[48] Fe,[53] Ga,[54] In[55]) octahedra linked by BDC units to give rhombic channels of approximately 0.85 nm free diameter (*Fig. 1.10*). MIL-53 is porous to N_2 at 77 K, with an average (Langmuir) surface area of 1500 $m^2\ g^{-1}$.[56] On adsorption of CO_2, H_2O, CH_4, C_2H_6 and longer alkanes, MIL-53 shows a *breathing effect*, where the initially large pore structure contracts at low adsorbate pressure to a narrow pore form, due to interactions between the structure and the adsorbates.[57, 58] Increasing the adsorbate pressure further causes the structure to open up again into a high-pressure form. For adsorbates with low enthalpies of adsorption (e.g. CH_4, N_2) no breathing effect is observed.[58] Such adsorbate selective responsiveness might suggest applications in gas separation for MIL-53.

The two giant-pore frameworks, MIL-100[50] and MIL-101,[49] were prepared from M^{3+} cations and trimesic acid or H_2BDC, respectively. Conditions were selected favouring the formation of the same trimeric $M_3^{3+}(\mu_3\text{-O})$ clusters present in MIL-88, yielding in both cases microcrystalline powders with extremely complex diffraction patterns. The metal:organic ratio of the solids suggested the presence of super-tetrahedra (S.T. — *Fig. 1.11b*).[50] Taking the example of MIL-100,[50] three candidate structures were obtained through the Automated Assemble of Secondary Building Units (AASBU) approach, in which SBUs (in this case the S.T.) are linked to form a corner-, edge- or face-sharing network of polyhedra in three dimensions.[59] Comparing the simulated powder patterns of the three candidate structures to the experimentally obtained patterns, the best fit was obtained with a structure based on the MTN zeolite network. Both MIL-100 and MIL-101 share the same MTN network with two types of mesoporous cage present in a 2:1 ratio (*Fig. 1.11a*). In MIL-100 the two cages have free diameters of 25 and 29 Å respectively,[50] whereas in MIL-101, due to the different construction of the S.T., the cages are larger with

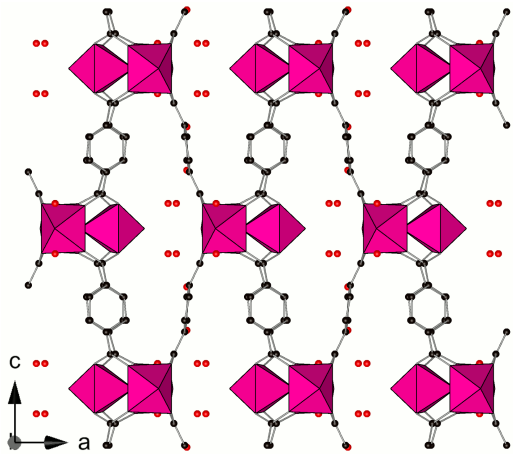

Figure 1.9: Structure of MIL-88B(Cr),[45] viewed along the *b* axis. Structure shown is a small pore form. On solvent exchange the pores open, thanks to the flexibility of the structure.

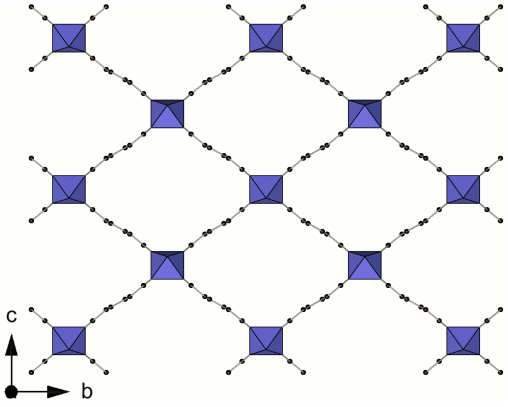

Figure 1.10: The fully open form of MIL-53(Al),[51] viewed along the *a*-direction. Pores in the structure are responsive to temperature and pressure. Pore opening/closing occurs through hinging of the carboxylate groups.

free diameters of 29 and 34 Å.[49] As a consequence MIL-101 has a greater porosity, as measured by (Langmuir) surface area (5900 $m^2\ g^{-1}$), than MIL-100 (3100 $m^2\ g^{-1}$).

From these few examples it is clear that the carboxylic acid is a versatile framework-forming functional group yielding both highly-porous and flexible materials. An alternative functional group is the phosphonic acid, RPO_3H_2, which may exhibit a greater diversity coordination modes, thanks to the presence of three (rather than two) O atoms able to engage in coordinative bonding (*Fig. 1.12*). Many phosphonic acids are also synthesised through a modified Mannich reaction (see *Section 3.1*) and thus have an α-amino group which may also bond to metal cations. The exact number of coordinative bonds, and thus the network formed by a given phosphonate, may be controlled by the synthesis pH conditions. In addition metal phosphonates have shown a higher thermal stability than similar carboxylate structures,[60] making them suitable for use under demanding industrial conditions. In recent years there has been an expansion in the number of known phosphonates. We now review important developments leading to these new materials and the current state of the art.

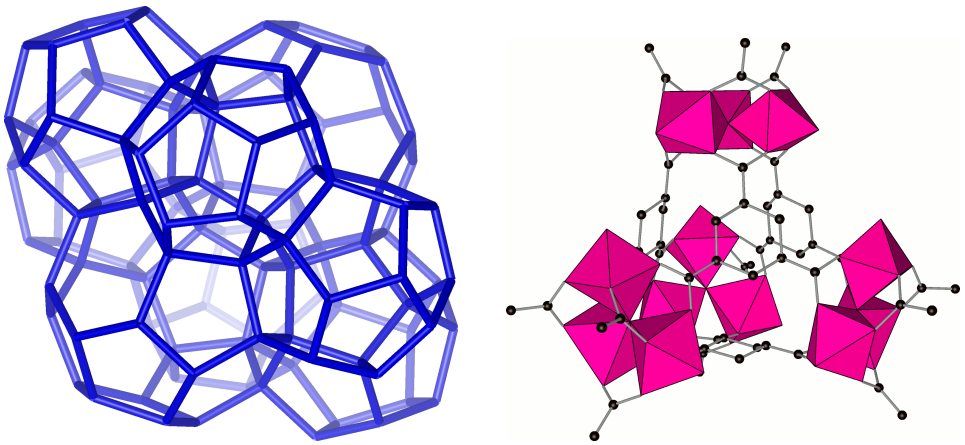

(a) (b)

Figure 1.11: MIL-100 and MIL-101 both adopt the MTN network (*left*). The tetrahedral building unit of each structure is a supertetrahedral (S.T.) SBU constructed from trimeric M_3O clusters (*right*: S.T. of MIL-100).A hierarchical pore network is formed, with two larger cages of the MTN network and a smaller cage delimited within each S.T.

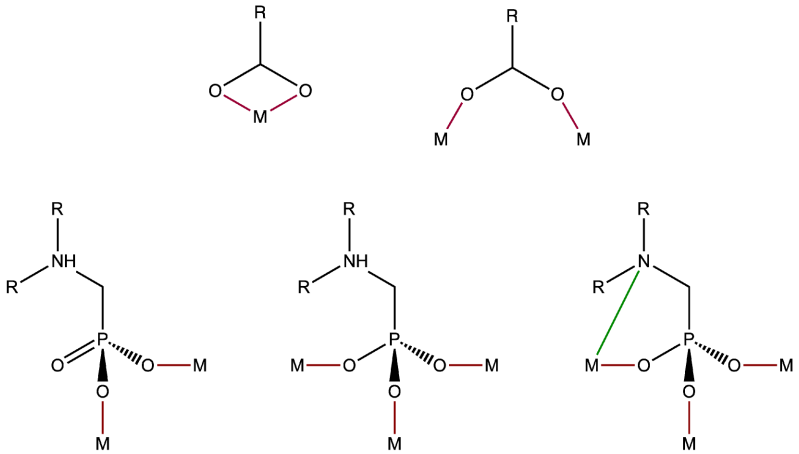

Figure 1.12: Comparison of some of the coordination modes observed in carboxylate MOFs (*top*) and in phosphonate MOFs (*bottom* — see *Sections 1.4 and 1.4.2*). The third O atom and the α-amino group allow the PO_3C group to adopt a greater range of coordination modes.

1.4 Porous Metal Phosphonates

Much early work on metal phosphonates focussed on the preparation of porous derivatives of α- and γ-zirconium phosphates (α-ZrP & γ-ZrP). α-ZrP consists of a single layer of ZrO_6 octahedra with O atoms from six distinct triply coordinated phosphate tetrahedra. The fourth O atom of each phosphate tetrahedron is an OH group which projects into the interlayer region (*Fig. 1.13a*).[61] γ-ZrP has a double layer structure of ZrO_6 octahedra with four O atoms provided by fully coordinated phosphate groups and two O atoms from dihydrogenphosphate groups on the surface of the layer. The protonated dihydrogenphosphate O atoms project into the interlayer space(*Fig. 1.13b*).[62]

Through the decomposition of zirconium fluoride complexes in the presence of phosphonic acids, Alberti *et al.* prepared a derivative of the α-ZrP structure in which organic moieties replace OH groups projecting into the interlayer region.[63] Further examples of this type were provided by Dines and DiGiacomo, who also demonstrated significant porosity in some materials ($Zr(O_3PCH_3)_2$: 260–500 $m^2\ g^{-1}$) and extended the range of structures to other M^{4+} cations (*Fig. 1.14*).[64] Functionalised α-ZrP and γ-ZrP have been prepared by reaction of the parent phase in liquid ethylene oxide and in ethylene oxide aqueous solution, respectively.[65] γ-ZrP phosphonate derivatives have been prepared by Yamanaka and co-workers, through exchange of dihydrogenphosphate groups.[66, 67] Using a more complete structural model, Alberti *et al.* showed that partial or complete topotactic replacement of dihydrogenphosphate groups is possible with a variety of phosphonic

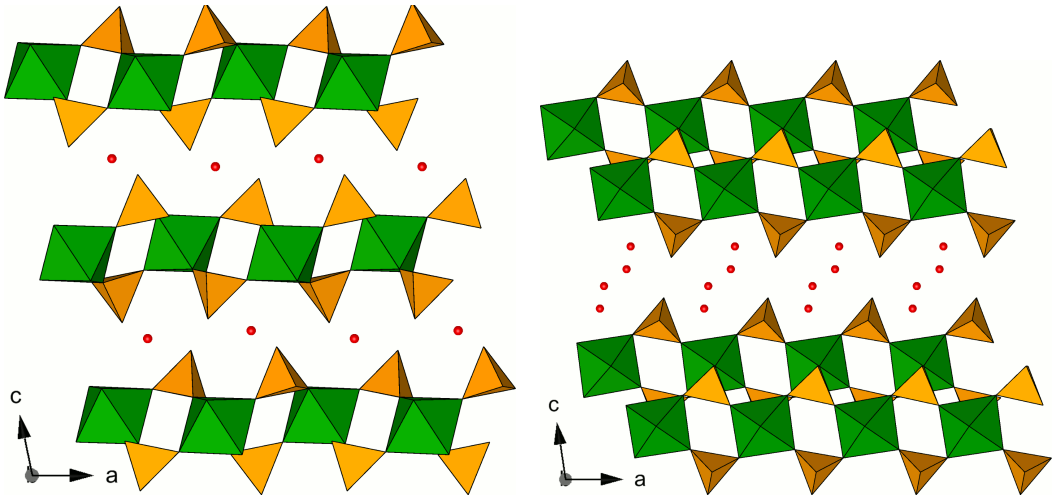

(a) α zirconium phosphate.[61] (b) γ zirconium phosphate.[62]

Figure 1.13: View along the *b*-axis of two zirconium phosphate phases. Zr polyhedra shown in green.

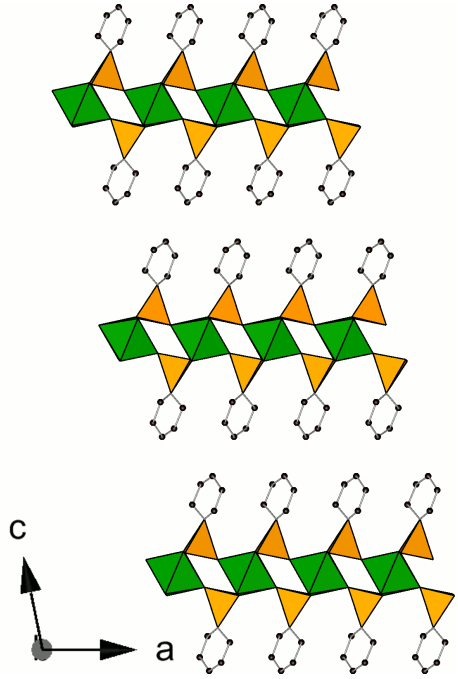

Figure 1.14: Example of a layered phosphonate derivative of α-ZrP.[72] Layers have the α-ZrP structure, but are capped with phenyl rings rather than OH groups as in the parent structure.

acids, though direct synthesis of these γ-ZrP derivatives is not.[68] Ortiz-Avila *et al.* prepared polyether-functionalised derivatives of α-ZrP by direct reaction of $ZrOCl_2$ with polyether phosphates[69] and polyimine α-ZrP derivatives through direct reaction with $ZrOCl_2$ and polyaminophosphonic acids.[70] Both the polyether and polyimine derivatives of α-ZrP behave as ion conductors, whilst in the protonated state the polyimine materials may act as anion exchangers.[71] Other applications that have been suggested include shape-selective catalysis, molecular sieving and proton conduction.[68]

Following the observation of porosity in phosphonate-functionalised α-ZrP,[64] Dines *et al.* attempted to prepare microporous ZrP derivatives by pillaring ZrP layers with bisphosphonic acid ligands, using three routes:[73] co-precipitation of $ZrOCl_2$ with bisphosphonic acid and a second smaller phosphonate/phosphate; anion substitution[66] of phosphate groups in γ-ZrP for bisphosphonic acid; and co-precipitation of a mixed bisphosphate ester/bisphosphonic acid ZrP derivative, removing the ester by hydrolysis. Only the last of these was successful in preparing a porous material, with a surface area of 209 m^2 g^{-1}. In the second approach, pillared layered ZrP derivatives were obtained with flexible bisphosphonates only (though no porosity is reported); with rigid bisphosphonates, bilayered structures were obtained. Dines *et al.* report only poorly crystalline products for the

first method. Clearfield and co-workers have shown that Zr has a preference for coordination by phosphonates rather than by phosphites/phosphates and therefore that highly pillared products are likely.[71] Using bisphosphonic acids without a spacer phosphite/phosphate, Clearfield observed a dependence of the surface area on the solvent system used: little or no surface area in water-alcohol; up to 250 $m^2\ g^{-1}$ in DMSO, with greater surface areas obtained when spacers are included.[71] Clearfield indicates that porosity is due to both microporous and mesoporous spaces in the solid,[71] though Alberti *et al.* suggest that spacing between phosphonate groups in a fully pillared material is too small to result in porosity and that observed porosity is due to intercrystalline mesoporosity.[74] To produce microporous pillared layered ZrP derivatives with a more regular distribution of pillars, Alberti *et al.* reacted the sterically bulky 3,3′,5,5′-tetramethylbiphenylbis(phosphonic acid) with $ZrOCl_2$ to give a porous pillared ZrP derivative with a (BET) surface area of 375 $m^2\ g^{-1}$.[75]

These examples indicate there is little possibility of preparing of creating layered metal phosphonate materials with similar porosity to the carboxylate MOFs (*vide supra*). Therefore another approach to produce porous metal phosphonates is necessary.

1.4.1 Framework Metal Phosphonates

The unidirectional channel materials reported from reactions of methylphosphonic acid were some of the first examples of framework metal phosphonates without layered structures. The first of these materials, β-Cu(O_3PMe) has a framework constructed around helical chains of edge-sharing square-based pyramidally coordinated Cu^{2+} cations, coordinated only by fully coordinated PO_3C groups, and linked to three other chains.[76] A honeycomb array of $\sim$ 3 Å channels lined with methyl groups is formed by this network, but these are too small to admit gas molecules. Two related Al^{3+} methylphosphonate frameworks reported by Maeda *et al.*, AlMePO-α ($Al_2(O_3PMe)_3{\cdot}xH_2O$, x = 0-1.5 — *Fig. 1.15a*)[77] and AlMePO-β ($Al_2(O_3PMe)_3{\cdot}H_2O$ — *Fig. 1.15b*),[78, 79], provide further examples of materials with unidirectional channels constructed from fully coordinated PO_3C tetrahedra. Both AlMePO-α and AlMePO-β contain octahedral and tetrahedral Al^{3+} in a 1:3 ratio. The two structures differ in that AlMePO-β crystallises in a higher symmetry space group ($R\,3c$) than AlMePO-α ($P\,31c$). AlMePO-α has been shown to be the more thermodynamically stable phase by both simulation and experiment. Conversion of AlMePO-β to AlMePO-α proceeds via a topotactic phase transition under a flow of moist N_2 gas at $\sim$ 450°C.[60] Channels in both structures are lined with methyl groups, with channels in AlMePO-β being approximately circular

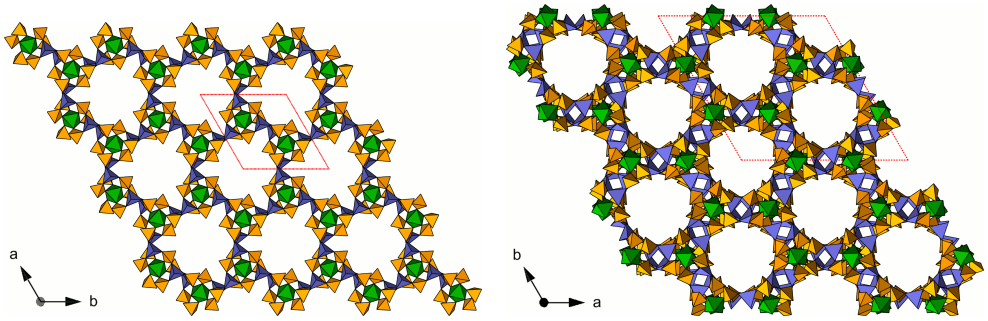

(a) AlMePO-α (b) AlMePO-β

Figure 1.15: AlMePO structures viewed along the c-axis. Channels in AlMePO-β have an approximately circular cross-section, whilst in AlMePO-α they are more triangular. Octahedral Al^{3+} sites shown in green; tetrahedral Al^{3+} sites in mauve; unit cell indicated by red lines.

in cross-section with a free diameter of 6 Å, whilst channels in AlMePO-α are, due to the higher symmetry, almost equlilateral triangular in cross-section (with triangle side length of $\sim$ 7 Å). Deuterium solid state NMR studies have shown that the methyl groups on the walls of the channels are rapidly rotating, even at low temperatures,[80] resulting in unusual adsorption properties for small gas molecules such as N_2 and H_2O.[81] The hydrophobicity of the channels makes AlMePOs good sorbents for a range of hydrocarbons.[81] NMR studies have shown a high mobility for adsorbed monoaromatic hydrocarbons, with adsorbates in AlMePO-β having a greater mobility thanks to the wider channels of the framework, even at low temperature, indicating a low entropy loss on adsorption compared to similar sorbents.[82] AlMePO-α has also been shown to be a selective adsorbent of ethyl chloride in the presence of vinyl chloride, which is of interest industrially in the purification of streams of vinyl chloride, the monomer of PVC.[83]

After these initial reports, interest in the synthesis of framework metal phosphonates increased dramatically. However, subsequent studies were unsuccessful in preparing materials with permanent porosity. For example $Co_2(O_3PCH_2PO_3)\cdot H_2O$ of Lohse and Sevov,[84] containing $\sim$ 2 Å wide channels lined with methylene groups and chemisorbed water molecules, is a three-dimensional open-framework but the channels are too small to admit gas molecules. Ni^{2+}[85] and Zn^{2+}[86] isostructural analogues have also been reported, labelled VSB-3. A second example is provided by $NaScMePO_3\cdot H_2O$ with two parallel channel systems.[87] The first is lined with methyl groups with a free diameter of $\sim$ 2 Å, which is too small to admit adsorbates. The second is occupied by physisorbed water, which may be reversibly removed, though the dehydrated material is not porous to N_2.

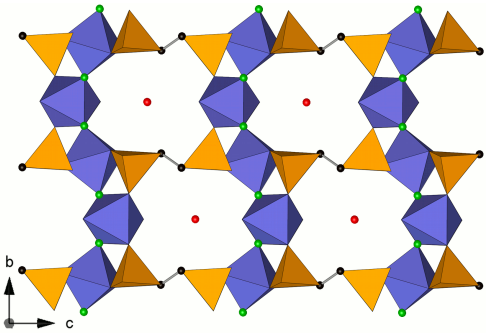

Figure 1.16: $Al_2[O_3PC_2H_4PO_3](H_2O)_2F_2{\cdot}H_2O$ reported by Harvey *et al.*[88] viewed along the *a*-direction showing channels within the structure.

Syntheses using the longer ethylenedisphosphonic acid ligand have also been reported. Harvey *et al.* synthesised $Al_2[O_3PC_2H_4PO_3](H_2O)_2F_2{\cdot}H_2O$,[88] constructed from chains of corner-sharing AlO_4F_2 octahedra, parallel to the *b*-direction. Alternating octahedra have two F^- in *cis* and *trans* configurations, linked by μ_2-F^- along the chains. Chains are linked in the *a*-direction by fully coordinated PO_3C tetrahedra and in the *c*-direction by the ethylene backbone of the ligand, forming $\sim 5 \times 5$ Å channels which are occupied by a physisorbed water in the as-prepared material (*Fig. 1.16*). The structure may be dehydrated, but does not rehydrate, due to the hydrophobic nature of the channels. Harvey *et al.* showed that the structure could be made porous by co-precipitating a mixed $Al^{(III)}$ ethylenediphosphonate/phosphite (*c.f.* Dines — *vide supra*).[89] This mixed phosphonate/phosphite readsorbed up to $\sim$ 92 % of the mass of water lost on dehydration (compared to only $\sim$ 57 % for the pure phosphonate). The degree of readsorption is dependent on the amount of phosphite incorporated into the structure.

A complete review of similar open-framework solids prepared with alkylphosphonates is provided by Maeda.[90] Many of these materials are examples of inorganic frameworks decorated with organic groups, where the organic group does not play a structural role in the framework. In an attempt to obtain more porous materials, efforts have focussed on the use of longer di-, tri- or indeed tetraphosphonic acid linkers, though with such linkers there is a greater likelihood of forming layered materials and it is therefore necessary to consider how this might be avoided. In these materials the organic group plays a true structural role, for example in linking unidirectional chains together to form a channel network. Some examples of porous phosphonates are now presented, though a more complete review of the area is provided by Shimizu *et al.*[91]

Vasylyev *et al.* report the synthesis of $Ti^{(IV)}$[92] and $V^{(III)}$[93] materials with

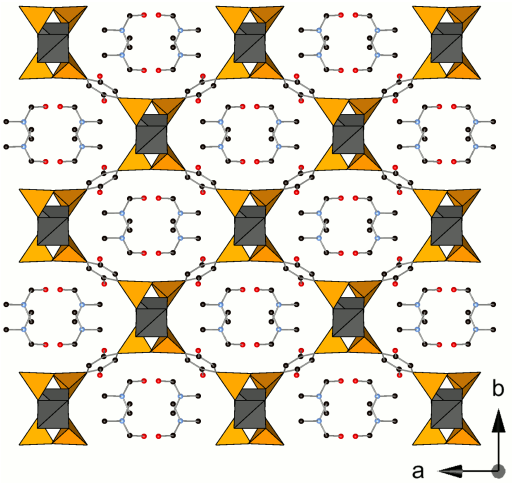

Figure 1.17: Zn^{2+} 1,4-dihydroxy-2,5-benzenediphosphonate of Liang *et al.*[95] viewed along the *c*-direction. Physisorbed DMF molecules shownin the channels.

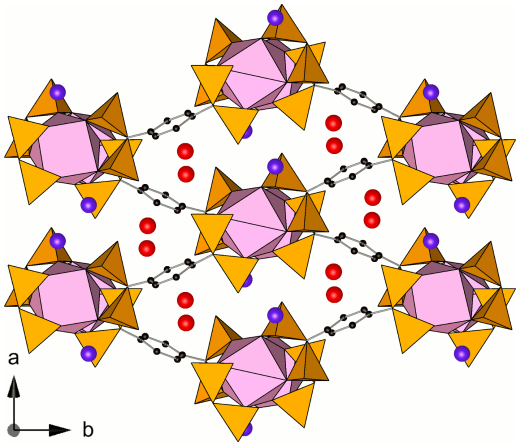

Figure 1.18: La^{3+}/Na^{+} tetraphosphonate reported by Plabst *et al.*[97] viewed along the *c*-direction.

the ligand 1,3,5,7-tetrakis(4-phenylphosphonic acid)adamantane. Both the $Ti^{(IV)}$ and $V^{(III)}$ forms are porous to N_2 with (BET) surface areas of $\sim$ 550 m^2 g^{-1} and $\sim$ 120 m^2 g^{-1}, respectively. Analysis of the pore size distribution of the $Ti^{(IV)}$ material shows both micro- and mesoporosity, with maxima at 38 Å and 13.5 Å respectively.[92] Both materials are poorly crystalline, with only two broad peaks at less than 12° 2θ in the powder X-ray diffraction patterns (Cu K_α). From the expected connectivity and the porosity measurements a structural model was proposed for the $Ti^{(IV)}$ material, with 22 Å and 4.8 Å voids.[92] Taylor *et al.* used the same ligand in the preparation of a more crystalline porous $Cu^{(II)}$ phosphonate, based on a diamondoid network of tetrahedral trimeric Cu^{2+} clusters and tetraphosphonate linkers.[94] The structure is doubly interpenetrated, but is still porous to N_2 with a (BET) surface area of $\sim$ 180 m^2 g^{-1}.

Reaction of 1,4-dihydroxy-2,5-benzenediphosphonic acid and $Zn(ClO_4)_2$ yields a network of ZnO_3P chains connected to four others in two dimensions to form an array of $\sim$ 10 Å rhombic channels. Channels are initially filled with DMF molecules (the crystallisation solvent) which may be removed on heating (*Fig. 1.17*).[95] The structure is porous to N_2 and CO_2 with (BET) surface areas for both adsorbates of $\sim$ 200 m^2 g^{-1}. The remarkable feature of this framework is that, whereas layered phases are obtained in the reaction of 1,4-benzenediphosphonic acid with $Zn^{(II)}$,[96] in this structure chains form. This suggests that the hydroxyl groups perturb the packing of the structure, disfavouring the formation of layers.[95]

Plabst and Bein report the synthesis of three structure types through the reaction

of 1,4-phenylenebis(methylidyne)tetrakis(phosphonic acid) with Ln^{3+} cations using high-throughput synthesis to elucidate the relationship between the synthesis conditions and the frameworks formed.[97] Two of the structures consist of layers of Ln^{3+} cations coordinated by phosphonate groups to form isolated LnO_8 or edge-sharing dimeric Ln_2O_{14} chains, with the organic portion of the linker joining the chains into layers. A H-bonding network develops between interlayer water molecules and protonated PO_3C groups to hold the structure together. The third framework, $NaLn(L_{Tet}H_4)\cdot 4H_2O$ (Ln = La, Nd, Gd, Dy; $\mathbf{L}_{Tet}$ = tetraphosphonate) is formed from chains of isolated LnO_8 polyhedra linked in two dimensions to form a trellis-like network of unidirectional channels filled with hydrated Na^+ cations and physisorbed water molecules (*Fig. 1.18*). Both physisorbed and Na-coordinating water molecules may be reversibly removed from the structure, resulting in a slight contraction of the channels to allow coordination of the Na^+ cations by PO_3C O atoms.[98] Ion exchange experiments have also been performed, indicating that Na^+ may be removed, but that the framework is selective to the coordination of monovalent cations.[98]

1.4.2 Metal Phosphonate Frameworks Formed with N,N′-piperazinebis(methylenephosphonic acid) and Related Ligands

The use of monofunctional ligands (i.e. containing only phosphonic acids) has provided a few examples of porous materials. However the bifunctional ligand N,N′-piperazinebis(methylenephosphonic acid) ($H_4\mathbf{L}$) and the related ligands N,N′-2-methylpiperazinebis(methylenephosphonic acid) ($H_4\mathbf{L}'$) and N,N′-2,5-dimethylpiperazinebis(methylenephosphonic acid) ($H_4\mathbf{L}''$) have produced as great a structural diversity of metal phosphonates and by far the greatest range of permanently porous metal phosphonates of any one family of ligands to date.

$H_4\mathbf{L}$ was first used in the preparation of a coordination polymer by Choi *et al.*, who report the preparation of $Cd(OH)(H_2O)_3(\mathbf{L}H_3)\cdot xH_2O$, a linear chain compound of CdO_6 octahedra coordinatively linked through monodentate $H_3\mathbf{L}^-$ units.[99] The first phosphonate framework prepared with $H_4\mathbf{L}$, reported by the group of Zubieta, was $VO(H_2O)(\mathbf{L}H_2)$,[100] in which layers of PO_3C corner-share with $V^{4+}O_6$ octahedra in a bridging mode to form a layered structure of linked $[V_4P_4O_8]$ rings in the (1 0 0) plane, pillared in the third dimension through covalently bound protonated piperazinyl units with a chair conformation (*Fig. 1.19*). Pendant P=O groups engage in H-bonding with protonated piperazinyl N atoms, which is a feature of many structures formed with $H_4\mathbf{L}$. Isostructural analogues of this

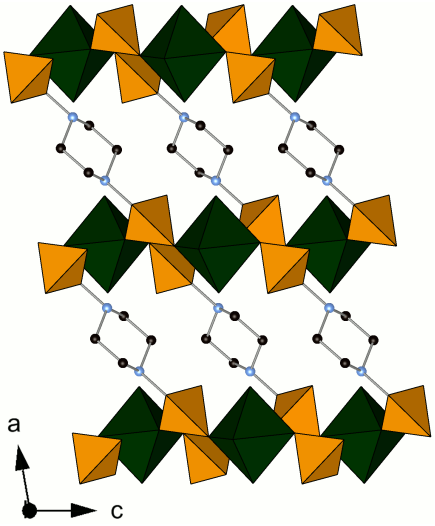

Figure 1.19: Layered vanadyl phase viewed along the *b*-axis, showing the pillaring piperazinyl ligands.

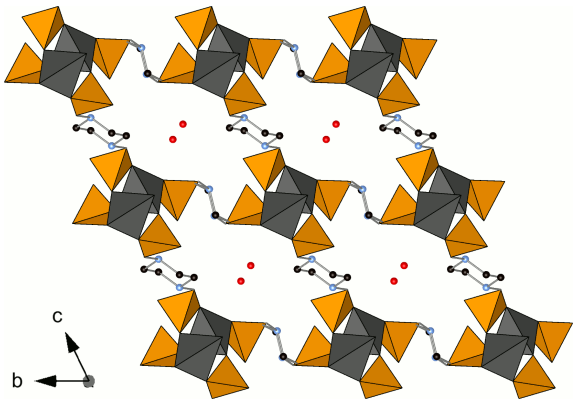

Figure 1.20: First framework structure reported with $H_4\mathbf{L}$, $M(\mathbf{L}H_2)\cdot xH_2O$, viewed along the channel axis with physisorbed water occupying the narrow channels. Metal tetrahedra shown in grey.

framework have recently been reported with Zr^{4+} cations, where the vanadyl O atom and the water molecule are replaced by two F^- anions,[101] and with Sb^{3+} cations, in which the vanadyl O atom is replaced by a lone pair.[102] Neither the $V^{(IV)}$, nor $Zr^{(IV)}$, nor $Sb^{(III)}$ structures are porous. Zubieta and co-workers report the synthesis of a second framework, $M(\mathbf{L}H_2)\cdot xH_2O$ (M = Mn, Co) with a three dimensional channel network (*Fig. 1.20*).[103] Tetrahedrally coordinated M^{2+} cations and PO_3C tetrahedra corner-share to form 8-membered $[M_2P_2O_4]$ rings, which link to form chains in the *a*-direction. Pendant P=O groups again form H-bonds with protonated piperazinyl moieties, which have a chair conformation. The chains are bridged together by bisphosphonate units, with each phosphonic acid coordinating with two O atoms, to give an array of narrow rhombic channels. The framework shows reversible uptake of water molecules, but the dehydrated structure shows no permanent porosity to other small gas molecules. $Zn^{(II)}$ and $Fe^{(II)}$ analogues of this framework have also been reported.[104, 105]

These frameworks show the two most common structural motifs observed with piperazine-derived linkers: layered structures, where inorganic layers are pillared by piperazinyl units and unidirectional chain structures, where inorganic chains linked in two or more directions to form frameworks with channel structures. A variety of layered phases have been reported and these are discussed in terms of the metal phosphonate rings which link to form their layers. Unidirectional chain structured materials will then be discussed, including the only two porous framework materials prepared with $H_4\mathbf{L}$ and its derivatives, with reference to the different structural motifs observed in the structures of the chains.

Metal Phosphonates with H_4**L** with Layered Structures

Reactions of $Zn^{(II)}$ at elevated pH form Zn_2**L** in which tetrahedral Zn^{2+} cations are coordinated by three O atoms and a piperazinyl N atom.[104] The building unit of this structure, like M(**L**H_2)·xH_2O, is the [$Zn_2P_2O_4$] 8-membered ring, which in Zn_2**L** is polymerised into undulating layers of alternating 8- and 16-membered rings in the (1 0 1) plane through coordination of all three O atoms in each PO_3 group. Layers are pillared by piperazinyl groups coordinating through their N atoms to give a denser, non-porous framework than the phase reported by Zubieta and co-workers.

Recently Zhang *et al.* have reported a third Zn^{II} structure, Zn_2**L**·2H_2O, also prepared at elevated pH, in which tetrahedral Zn^{2+} cations are again coordinated by three PO_3C O atoms and one piperazinyl N atom.[102] In this pillared layered structure 12-membered [$Zn_3P_3O_6$] rings, rather than the 8-membered rings of Zn_2**L**, are polymerised into undulating layers in the (0 0 1) plane. These layers are again pillared by piperazinyl moieties, in a chair conformation, through fully coordinating PO_3C groups and piperazinyl N atoms. A related phase, Cu_2**L**·2H_2O, was reported by Wang *et al.*, in which Cu^{2+} cations are coordinated in a square-based pyramidal geometry by three PO_3C O atoms, a piperazinyl N atom and an additional O atom from a water molecule.[106] Layers have the same connectivity as Zn_2**L**·2H_2O, based on 12-membered rings, but due to the different coordination environment of the Cu^{2+} cations, the pillaring between the layers is different.

In addition to Sb(H_2O)(**L**H_2), two further pillared layered frameworks have been reported with main group elements. In Sn(**L**H_2) pseudo-trigonal bipyramidal Sn^{2+} cations are coordinated by four O atoms from four different bridging PO_3C tetrahedra, with the fifth coordination site occupied by a lone pair.[107] Rectangular [$Sn_4P_4O_8$] rings are linked to form layers in the (0 0 1) plane by piperazinyl ligands in a chair conformation, but with one methylenephosphonate group axial and one equatorial. Protonated piperazinyl N atoms H-bond with the pendant P=O group of one PO_3C tetrahedron and the lone pair of the Sn. The third main group pillared layered structure, $Pb_3(OH)_2$**L**, consists of ribbons of edge-sharing distorted PbO_5N (with a long 2.86 Å Pb-O contact) and PbO_6 octahedra.[107] The third PO_3C O atom links the ribbons into layers in the (1 0 0) plane and layers are pillared in the third dimension by N-coordinating piperazinyl groups.

Trivalent Framework Metal Phosphonates with H_4**L**

The second reported unidirectional chain structured framework, and the first porous framework bisphosphonate material, was MIL-91 (M(**L**H_2)·xH_2O), M = $Al^{(III)}$(OH), $Ti^{(IV)}O$).[108] MIL-91 is based on corner-sharing "tancoite" chains[109] of MO_6

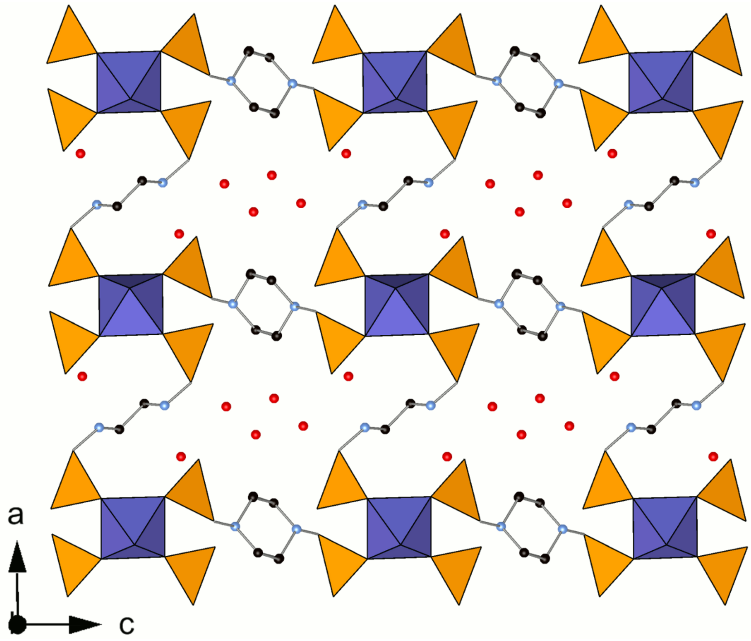

Figure 1.21: First porous framework material with H_4**L**, MIL-91(Al), viewed along *b*-direction parallel to the Al-(OH)-Al chains, showing the 4 Å channels occupied by physisorbed water molecules.

octahedra, where corner-sharing O atoms are protonated in the Al^{III} form. Chains are linked to four others via two crystallographically distinct sets of ligands to form square cross-section channels (*Fig. 1.21*). Each PO_3C group binds to two metal cations via two O atoms, with the third P=O group able to engage in H-bonding to an adjacent protonated N atom of a piperazine ring. H-bonding within the framework provides a driving force during synthesis to direct crystallisation of the framework and also provides an enthalpic stabilisation in the final material, though above 200°C these interactions are no longer able to stabilise the structure, leading to framework collapse. Physiorbed water molecules in the $\sim$ 4 Å channels engage in H-bonding with the framework and may be easily and reversibly removed without significant disruption of the framework. Permanent porosity within the framework has been analysed by N_2 adsorption measurements at 77 K indicating pore volumes of 0.195 $cm^3\ g^{-1}$ (Al) and 0.19 $cm^3\ g^{-1}$ (Ti), with (Langmuir) surface areas for both solids of approximately 500 $m^2\ g^{-1}$.[108]

Subsequent efforts to produce porous frameworks with the H_4**L** linker focussed on the use of other trivalent cations and have yielded a wealth of different chain structured frameworks, particularly with the rare-earth cations (Sc, Y, La–Lu). The first examples, La_2(**L**H_2)(**L**H_4)Cl_2 and La_2(**L**H_2)(**L**H_3)Cl reported by Groves *et al.*, both have chains parallel to the *a*-direction with similar motifs of LaO_7 polyhedra linked by fully coordinated PO_3C tetrahedra.[110] Chains are linked by

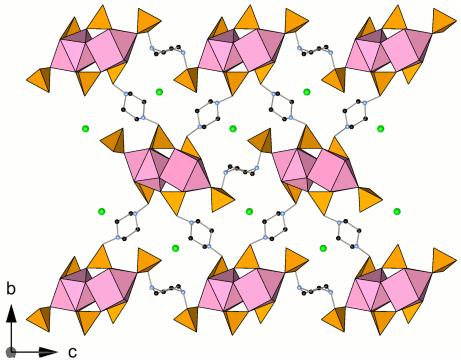

Figure 1.22: $La_2(\mathbf{L}H_2)(\mathbf{L}H_4)Cl_2$ phase reported by Groves *et al.*[110] viewed along the *a*-direction. Templating Cl^- anions shown as green spheres.

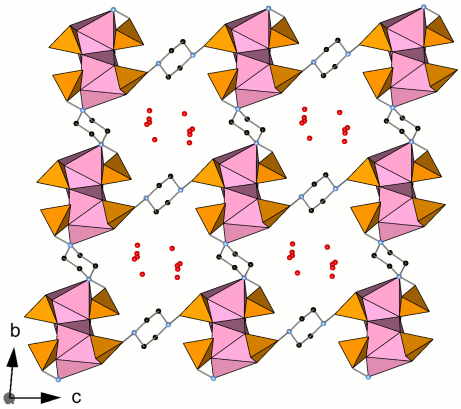

Figure 1.23: $Ln\mathbf{L}(\mathbf{L}H_2)\cdot 4.5H_2O$ phase reported by Mowat *et al.*[111] showing the LnO_7N polyhedra, coordinated by both PO_3C groups and a piperazinyl N atom.

two crystallographically distinct groups of ligands, one with both PO_3C groups fully coordinated, of which there are twice as many, and the other with both PO_3C groups monodentate. Channels in both structures are occupied by extra-framework Cl^- ions. Differences arise between the two structures in the configuration of the monodentate linker. In $La_2(\mathbf{L}H_2)(\mathbf{L}H_4)Cl_2$ (*Fig. 1.22*) both methylenephosphonate groups are axial to maximise the number of H-bonding interactions within the framework and with extra-framework Cl^- ions, whereas in $La_2(\mathbf{L}H_2)(\mathbf{L}H_3)Cl$ one group is axial and one equatorial. The final structure is determined by how extensive the H-bonding network formed during synthesis is. With more Cl^- in solution, a more extensive H-bonding network can develop, and formation of $La_2(\mathbf{L}H_2)(\mathbf{L}H_4)Cl_2$ is favoured.

With other light lanthanide cations, $H_4\mathbf{L}$ produces two phases depending on the pH of the synthesis gel. Without modification of the initial pH, the ligand remains partially protonated and the phase $Ln\mathbf{L}(\mathbf{L}H_2)\cdot 4.5H_2O$ (Ln = La, Ce) is obtained.[111] In this structure, chains of edge-sharing LnO_7N polyhedra (in the case of La, with a long La-N contact of 2.87 Å) parallel to the *a*-direction are coordinated by two distinct groups of linkers, as in Groves' $La^{(III)}$ structures.[110] In the first group, both PO_3C tetrahedra fully coordinate the Ln^{3+} cation and both N atoms are protonated; in the other group both PO_3C tetrahedra are bidentate and both N atoms coordinate the Ln^{3+} cation. Chains are linked to four others by piperazinyl groups in a chair conformation, with the protonated N atoms of one group of linkers H-bonded to the pendant P=O bonds of the second, forming channels parallel to the *a*-direction (*Fig. 1.23*). The material shows reversible dehydration, but the dehydrated structure is not permanently porous. If the pH is raised with the

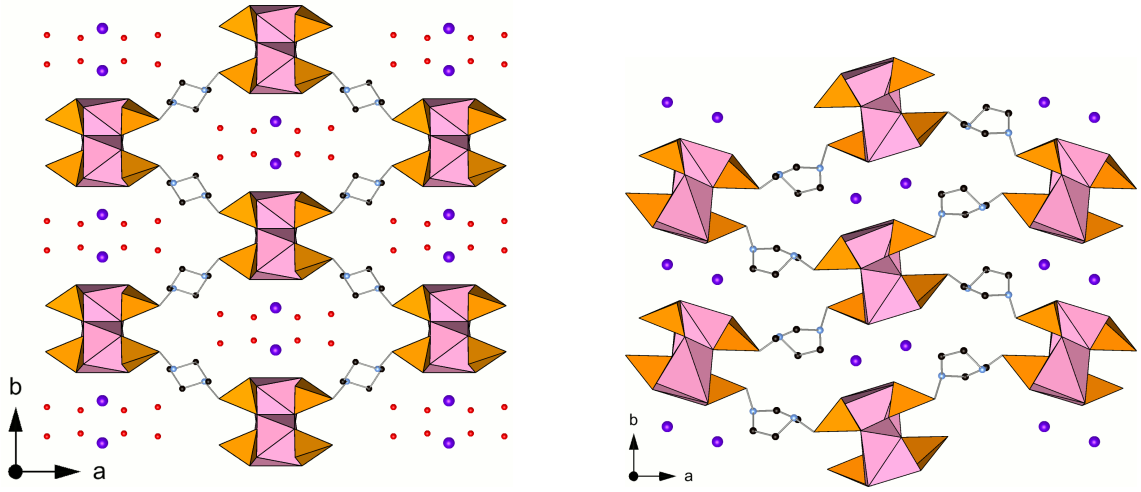

Figure 1.24: The as-prepared (*left*) and dehydrated (*right* structures of MLn**L**·4H_2O. On dehydration the ligand changes conformation from chair to boat. This transition is fully reversible.[111]

addition of alkali metal hydroxides, the ligand is fully deprotonated and the phase MLn**L**·4H_2O (M = Na, K, Cs; Ln = La–Nd) forms.[111] 8-fold coordinate Ln^{3+} cations are linked into chains by fully coordinated PO_3C groups, which themselves link three different Ln^{3+} cations. Chains are linked to four others by piperazinyl groups in a chair configuration, forming a trellis-like arrangement of channels parallel to the *c*-direction (*Fig. 1.24a*). Channels are occupied by hydrated alkali metal cations which balance the charge of the framework and may be exchanged, as also recently observed with the Ln tetraphosphonate of Plabst *et al.*[98] Physisorbed water molecules, coordinating the alkali metal, may be reversibly removed, though on dehydration the material undergoes a phase transition in which the piperazinyl rings adopt a boat conformation, essentially closing the channels and resulting in the loss of permanent porosity (*Fig. 1.24b*).

Using H_4**L**′ or H_4**L**″ instead, at elevated pH an isostructural analogue of MLn**L**·4H_2O with a slightly increased unit cell volume is obtained. At unmodified pH however, a different structure, Ln(**L**′H)·4H_2O (Ln = Ce, Nd; **L**′ = **L**′, **L**″) is formed.[111] LnO_7 polyhedra are linked by PO_3C groups, each using two O atoms to coordinate two Ln^{3+} cations into chains with a similar motif to Groves' $La^{(III)}$ structures.[110] All linkers are identical, having a chair conformation with both methylenephosphonate groups equatorial. Chains are linked to four others to form an array of rhombic channels parallel to the *a*-direction occupied by physisorbed water molecules (*Fig. 1.25*). Like Ln**L**(**L**H_2)·4.5H_2O and MLn**L**·4H_2O, this structure shows reversible dehydration but no permanent porosity.

For intermediate ionic radius Ln^{3+} cations, such as Nd, a further framework has

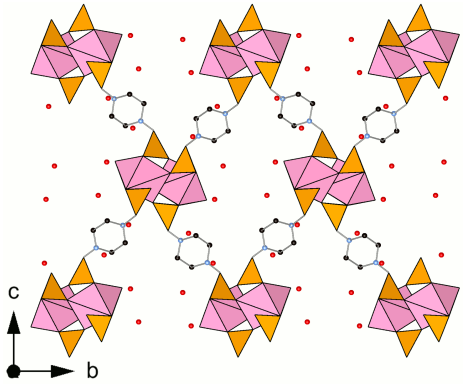

Figure 1.25: $Ln(\mathbf{L'}H)\cdot 4H_2O$ phase reported by Mowat *et al.* viewed along the *a*-direction.[111]

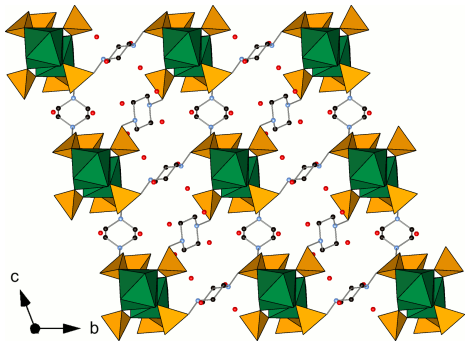

Figure 1.26: $Nd_2(\mathbf{L}H_2)_3\cdot 9H_2O$ phase, with chains constructed from dimeric Nd_2O_{14} units, viewed along the *a*-direction.[112] Nd polyhedra in green.

been reported with $H_4\mathbf{L}$, $Nd_2(\mathbf{L}H_2)_3\cdot 9H_2O$.[112] Inorganic chains in this framework are constructed from Nd_2O_{14} dimers, with each Nd^{3+} cation 8-fold coordinated by a water molecule and six PO_3C groups, two of which bridge to the neighbouring dimer to form the chain. All of the PO_3C groups in each of the three crystallographically distinct linkers coordinate through two O atoms, and each inorganic chain is connected to six others (*Fig. 1.26*). No porosity data are reported for this phase.

Using the smaller radius rare-earth cations with $H_4\mathbf{L}$ the structure $Ln_2(\mathbf{L}H_2)_3\cdot xH_2O$ (Ln = Gd, Yb, Y; x = 3 (Gd & Yb), 5 (Y)) is formed.[112] Inorganic chains of MO_6 octahedra are linked to neighbours by three PO_3C units, each binding to two different metal cations in a bridging mode. Chains are linked to four others by two crystallographically distinct sets of chair conformer ligands, to form an array of square cross-section channels (*Fig. 1.27*). One set of ligands, with one methylenephosphonate axial and one equatorial, links chains to form structural layers in the (0 0 1) plane. The second group of ligands, disordered over two sites with both methylenephosphonate groups equatorial, links these layers in the third dimension. Channels between layers are occupied by physisorbed water molecules which may be reversibly removed, causing a structural transition with a consequent contraction in unit cell volume (due to a reduction in the *c*-parameter, in the case of Y, of 12 %), causing the channels to close on dehydration. The dehydrated material is not permanently porous, though dehydration is reversible. More recent work on this material has revealed new structural insights into this dehydration behaviour (*Section 4.3.4*).

The recently reported $Zr^{(IV)}$ phosphonate phase, $Zr_2H_4\mathbf{L}_3\cdot 9H_2O$, has a chain motif closely related to that of $Ln_2(\mathbf{L}H_2)_3\cdot xH_2O$.[101] Chains in this structure differ in having three-fold symmetry and linking to six others via piperazinyl groups in

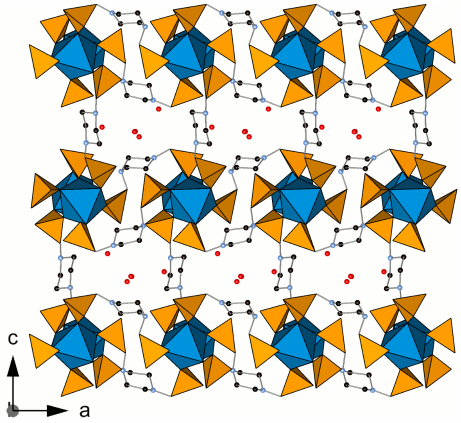

Figure 1.27: $Ln_2(\mathbf{L}H_2)_3{\cdot}xH_2O$ structure formed with $Gd^{(III)}$, $Yb^{(III)}$ and $Y^{(III)}$ viewed along the *a*-direction.[112] Ln polyhedra in blue.

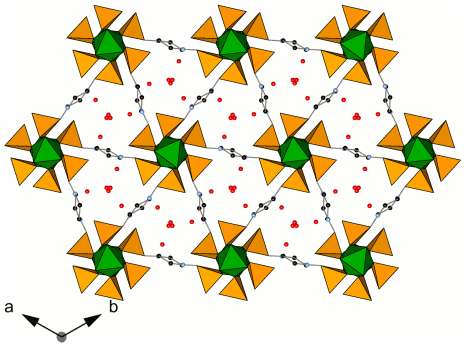

Figure 1.28: $Zr_2H_4\mathbf{L}_3{\cdot}9H_2O$ viewed along the *c*-direction, showing narrow 3 Å channels.[101] Zr shown in green.

a chair conformation to form narrow, triangular 3 Å channels (*Fig. 1.28*). Charge balance is maintained in the structure by four disordered protons distributed across three ligands. The structure may reversibly lose physisorbed water molecules occupying the channels, but dehydration results in contraction of the channel free-diameter and so the material shows no porosity to N_2.

Divalent Framework Metal Phosphonates with $H_4\mathbf{L}$

To date the most porous material produced with $H_4\mathbf{L}$ is STA-12, $M_2(H_2O)_2\mathbf{L}{\cdot}xH_2O$ (M = Mn, Fe, Co, Ni).[105, 113] $Mn^{(II)}$, $Fe^{(II)}$ and $Co^{(II)}$ forms of STA-12 are prepared at elevated synthesis pH, to avoid co-crystallisation of the phase $M(\mathbf{L}H_2){\cdot}xH_2O$ of LaDuca *et al.* (*vide supra*).[103] By contrast, STA-12(Ni) crystallises over a wide-range of pH conditions, as $Ni^{(II)}$ preferentially adopts an octahedral coordination environment and so competitive crystallisation of either $M(\mathbf{L}H_2){\cdot}xH_2O$ or an analogue of Groves' $Zn_2\mathbf{L}$ is disfavoured. The structure of STA-12 consists of helical chains of edge-sharing MO_5N octahedra with coordination provided by bridging PO_3C groups, a piperazinyl N atom and a chemisorbed water molecule.[114] Chains have a three-fold rhombohedral symmetry and are linked to three others through N atoms of piperazinyl groups, in a chair conformation, with both methylenephosphonate groups axial. A honeycomb array of $\sim$ 0.9 nm circular cross-section channels is formed, occupied by physisorbed water molecules H-bonded to pendant P=O groups of the helical chains and to the chemisorbed water molecules (*Fig. 1.29a*). Both physisorbed and chemisorbed water molecules may be reversibly removed from the structure in a two step process. On dehydration there is a structural transition to a triclinic material in which the metal octahedra become

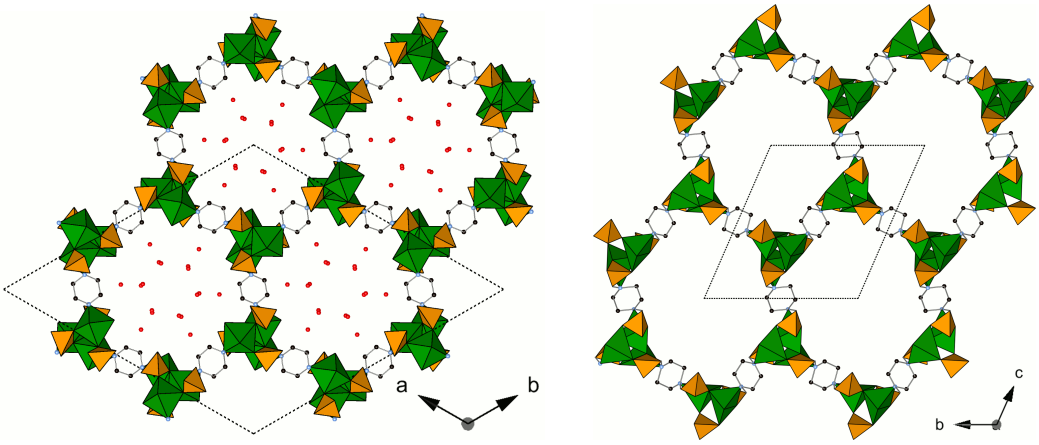

Figure 1.29: The as-prepared (*left*) and the fully dehydrated (*right*) structures of STA-12(Ni), showing the change from a circular to elliptical cross-section channels as a result of the structural transition from $R\bar{3}$ to $P\bar{1}$.[114]

5-fold coordinate and two thirds of the PO_3C tetrahedra become fully coordinating (*Fig. 1.29b* — a detailed description of the dehydration behaviour of STA-12(Ni) is given by Miller *et al.*).[114] As a result of this transition, the channels become elliptical but remain open, and the material is porous to a range of small gas molecules including, N_2, CO_2, and CH_4.[114] The dehydrated structure presents several different sites for adsorbed molecules, including Lewis acidic coordinatively unsaturated sites (CUS) and P=O adsorption sites. The transition on dehydration may be prevented by replacement of $H_4\mathbf{L}$ with $H_4\mathbf{L}'$ during synthesis, to form an isostructural material in which the methyl groups prevent the distortion of the structure, leading to a more open pore structure and a greater pore volume. Using $H_4\mathbf{L}''$, however, the linker decomposes and, in the case of Ni, the nickel phosphate VSB-5 is obtained.[113]

Reaction of divalent cations with $H_4\mathbf{L}'$ at high M:L ratio produces another phase with an open pore structures, $[Co_4\mathbf{L}'_{1.5}(AcO)_{1.5}(OH,H_2O)_3]\cdot 0.5NH_4 5.5H_2O$.[105] One CoO_6 octahedron edge-shares with three CoO_5N octahedra to form tetrameric clusters, with additional metal coordination provided by bidentate acetate groups. Tetramers link to neighbours above and below through PO_3C groups. Tetramer chains are in turn linked to three others through N-coordinating piperazinyl groups to form a hexagonal array of unidirectional channels (*Fig 1.30*). No significant porosity has been observed for this material so far, although it should be a large pore solid.

Du *et al.* provide the only example to date of an alkaline earth metal bisphosphonate formed with $H_4\mathbf{L}$.[115] Chains of edge-sharing 8-fold coordinate

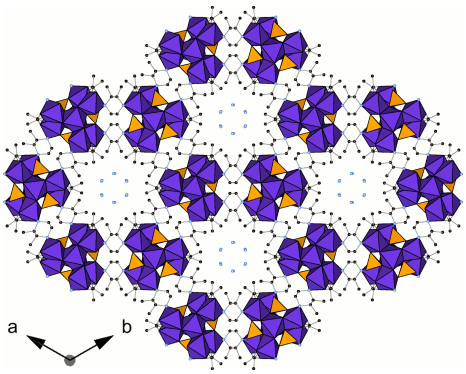

Figure 1.30: Co phase reported by Groves *et al.*, with chains constructed from tetrameric Co clusters linked in the *c*-direction by PO_3C groups. Clusters are capped with acetate groups.[105] Blue spheres in pores are NH_4 cations.

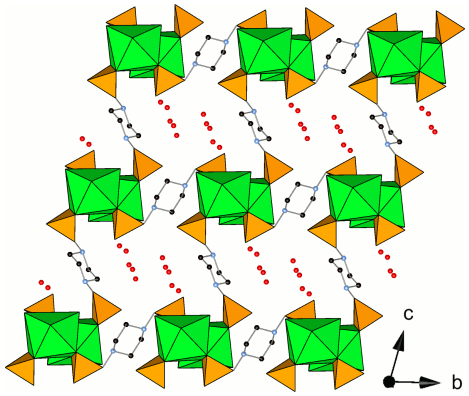

Figure 1.31: $[Sr(\mathbf{L}H_2)]\cdot 3H_2O$ reported by Du *et al.* viewed along the *a*-direction, showing the 5 Å channels occupied by physisorbed water molecules.[115] Sr polyhedra are showing in green.

$Sr^{(II)}$ polyhedra run parallel to the *a*-direction, with coordination provided by six O atoms (four of which are μ_2 bridging) from three PO_3C tetrahedra and two O atoms from water molecules. Chains are linked in the *b*- and *c*-directions by two crystallographically distinct sets of protonated piperazinyl moieties in chair conformations which H-bond with pendant P=O groups and water molecules coordinating the Sr^{2+} cation (*Fig. 1.31*). An array of approximately square cross-section $\sim$ 5 Å channels run parallel to the chain occupied by physisorbed water molecules, which may be removed on heating. No porosity data was reported.

Longer Ligands and Isoreticular Chemistry

The most porous carboyxlate materials reported were prepared through the use of isoreticular chemistry (*vide supra*). Using longer topologically identical linkers, structures were prepared with large pores which remain open on dehydration. N,N′-4,4′-bipiperidinebis(methylenephosphonic acid) ($H_4\mathbf{LL}$) is topologically identical to $H_4\mathbf{L}$ and $\sim$ 4 Å longer (*Section 6*). Costantino *et al.* have used this ligand in the synthesis of a $Ce^{(IV)}$ mixed phosphonate-sulphate material (*Fig. 1.32*).[116] CeO_7 polyhedra are coordinated by a water molecule, two O atoms from two bridging SO_4 groups and four O atoms from four fully coordinated PO_3C groups, two of which are shared μ_2 with a neighbouring Ce polyhedron to form Ce_2O_{12} dimers. Dimers are linked to form layers in the (0 1 0) plane, which are pillared by bipiperidinyl moieties, leaving narrow $\sim$ 3 Å channels between layers, occupied by physisorbed water molecules. Water molecules may be removed from the structure by heating, but the authors do not report if dehydration is reversible or if the material is porous.

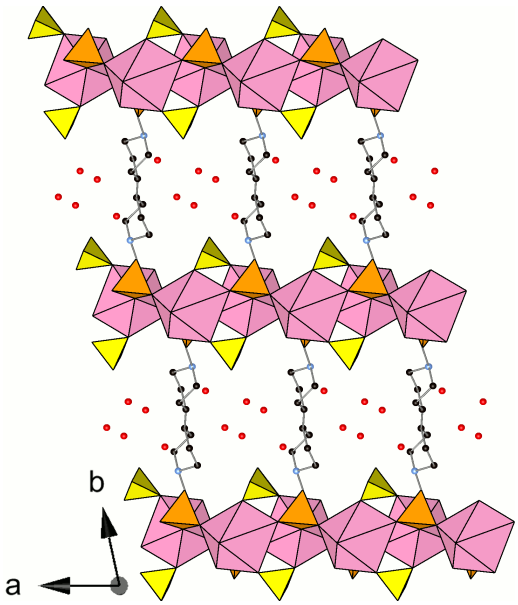

Figure 1.32: Cerium phosphonate-sulphate pillared layered material reported by Costantino *et al.*.[116] Sulphate tetrahedra shown in yellow.

1.5 Summary

The important feature of $H_4\mathbf{L}$ which leads to the great diversity of structures formed with this ligand and its derivatives is the presence of the α-amino functionality. Depending on the synthesis conditions, this group may or may not be protonated. If it is protonated then it is able to form extended H-bonding networks which may help to stabilise the structure formed (chain structures $La_2(\mathbf{L}H_2)(\mathbf{L}H_4)Cl_2$ and MIL-91; layered structure $VO(H_2O)(\mathbf{L}H_2)$). When not protonated, the amino group may engage in coordinative bonding to the metal centre as in STA-12. This coordinative flexibility comes in addition to the flexibility of the PO_3C group itself, which may use one, two or three O atoms to coordinate the metal, as it does in forming the various $Ln^{(III)}$ structures ($La_2(\mathbf{L}H_2)(\mathbf{L}H_4)Cl_2$ — monodentate & bidentate; $MLn\mathbf{L}\cdot 4H_2O$ — fully coordinating). The ligand is itself also structurally flexible, capable of showing both boat and chair conformations (in the as-prepared and dehydrated structures of $MLn\mathbf{L}\cdot 4H_2O$) or axial/equatorial arrangement of methylenephosphonate groups ($Ln_2(\mathbf{L}H_2)_3\cdot xH_2O$). Layered structures are readily classified, based on the number of members forming the rings and whether one or more types of ring are present in the layers (*e.g.* $[M_nP_nO_{2n}]$, n = 2, 3 or 4, have been reported). Unidirectional chain structures may be classified in a similar way, by considering connectivity of the metal polyhedra. For octahedral and tetrahedral M^{2+} cations, chains tend to be constructed of isolated $M^{(II)}$ polyhedra linked by bridging phosphonates, the exception to this being STA-12 (*Fig. 1.33*). For the $M^{3+/4+}$ cations the situation is more complicated. The smaller octahedral cations may form corner-sharing chains, as in the MIL-91 structure. With larger cations, increased strain would be placed on the M-O-M bridges of such a chain and thus an alternative motif of isolated octahedra bridged together by three PO_3C groups is adopted ($Ln_2(\mathbf{L}H_2)_3\cdot xH_2O$ or $Zr_2H_4\mathbf{L}_3\cdot 9H_2O$). With the larger Ln^{3+} cations, in 7- or 8-fold coordination, a range of chain structures are observed, usually based around a double-chain motif, with isolated $Ln^{(III)}$ polyhedra, dimeric edge-sharing $Ln^{(III)}$ units or fully polymerised, edge-sharing chains of $Ln^{(III)}$ polyhedra. The porosity of the resulting framework is then dependent upon the number of chains that each chain is linked to: the more chains that link, the smaller the pores and the lower the likelihood that the structure will be porous (*e.g.* each chain linked to four others in porous MIL-91 *vs* each chain linked to six others in non-porous $Zr_2H_4\mathbf{L}_3\cdot 9H_2O$). Finally the dehydration behaviour of the structure is also important: the flexibility of the $H_4\mathbf{L}$ linker means that channels may close in response to the removal of physisorbed water ($Ln_2(\mathbf{L}H_2)_3\cdot xH_2O$) or at least a structural transition might be expected (STA-12).

Despite the flexibility of the molecule, $H_4\mathbf{L}$ has been successfully used in

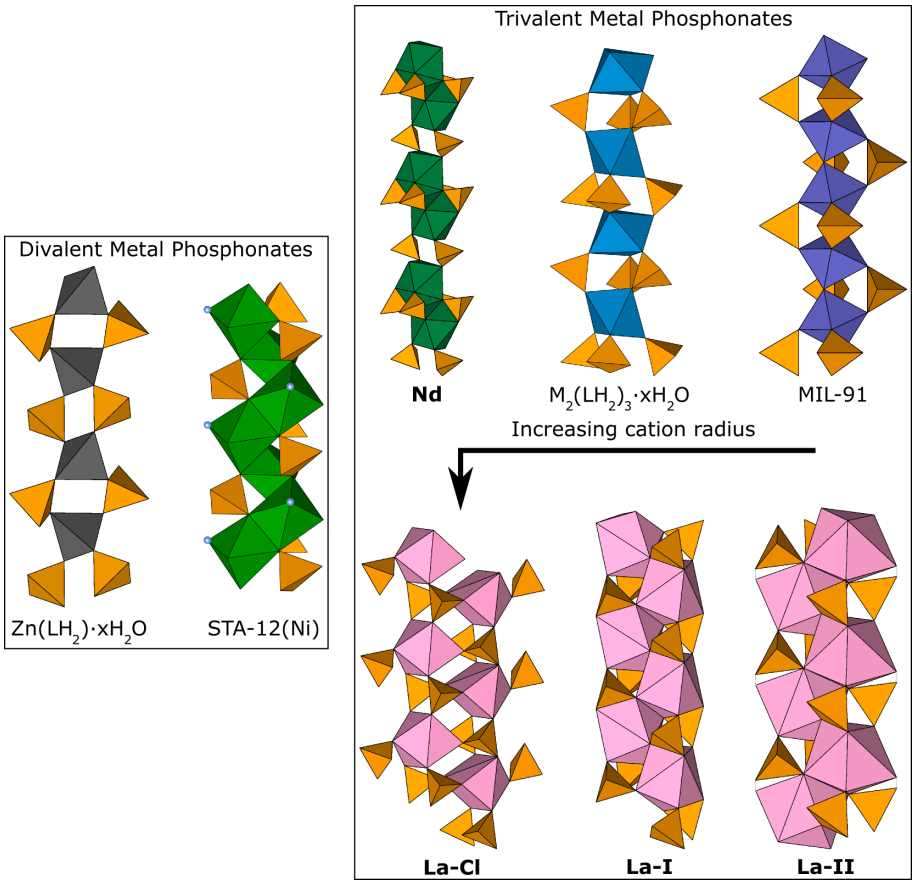

Figure 1.33: Comparison of the metal phosphonate chains in selected divalent and trivalent frameworks formed with $H_4\mathbf{L}$ and its derivatives. M^{2+} cations show both edge-sharing and isolated cation motifs. For M^{3+} cations, radius determines the structure of the chains. Smallest radii form corner-sharing chains of octahedra. With increasing radius chains with isolated octahedra form. With the largest radii, cations become 7- and 8-fold coordinated and are able to form a mixture of isolated cation, dimeric cluster or fully edge-sharing metal phosphonate chains. **Nd** — $Nd_2(\mathbf{L}H_2)_3{\cdot}9H_2O$; **La-Cl** — $La_2(\mathbf{L}H_2)(\mathbf{L}H_4)Cl_2$; **La-I** — $MLn\mathbf{L}{\cdot}4H_2O$; **La-II** — $Ln(\mathbf{L}'H){\cdot}4H_2O$.

the preparation of two highly porous metal phosphonate materials: MIL-91 and STA-12. The STA-12 structure is of particular interest because of the large pore size and its porosity to a range of different gases. STA-12(Ni) also showed some selectivity for the binding of CO_2 over CH_4. This is, at least in part, due to the strong interactions between the coordinatively unsaturated sites in the walls of the channels of the dehydrated material and the CO_2 adsorbate. The pendant P=O sites also provide a second site for CO_2 molecules to interact with the framework. These features are likely to be shared with other frameworks formed with $H_4\mathbf{L}$ and related linkers. There is still much scope for investigating the behaviour of these ligands with a range of cations, including the heavier $Ln^{(III)}$ cations (Gd–Yb). The chemistry of $H_4\mathbf{L}'$ and $H_4\mathbf{L}''$ has also not been widely investigated with any M^{3+} cations. Furthermore the application of isoreticular synthesis, using N,N'-bipiperidinebis(methylenephosphonic acid), to these systems is as yet uninvestigated. This work will attempt to address some of these points, with the aim of preparing new material showing selective adsorption of, for example, CO_2.

Chapter three will first report the synthesis of a range of ligands related to $H_4\mathbf{L}$ including $H_4\mathbf{L}'$, $H_4\mathbf{L}''$ and $H_4\mathbf{LL}$. Chapter four will look at the reactions of $H_4\mathbf{L}$, $H_4\mathbf{L}'$ and $H_4\mathbf{L}''$ with rare-earth cations and reinvestigate the chemistry of $Y_2(\mathbf{L}H_2)\cdot 5H_2O$. Chapter five reports the first synthesis of a porous alkaline earth metal framework with $H_4\mathbf{L}$, STA-12(Mg), and compares this new material with previously reported STA-12 structures. Chapter six will present the results of the first use of $H_4\mathbf{LL}$ as a ligand in isoreticular synthesis, as well as some additional phases prepared in the course of this work. An epilogue is also included, detailing the results of an additional project undertaken in collaboration with co-workers at the University of Edinburgh, looking at the flexibility and adsorptive responsivity of a variety of Zeolitic Imidazole Frameworks with the sodalite topology.

Chapter 2

Synthesis and Characterisation Techniques

Materials in this work are prepared by solvothermal synthesis (see *Section 2.1*). All materials were initially characterised by powder X-ray diffraction to determine phase purity (see *Section 2.2.2*). With phase pure samples, and if a suitable model was available, structural refinement by Rietveld methods was performed. In the absence of a starting model, a structural model was developed by model building. If suitably sized single crystals were obtained, single crystal X-ray diffraction data were collected for structure determination (see *Section 2.2.1*). Phase purity and crystal structures of specific diamagnetic samples were confirmed by solid state ^{13}C and ^{31}P NMR, with data obtained by D. M. Dawson (yttrium phosphonates) and J. M. Griffin (STA-12(Mg) and yttrium phosphonates). Spectra were collected using Bruker Avance III spectrometers operating at magnetic field strengths of 9.4 or 14.1 T using 4 mm NMR rotors at a MAS rate of 10 kHz. ^{13}C chemical shifts were referenced relative to tetramethylsilane, using the CH_3 resonance of L-alanine at 20.5 ppm as a secondary reference. ^{31}P chemical shifts were referenced relative to 85 % $H_3PO_{4(aq)}$, using BPO_4 at -31.2 ppm as a secondary reference. ^{13}C transverse magnetisation was obtained by cross polarisation (CP) from ^{1}H using a contact pulse duration of 1 ms (ramped for ^{1}H). Two-pulse phase modulation (TPPM) ^{1}H decoupling was applied during acquisition. ^{13}C CP MAS NMR spectra were acquired with between 100 and 200 transients separated by a recycle interval of three seconds. ^{31}P MAS NMR spectra were obtained by direct polarisation of ^{31}P, using between 16 and 32 transients separated by a recycle interval of 60 seconds. Characterisation of ligands by ^{1}H, ^{13}C and ^{31}P solution-state NMR was performed on a Bruker Avance II 400 MHz spectrometer, using a combination of one dimensional solvent-suppressed ^{1}H, DEPTQ ^{13}C and ^{31}P (no-decoupling) experiments and two dimensional COSY

(^{1}H-^{1}H) and HSQC (^{1}H-^{13}C) experiments. Thermogravimetric analysis (TGA) was performed in a flow of dry air using either a Netzsch TG 209 or a Rheometric TGA 1000M. Scanning electron micrographs and Energy Dispersive X-ray (EDX) analyses were collected using a JEOL JSM 5600 SEM fitted with an Oxford Instruments EDX detector. Elemental analsis (CHNS) of phase pure samples was determined with a CE Instruments EA1110 CHNS analyser (data collected by S. Williamson).The porosity of each material to a range of gases was also investigated (see *Section 2.3.1*). Magnetic susceptibility measurements were made using an Quantum Design MPMS-1 SQUID.

Infrared (IR) and UV/Vis measurements of dehydrated materials were made at the Università di Torino (Turin, Italy) by S. Chavin in the group of S. Bordiga. IR spectra were collected using a Bruker IFS66 spectrometer at a resolution of 2 cm^{-1} using MCT or DTGS detectors. Samples were deposited from aqueous suspension as thin films onto Si wafers, which were mounted in environmental cells, allowing thermal treatment at high vaccuum, dosing of gases and *in situ* collection of IR spectra. For UV/Vis measurements, pelletized samples of material were dehydrated in a quartz glass cell under vacuum and at elevated temperature. Spectra were collected on the dehydrated pellets using a Varian Cary 5 spectrophotometer fitted with a reflectance sphere.

2.1 Synthesis

Solvothermal synthesis may be defined as the heating of a reaction solution, in either aqueous or non-aqueous solvents, in a sealed vessel to temperatures in excess of the boiling point of the solvent and at pressures greater than 1 bar. The most common solvent used in solvothermal synthesis is water, in which case the technique is explicitly referred to as *hydrothermal synthesis*, though other reported solvent systems include methanol,[44] DEF,[117] DMF/pyridine,[52] benzene,[118] ethylenediamine, ethanolamine,[119] and poly(ethylene glycol).[120] A wide range of materials have also been prepared solvothermally including synthetic minerals (notably α-quartz),[121] main group materials (diamond, carbon & boron nitrides),[121] zeolites,[13] perovskites,[122] molecular metal clusters[123] and, most importantly for this work, MOFs.[44, 117, 52] MOFs have also been synthesised by non-solvothermal methods and these have been reviewed elsewhere.[124]

Solvothermal synthesis offers a range of parameters which may be varied to alter the product of a reaction. Parameters may be classified into two principal groups: chemical parameters, such as the reagents present and the nature of the solvent (*vide*

Figure 2.1: Steel autoclave (*left*) and screw top (*right*) with a PTFE liner (*centre*).

infra), and thermodynamic parameters, including reaction temperature, pressure and time.[121] Of the chemical parameters, the metal salt counterion has a strong influence on reaction products as it may template structures[110] and change the reaction pH, which is particularly important for α-aminophosphonate MOFs where H-bonding networks drive crystallisation of certain phases (see *Section 1.4.2* for examples). Changes to the thermodynamic parameters also induce changes in the physical and chemical properties of the solvent system, leading to different crystallisation products (*vide infra*).

Solvothermal reactions may be carried out in a variety of different reaction vessels, some applying pressure externally, others using differential temperature gradients.[125] Reactions discussed within the scope of this work will be performed using stainless steel autoclaves, designed to withstand the raised pressures of solvothermal reactions, fitted with Teflon® (PTFE) liners (*Fig. 2.1*). Reactions are performed in PTFE liners to protect the autoclave from corrosion by the reaction solution and to ensure there is no contamination of the reaction due to dissolution of the autoclave by the solution. PTFE is an extremely durable material with a lifetime in excess of 100 reactions[126] and is inert to reactions in either acid or alkaline media.

The elevated pressure and temperature conditions of solvothermal synthesis result in changes in the physical and chemical behaviour of the solvent. For example, in hydrothermal reactions at 1000°C and 150–200 kbar water has a density of 1.7–1.9 g ml^{-1} and is thought to be completely dissociated into H_3O^+ and OH^-, behaving as a molten salt.[125] However, the use of PTFE limits the accessible temperature and pressure ranges for reactions, with $T_{max} < 270$°C (543 K)[1] and $p_{max} \sim 150$ atm. Again considering hydrothermal synthesis, temperatures less than 270°C and pressures less than 100 bar fall below the critical point of water[2] (*Fig. 2.2*).

[1] m.p.(PTFE) = 327°C; above 270°C substantial creep of the liner is expected.[127]
[2] p_{crit} = 218.3 atm; T_{crit} = 647.4 K[128]

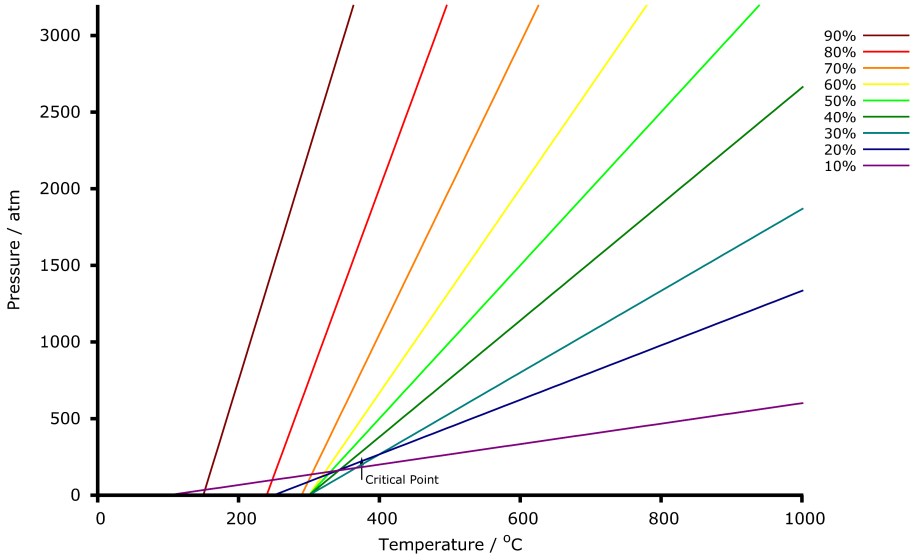

Figure 2.2: For pure water, the dependence of pressure inside the reaction vessel on temperature, with the fill volume of the reaction vessel shown as a parameter. *After Rabenau.[125]*

However, subcritical, superheated solutions will still exhibit significantly altered solubilising properties, allowing otherwise insoluble reagents to be co-solvated. Once in solution, solutes have a greater mobility than at room temperature and pressure due to the decreased viscosity of the solution. These factors also promote the growth of crystals, usually leading to the nucleation of metastable kinetic phases rather than the thermodynamic products favoured by conventional techniques.[125, 123]

Similar changes of physical properties would be expected in other solvent systems; however the critical point for these will be different to that of water, possibly making supercritical solutions accessible in the pressure and temperature regimes described. Solvents other than water also exhibit different solubilising powers and viscosities (and therefore ion mobilities), suggesting the formation of alternative products to those formed from analogous aqueous reactions. It follows that mixed solvent solutions should offer highly tunable reaction conditions.

A disadvantage of the solvothermal method is that, due to reactions being performed in sealed vessels, the reaction mechanism is largely unknown. Efforts have, however, been made to determine the species present in solvothermal reactions, using a wide range of *in situ* techniques including X-ray and neutron diffraction, NMR, EXAFS and AFM.[129] In the context of MOF synthesis, EXAFS has been used to follow the presence of trimeric units throughout the synthesis of MIL-89,[130] whilst EDXRD has been used extensively in determining crystallisation processes in a range of MOFs, including HKUST-1 and MIL-53,[131] and also in

CAU-1-$(OH)_2$.[132] In this latter example, EDXRD was used to follow crystallisation kinetics to obtain information about the mechanism of the reaction and also to understand the differences in mechanism between heating by conventional methods or by microwave. AFM has been used to study the growing crystal surfaces of HKUST-1[133] and ZIF-8.[134]

Syntheses in this work were performed in 15 or 40 ml custom built autoclaves fitted with PTFE liners. Insoluble reagents were added directly in to the liner whilst soluble reagents and additional solvent were loaded by syringe. Reactions were then stirred at room temperature for up to one hour before the autoclaves were sealed and the reactions heated to a desired temperature using isothermal forced-draft ovens (i.e. conventional, convective/conductive heating). After cooling, reactions were filtered, washed with solvent and dried at 40°C overnight. Phase identification was performed by powder X-ray diffraction (*Section 2.2*).

2.1.1 High-Throughput Solvothermal Synthesis

Due to the large parameter space available in solvothermal reactions, systematic variation of conditions to determine the phases prepared in a given system and determination of the conditions necessary to obtain single phase samples of each material is a time consuming process. High-Throughput (HT) synthesis allows a more rapid investigation of the parameter space.[135] Using a *discovery array*, a wide range of reaction conditions may be investigated to find new phases. Once a new phase has been identified, a *focussed array* may be used to investigate a smaller area of the parameter space to fine-tune the synthesis conditions.[136] Rapid synthesis of new phases may be easily achieved; however, it is also necessary to have a HT characterisation method (such as a specially adapted powder X-ray diffractometer) in order to determine the stability fields of each phase. Although a given phase may be prepared in a HT reaction, scaling up to a larger scale batch reactor may not yield the same phase,[135] though the relationships between phase stability fields are maintained regardless of scale.

The HT synthesis reported in this work was carried out in collaboration with the group of Norbert Stock at Christian-Albrechts-Universität zu Kiel (Kiel, Germany), using a custom built 24-reactor block. Each reactor was fitted with a 3 ml PTFE liner into which insoluble reagents were loaded directly. Soluble reagents and additional solvent were added using calibrated micropipettes up to a volume of 1.5 ml. Reactions were stirred for up to one hour at room temperature. Liners were then sealed by covering the block with a flexible 0.5 mm thick PTFE sheet and a rigid 1 mm PTFE sheet. The sheets were secured by screwing down the top

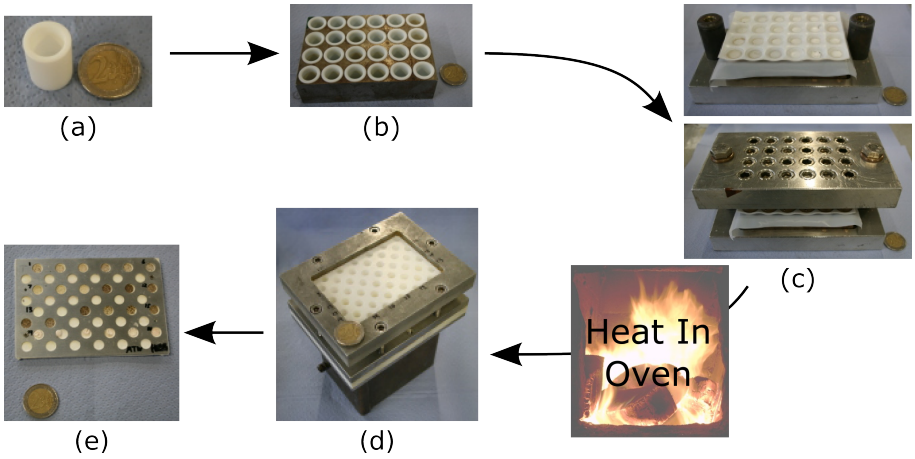

Figure 2.3: Sequence of steps for preparing a HT reaction. (a) Reagents are loaded into PTFE liners which are are inserted into the reactor block (b). (c) Reactions are sealed with PTFE sheets, secured by studs from reactor lid and heated in the oven. (d) Reactions are filtered using a filter-block and loaded into a multi-well sample holder (e) for HT powder diffraction analysis. Two Euro coin for scale.

of the unit, pushing a sprung stud onto the top of each liner. Reactions were then conventionally heated using programmable forced-draft ovens. After filtering using a custom built HT filter-block, samples were characterised using a Stoe Stadi P Combi High-Throughput powder X-ray diffractometer fitted with a Cu K_α monochromated radiation source.

2.2 X-Ray Diffraction

X-ray diffraction has been extensively reviewed elsewhere.[137, 138, 139] The following discussion is intended as a summary of the technique.

X-rays are a form of electromagnetic radiation with a short wavelength of approximately 1 Å. X-rays may also be considered as particles, undergoing either elastic (energy conserved) or inelastic (energy not conserved) collisions with matter. In X-ray diffraction experiments only the elastically scattered X-rays are considered, so incident and diffracted beams have the same wavelengths.

Diffraction occurs when a propagating wave passes between two objects separated by a distance similar to its wavelength. Beyond the gap the waves propagate with a curved wavefront. When coherent waves pass through a diffraction grating (a series of parallel, narrow, regular slits) the wavefronts produced interfere with one another constructively or destructively to produce a diffraction pattern. Atoms are arranged in crystals in a repeating pattern, much like the slits of a diffraction grating. Max von Laue proposed that a diffraction pattern could be obtained from

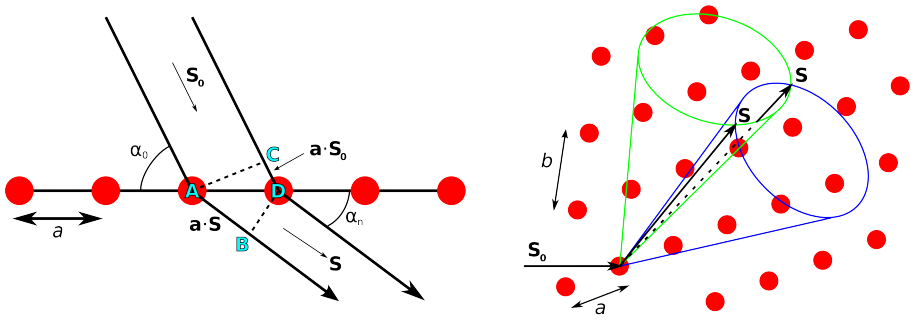

Figure 2.4: Laue diffraction in a one- (*left*) and two-dimensional (*right*) crystal. $\mathbf{S_0}$, incident beam; $\mathbf{S}$, diffracted beam; red circles, lattice points; a & b, lattice vectors; green & blue (*right*), cones of diffracted beams.

a crystal by using X-ray radiation, as it has a similar wavelength to the interatomic spacing. Using "white" (rather than monochromated) X-rays Laue was able to produce a diffraction pattern of intersecting rings of spots of varying intensities. Each spot corresponds to a diffraction condition being satisfied, *i.e.* two in phase waves interfering constructively. Constructive interference is achieved when the path difference between the two waves, $\vec{AB} - \vec{CD}$ (*Fig. 2.4*), is equal to an integer number of wavelengths.

In a one dimensional crystal, with scatterers at a repeat distance of a, this diffraction condition, the *Laue Condition*, is satisfied when

$$(\vec{AB} - \vec{CD}) = a(cos\alpha_n - cos\alpha_0) = n\lambda$$

leading to a cone with axis parallel to the a direction and apical angle α_n (*Fig. 2.4*). In two and three dimensions, similar equations may also be derived for the b and c directions which, with the first equation, may be written in a vector form,

$$\begin{aligned} a(cos\alpha_n - cos\alpha_0) &= \mathbf{a} \cdot (\mathbf{S} - \mathbf{S_0}) = n_x\lambda \\ b(cos\beta_n - cos\beta_0) &= \mathbf{b} \cdot (\mathbf{S} - \mathbf{S_0}) = n_y\lambda \\ c(cos\gamma_n - cos\gamma_0) &= \mathbf{c} \cdot (\mathbf{S} - \mathbf{S_0}) = n_z\lambda \end{aligned}$$

In the two and three dimensional cases, diffraction is only satisfied along the vectors of intersection of the cones (two vectors in two dimensions - *Fig. 2.4*; one vector in three dimensions). Diffraction patterns are recorded as an array of spots, as the image is a projection on to the Ewald sphere.

An alternative description of diffraction was proposed by William L. Bragg in 1912, in which diffraction spots are the result of "reflections" from sets of parallel

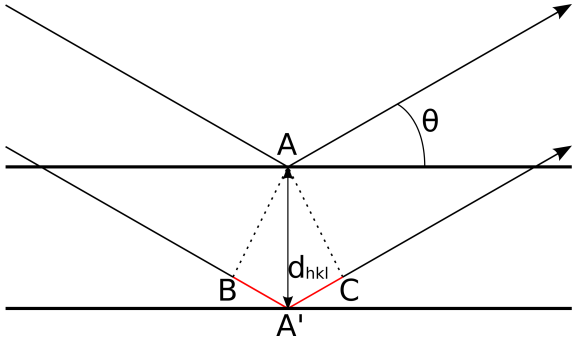

Figure 2.5: Bragg diffraction. Path of two scattered X-ray beams with path difference shown in red.

evenly spaced lattice planes within a crystal, called *Miller planes*. Individual Miller planes or sets of planes are identified by their Miller indices, denoted h, k and l. In Bragg's model (*Fig. 2.5*), an X-ray beam is incident on a lattice plane at A and reflects off at an angle θ related to the scattering angle 2θ. A second beam is incident on a neighbouring Miller plane, separated from the first by a spacing of d_{hkl}. The path difference of the two beams, $B\vec{A}' + A'\vec{C}$, must again be equal to an integer number of wavelengths, $n\lambda$. Bragg's Law expresses this condition as

$$n\lambda = 2d_{hkl}sin\,\theta \ .$$

The Bragg equation can be derived from the Laue equations.

X-ray diffraction probes the long range order of the crystal and so it is important that the crystal is not twinned and is as defect free as possible. Twinning or other defects can lead to blurring or splitting of diffraction spots which makes later analysis more complicated. Diffraction spots from certain lattice planes may also be *systematically absent* as the symmetry of the crystal causes diffracted beams to interfere destructively. Diffraction conditions have been determined for each translational symmetry element, for example, the I-centered lattice has $h+k+l = 2n$. Using these reflection conditions and the systematic absences of the diffraction pattern, it is possible to partially determine the space group, the collection of symmetry operations describing the atomic scale symmetry of the structure.

Structural information is obtained from the intensities as well as positions of the spots in a diffraction pattern. The intensity, I_{hkl}, of a given peak is dependent on the structure factor, F_{hkl}, of that peak,

$$I_{hkl} \propto |F_{hkl}|^2 \ . \tag{2.1}$$

The structure factor is a vector quantity with amplitude $|F_{hkl}|$ and phase $\phi(hkl)$

$$F_{hkl} = |F_{hkl}| e^{i\phi(hkl)} \ . \tag{2.2}$$

From measurement of the intensity of a given reflection, the magnitude of the structure factor may be found. The phase of the structure factor, however, comes from the incident X-ray beam, and this cannot be determined experimentally. This is the *phase problem* (*eqn. (2.2)*).

Each F_{hkl} describes the scattering of X-rays by a specific set of Miller planes, and is dependent upon the electron density, $\rho(xyz)$, within each volume element of the crystal, dV:

$$F_{hkl} = \int \rho(xyz)\, e^{2\pi i(hx_n + ky_n + lz_n)}\, dV \ .$$

In this model, electron density is assumed to be continuous throughout the crystal. In a real crystal, electron density is localised around the n atoms making up the crystal. This discrete distribution of electron density is better expressed as the sum over all atoms,

$$F_{hkl} = \sum_n f_n\, e^{2\pi i(hx+ky+lz)} \ . \tag{2.3}$$

The atomic scattering factor, f_n, is the sum of the abilities of each electron around the nth atom to scatter X-rays. It is therefore dependent on the number of electrons around a given atom. It is also dependent on the angle through which X-rays are scattered, decreasing with $(\sin\theta)/\lambda$, and on the amount of thermal motion, U_n. A correction is therefore applied to *eqn. (2.3)*,

$$F_{hkl} = \sum_n f_n\, e^{2\pi i(hx+ky+lz)}\, e^{-8\pi^2 U_n \sin^2\theta\,/\,\lambda^2} \ .$$

Structure solution relies on transformation of the observed structure factors to an electron density map. In principle this can be achieved by Fourier transformation of the structure factors, expressed here as a summation since the structure factors are discrete,

$$\rho(xyz) = \frac{1}{V} \sum_{h,k,l} |F_{hkl}|\, e^{i\phi(hkl)}\, e^{-2\pi i(hx+ky+lz)} \ .$$

However, only the amplitude term $|F_{hkl}|$ is obtained from the diffraction experiment (*eqns. (2.1), (2.2)*), so it is not possible to directly calculate the electron density from the diffraction pattern. The phase problem has been addressed by several methods, the most successful of which is *direct methods* (*vide infra*).

2.2.1 Single Crystal X-Ray Diffraction

A single crystal is a solid with all asymmetric units arranged in identical unit cells which are oriented in the same direction and within the same grain. Such crystals give the sharpest diffraction spots since scattering is coherent. The crystal is mounted on a fine glass fibre on a goniometer head, before being attached to a computer-controlled diffractometer. Irradiating the crystal produces diffraction spots in three dimensions, which are recorded by a detector. The diffractometer moves the crystal into different orientations using a goniometer, so that sufficient spots to allow structure solution may be recorded.

Diffraction data were collected using one of four diffractometers: a Rigaku AFC8/Saturn 70 or Rigaku AFC7/Mercury CCD diffractometer, using an MM-007 high-brilliance rotating anode Mo K_α source fitted with VariMax optics; a Rigaku AFC10/Saturn 92, using an MM-007 high-brilliance rotating anode Cu K_α source; or a Rigaku CCD system, equipped with a computer controlled ACTOR™ SM robotic sample changer and using a Mo K_α sealed tube source. Structure solution made use of direct methods routines incorporated in the SHELX-97[140], Sir2008, Sir2004 and Sir97 suites.[141, 142, 143]

Direct Methods

Direct methods are a collection of statistical techniques which attempt to determine the phase of a diffracted beam by using relationships between its amplitude, $|F_{hkl}|$, and its phase, $\phi(hkl)$. Normally these quantities are independent but thanks to two properties of the electron density map it is possible to relate them:

i) $\rho(xyz)$ must be positive everywhere;

ii) Electron density is localised around discrete atoms.

In direct methods, the structure factors are normalised for the variation of atomic scattering factor with scattering angle and thermal motion to *normalised structure factors*, $E(hkl)$,

$$E(hkl) = \frac{1}{(\sum_n f_n^2)^{\frac{1}{2}}} \sum_n f_n e^{2\pi i(hx_n + ky_n + lz_n)} \ .$$

Strong beams – beams having the highest amplitude – are used in direct methods as these will have the greatest effect on the calculated electron density map. The phases of these beams may be related by triplet or quartet relationships, such as

that derived by Sayre,

$$S(h,k,l) \simeq S(h',k',l') \cdot S(h-h',k-k',l-l')$$

Only a small subset of beams are used in the calculation of the related beams' phases. Thus the related phases are only probably correct. The probability of the phase being correct may also be calculated.

Completion and Refinement

Often direct methods will not locate all atoms in the structure. However, missing atoms may be located by generating a Fourier difference map,

$$\Delta\rho(xyz) = \frac{1}{V}\sum_{hkl}(F^o_{hkl} - F^c_{hkl})\, e^{2\pi i(hx+ky+lz)} \ .$$

F^c_{hkl}s are calculated from the electron density of atoms in the model (using *eqn. (2.2)*), whilst F^o_{hkl}s are calculated using the observed amplitudes and the phases determined from direct methods. Difference maps show maxima where there is electron density which has not been accounted for by the atoms currently in the model, whilst minima indicate too much electron density in a given region. Atoms can be assigned to peaks and a new difference map calculated until all atoms have been identified. In order to use Fourier difference maps effectively, they may also require some cycles of refinement. Structural refinement uses a least-squares method,

$$S = \sum_{hkl} w_{hkl}(|F^o_{hkl}| - |F^c_{hkl}|)^2$$

where w_{hkl} is a weighting factor given to each structure factor. S is minimised by refining parameters including atomic coordinates, thermal parameters and site occupancy. Refinement is carried out until S cannot be reduced any further.

Refinements of crystal structures in this work used the SHELXS routine of the SHELX-97 suite.[140]

2.2.2 Powder X-ray Diffraction

A powder sample contains a large number of crystallites orientated in many different ways. When irradiated with monochromated X-rays, a diffraction pattern will be obtained for each crystallite simultaneously. Due to the many orientations of the crystallites, the diffracted beams from a given set of Miller planes propagate away from the sample in a cone at a fixed 2θ angle from the incident beam (*Figure 2.6*).

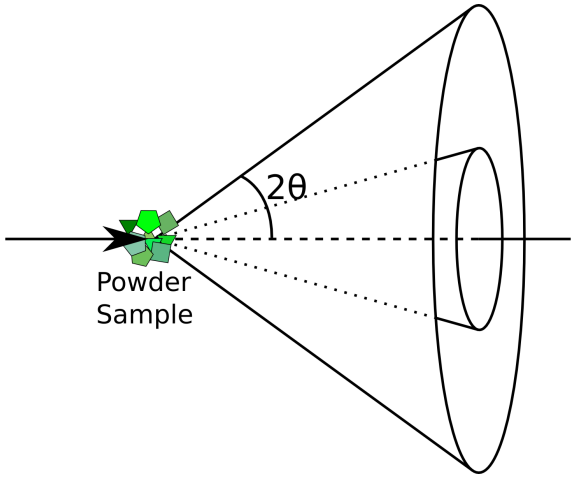

Figure 2.6: Cones of diffracted X-rays produced by a powder sample. *After Clegg.[137]*

This averaging effect is increased by rotating the sample whilst it is in the beam. The intensities of the diffraction cones are measured along a line about the equator of the cone by using a computer controlled moving detector.

Samples were analysed on Stoe Stadi P laboratory powder diffractometers in either Debye-Scherrer or transmission geometries, using either Cu K_α or Fe K_α radiation. Fe K_α was used to collect powder patterns of materials containing iron and cobalt, since with Cu K_α these materials fluoresce to give a high background which may obscure peaks in the diffraction pattern. Additional data sets were collected on a Panalytical Empyrean powder diffractometer in either transmission or Bragg-Bretano geometry. Several data sets were also collected using synchrotron radiation at beamline ID31 of the ESRF (Grenoble, France)[144] and beamline I11 of the Diamond Light Source (Harwell, Oxfordshire, UK),[145] where in both instances a Debye-Scherrer geometry was used.

Powder diffraction patterns provide a fingerprint of the solid. However, as three dimensional data is converted into one dimension, a lot of structural information can be obscured or lost due to peak overlap, making structure solution from powder data a more complicated task.

Solution from Powder

Structure solution from powder diffraction data involves five main steps:[146]

i) Indexing and determination of the unit cell

ii) Decomposition of the powder pattern into integrated intensities, I_{hkl}

iii) Assignment of space group from systematic absences

iv) Structure determination (*vide infra*)

v) Refinement — Rietveld method[147] (*vide infra*)

To index unit cells, peaks were located using the EXPO2009[148] (or EXPO2004[149]) or WinPLOTR[150] (in the FullProf suite) programs. Indexing used the routines implemented in ITO,[151] DICVOL[152] or TREOR.[153] Each program outputs a selection of unit cells ranked by Figure of Merit (F.O.M.) (e.g. de Wolff's M_{20} F.O.M.).[154] The cell with the best F.O.M. is then refined using LeBail analysis routines[155] of the GSAS[156]/EXPGUI[157] or EXPO2004/2009 suites of programs, allowing the extraction of integrated intensities from the powder pattern.

At this point, structure solution from powder can take several routes. In the absence of further information, direct methods (*vide supra*) or similar single crystal routines may be used to generate a model structure. Alternatively, if the contents of a unit cell are known from other chemical methods (e.g. elemental analysis, EDX, density measurements) then these components may be placed within a unit cell-sized box and potential structures determined by energy minimisation using, for example, simulated annealing. Finally, if there is some confidence about the structure, a model may be constructed manually using an existing structure as a starting point.

Rietveld Refinement and Completion

As with single crystal data, the structural model allows the calculation of structure factors (F_{hkl}), which may themselves be used to obtain a Fourier difference map to locate electron density missing from the model. Due to the reduced amount of data in a powder diffraction experiment, refinement of the structure together with a Fourier difference mapping is important to locate electron density. *Rietveld refinement* minimises the difference between the observed diffraction profile and that calculated from the structural model using a least-squares function,[147]

$$S = \sum w_i |y_{io} - y_{ic}|^2 \text{ where } w_i^{-1} = \sigma_{ip}^2 + \sigma_{ib}^2 \ .$$

Here y_{io} is the observed intensity and σ_{ip} and σ_{ib} are the standard deviations of the peaks and background respectively. y_{ic} is the calculated intensity, a function of the unit cell parameters, atomic positions, background function, instrumental parameters and peak profile function. Each of these contributions may be refined independently within the Rietveld refinement software. From the model determined in the structure solution step (and subsequently refined) structure factors (F_{hkl}) may be calculated. Using these, Fourier difference maps may be used to locate electron

density missing from the model in a similar way in which they were used in single crystal refinements.

The GSAS[156]/EXPGUI[157] suite of programs allows each of these parameters to be refined separately to refine a crystal structure.

2.3 Adsorption and Diffusion

Microporous solids such as MOFs are able to take molecules from the liquid or gas phase surrounding them into their pore spaces. This leads to applications in drug delivery[158], gas storage and gas separation[56, 159] and catalysis[160]. Understanding of the processes governing adsorption and diffusion is therefore important to aid in the tailored design of microporous materials.

2.3.1 Adsorption

Adsorption describes the binding of gas or liquid molecules to a liquid or solid surface. In conventional surface science, adsorption is studied on open, atomically-smooth surfaces of metal single crystals with well defined Miller indices. Molecules may be bound to surfaces by either *physisorption* or *chemisorption*.[161] Physisorbed molecules are bound to a surface by weak Van der Waals interactions, such as dispersive forces or dipole-dipole interactions, with enthalpies of between a few kJ mol^{-1} to tens of kJ mol^{-1}. Due to the small interaction enthalpy, physisorption is only observed at low temperatures and is a non-activated and fully reversible process. Chemisorption involves the transfer of electronic charge between adsorbate and surface to form a chemical bond, which may also lead to the dissociation of adsorbing species. Adsorption enthalpies vary from tens of kJ mol^{-1} to a few hundred kJ mol^{-1}. Due to the stronger interaction, desorption becomes an activated process. Chemisorption is not a fully reversible process and chemisorbed species may still be adsorbed at room temperature or higher.

For open surfaces various models of adsorption have been developed, including the Langmuir and Brunauer Emmett Teller (BET) models. Both the Langmuir and BET models assume that surface adsorbates are in dynamic equilibrium with a fluid phase above the surface, with adsorbates able to freely adsorb and desorb from the surface. Adsorption is also assumed to occur at a fixed temperature (i.e. isothermally).

In the Langmuir model adsorbent surfaces are assumed to be uniform with all adsorption sites equivalent, whilst neighbouring adsorbed molecules are assumed not

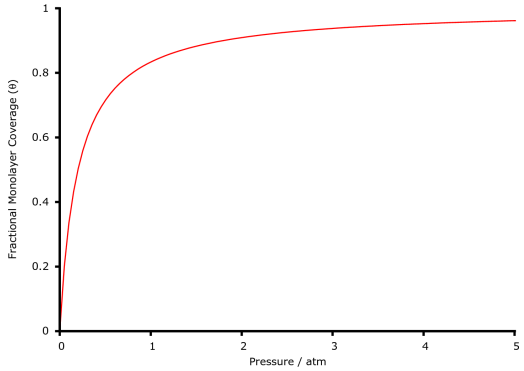

Figure 2.7: The Langmuir isotherm. Coverage tends asymptotically towards $\theta = 1$.

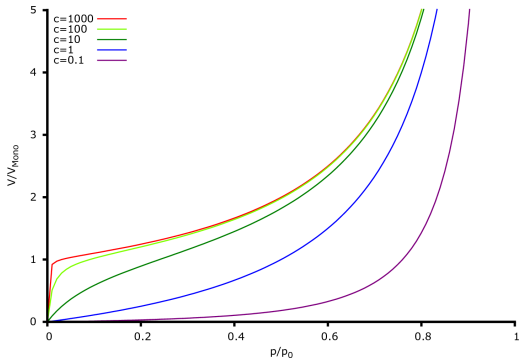

Figure 2.8: The BET isotherm, showing several values of c. *After Atkins & de Paula[128].*

to interact. Furthermore, adsorption is limited to a coverage of one monolayer.[128] The rate of adsorption is dependent on the pressure of the adsorbate gas (p) and the number of vacant surface sites ($n(1-\theta)$, where n is the total number of adsorption sites and θ is the percentage surface coverage). The rate of desorption is dependent only on the number of occupied adsorption sites ($n\theta$). At equilibrium these rates may be equated which gives the Langmuir isotherm:[161]

$$\theta = \frac{Kp}{1 + Kp} \tag{2.4}$$

where $K = \frac{k_{Ads}}{k_{Des}}$ and k_{Ads} and k_{Des} are the rate constants for the adsorption and desorption processes respectively.

The BET model extends the Langmuir model to multilayer adsorption. Additional layers adsorb on top of the first monolayer, as if onto the free surface, with the adsorption of each isolated layer described by the Langmuir model. The BET equation is expressed in terms of fractional monolayer volumes:[162]

$$\frac{V}{V_{Mono}} = \frac{cp}{(p_0 - p)\left[1 + (c-1)\left(\frac{p}{p_0}\right)\right]} \tag{2.5}$$

where V_{Mono} is the volume of one monolayer, p is the equilibrium pressure, p_0 is the saturation pressure of the adsorbate at the isotherm temperature, and c is a constant dependent on the enthalpies of desorption from the monolayer and the enthalpy of vaporisation:

$$c = e^{(\Delta H_{Des} - \Delta H_{Vap})/RT} .$$

When $c \gg 1$, the monolayer forms rapidly, followed by the gradual assembly of subsequent multilayers. For $c \leq 1$ the monolayer forms slower than or at the same

rate as multilayers (*Figure 2.8*).[162] Rearranging *eqn. (2.5)* to a linear form, the slope and the intercept of a plot of $\frac{p}{p_0}$ against $\frac{p/p_0}{V(1-p/p_0)}$ can be used to determine the surface area, provided the molecular cross-section of the adsorbate is known.

The surfaces involved in adsorbing molecules in porous solids differ, however, from the open surfaces on which the Langmuir and BET models of adsorption were developed. In these materials small molecules capable of diffusing through the pore openings may access the internal surface which is many times larger than the external surface of the particle. These internal surfaces are neither open, nor atomically flat, nor do they have a homogenous distribution of adsorption sites. Also the enclosed nature of micropores may hinder multilayer formation. As a result, the Langmuir and BET are not strictly valid for assessing the surface area of porous solids, though both are commonly used to provide comparisons between different materials.

Pore volumes may be measured as an alternative to surface area to characterise the porosity of a porous material. Dubinin-Radushkevich (D-R) theory is based on the Polányi potential theory in which physisorption isotherm data may be expressed as a temperature invariant *characteristic curve*.[163] The Dubinin-Radushkevich equation is,

$$\frac{V}{V_0} = e^{-\frac{[-RTln(p/p_0)]^2}{(\beta E_0)^2}}$$

where $\frac{V}{V_0}$ is the fractional filling of the micropore volume V_0; E_0 is the *characteristic energy*; and β is a scaling factor. Using a linear form of the D-R equation, the micropore volume of a material may be determined from the intercept of a plot of A^2 (where $A = \frac{-RT\ln(p/p_0)}{\beta}$) against $\ln V$.

The porosity of activated forms of open-pore framework materials in this work was initially investigated by N_2 adsorption at 77 K. Materials were activated at elevated temperature (100–200°C) and reduced pressure ($\sim 1 \times 10^{-4}$ Torr) for 2–4 hours, with isotherms collected using a Micromeritics Tristar II 3020 volumetric porosimeter. If the sample was found to be porous, a lower starting pressure N_2 isotherm was collected at 77 K using a Micromeritics 2020 volumetric porosimeter. Where insufficient sample was available for either of these porosimeters, data was collected using a Hiden-Isochem IGA. Adsorption isotherms for CO_2 adsorption at 195, 273 and 298 K and CH_4 at 195 and 273 K were collected using a Hiden-Isochema IGA gravimetric instrument. High-pressure adsorption measurements of CO2, methane, ethane, propane and butane adsorption were collected at 298 K using a bench-scale open-flow adsorption/desorption volumetric apparatus described in detail elsewhere.[164]

Simulating Adsorption

In addition to experimental adsorption measurements, the adsorption of gas molecules by porous solids may be investigated by computer simulation. Two approaches are commonly used for this: quantum mechanical calculations and molecular simulations. Both methods parameterise the intermolecular interactions in terms of electrostatic and dispersive (i.e. van der Waals) interactions. Keskin *et al.* provide a comprehensive review of simulation techniques applied to MOFs.[165]

Quantum mechanical approaches use approximations of the multibody Schrödinger equation to determine not only adsorptive properties of a system, but also physical properties such as lattice constants and point charges.[165] The most common approach used is *density functional theory* (DFT), as it relatively computationally cheap. DFT has been widely used in predicting structural properties of MOFs, though for adsorption it has been less successful as it does not predict dispersive interactions with sufficient precision. A more precise description may be achieved using high level *ab initio* methods, though these tend to be extremely computationally intensive.[165]

By contrast, molecular simulation is much less computationally intensive, as van der Waals interactions are approximated using a *force field* approach.[165, 166] Adsorbents are modelled using an atomistic representation of the MOF, derived from the desolvated structure. The framework is assumed to be rigid and periodic boundary conditions are applied to avoid finite size effects.[166] Force fields define the interactions between each pair of atoms in the adsorbate/adsorbate and adsorbate/adsorbent systems, using Lennard-Jones parameters and partial charges to describe van der Waals and electrostatic interactions respectively. Bond deformations of the adsorbate may also be included in the force-field.[166] For framework elements the UFF,[167] DREIDING[168] or OPLS-AA[169] force fields are commonly used. Adsorbates may be modelled either atomistically (like the framework), in which case the same force field may be used, or alternatively groups of atoms may be modelled together by a so-called united atom approach, modelling for example a CH_2 group as a single sphere. The TraPPE force field contains interaction parameters for adsorbates modelled by this approach.[170]

Isotherms may be obtained by predicting adsorption equilibria using Grand Canonical Monte Carlo (GCMC) simulations. GCMC mimics experimental conditions by fixing the chemical potential, volume and temperature of the system, whilst allowing the number of molecules to vary.[166] At every pressure step of the isotherm, millions of Monte Carlo insertion, deletion, translation or rotation steps are performed with acceptance criteria based on Boltzmann weighting. Of

these steps, an initial fraction (usually 40 %) are used for equilibration, with the remaining 60 % used to calculate the simulation average for a given pressure.[166]

In this work the MUSIC general purpose simulation code will be used to simulate adsorption isotherms,[171] using the UFF force field[167] to describe the framework and either UFF or TraPPE[170] for the adsorbate.

Determination of Surface Area - Experiment vs Simulation

Using an atomistic model of the framework, the surface area may be directly computed and compared against experimentally derived BET and Langmuir surface areas. However, different authors define surface area in different ways: the van der Waals surface (also Corey-Pauling-Koltun) assumes atoms are hard overlapping spheres of van der Waals radius and the surface area is the combined surface area of all spheres; the Connolly surface describes the surface mapped out by the outer edge of a probe molecule "rolled" over a surface; and the solvent accessible surface area is the surface mapped out by the centre of a probe molecule "rolled" over a surface[172] (*Fig. 2.9*).

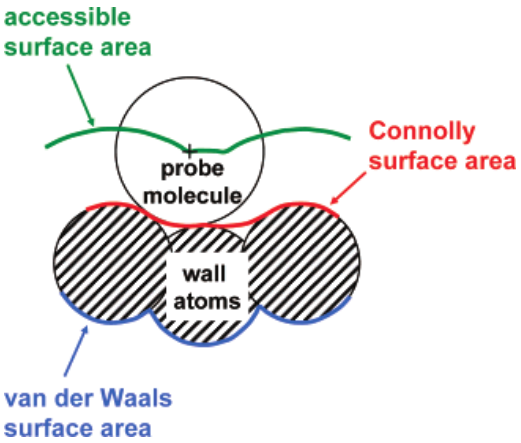

Figure 2.9: Accessible surface area determined by "rolling" a probe molecule over the surface. *After Düren et al.[173]*

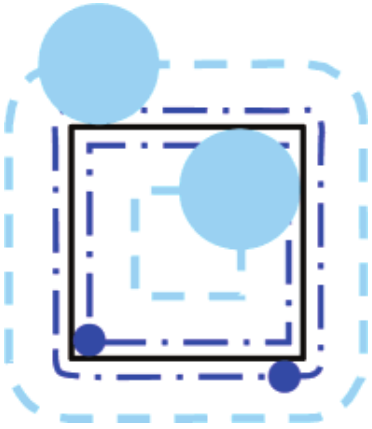

Figure 2.10: The effect of edges and corners on the accessible surface area. *After Düren et al.[173]*

Düren *et al.* calculated the accessible surface area geometrically using probe molecules of varying sizes and compared this with experimentally determined BET surface areas for a range of MOFs.[173] The accessible surface area is sensitive to structural factors such as the proportion of the surface made up of edges and corners (*Fig. 2.10*) and also to the size of the probe molecule, which does not affect the Connolly surface, leading to the suggestion that the accessible surface rather than the Connolly surface should be used to analyse porous frameworks. Düren *et al.*

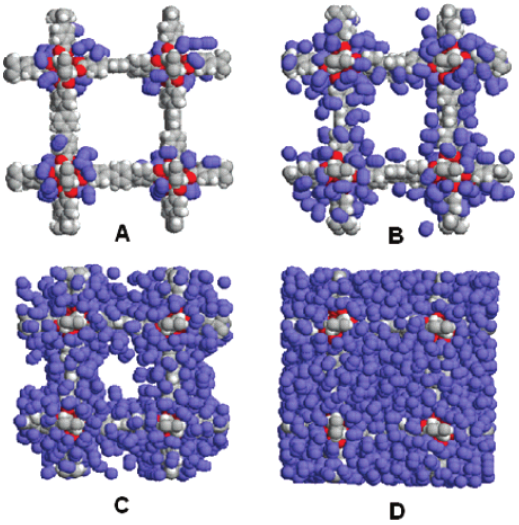

Figure 2.11: Snapshots showing the change in adsorbate distribution with increasing loading (**A**–**D**) from the simulation of N_2 adsorption in IRMOF-16. *After Walton et al.*[174]

also show good agreement between experimentally determined BET surface areas and the accessible surface area.

In two recent papers Snurr and co-workers have used the geometrically determined accessible surface area to evaluate the validity of the BET method for determining surface areas in microporous materials. Walton *et al.* compared BET surface areas calculated using data from both GCMC simulations and experiments with the accessible surface areas of a series of IRMOF materials with increasing length linkers (and hence pore sizes),[174] whilst Bae *et al.* performed similar experiments for a series of nanoporous (<7 Å diameter pores) MOFs and zeolites.[175] Walton *et al.* used simulations to investigate whether multilayer formation (a primary assumption of BET theory) occurs during adsorption in microporous MOFs and reported how adsorbate distribution within the pores changes with loading (*Fig. 2.11*). At low loading the adsorbates preferentially adsorb at corner metal-oxide sites. As the loading increases a complete monolayer is formed within the pore and following this, for large pore MOFs, multilayers form with complete pore filling achieved at low partial pressures: for MOF-5 (IRMOF-1) $\frac{p}{p_0} \approx 0.2$. Standard BET surface area analysis is usually carried out in the range $0.05 < \frac{p}{p_0} < 0.3$. However, for microporous solids with small pore sizes this range may be inappropriate as pores in the solid fill rapidly. Rouquerol *et al.* proposed two criteria for selecting a pressure range over which the BET surface area should be determined for microporous solids:[176] firstly, the intercept of the linear form of the BET equation (*eqn. (2.5)*) must be positive; and secondly, a pressure range should be selected such that $V_{Mono}\left(1 - \frac{p}{p_0}\right)$ increases with increasing $\frac{p}{p_0}$. These

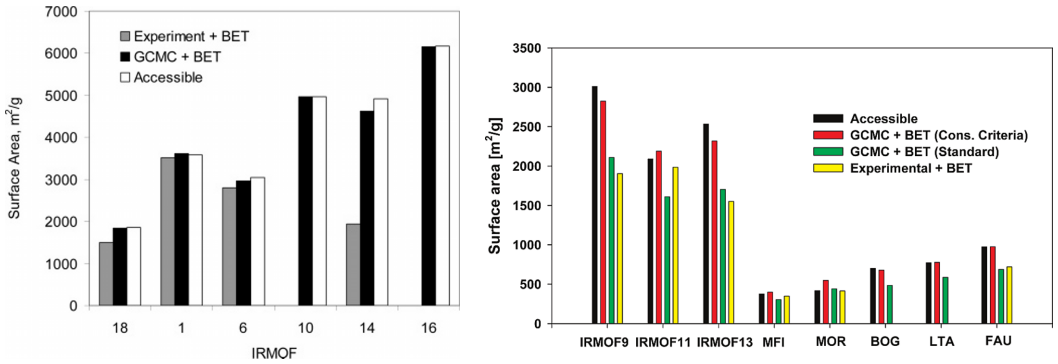

(a) (b)

Figure 2.12: Comparison of the BET surface areas calculated from experiment and simulation (using both standard and consistency criteria pressure ranges — *right*) against accessible surface area calculated geometrically[173] for a range of MOFs and zeolite. *After Walton et al.*[174] (*left*) & *Bae et al.*[175] (*right*).

consistency criteria were used to calculate BET surface areas from simulated data which were found to be in good agreement with both experimental BET surface areas and also calculated accessible surface areas for all IRMOFs except IRMOF-14 (*Fig. 2.12a*). IRMOF-14 is thought to have a much lower surface area due to either crystal defects, interpenetration or pore blocking in the experimental sample. All of the simulated BET surface areas slightly over-predict the experimental values since the simulated data use perfect crystals, whereas experimental data were collected from real materials which will contain some defects and blocked pores.

Bae *et al.* also found good agreement between simulation BET and accessible surface areas using the consistency criteria for nanoporous adsorbents (*Fig. 2.12b*), though experimental surface areas were found to be much smaller, thought to be due to the standard BET range being used to calculate the surface area. Using the standard BET range with the simulated data, good agreement was found between simulated and experimental surface areas.[175] Bae *et al.* also investigated the variation of heat of adsorption (Q_{st}) with loading in the consistency criteria pressure range (*Fig. 2.13*). A plateau in Q_{st} is found at the start of the consistency criteria BET linear region, with a value greater than the heat of condensation of the adsorbate (N_2: 5.56 kJ mol^{-1}), indicating first monolayer formation (adsorbent-adsorbate interactions), which is the correct region to calculate the surface area of the adsorbent from. Both these papers provide some validation for the use of the BET to obtain quantitive experimental surface area values, even though the absence of multilayer formation invalidates the BET theory.

Turner *et al.* calculated surface areas of a series of MOFs using *procrystal electron density*, by calculating the sum of the spherical electron densities located about

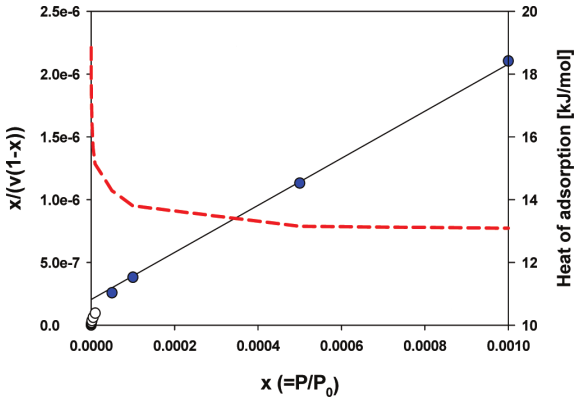

Figure 2.13: Variation of Q_{st} (red dashes) with N_2 loading at low pressure IRMOF-13. Blue circles are data points used in calculating the BET surface area. The initial decrease in Q_{st} is due to preferential adsorption in small pores. *After Bae et al.*[175]

appropriate nuclear positions.[172] For MOFs, the 0.0003 au isosurface was used as this reduces the contribution of re-entrant pores. Reasonable agreement was found with both reported Langmuir and BET surface areas, though the procrystal isosurface over-predicts the surface area in all cases due to the presence of small adsorbate inaccessible pores which contribute to the surface area of the framework, especially with catenated MOFs, as well as the reasons outlined previously (*vide supra*). A very good agreement was found between the procrystal surface area and the experimental pore volumes calculated from D-R equation.[172]

2.3.2 Diffusion

Models of adsorption consider an equilibrium situation where adsorbate molecules freely access the adsorption surface (see *Section 2.3.1*). However, the structure of microporous solids can restrict access to sites of adsorption, so it is necessary to consider the diffusion process. Diffusion occurs either by activated jumps between neighbouring adsorption sites or movements across pores.[10] The rate is dependent upon the strength of the interaction between adsorbate and surface, the distance between sites to complete the jump and the amount of site and pore blocking due to defects or other adsorbates.

Two modes of diffusion occur simultaneously within micropores: self-diffusion and transport diffusion. Self-diffusion is diffusion in the absence of a chemical-potential gradient[177], i.e. at equilibrium, whereas transport diffusion is a non-equilibrium process in which a chemical-potential causes diffusion.

As measurement of diffusion with nanoporous materials is experimentally challenging, little is currently known about diffusion within MOFs and almost

all the information available has come from molecular simulations.[165] Diffusion through micropores has been modelled by combined molecular dynamics (MD) and GCMC methods. Xu *et al.*[178] used transport diffusion MD studies in micropores to show how loading affects diffusivity within a pore. Düren *et al.* simulated transport with a variety of pore geometries and surface types.[179] It was found that diffusion is independent of pore surface structure, for systems with strong adsorbate-surface interactions, compared to adsorbate-adsorbate interactions. In such systems, diffusing molecules have a weak interaction with the adsorbate covered surface, and so move relatively freely through the pores. Düren *et al.* suggest that in systems where the interaction between adsorbate and surface is weaker, a different transport profile would be expected and surface structure may become important in transport.

Chapter 3

Synthesis of Phosphonic Acid Ligands

A wide range of coordination polymers have been prepared using bisphosphonic acid ligands as the linker — examples have been reviewed elsewhere in this work (*Section 1.4*). Phosphonic acids may be regarded as organic derivatives of phosphoric acid (H_3PO_4) in which one of the OH groups is substituted by an organic group (R). Phosphonic acids have the general formula $RPO(OH)_2$. The P atom is sp^3 hybridised and therefore substituents are arranged in a tetrahedral geometry about the central atom (*Fig. 3.1*).

Synthetically the challenge in preparing a phosphonic acid is the formation of the C-P bond. A wide range of synthetic approaches to this problem has recently been reviewed.[180] The most commonly applied approaches are the Michaelis-Arbuzov reaction, catalytic cross-coupling reactions and the modified Mannich reaction, originally reported by Moedritzer and Irani.[181] The Michaelis-Arbuzov and catalytic cross-coupling reactions are quite closely related to one another. In the Michaelis-Arbuzov reaction, a primary alkyl halide reacts directly with trialkylphosphite to form a phosphonium halide salt. Aryl and alkenyl halides have less electrophilic C-X bonds and therefore either a $Ni^{(II)}$ or $Pd^{(II)}$ catalyst is needed

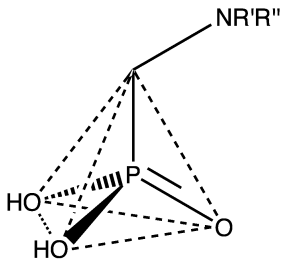

Figure 3.1: Tetrahedral geometry of phosphonic acid group.

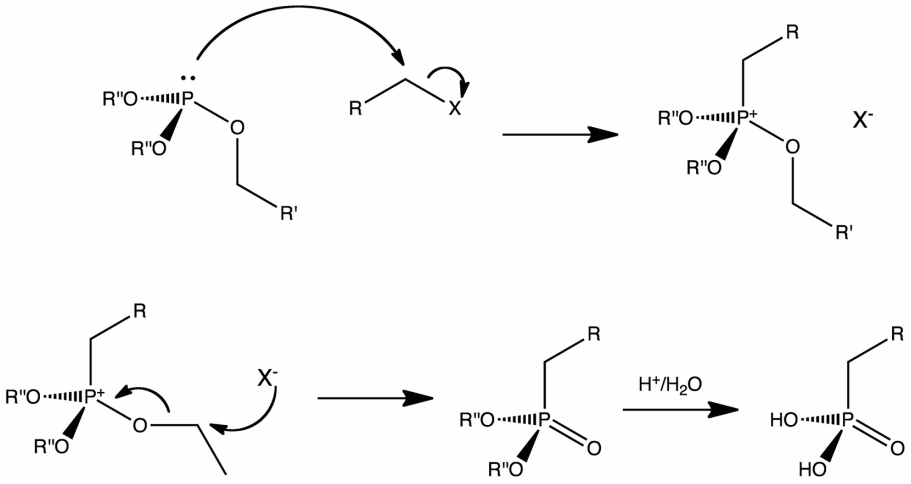

Figure 3.2: Michaelis-Arbuzov reaction mechanism for the preparation of phosphonic acids from primary alkyl halides. For aryl or alkenyl halides, a $Ni^{(II)}$ or $Pd^{(II)}$ catalyst is needed to first form the phosphonium halide salt.

to form the salt. Once generated, the salt eliminates an alkyl halide to leave a dialkyl alkyl phosphonate which may be converted to the acid by hydrolysis (*Fig. 3.2*).

In the modified Mannich reaction α-aminomethylphosphonic acids are prepared from primary or secondary amines. The reaction proceeds by nucleophilic attack of the amine on formaldehyde, activated by protonation of the formaldehyde O atom by the acid catalyst. Water is then eliminated, forming an electrophilic iminium cation which is attacked by phosphorous acid (H_3PO_3), forming the phosphonic acid following loss of a proton (*Fig. 3.3*).

All ligands in this work were prepared through the modified Mannich reaction. In order to prepare bisphosphonic acid ligands suitable for forming extended networks, cyclic diamines were used as the substrate. This also has the advantage that, provided the reaction goes to completion, a single component product is obtained as each amine may only be mono-methylenephosphonylated. It was also found that phase pure products (according to ^{1}H, ^{13}C and ^{31}P solution-state NMR spectroscopy) were obtained directly from syntheses, from the ligand which crystallised on cooling of the reaction mixture. Syntheses were adapted from those reported by Mowat[182, 111] with all ligands fully characterised by NMR for the first time, with further characterisation by elemental analysis (where possible). A typical synthesis using piperazine as the substrate is given (*Section 3.1*). The synthesis of six bisphosphonic acid ligands has been attempted ($H_4\mathbf{L}$, $H_4\mathbf{L}'$, *R*-$H_4\mathbf{L}'$, $H_4\mathbf{L}''$, $H_4\mathbf{LL}$ and $H_4\mathbf{LC_3L}$) and the results of these syntheses and characterisation of each ligand is reported. In addition, a carboxyphosphonic acid ($H_3\mathbf{LC}$) and a monophosphonic acid ($H_2\mathbf{L}_{pip}$) have been prepared to investigate the flexibility of this

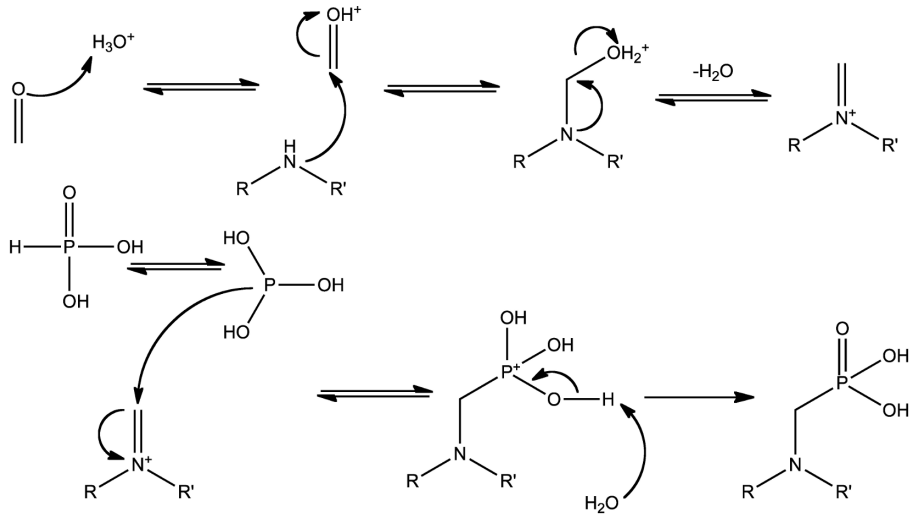

Figure 3.3: Modified Mannich reaction for the preparation of α-aminomethylphosphonic acids, first reported by Moedritzer & Irani.[181]

reaction and for comparison of crystal structures.

3.1 Typical Synthesis of Bis-α-aminomethylphosphonic acid Ligand

In a typical synthesis of N,N′-piperazinebis(methylenephosphonic acid) ($H_4\mathbf{L}$) piperazine (Sigma) (7.75 g, 0.09 mol) was dissolved in distilled water (70 ml) with phosphorous acid (Sigma) (19.19 g, 0.23 mol) and hydrobromic acid (Sigma, 48 wt.% aqueous solution) (74 ml, 0.65 mol). Formaldehyde (Alfa Aesar, 35 wt.% aqueous solution) (38.5 ml, 0.52 mol) was added to the reaction dropwise over 20 minutes. The reaction was then refluxed at 120°C for 20 hours. On cooling a white precipitate was obtained. Solid was separated by filtration, washed with ethanol-water solution (90:10, 3× 30 ml) to remove unreacted phosphorous acid and HBr residue, and dried overnight at 40°C. The volume of the filtrate was then reduced by ∼70 % and the remaining solution placed in the fridge overnight to crystallise any remaining ligand. Solids obtained from the filtrate were also collected by filtration, washed with ethanol-water solution and dried overnight. Products were characterised by elemental analysis ^{1}H, ^{13}C, ^{31}P solution-state NMR spectroscopy, powder and single crystal X-ray diffraction.

Syntheses of the other ligands followed similar synthetic procedures — any differences in the syntheses will be described. In all reactions a stoichiometric ratio of 0.09 : 0.23 : 0.52 (amine N atom : H_3PO_3 : CH_2O) was used. Although only

catalytic, HBr molar concentration was also scaled with other reagents (Zoń *et al.* indicate that a molar excess of acid is important).[180] It was not possible to obtain single crystals suitable for diffraction for all ligands. Discrepancies in elemental analysis results are thought to be due to residual HBr coordinated to the ring N atoms and inclusions of solvent in the samples (for example, NMR shows evidence of ethanol and water may also be incorporated).

3.2 Synthesis and Characterisation of Bisphosphonic Acid Ligands

3.2.1 N,N′-piperazinebis(methylenephosphonic acid)

N,N′-piperazinebis(methylenephosphonic acid) ($H_4\mathbf{L}$ — *Fig. 3.4*) was synthesised using piperazine (Sigma) as the substrate in the modified Mannich reaction, using a reaction ratio of 0.09 : 0.46 : 1.04 (piperazine : H_3PO_3 : CH_2O). In a typical reaction (0.20 mol piperazine) a yield of 83.9 % was obtained.

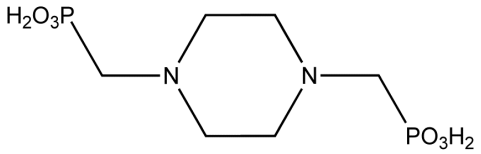

Figure 3.4: N,N′-piperazinebis(methylenephosphonic acid) — $H_4\mathbf{L}$.

Elemental analysis, expected (calculated for $C_6H_{16}N_2O_6P_2$): C 26.29 %, H 5.88 %, N 10.22 %; found: C 20.00 %, H 5.13 %, N 7.51 %.

The piperazine ^{1}H spectrum at 298 K was found to show a broad singlet, attributed to the coalescence of all of the ring ^{1}H resonances. To investigate this, ^{1}H spectra were recorded at both 298 K and 353 K. The presence of a sharp singlet in the 353 K spectrum indicates this is indeed a temperature-dependent effect due to the coalescence of the resonances of several ^{1}H environments. ^{1}H (300 MHz, D_2O/NaOH, 298 K): δ = 2.4 (broad s, 8H), 2.27 (d, ^{2}J(H-P) = 12 Hz, 4H). ^{1}H (300 MHz, D_2O/NaOH, 353 K): δ = 2.97 (s, 8H), 2.27 (d, ^{2}J(H-P) = 12.2 Hz, 4H). ^{13}C (400 MHz, D_2O/NaOH): δ = 57.07 (d, ^{1}J(C-P) = 140.4 Hz), 53.7 (d, ^{3}J(C-P) = 8.5 Hz). ^{31}P (400 MHz, D_2O/NaOH): δ = 14.35 (t, ^{2}J(P-H) = 12.2 Hz).

$H_4\mathbf{L}$ was obtained from the modified Mannich reaction as a fine white powder. Crystals suitable for single crystal X-ray diffraction were obtained from a reaction of $CdCl_2$ and $H_4\mathbf{L}$ heated hydrothermally at 190°C for 48 hrs. Only recrystallised ligand was obtained from this reaction. The structure of $H_4\mathbf{L}$ was solved using

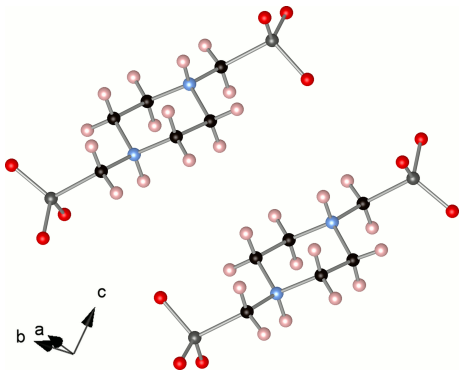

Figure 3.5: Asymmetric unit showing the two symmetry inequivalent molecules of $H_4\mathbf{L}$.

direct methods routines within the Sir2008 package[142] in orthorhombic space group $Pna2_1$ (a = 20.568(5) Å, b = 16.214(4) Å, c = 6.6274(17) Å, V = 2210.1(10) Å^3). The structure was refined using the SHELXL routine of SHELX-97.[140] All non-H atoms were located from the original structure solution. Protons were placed geometrically on C atoms with riding constraints on their coordinates and U_{Iso} parameters. Protons on N atoms were located by Fourier difference maps. It was necessary to restrain the bonding distance (N4-H8: 1.0 Å) and also non-bonding distances between amino protons and C atoms α to the N atom (e.g. H8$\cdots$C4: 2.08 Å). It was not possible to locate the remaining phosphonic acid protons. Further cycles of refinement were performed until Fourier difference maps indicated no significant unaccounted for electron density. A final fit of R = 0.0877 (R_w = 0.2262) was obtained.

The asymmetric unit of $H_4\mathbf{L}$ (*Fig. 3.5*) consists of two symmetry inequivalent $H_4\mathbf{L}$ molecules. Both molecules have a chair conformation and have two protonated piperazinyl N atoms. Protons engage in H-bonding with PO_3C groups of neighbouring $H_4\mathbf{L}$ molecules (O$\cdots$H: 1.63(3)–1.68(5) Å). PO_3C groups also H-bond with PO_3C groups in neighbouring molecules (short O$\cdots$O contacts: 2.465(11)–2.491(11) Å). Molecules are arranged in sheets in the *bc*-plane, within which an extensive H-bonding network is developed (*Fig. 3.6*). The degree of H-bonding within the sheets is maximised by the molecules adopting a zig-zag like arrangement along the *b*-direction, with neighbouring molecules aligned at $\sim 90^\circ$ to one another.

To confirm the crystal structure of the ligand determined by single crystal diffraction is the same as the crystal structure of the bulk, simulated and experimental powder X-ray diffraction patterns of the ligand were compared (*Fig. 3.7*). The two patterns are very different, indicating that the structure determined is not representative of the ligand crystallised from the Mannich reaction. The solved structure is probably a polymorph which crystallises under hydrothermal

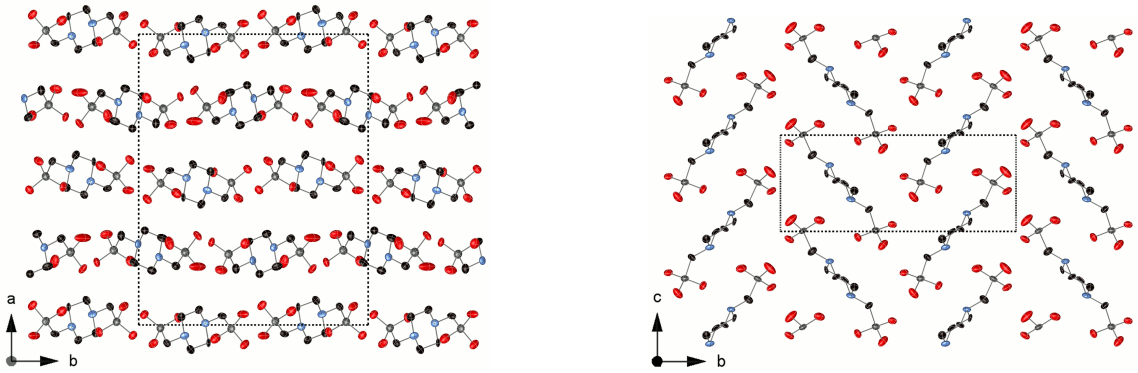

(a) (b)

Figure 3.6: Packing diagram for the crystal structure of $H_4\mathbf{L}$, showing the arrangement of the sheets viewed along the *c*-axis (*left*) and the structure within the sheets, with neighbouring molecules inclined at $\sim 90°$ to one-another (*right*). Dotted lines indicate unit cell. Protons omitted for clarity.

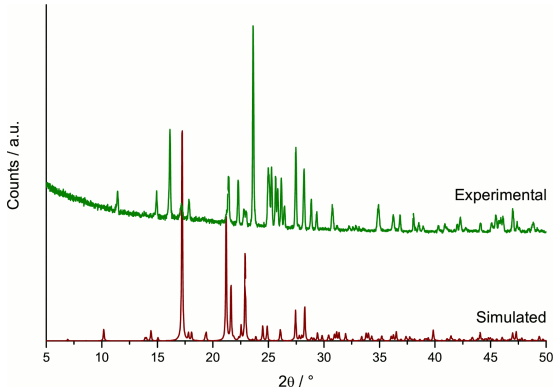

Figure 3.7: Comparison of simulated (from the single crystal structure — red) and experimental (from the bulk powder — green) powder X-ray diffraction patterns (Cu K_α) of $H_4\mathbf{L}$.

conditions.

The experimental diffraction data were successfully indexed using the TREOR routines of EXPO2009[153, 148] in a monoclinic space group with cell parameters $a = 12.037(7)$ Å, $b = 10.958(3)$ Å, $c = 11.294(3)$ Å, $\beta = 105.75(4)°$, $V = 1434(16)$ Å^3 (F.O.M. $M_{20} = 21$).[154]

3.2.2 N,N′-2-methylpiperazinebis(methylenephosphonic acid)

Racemic N,N′-2-methylpiperazinebis(methylenephosphonic acid ($H_4\mathbf{L}'$ — *Fig. 3.8*) was prepared by the modified Mannich reaction from racemic 2-methylpiperazine (Alfa Aesar). Although the same modified Mannich reaction described was used (*Section 3.1*), with a stoichiometric ratio of 0.09 : 0.46 : 1.04 (2-methylpiperazine : H_3PO_3 : CH_2O), no solid was obtained on cooling. Instead it was necessary to reduce the volume of the solvent by $\frac{2}{3}$, then to add ethanol (*ca.* 2× remaining solvent volume) and refrigerate overnight to aid crystallisation. Initial solids were often highly water soluble and it was therefore necessary to repeat this step several times. The high solubility is due to the presence of HBr in the solvent. The role of ethanol is to reduce the water content of the solution and to facilitate the removal of HBr from the solution. In a typical synthesis (0.01 mol racemic 2-methylpiperazine) a yield of 78.5 % was achieved. The reaction has been sclaed up (0.2 mol racemic 2-methylpiperazine) and gave a similar yield. The solid was obtained as a fine white crystalline powder. It has not been possible to obtain crystals suitable for single crystal diffraction.

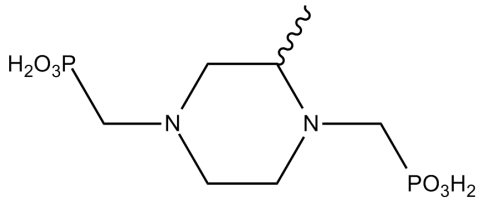

Figure 3.8: N,N′-2-methylpiperazinebis(methylenephosphonic acid) — $H_4\mathbf{L}'$.

Elemental analysis, expected (calculated for $C_7H_{18}N_2O_6P_2$): C 29.18 %, H 6.30 %, N 9.72 %; found: C 27.60 %, H 6.79 %, N 9.05 %.
^{1}H (400 MHz, D_2O/NaOH): δ = 2.96 (d, $^2J_{Gem}$ = 12.2 Hz, 1H), 2.84 (d, $^2J_{Gem}$ = 11.2 Hz, 1H), 2.77 (d, $^2J_{Gem}$ = 11.7 Hz, 1H), 2.63 (dd, ^{2}J(H-P) = 14.8 Hz, $^2J_{Gem}$ = 14.8 Hz, 1H), 2.46 (m, 2H), 2.28 (m, 3H), 2.10 (dd, $^2J_{Gem}$ = 11.0 Hz, $^3J_{Ax-Ax}$ = 11.0 Hz, 1H), 1.81 (dd, $^2J_{Gem}$ = 11.1 Hz, $^3J_{Ax-Ax}$ = 11.1 Hz, 1H), 0.87 (d, ^{3}J = 6.2 Hz, 3H). ^{13}C (400 MHz, D_2O/NaOH): δ = 61.05 (d, ^{3}J(C-P) = 8.8 Hz), 57.00 (d, ^{1}J(C-P) = 140.1 Hz), 55.50 (d, ^{3}J(C-P) = 10.4 Hz), 53.76 (d, ^{3}J(C-P) = 8.0 Hz), 51.98 (s), 51.61 (d, ^{1}J(C-P) = 136.5 Hz), 16.96 (d, ^{4}J(C-P) = 7.1 Hz). ^{31}P (400 MHz, D_2O/NaOH): δ = 15.23 (dd, ^{2}J(P-H) = 14.8 Hz, ^{2}J(P-H) = 9.4 Hz), 14.37 (t, ^{2}J(P-H) = 12.4 Hz).

N,N′-*R*-2-methylpiperazinebis(methylenephosphonic acid)

Enantiopure N,N′-*R*-2-methylpiperazinebis(methylenephosphonic acid) (*R*-$H_4\mathbf{L}'$ — *Fig. 3.9*) was prepared by the same method as the racemic form, but using enantiopure *R*-2-methylpiperazine (Sigma) as the substrate in the reaction. As with $H_4\mathbf{L}'$ it was difficult to crystallise the *R*-$H_4\mathbf{L}'$. *R*-$H_4\mathbf{L}'$ was finally crystallised by repeatedly washing with ethanol and reducing the volume of the solution *in vacuo*. In a typical synthesis (1.1×10^{-2} mol *R*-2-methylpiperazine) a yield of 54.7 % was achieved. The lower yield than either $H_4\mathbf{L}$ or $H_4\mathbf{L}'$ is attributed to the difficulties in crystallising the solid. The final solid is a fine white microcrystalline powder. It has not been possible to obtain crystals suitable for single crystal diffraction.

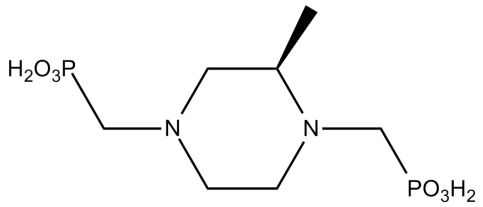

Figure 3.9: N,N′-*R*-2-methylpiperazinebis(methylenephosphonic acid) — *R*-$H_4\mathbf{L}'$.

Elemental analysis, expected (calculated for $C_7H_{18}N_2O_6P_2$): C 29.18 %, H 6.30 %, N 9.72 %; found: C 27.48 %, H 6.47 %, N 8.78 %.

^{1}H and ^{31}P NMR spectra were collected for *R*-$H_4\mathbf{L}'$ for identification purposes and to ensure phase purity of the product. Spectra were assigned with reference to the spectra of closely related $H_4\mathbf{L}'$. ^{1}H (300 MHz, D_2O/NaOH): δ = 3.00 (d, $^2J_{Gem}$ = 12.3 Hz, 1H), 2.84 (dd, $^2J_{Gem}$ = 13.8 Hz, $^2J_{Gem}$ = 13.8 Hz, 2H — two independent ^{1}H environments with same shift), 2.66 (dd, ^{2}J(H-P) = 14.7 Hz, $^2J_{Gem}$ = 14.7 Hz, 1H), 2.47 (m, 2H), 2.32 (m, 3H), 2.14 (dd, $^2J_{Gem}$ = 10.8 Hz, $^3J_{Ax-Ax}$ = 10.8 Hz, 1H), 1.85 (dd, $^2J_{Gem}$ = 11.1 Hz, $^3J_{Ax-Ax}$ = 11.1 Hz, 1H), 0.90 (d, ^{3}J = 6.3 Hz, 3H). ^{31}P (300 MHz, D_2O/NaOH): δ = 16.43 (dd, ^{2}J(P-H) = 14.8 Hz, ^{2}J(P-H) = 9.5 Hz), 15.57 (t, ^{2}J(P-H) = 12.3 Hz).

3.2.3 N,N′-2,5-dimethylpiperazinebis(methylenephosphonic acid)

N,N′-2,5-dimethylpiperazinebis(methylenephosphonic acid) ($H_4\mathbf{L}''$ — *Fig. 3.10*) was synthesised using *trans*-2,5-dimethylpiperazine (Sigma) as the substrate in the modified Mannich reaction. Like $H_4\mathbf{L}$, $H_4\mathbf{L}''$ crystallised on cooling the reaction. A typical synthesis (9.0×10^{-3} mol *trans*-2,5-dimethylpiperazine) gave a yield of 79.4 %. $H_4\mathbf{L}''$ was obtained as a fine white microcrystalline powder. It has not been possible to prepare crystals suitable for diffraction.

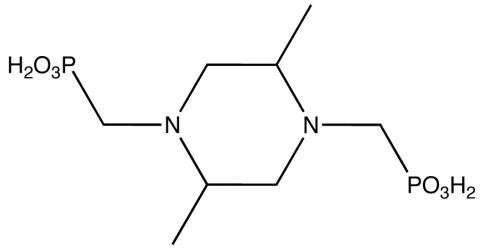

Figure 3.10: N,N′2,5-dimethylpiperazinebis(methylenephosphonic acid) — $H_4\mathbf{L}''$.

Elemental analysis gave C 29.38 %, H 6.76 %, N 8.11 % (calculated for $C_8H_{20}N_2O_6P_2$: C 31.80 %, H 6.67 %, N 9.27 %).
^{1}H (400 MHz, D_2O/NaOH): δ = 3.20 (dd, $^2J_{Gem}$ = 12.4 Hz, $^3J_{Eq-Ax}$ = 2.6 Hz, 2H), 2.86 (dd, ^{2}J(H-P) = 14.9 Hz, $^2J_{Gem}$ = 14.9 Hz, 2H), 2.65 (m, 2H), 2.48 (dd, $^2J_{Gem}$ = 14.8 Hz, ^{2}J(H-P) = 9.3 Hz, 2H), 2.37 (dd, $^2J_{Gem}$ = 11.7 Hz, $^3J_{Ax-Ax}$ = 11.7 Hz, 2H), 1.12 (d, ^{3}J = 6.2 Hz, 3H). ^{13}C (400 MHz, D_2O/NaOH): δ = 59.58 (s), 56.04 (d, ^{3}J(C-P) = 10.3 Hz), 51.61 (d, ^{1}J(C-P) = 136.6 Hz), 16.41 (s). ^{31}P (400 MHz, D_2O/NaOH): δ = 15.25 (dd, ^{2}J(P-H) = 14.7 Hz, ^{2}J(P-H) = 9.8 Hz).

3.2.4 N,N′-4,4′-bipiperidinebis(methylenephosphonic acid)

N,N′-4,4′-bipiperidinebis(methylenephosphonic acid) (H_4**LL** — *Fig. 3.11*) was prepared using 4,4′-bipiperidine dihydrochloride (Alfa Aesar) as the substrate in the modified Mannich reaction. The same reaction protocol was used in the preparation of H_4**LL** as H_4**L**. In a typical reaction (0.018 mol piperazine) a yield of 94.2 % was obtained.

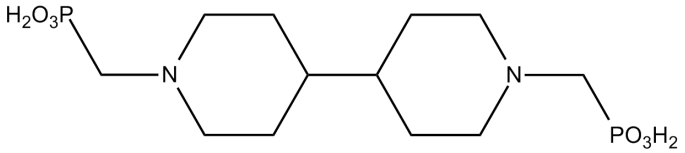

Figure 3.11: N,N'-bipiperidinebis(methylenephosphonic acid) — H_4**LL**.

Elemental analysis gave C 33.01 %, H 7.90 %, N 6.35 % (calculated for $C_{12}H_{26}N_2O_6P_2$: C 40.45 %, H 7.36 %, N 7.86 %).
^{1}H (400 MHz, D_2O/NaOH): δ = 2.87 (d, $^2J_{Gem}$ = 11.7 Hz, 4H), 2.29 (d, ^{2}J(H-P) = 12.1 Hz, 4H), 1.98 (dd, $^2J_{Gem}$ = 11.2 Hz, $^3J_{Ax-Ax}$ = 11.2 Hz, 4H), 1.5 (d, $^2J_{Gem}$ = 12Hz, 4H), 0.90 (m, 6H). ^{13}C (400 MHz, D_2O/NaOH): δ = 57.23 (d, ^{1}J(C-P) = 139.4 Hz), 54.61 (d, ^{3}J(C-P) = 7.5 Hz), 39.31 (s), 28.53 (s). ^{31}P (400 MHz, D_2O/NaOH): δ = 15.05 (t, ^{2}J(P-H) = 11.9 Hz).

H_4**LL** was prepared as a fine white powder. Suitable crystals for single crystal X-ray diffraction experiments were obtained by heating a sample of H_4**LL** hydrothermally for 24 hrs at 190°C. Large colourless needle crystals were obtained after recrystallisation. The structure was solved using the direct methods routines of the SHELX-97 package,[140] in monoclinic space group $P\,2_1/c$ (a = 10.240(3) Å, b = 6.0262(16) Å, c = 15.832(5) Å, β = 95.866(4)°, V = 971.8(5) Å^3). All non-H atoms within the ligand were located from the initial solution. The structure was then refined using the SHELXL program of the SHELX-97 suite.[140] Water molecule O atoms were quickly located by Fourier difference maps. Protons were placed geometrically on C atoms with their positions and U_{Iso} values riding on the C atom to which they are bound. Amino and phosphonate protons were located by Fourier difference maps and their positions and U_{Iso} values allowed to refine freely. It was not possible to locate protons of the water molecules of crystallisation. Cycles of refinement were continued until no further significant changes to the structure were observed or peaks in the Fourier difference maps were located. A final fit of R = 0.0511 (R_w = 0.1560) was achieved.

The asymmetric unit consists of one piperidine ring and two water molecules of crystallisation (*Fig. 3.12a*). The ring adopts a chair conformation with a protonated

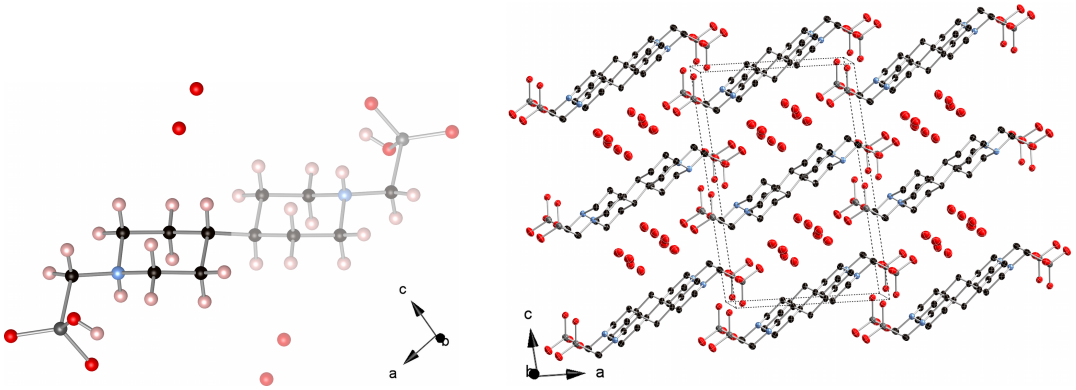

(a) (b)

Figure 3.12: Crystal structure of H_4**LL**. Two asymmetric units of H_4**LL** are shown (one greyed out — *left*). A centre of symmetry is located between the two C4 atoms bridging the rings together. A packing diagram is also given (*right*) with protons omitted for clarity. Dotted lines indicate unit cell.

piperidinyl N atom. The PO_3C group is mono-deprotonated to balance the charge on the molecule. The complete molecule has a centre of symmetry between the two C4 atoms which link the piperidine rings together. Molecules form layers parallel to the $(1\,0\,\overline{3})$ plane, with PO_3C groups engaging in H-bonding interactions with water molecules of crystallisation within the layer ((P)O$\cdots$O: 2.733(4)–2.741(5)Å). Layers are held together by further H-bonding interactions between protonated piperidinyl N atoms and PO_3C O atoms (H10$\cdots$O1: 1.94(3)Å) and protonated PO_3C O atoms and O atoms in neighbouring PO_3C groups (H20$\cdots$O1: 1.781(3)Å).

3.2.5 1,3-bis(N-phosphonomethylene-4-piperidinyl)propane

1,3-bis(N-phosphonomethylene-4-piperidinyl)propane ($H_4\mathbf{LC_3L}$ — *Fig. 3.13*) was prepared using 1,3-bis(4-piperidinyl)propane as the substrate in the modified Mannich reaction, with a reaction ratio of 0.09 : 0.46 : 1.04 (1,3-bis(4-piperidinyl)-propane : H_3PO_3 : CH_2O). The reaction was performed as described (*Section 3.1*). However, on cooling, no solid was obtained from the reaction. The reaction solution was reduced in volume and cooled overnight in the fridge. The solution was then washed with ethanol five times before product was obtained. A typical synthesis (1.0×10^{-2} mol 1,3-bis(4-piperidinyl)propane) gave a yield of 64.4 %. The lower yield is attributed to the difficulties in crystallising $H_4\mathbf{LC_3L}$. The final solid was obtained as a very fine white powder. Elemental analysis data have not been collected on this ligand due to large amounts of solvent ethanol in the final product (*vide infra*).

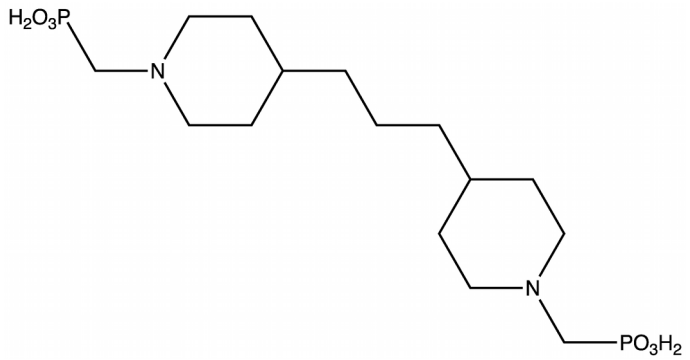

Figure 3.13: 1,3-bis(N-phosphonomethylene-4-piperidinyl)propane — $H_4\mathbf{LC_3L}$.

Only ^{1}H (400 MHz, D_2O/NaOH) and ^{31}P (400 MHz, D_2O/NaOH) NMR spectra have been collected for a sample of $H_4\mathbf{LC_3L}$, as it has so far proven impossible to collect a ^{13}C NMR spectrum. ^{1}H spectra are dominated by two resonances at 3.4 ppm and 0.9 ppm assigned to ethanol. A doublet resonance at 2.25 ppm is assigned to methylene protons of the methylenephosphonic acid group, coupling to the P atom. Further assignment has been hindered by the lack of ^{13}C spectra and the large multiplet, overlain by the ethanol resonance, at $\sim$ 0.9 ppm. ^{31}P spectra show a single triplet resonance at 15.13 ppm assigned to the two equivalent CPO_3 groups. The single resonance in the ^{31}P spectrum indicates a successful synthesis of the target molecule — unreacted H_3PO_3 would not be split into a triplet and a mixed mono- and bisphosphonation would show at least two resonances.

3.2.6 1-(phosphonomethylene)piperidine-4-carboxylic Acid

1-(phosphonomethylene)piperidine-4-carboxylic acid (H_3**LC** — *Fig. 3.14*) was synthesised using the same modified Mannich reaction with 4-piperidinecarboxylic acid (isonipecotic acid — Sigma) as the substrate. As there is only one N atom available to react, a reaction ratio of 0.01 : 0.026 : 0.058 (4-piperidinecarboxylic acid : H_3PO_3 : CH_2O) using an excess of HBr as the catalyst. In a typical reaction (4-piperidinecarboxylic acid, 0.01 mol) a yield of 87.7 % was obtained.

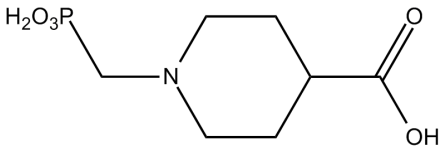

Figure 3.14: 1-(phosphonomethylene)piperidine4-carboxylic Acid — H_3**LC**.

Elemental analysis gave C 35.43 %, H 6.18 %, N 5.70 % (calculated for $C_7H_{14}NO_5P \cdot H_2O$: C 37.67 %, H 6.32 %, N 6.28 %).
^{1}H (400 MHz, D_2O/NaOH): δ = 2.85 (d, $^2J_{Gem}$ = 11.7 Hz, 2H), 2.31 (d, ^{2}J(H-P) = 12.1 Hz, 2H), 2.08 (ddd, $^2J_{Gem}$ = 12.1 Hz, $^3J_{Ax-Ax}$ = 12.1 Hz, $^3J_{Ax-Eq}$ = 1.8 Hz, 2H), 1.94 (tt, $^3J_{Ax-Ax}$ = 11.7 Hz, $^3J_{Ax-Eq}$ = 3.8 Hz, 1H), 1.62 (dd, $^2J_{Gem}$ = 12.8 Hz, $^3J_{Eq-Ax}$ = 3.3 Hz, 2H), 1.36 (ddd, $^2J_{Gem}$ = 12.8 Hz, $^3J_{Ax-Ax}$ = 12.8 Hz, $^2J_{Ax-Eq}$ = 3.3 Hz, 2H). ^{13}C (400 MHz, D_2O/NaOH): δ = 185.17 (s), 57.11 (d, ^{1}J(C-P) = 139.4 Hz), 53.76 (d, ^{3}J(C-P) = 8.1 Hz), 43.72(s), 28.62 (s). ^{31}P (400 MHz, D_2O/NaOH): δ = 14.89 (t, ^{2}J(P-H) = 12.1 Hz).

Crystals suitable for single crystal X-ray diffraction were obtained by hydrothermal heating of a sample H_3**LC** at 190°C for 24 hrs. The structure of H_3**LC** was previously reported by Stock *et al.*[183] but is reported here for comparison with the other crystal structures. The structure of H_3**LC** was solved using direct methods routines within the Sir2008 package[142] in monoclinic space group $P\,2_1/n$ (a = 6.3321(16) Å, b = 25.684(6) Å, c = 7.1642(18) Å, β = 94.957(5), V = 1160.8(5) Å^3). All non-H atoms were located directly from the structure solution. Protons were placed geometrically on C atoms with their positions and U_{Iso} values constrained to ride on the C atom they are bonded to. The proton on the piperazinyl N atom, the carboxylate proton and the protons bonded to the water molecules of crystallisation were located by Fourier difference maps and their positions and U_{Iso} parameters allowed to refine freely. There was some evidence of a proton associated with the PO_3C group, but this refined to an unreasonably large U_{Iso} value and was removed from the structure. The final fit of the data gave R = 0.0554 (R_w = 0.1482).

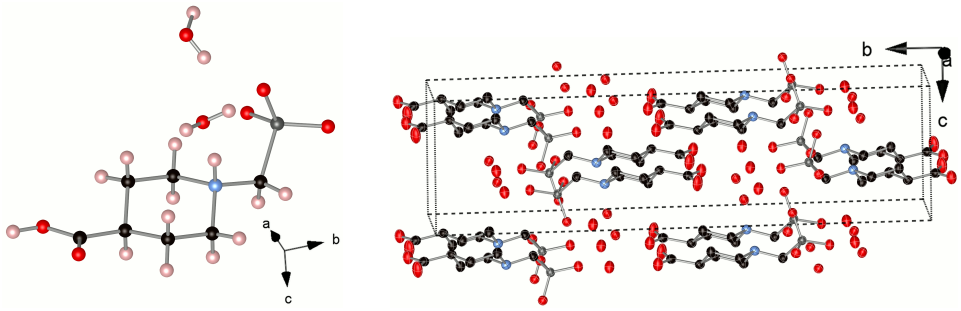

(a) (b)

Figure 3.15: Crystal structure of H_3**LC**, showing the asymmetric unit with two water molecules of crystallisation (*left*) and the packing of the crystal structure (*right*). Dotted lines indicate unit cell. Protons omitted for clarity.

The piperidine ring of H_3**LC** adopts a chair conformer, with the piperazinyl N atom protonated. To balance the charge of the molecule the phosphonic acid is deprotonated, suggesting H_3**LC** is a zwitterion in the solid state. The carboxylic acid group retains its proton. The crystal structure is held together by a H-bonding network involving the protonated piperazinyl N atoms, carboxylate and PO_3C groups and water molecules of crystallisation (donor (D) acceptor contacts in the range D$\cdots$H: 1.60(4)–1.85(4)).

3.2.7 N-piperidinylmethylenephosphonic acid

N-piperidinylmethylenephosphonic acid ($H_2\mathbf{L}_{pip}$— *Fig. 3.16*) was synthesised using the modified Mannich reaction with piperidine (Alfa Aesar) as the starting material. A reaction ratio of 0.01 : 0.026 : 0.058 (piperidine : H_3PO_3 : CH_2O) with an excess of HCl catalyst. Reflux was performed as described (*Section 3.1*). On cooling the reaction, no solid was obtained. The same methods used to crystallise $H_4\mathbf{L}'$ were employed (*Section 3.2.2*), but no solid could be obtained. The reaction was left to stand for $\sim$ 1 year, after which time large hexagonal plate-like crystals were obtained. It was not possible to calculate a reaction yield or perform elemental analysis as the crystals could not be separated from the mother liquor or washed without dissolution.

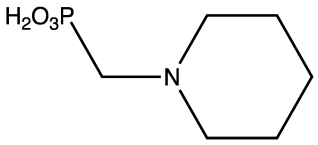

Figure 3.16: N-piperidinylmethylenephosphonic acid — $H_2\mathbf{L}_{pip}$.

^{1}H (400 MHz, D_2O/NaOH): 3.53 (d, $^2J_{Gem} = 11.6$ Hz, 2H), 3.18 (d, ^{2}J(H-P) = 13.2 Hz, 2H), 2.96 (td, $^2J_{Gem}$ 12.3 Hz, $^3J_{Ax-Eq} = 3.2$ Hz, 2H), 1.80 (d, $^2J_{Gem} = 14.8$ Hz, 2H), 1.66 (m, 3H), 1.39 (m, 1H). ^{13}C (400 MHz, D_2O/NaOH): 55.25 (d, ^{3}J(C-P) = 5.1 Hz), 53.27 (d, ^{2}J(C-P) = 138.3 Hz), 22.62 (s), 20.64 (s). ^{31}P (400 MHz, D_2O/NaOH): 7.90 (t, ^{2}J(P-H) = 12.8 Hz.

$H_2\mathbf{L}_{pip}$ was obtained as large single crystals, suitable for single crystal X-ray diffraction. The structure was solved using the direct methods routines of the Sir2008 package,[141] in the orthorhombic space group $P\,b2_1a$ (a = 7.153(2) Å, b = 9.496(3) Å, c = 13.869(4) Å, V = 942.1(5) Å^3). Non-H atoms of the ligand were identified from the structure solution. Refinement used the least squares routines of the SHELX-97 package.[140] Fourier difference maps from the first cycles of refinement indicated the presence of a heavier scatterer than an O atom (U_{Iso} became very small when assigned as O) as a separate fragment and within an H-bonding distance of the piperidinyl N atom. This was assigned as Cl (from the catalyst). Further cycles of refinement were performed and a proton was identified on the piperidinyl N atom. H atoms were placed geometrically on C atoms with coordinates and U_{Iso} parameters set to ride on the C atom they are bound to. Fourier difference maps were again used to place protons on PO_3C O atoms. It was necessary to restrain the U_{Iso} parameters of H9 to the O atom it bonds to (O1). Further cycles of refinement were performed until no further significant changes to the structure

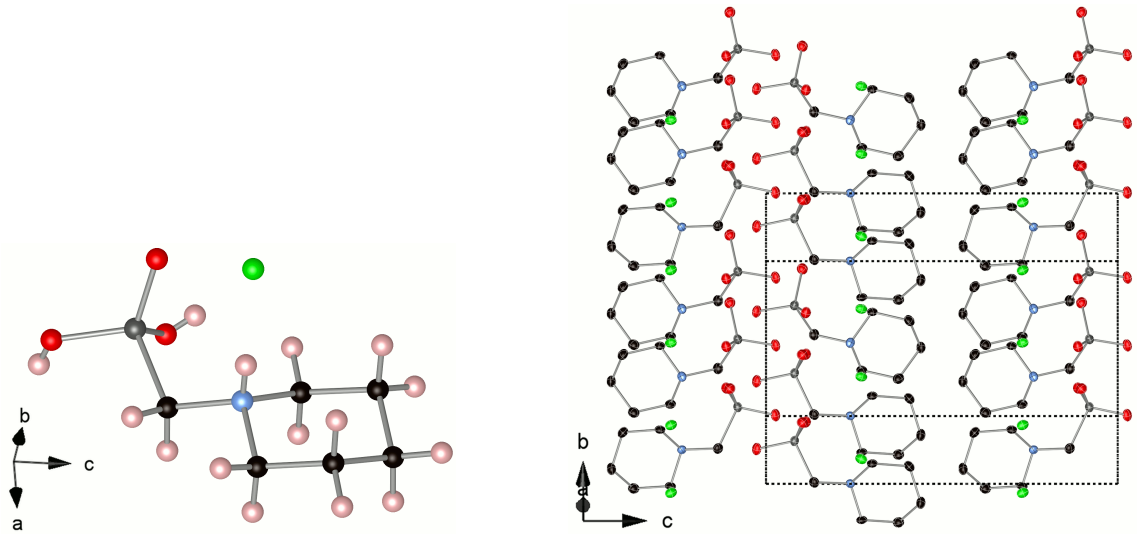

(a) (b)

Figure 3.17: Crystal structure of $H_2\mathbf{L}_{pip}$, showing the asymmetric unit including the Cl^- anion (*left*) and the packing of the crystal structure (*right*). Dotted lines indicate unit cell. Protons omitted for clarity.

were observed. A final fit of R = 0.0383 (R_w = 0.0873) was achieved.

The asymmetric unit of $H_2\mathbf{L}_{pip}$ consists of one complete ligand molecule, with the piperidine ring in a chair conformation, and a molecule of hydrochloric acid (HCl) (*Fig. 3.17a*). The two residues form a single adduct, with the proton of the HCl molecule donated to the basic piperidinyl N atom. An extensive H-bonding network is developed between the protonated N atom, Cl^- anion and CPO_3H_2 groups. Cl^- H-bonds with the protonated N atom ((N)H7$\cdots$Cl1: 2.37(4) Å) and with the protonated PO_3C group ((O)H8$\cdots$Cl1: 2.31(5) Å). Protonated PO_3C groups also engage in H-bonding to PO_3C groups in neighbouring molecules ((O)H9$\cdots$O3: 1.83(5) Å). The molecules are arranged in the crystal structure to maximise the possible H-bonding contacts. Hydrophobic groups are also arranged in close proximity to one another, benefiting from dispersive interactions (*Fig. 3.17b*).

3.3 Summary

The modified Mannich reaction of Moedritzer and Irani[181] has been successfully used to prepare a range of mono- and bis-(N-methylenephosphonic acids). The synthesis has been improved and extended following the work of Mowat,[182, 111] reliably crystallising high yields of the more soluble α-methylenephosphonic acids through the use of ethanol to wash out and dilute halide ion concentration (*vide infra*). With the exception of $H_4\mathbf{LC}_3\mathbf{L}$, the structures of all molecules were successfully characterised by NMR for the first time and these confirm the success and versatility of the synthetic method.

Crystal structures of four of the ligands were reported (the structure of $H_3\mathbf{LC}$ was previously known).[183] A common feature identified in the crystal structures of $H_4\mathbf{L}$, $H_4\mathbf{LL}$, $H_3\mathbf{LC}$ and $H_2\mathbf{L}_{\text{pip}}$ is the development of an extensive H-bonding network. H-bonding networks of $H_4\mathbf{L}$, $H_4\mathbf{LL}$ and $H_3\mathbf{LC}$ all involve only interactions of the protonated piperazinyl N atom, PO_3C and, in the case of $H_3\mathbf{LC}$ and $H_4\mathbf{LL}$, water molecules of crystallisation. $H_4\mathbf{L}$ is unusual amongst the structures reported as it consists of sheets of H-bonding $H_4\mathbf{L}$ molecules (in the *ab*-plane) which have no apparent H-bonding interactions between them. Sheets are most likely held together by dispersive interactions. An explanation for why the non-bonding interactions are different in the structure of $H_4\mathbf{L}$ compared to the other structures is provided by powder X-ray data. Simulated diffraction patterns for this structure and experimental data for the bulk powder are different, indicating the structure solved from single crystal is in fact a polymorph formed under hydrothermal conditions.

In all structures the relatively basic amino group is protonated, either by loss of a proton from the PO_3C groups ($H_4\mathbf{L}$, $H_4\mathbf{LL}$, $H_3\mathbf{LC}$) to form a zwitter ion or by formation of an adduct with HCl ($H_2\mathbf{L}_{\text{pip}}$). Protonation of this group is also a common feature of MOFs formed with ligands of this type (see *Section 1.4.2*). The formation of an adduct by $H_2\mathbf{L}_{\text{pip}}$ and the extensive involvement of the Cl^- anion in the H-bonding network indicate the difficulty in removing the reaction catalyst from the phosphonic acid product. Residual catalytic HCl or HBr is often incorporated into the product of the Mannich reaction and halide anions have been found in MOFs formed with these ligands, where the only source could be the ligand (see *Sections 1.4.2 & 6.6.1* for examples). Adduct formation also aids the solubilisation of the phosphonic acid product and it is this which is thought to hinder crystallisation of $H_4\mathbf{L}'$ and $H_4\mathbf{LC}_3\mathbf{L}$.

Future work on the synthesis of ligands would focus on finding a method of removing halide ions from reaction solutions to encourage crystallisation of the phosphonic acid product. This might be achieved by a selective halide scavenger

or alternatively by some form of phase transfer process. In respect of metal phosphonate synthesis, longer and/or more rigid α-methylenephosphonic acids are a desirable synthetic target. The current synthesis is essentially a one-pot reaction. However a stepwise assembly of (rigid) building blocks with terminal secondary amines could lead to a range of rigid substrates suitable for the Mannich reaction. Functionalisation of the reported bisphosphonic acids should lead to new structures or facilitate tuning of reported structures for specific applications.

Chapter 4

Trivalent Metal Bisphosphonates

A range of trivalent metal bisphosphonates have already been reported using a variety of lanthanide and tri- and tetravalent transition metal/p-block cations with $H_4\mathbf{L}$ and related ligands (see *Section 1.4.2*). Reactions of the larger Ln^{3+} cations have been extensively investigated and shown to form different structures depending on the steric bulk of the ligand and the pH of the synthesis gel.[111] Reactions of the smaller Ln^{3+} cations, $Gd^{(III)}$, $Yb^{(III)}$ and the chemically similar d-block metal $Y^{(III)}$, form the phase $M_2(\mathbf{L}H_2)_3 \cdot xH_2O$ with $H_4\mathbf{L}$.[112] Using racemic $H_4\mathbf{L}'$, Miller reported the crystallisation of the framework type STA-13 with $Sc^{(III)}$ and $Y^{(III)}$.[184] Only two coordination polymers of tri- or tetravalent transition metals have been reported, MIL-91(Ti)[108] and the phase $VO(H_2O)(\mathbf{L}H_2)$.[100]

This chapter reports the reinvestigation of the phase $Y_2(\mathbf{L}H_2)_3{\cdot}5H_2O$ ($Y_2(\mathbf{L}H_2)_3$) and also the results of reactions of the ligands $H_4\mathbf{L}'$, R-$H_4\mathbf{L}'$ and $H_4\mathbf{L}''$ with $Y^{(III)}$, which crystallise, respectively, $Y_2(\mathbf{L}'H_2)_3 \cdot 7H_2O$ (STA-13(Y)), $Y_2(R\text{-}\mathbf{L}'H_2)_3 \cdot 5H_2O$ ($Y_2(R\text{-}\mathbf{L}H_2)_3$) and a new phase, the structure of which is currently unknown. Factors determing the phase crystallised have been investigated and the as-prepared and dehydrated structures of $Y_2(\mathbf{L}H_2)_3$, STA-13(Y) and $Y_2(R\text{-}\mathbf{L}H_2)_3$ fully characterised. STA-13 was also prepared with a range of other trivalent cations to investigate the range of cation radius over which the network will crystallise. Porosities of each metal form of STA-13 are reported. Reactions of trivalent transition metal $Fe^{(III)}$ with $H_4\mathbf{L}$ and $H_4\mathbf{L}'$ have been investigated and found to prepare the phases MIL-91(Fe) and $[Fe_4\mathbf{L}_{1.5}(AcO)_{1.5}(OH,H_2O)_3]{\cdot}0.5NH_4 5.5H_2O$ ($\mathbf{L}$ = $\mathbf{L}$, $\mathbf{L}'$), the latter of which is an analogue of the phase reported by Groves *et al.*[105]

4.1 Rare-Earth Bisphosphonates

Rare-earth elements are defined as members of the lanthanide series (La–Lu) and elements with similar chemical properties such as Y and Sc. Hydrothermal reactions of $GdCl_3$, $YbCl_3$ and either $Y(AcO)_3$ or YCl_3 with $H_4\mathbf{L}$ at pH 6–7 form an open-framework material with stoichiometry $M_2(\mathbf{L}H_2)_3 \cdot xH_2O$.[112] The as-prepared structure of the $Y^{(III)}$ and $Yb^{(III)}$ forms of this material were not explicitly described, whilst the $Y^{(III)}$ form was observed to undergo a structural transition on dehydration, which was also not fully investigated. Miller reported the crystal structure of the porous framework material STA-13, crystallised from reactions of $Sc^{(III)}$ and $Y^{(III)}$ with racemic $H_4\mathbf{L}'$.[184] The structure of this material is reported for $Sc^{(III)}$, though with some uncertainty over the positions of the Me groups. The structure of the $Y^{(III)}$ was partially solved from single crystal X-ray diffraction, but a complete structure was not reported.

This section reports investigations of the reactions of $Y(AcO)_3$ and $H_4\mathbf{L}$ to verify and optimise the synthesis conditions of $Y_2(\mathbf{L}H_2)_3 \cdot xH_2O$[112] and to identify other phases present in the Y-$H_4\mathbf{L}$ system. The reactions of $Y(AcO)_3$ with ligands (racemic) $H_4\mathbf{L}'$, *R*-$H_4\mathbf{L}'$ and $H_4\mathbf{L}''$ have also been investigated and three principal phases identified (*Fig. 4.1*), including for $H_4\mathbf{L}'$, STA-13(Y).

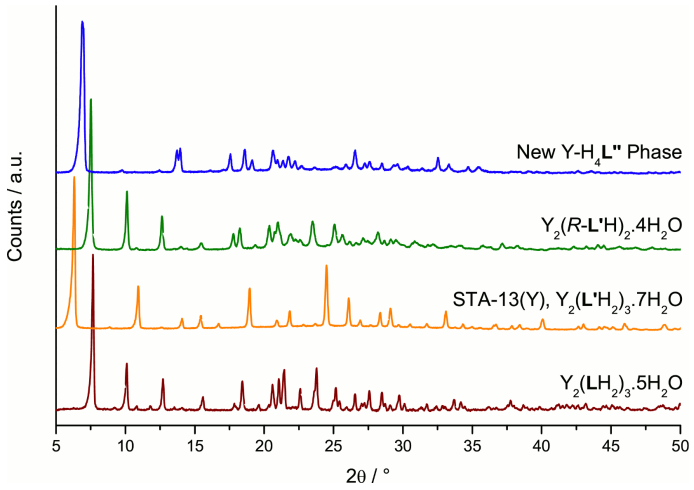

Figure 4.1: Laboratory powder diffraction patterns (Cu K_α) of principal phases identified in reactions of $Y(AcO)_3$ with $H_4\mathbf{L}$ ($Y_2(\mathbf{L}H_2)_3$ — maroon), $H_4\mathbf{L}'$ (STA-13(Y) — orange), *R*-$H_4\mathbf{L}'$ ($Y_2(R\text{-}\mathbf{L}H_2)_3$ — dark green) and $H_4\mathbf{L}''$ (Y-$H_4\mathbf{L}''$U1 — blue).

Phase pure samples of each material have been obtained and, where possible, Rietveld refinements used to confirm their structures. The porosity of each phase has also been investigated and for STA-13 the results of molecular simulations to better understand the porosity have been reported.

The synthesis of STA-13 has also been extended to a range of rare-earth elements, with unit cell parameters determined by Le Bail analysis.[155]

4.2 Synthesis

In a typical hydrothermal synthesis of $Y_2(\mathbf{L}H_2)_3$, $H_4\mathbf{L}$ (0.456 g, 1.67×10^{-3} mol) was stirred in water (20 ml, 1.11 mol). If necessary, potassium hydroxide (Alfa Aesar) solution (1.96 ml, 0.1 g ml^{-1}, 3.50×10^{-3} mol) was then added to modify the pH and to aid in ligand solubilisation. Finally yttrium acetate hydrate (Alfa Aesar) (0.375 g, 1.11×10^{-3} mol) was added, to afford a final gel composition of 1.0 : 1.50 : 3.15 : 1000 (Y : $H_4\mathbf{L}$: KOH : H_2O). The reaction was then stirred for one hour at room temperature and the pH of the synthesis gel recorded (pH: 5). Reactions were then placed in an oven at 160–220°C for 16–170 hrs. Reactions were then cooled, filtered and washed with water before being placed in a drying oven at 40°C overnight. Solids were then analysed by powder X-ray diffraction.

For reactions of $H_4\mathbf{L}'$, *R*-$H_4\mathbf{L}'$ and $H_4\mathbf{L}''$ the same procedure was followed, except base was found to be unnecessary and in fact detrimental to crystallisation, forming amorphous products in each case. For all ligands, the gels had an initial pH of 5.

4.3 $Y_2(\mathbf{L}H_2)_3 \cdot 5H_2O$

Directly repeating the synthesis of $Y_2(\mathbf{L}H_2)_3 \cdot 5H_2O$ ($Y_2(\mathbf{L}H_2)_3$) reported by Groves *et al.*[112] did not yield the $Y_2(\mathbf{L}H_2)_3$ phase. Instead a phase labelled here Y-$H_4\mathbf{L}$U1 was obtained (see *Section 4.3.1*). In the same series of reactions $Y_2(\mathbf{L}H_2)_3$ was also obtained, though mixed with several other unknown phases. A large number of reactions were then performed to determine and optimise the synthesis conditions of $Y_2(\mathbf{L}H_2)_3$, during the course of which, in addition to $Y_2(\mathbf{L}H_2)_3$ and Y-$H_4\mathbf{L}$U1, at least four other unknown phases were identified by powder X-ray diffraction (*Fig. 4.2* and *Appendix 4.3.1*). Of these, only Y-$H_4\mathbf{L}$U4 has been prepared to a good degree of phase purity (*Table 4.1*).

The final optimised conditions for the synthesis of $Y_2(\mathbf{L}H_2)_3$ were a gel composition of 1.00 : 1.50 : 3.15 : 1000 ($Y(AcO)_3$: $H_4\mathbf{L}$: KOH : H_2O) with initial pH of 5, heated at 190°C for one week (168 hours). Phase purity was confirmed by laboratory powder X-ray diffraction.

Gels with and without KOH had an initial pH of 5, which indicates that the role of the KOH is not simply in modifying the initial synthesis pH. In the absence of KOH, $Y_2(\mathbf{L}H_2)_3$ was found to co-crystallise with other phases, whilst with too much

$Y(OAc)_3$: $H_4\mathbf{L}$: KOH : H_2O	pH	Temp. / °C	Time / hrs	Phase
0.79 : 1.0 : 0 : 1000	5	190	48	Mixed unknowns
1.57 : 1.5 : 3.60 : 1200	7	160	48	Y-$H_4\mathbf{L}$U1
0.79 : 1.5 : 3.60 : 300	6	160	189	Y-$H_4\mathbf{L}$U3 & $Y_2(\mathbf{L}H_2)_3$
0.79 : 1.5 : 3.60[a] : 300	5	160	48	Y-$H_4\mathbf{L}$U2 & $Y_2(\mathbf{L}H_2)_3$
1.0 : 1.5 : 3.60 : 500	6–7	160	48	Y-$H_4\mathbf{L}$U2 & $Y_2(\mathbf{L}H_2)_3$
2.0 : 1.5 : 1.44 : 300	6	190	191	Y-$H_4\mathbf{L}$U1
1.0 : 1.5 : 2.93 : 1200	6–7	190	179	$Y_2(\mathbf{L}H_2)_3$ (& Y-$H_4\mathbf{L}$U2)
1.0 : 1.5 : 3.15 : 1000	4–5	190	168	$Y_2(\mathbf{L}H_2)_3$
1.0 : 1.0 : 0 : 1000	4–5	190	18	Y-$H_4\mathbf{L}$U4

[a]NaOH used as base, instead of KOH.

Table 4.1: Selected reactions of $Y(AcO)_3$ with $H_4\mathbf{L}$ showing the optimised synthesis conditions of $Y_2(\mathbf{L}H_2)_3$ and also showing conditions from which four unknown phases have been prepared (see *Appendix, Section 4.3.1*). Reactions were performed in 40 ml PTFE lined autoclaves, using 20 ml H_2O.

KOH (i.e. pH 6–7) other unknown phases crystallise preferentially. The initial pH of the synthesis gel is influenced by both the KOH and $Y(AcO)_3$ concentrations. the acetate anions will establish an equilibrium, $AcO^- + H^+ \rightleftharpoons AcOH$, which buffers the solution pH. KOH also acts to solubilise the ligand and this may explain why a mixture of phases was obtained in its absence. Without KOH, the low solubility of the ligand means a low effective concentration of $H_4\mathbf{L}$ would be in solution favouring the formation of products with high metal:ligand ratios. Ligand crystals may also have high energy surfaces, which could result in different reactivity compared to the bulk solution. KOH plays a complicated dual role in the $Y(AcO)_3$-$H_4\mathbf{L}$ system, firstly controlling the gel pH and secondly solubilising the ligand to ensure a homogenous solution.

4.3.1 Unknown Phases in the $Y(AcO)_3$-H_4L System

Four phases have been identified in addition to structure $Y_2(\mathbf{L}H_2)_3$ in the $Y(AcO)_3$-$H_4\mathbf{L}$ system, of which only two, Y-$H_4\mathbf{L}$U1 and Y-$H_4\mathbf{L}$U4 have been obtained to any degree of phase purity (*Table 4.1*). Diffraction patterns of the best samples of each of the unknown phases have been collected (*Fig. 4.2*). Full characterisations of the phases Y-$H_4\mathbf{L}$U1 and Y-$H_4\mathbf{L}$U4 are reported in *Appendix 4.3.1.*

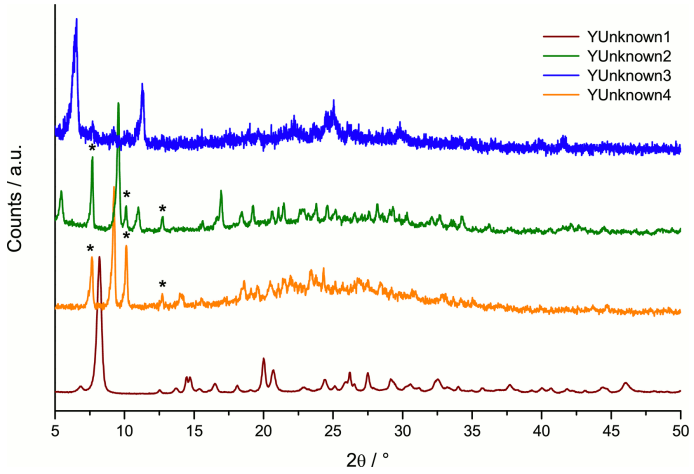

Figure 4.2: Laboratory powder X-ray diffraction patterns (Cu K_α) of unknown phases in the $Y(AcO)_3$-H_4**L** system: Y-H_4**L**U1 (maroon); Y-H_4**L**U2 (orange); Y-H_4**L**U3 (dark green); Y-H_4**L**U4 (blue). Asterisks indicate peaks due to co-crystallised structure $Y_2(\mathbf{L}H_2)_3$.

4.3.2 Characterisation of Structure $Y_2(\mathbf{L}H_2)_3$

Following synthesis of phase pure $Y_2(\mathbf{L}H_2)_3$, the composition of the phase was determined by elemental analysis, TGA and EDX. TGA data for $Y_2(\mathbf{L}H_2)_3$ were collected in the range 25–900°C under dry air (*Fig. 4.3*). The final solid is assumed to be Y_2O_3. Two principal weight loss events occur: the first is at 25–100°C (8.92 wt.%) and is consistent with the loss of ~ 5 molecules of water per formula unit; the second begins at 325°C and continues to above 900°C, indicating framework decomposition.

The plateau in the TGA data following the loss of physisorbed water molecules indicates the presence of a thermally stable dehydrated phase. This has been investigated by X-ray diffraction studies (see *Section 4.3.5*).

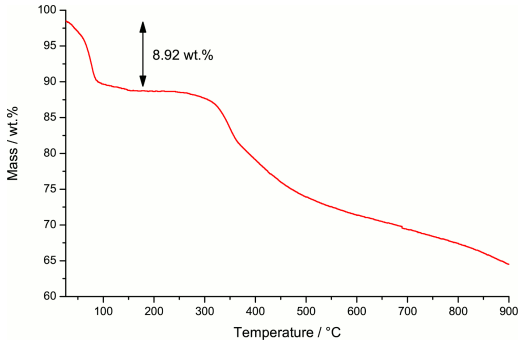

Figure 4.3: TGA of $Y_2(\mathbf{L}H_2)_3$ from 25–900°C under dry air showing principal weight loss events.

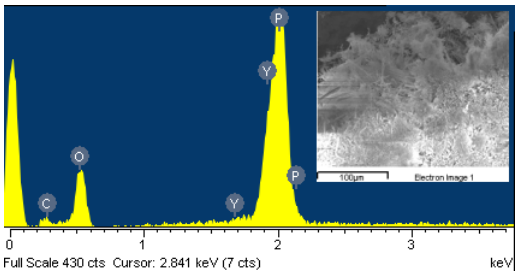

Figure 4.4: EDX spectrum of $Y_2(\mathbf{L}H_2)_3$ indicating elements found. Y : P ratio of 1.0 : 3.26. Inset shows the area analysed.

EDX data for a sample of $Y_2(\mathbf{L}H_2)_3$ indicated a Y : P ratio of 1.0 : 3.26 (*Fig. 4.4*), which agrees reasonably with the 2 : 3 metal:ligand ratio (two P atoms per ligand) expected for a phase of composition $Y_2(\mathbf{L}H_2)_3 \cdot 5H_2O$. This proposed composition was found to be in good agreement with elemental analysis: expected — C 19.9 %, H 4.8 %, N 7.8 %; found — C 19.2 %, H 4.4 %, N 7.6 %.

4.3.3 Structure of As-Prepared $Y_2(\mathbf{L}H_2)_3$

Rietveld refinement was used to confirm that $Y_2(\mathbf{L}H_2)_3$ is isostructural with the $Gd_2(\mathbf{L}H_2)_3 \cdot 3H_2O$ phase reported by Groves *et al.*[112] Laboratory powder X-ray diffraction data were collected on a Stoe Stadi P diffractometer equipped with a Cu K_α source. Data were collected at 298 K in a Debye-Scherrer geometry with the sample mounted in a 0.7 mm borosilicate glass capillary over the range 5–90° 2θ. Rietveld refinement (with the GSAS suite of programs[156, 157]) used the orthorhombic ($P\,22_12_1$) $Gd_2(\mathbf{L}H_2)_3 \cdot 3H_2O$ structure, reported from single crystal data,[112] as the starting model. Background and profile parameters were refined first, followed by the unit cell (a = 8.6736(3) Å, b = 9.7813(3) Å, c = 22.7964(9) Å, V = 1934.02(13) Å^3). For the structural refinement, it was necessary to restrain certain bonding distances to ensure the structure remained chemically sensible: octahedral Y-O (2.33 Å); tetrahedral P-O and P-C (1.49 Å and 1.88 Å respectively); and C-N and C-C (1.50–1.51 Å and 1.52 Å). Selected non-bonding distances were also restrained: O$\cdots$O and O$\cdots$C (P tetrahedra) (2.43 Å and 2.76 Å); N$\cdots$N (diagonal, cross-ring), C$\cdots$C (diagonal, cross-ring), N$\cdots$C (2$^{\text{nd}}$ neighbour, within ring), C$\cdots$C (2$^{\text{nd}}$ neighbour, within ring) and C$\cdots$C (2$^{\text{nd}}$ neighbour, outwith ring) (2.866 Å, 2.892 Å, 2.466 Å, 2.472 Å and 2.525 Å). Missing water molecules were located by Fourier difference mapping and their occupancies allowed to refine. Also, one of the two ligands present in the assymetric unit of the model was found to be flat, suggesting that two ligands occupy the same site, disordered over two configurations. This disorder was modelled by making N11A and C13 half occupied and creating new half occupied sites (N11B and C14) 0.5 Å away from N11A and C13 and applying restraints. To retain this disorder, restraints were applied: N11A$\cdots$N11B and C13$\cdots$C14 (both 0.525 Å). A good fit to the data was obtained after 2062 cycles (R_{wp} = 0.0388, R_p = 0.0303, R(F^2) = 0.0987, χ^2 = 1.805) and the Rietveld fit for this model is shown (*Fig. 4.5*).

The asymmetric unit for the final orthorhombic model has two crystallographically independent ligands: one complete ligand and one half ligand, which is also disordered across a 2_1 screw axis (*Fig. 4.6*). ^{13}C and ^{31}P solid-state MAS NMR spectra were collected on a sample of $Y_2(\mathbf{L}H_2)_3$ and assigned with reference to the

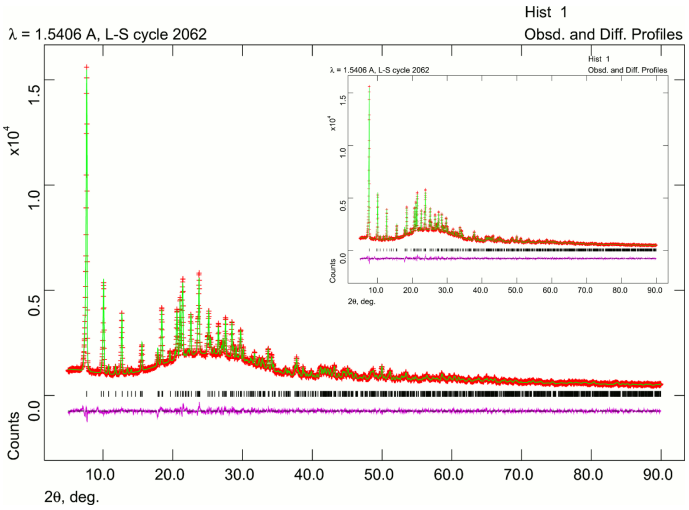

Figure 4.5: Rietveld fit for the refinement of $Y_2(\mathbf{L}H_2)_3$ using the $Gd_2(\mathbf{L}H_2)_3 \cdot 3H_2O$[112] model in orthorhombic space group $P\,22_12_1$. $R_{wp} = 0.0388$.

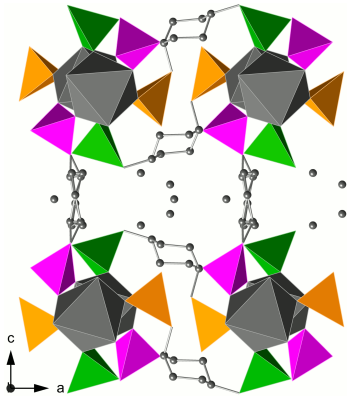

Figure 4.6: View along the *b*-axis showing the ordered & disordered ligands with three P environments highlighted in yellow, green & magenta.

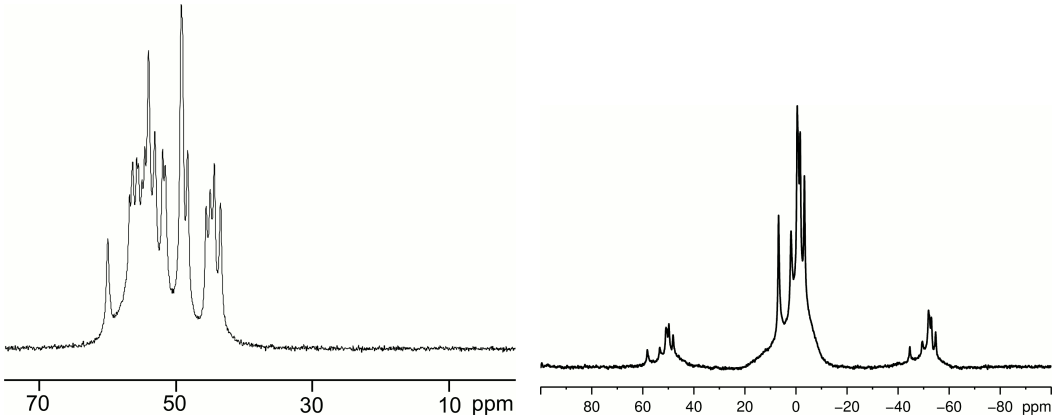

(a) (b)

Figure 4.7: ^{13}C *left* and ^{31}P *right* MAS NMR spectrum of $Y_2(\mathbf{L}H_2)_3$.

solution phase spectra of the ligand (*Fig. 4.7*). In the crystal structure there are three distinct P sites and ten C sites. Therefore three resonances were expected in the ^{31}P MAS NMR spectrum and 10 in the ^{13}C spectrum. Experimentally five overlapping resonances between 5 and -5 ppm were observed in the ^{31}P and at least 16 resonances are present in a multiplet centred at 52 ppm in the ^{13}C spectrum. There are two possible explanations for these additional resonances: either disorder in the structure has not been accounted for correctly or the structure is actually in a lower symmetry space group. As disorder has already been accounted for, a lower symmetry space group was sought.

The symmetry of orthorhombic space group $P\,22_12_1$ can be reduced, by removal of two symmetry operations, to one of three monoclinic space groups: $P\,211$, $P\,12_11$

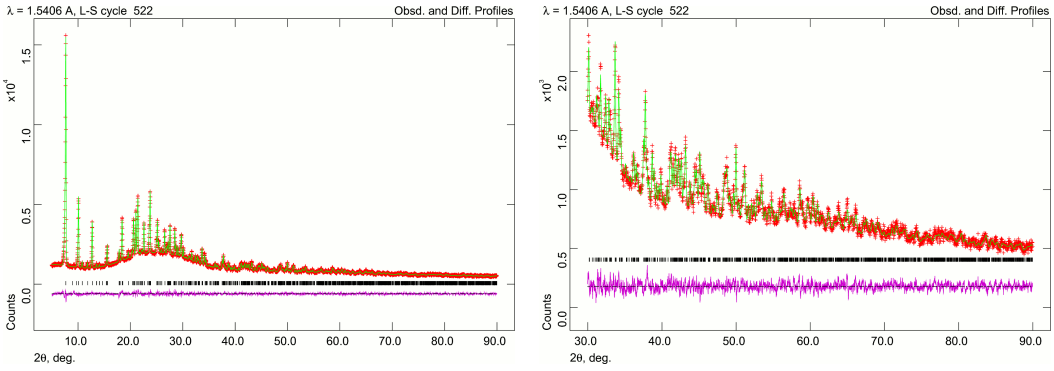

Figure 4.8: Final Rietveld fit for the refinement of $Y_2(\mathbf{L}H_2)_3$ in monoclinic space group $P\,112_1$. $R_{wp} = 0.0380$.

Bond	Distance / Å	Bond	Distance / Å	Bond	Distance / Å
Y1-O1	2.313(13)	P1-O1	1.480(13)	P14-O14	1.493(13)
Y1-O4	2.321(12)	P1-O2	1.478(13)	P14-O15	1.516(13)
Y1-O11	2.331(13)	P1-O3	1.492(22)	P14-O16	1.439(20)
Y1-O15	2.354(13)	P1-C1	1.898(14)	P14-C14	1.898(13)
Y1-O22	2.331(16)	P4-O4	1.496(13)	P21-O21	1.484(13)
Y1-O25	2.315(13)	P4-O5	1.479(13)	P21-O22	1.492(13)
Y2-O2	2.335(12)	P4-O6	1.497(22)	P21-O23	1.444(21)
Y2-O5	2.319(13)	P4-C4	1.878(13)	P21-C21	1.928(16)
Y2-O12	2.325(13)	P11-O11	1.484(13)	P24-O24	1.491(13)
Y2-O14	2.321(12)	P11-O12	1.481(13)	P24-O25	1.474(13)
Y2-O21	2.320(13)	P11-O13	1.502(20)	P24-O26	1.498(22)
Y2-O24	2.331(13)	P11-C11	1.881(13)	P24-C24	1.887(13)

Table 4.2: Selected bond distances in the as-prepared structure of $Y_2(\mathbf{L}H_2)_3$.

and $P\,112_1$. $P\,112_1$ was chosen as this space group allows the removal of the disorder from the ligand, and a new model was constructed for $Y_2(\mathbf{L}H_2)_3$. This model was then Rietveld refined against the powder diffraction data, using the final refinement of the orthorhombic model (*vide supra*) as the starting point for the refinement. A new cell was obtained with very similar dimensions to the orthorhombic cell and a monoclinic angle close to 90°: $a = 8.6744(3)$ Å, $b = 9.7820(3)$ Å, $c = 22.7997(9)$ Å, $\gamma = 90.120(5)°$, V = 1934.60(12) Å^3. The same restraints were used in the monoclinic refinement as before. A slightly improved fit to the data was obtained after 523 cycles ($R_{wp} = 0.0380$, $R_p = 0.0299$, $R(F^2) = 0.1049$, $\chi^2 = 1.711$) and the final Rietveld fit for $Y_2(\mathbf{L}H_2)_3$ is shown (*Fig. 4.8*). This model improves on the original orthorhombic solution since it is consistent with both the powder diffraction data and the MAS NMR spectra.

In $Y_2(\mathbf{L}H_2)_3$ there are two distinct Y cation sites, both with slightly distorted octahedral (YO_6) coordination environments (*Table 4.2*). Octahedra are linked into undulating chains parallel to the *b*-axis, with each pair of YO_6 octahedra linked by three PO_3C groups in a bridging mode (*Fig. 4.9a*). Neighbouring chains are linked in the *a*-direction by two piperazinyl groups, each possessing one axial and one equatorial methylenephosphonate group, to form a structural layer in the *ab*-plane (*Fig. 4.9b*). Protonated piperazinyl N atoms engage in H-bonding with pendant P=O groups (N$\cdots$O(P): 2.57(5)–2.61(5) Å) driving crystallisation and stabilising the less favourable axial configuration of the substituents. A second crystallographically distinct group of piperazinyl linkers, with both methylenephosphonate groups equatorial, link adjacent layers in the *c*-direction (*Fig. 4.9c*). Small pores are present between the layers, which in the as-prepared material are occupied by physisorbed water molecules which engage in H-bonding with protonated piperazinyl and pendant P=O groups (O/N$\cdots$O(H_2O): 2.83(5)–2.93(5) Å).

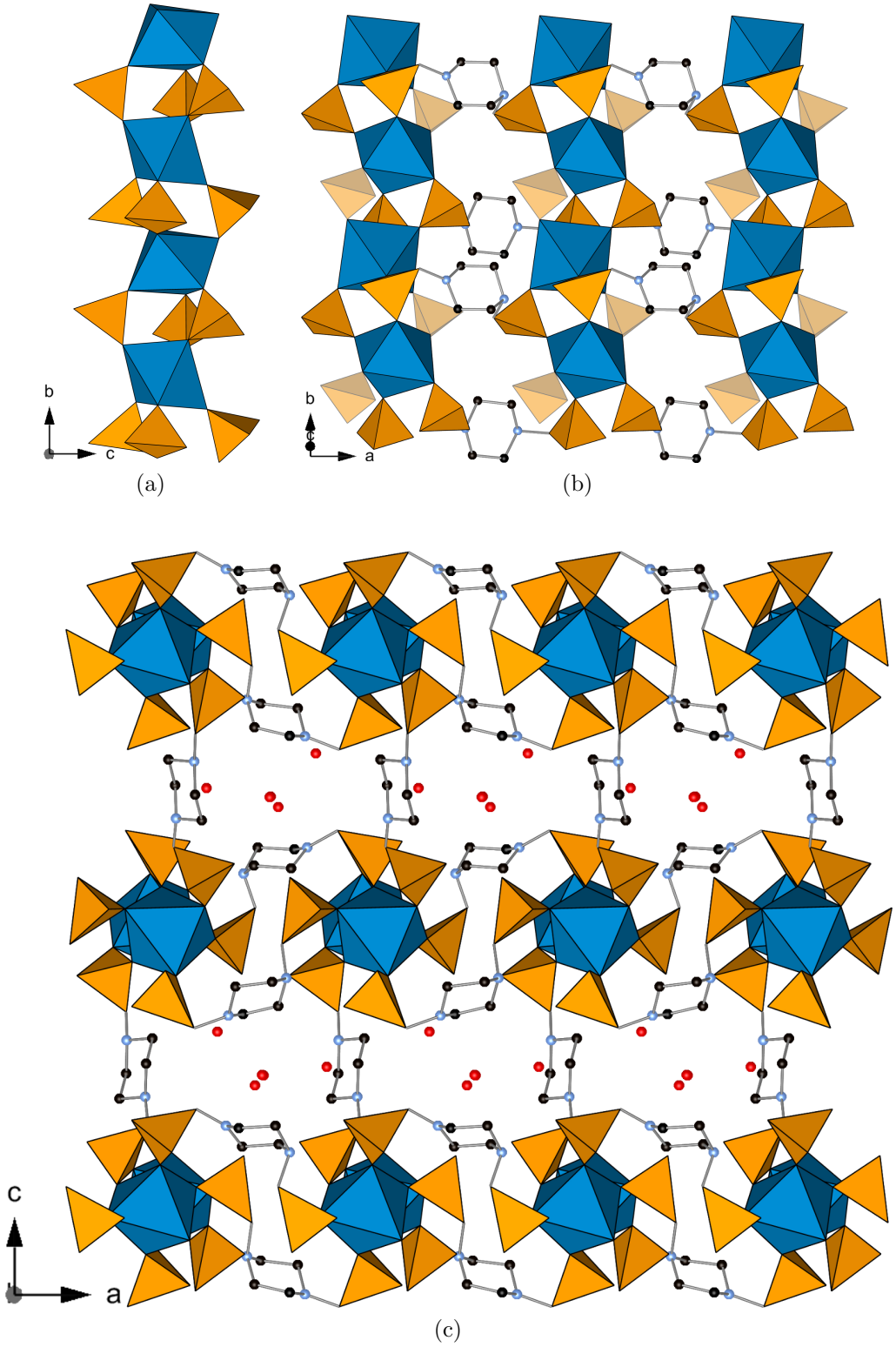

Figure 4.9: Structure of $Y_2(\mathbf{L}H_2)_3$. *Top Left:* Inorganic yttrium-phosphonate chain showing the linking PO_3C groups. *Top Right:* Chains link in the *c*-direction to form a layer. PO_3C groups involved in linking layers are transparent. *Bottom:* View along the *c*-direction, with chains linked into structural layers and linked in the third dimension to give small pores occupied by physisorbed water molecules.

4.3.4 Dehydration Behaviour of $Y_2(\mathbf{L}H_2)_3$

TGA analysis indicates that a thermally stable dehydrated phase is formed by $Y_2(\mathbf{L}H_2)_3$ when physisorbed water is removed from the material (i.e. by heating to 120°C). The behaviour of $Y_2(\mathbf{L}H_2)_3$ was analysed by laboratory powder X-ray diffraction. A sample of the as-prepared material was loaded into a 0.7 mm quartz glass capillary tube and dehydrated by heating to 120°C at reduced pressure (1×10^{-4} Torr) for three hours. The capillary was then flame sealed and a laboratory powder X-ray diffractogram (Cu K_α) collected. The diffraction data show the same shift in peak positions, indicating a structural transition on dehydration, reported previously by Groves *et al.*[112] The capillary was broken open and allowed to rehydrate under ambient conditions for five days. Another diffraction pattern was then collected, which showed that the structural transition (and therefore dehydration) is fully reversible (*Fig. 4.10*).

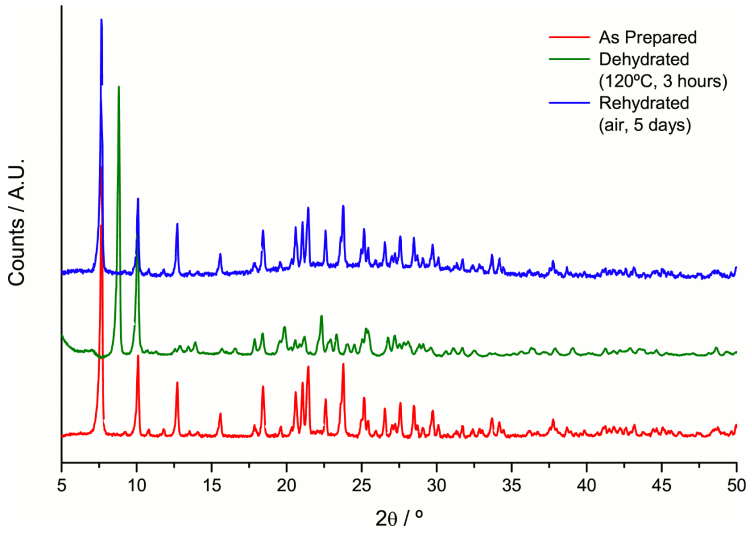

Figure 4.10: Laboratory powder diffraction patterns (Cu K_α) of as-prepared (red), dehydrated (dark green) and rehydrated (blue) samples of structure $Y_2(\mathbf{L}H_2)_3$.

The porosity of dehydrated structure $Y_2(\mathbf{L}H_2)_3$ ($Y_2(\mathbf{L}H_2)_3$-DH) was investigated by adsorption of N_2 at 77 K and CO_2 at 195 K. $Y_2(\mathbf{L}H_2)_3$-DH was found to be non-porous to both gases.

4.3.5 Structure of Dehydrated $Y_2(\mathbf{L}H_2)_3$

The structure of fully dehydrated $Y_2(\mathbf{L}H_2)_3$ ($Y_2(\mathbf{L}H_2)_3$-DH) was investigated by synchrotron powder X-ray diffraction. A sample of as-prepared $Y_2(\mathbf{L}H_2)_3$ was loaded into a 0.5 mm quartz glass capillary tube and heated at 120°C for three hours under vacuum (1×10^{-4} Torr). The capillary was then flame sealed. Synchrotron

powder X-ray diffraction data were collected at beamline I11 of Diamond Light Source (Harwell, Oxfordshire, UK).[145] Data were collected in a Debye-Scherrer geometry at 100 K over the range 1–140° 2θ using monochromated X-ray radiation of wavelength 0.825028 Å. Beam damage to the sample was minimised by cooling the sample and also by collecting data over three minutes, translating the capillary and collecting a further data set. In total eight data sets were collected which were summed together and binned with a step size of 0.002°. Prior to refinement, data at 2θ angles greater than 45°were discarded, as the peak intensity was relatively weak, and the remaining data were rebinned to a step size of 0.005°. Data were indexed using the TREOR routines of EXPO2009[153, 148] with an orthorhombic cell, a = 8.746(7) Å, b = 9.909(6) Å, c = 19.963(13) Å, β = 94.57(6)°, V = 1724(9) Å^3 (F.O.M. M_{20} = 16).[154] The space group $P\,2_1$ was selected as this was given the highest figure of merit by EXPO2009 (0.536 vs 0.220 for the next highest — $P\,2_1/a$). A simple structural transition can be also envisaged from the original orthorhombic model of $Y_2(\mathbf{L}H_2)_3$ in $P\,22_12_1$ reported by *Groves et al.*[112] to the new space group. A Le Bail fit of the structure was used to refine the cell and to obtain initial profile parameters for Rietveld refinement.[155]

The early stages of a Rietveld refinement, using the GSAS suite of programs,[147, 156, 157] was performed to probe what structural changes occur on dehydration to allow the shortening of the unit cell. A starting model for the refinement was obtained by reducing the symmetry of the orthorhombic model of $Y_2(\mathbf{L}H_2)_3$ from $P\,22_12_1$ (see *Section 4.3.3*) to monoclinic $P\,12_11$, with the disorder in the pillaring ligand retained. Unit cell and background parameters were refined first before structural refinement. Restraints were applied to certain bonding distances: Y-O (2.33 Å), P-O (1.50 Å), P-C (1.85 Å), C-N (1.51–1.53 Å) and C-C (1.53 Å). Restraints were also applied to non-bonding distances to ensure chemically sensible geometries about the Y cation, P atoms and the piperazinyl ring: $\cdots$O (Y octahedra) (3.30 Å); O$\cdots$O and O$\cdots$C (P tetrahedra) (2.45 Å and 2.74 Å respectively); N$\cdots$N and C$\cdots$C (diagonal, cross-ring) (2.90 Å and 2.90 Å); C$\cdots$N and C$\cdots$C (2$^{\text{nd}}$ neighbour, within ring) (2.50 Å and 2.50 Å); and C$\cdots$C (2$^{\text{nd}}$ neighbour, outwith ring) (2.50 Å). Only 2$^{\text{nd}}$ neighbour restraints were applied to the ring of the pillaring piperazinyl ligand to restrain its geometry. Positions of atoms within the structural layer (see *Section 4.3.3*) were refined first, with cycles of refinement repeated until the ligand in the layer had a chemically sensible geometry. Next, the atoms of the interlayer ligand only were refined. Finally, several cycles of refinement were performed of the positions of all atoms within the framework and their thermal (U_{Iso}) parameters. The final fit after 716 cycles was R_{wp} = 0.0778, R_p = 0.0621, (F^2) = 0.2500 and χ^2 = 142.2 (final fits are shown in *Fig. 4.11*).

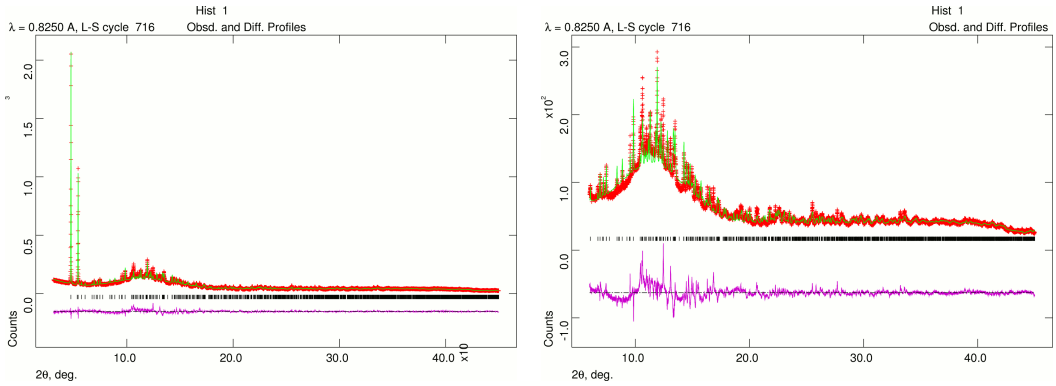

Figure 4.11: Final Rietveld fit for the refinement of the dehydrated structure of $Y_2(\mathbf{L}H_2)_3$ ($R_{wp} = 0.0778$).

Bond	Distance / Å	Bond	Distance / Å	Bond	Distance / Å
Y1-O1	2.18(3)	P1-O1	1.527(17)	P14-O14	1.478(16)
Y1-O2	2.13(2)	P1-O2	1.488(17)	P14-O15	1.444(17)
Y1-O4	2.04(2)	P1-O3	1.501(17)	P14-O16	1.524(17)
Y1-O5	2.48(3)	P1-C1	1.850(4)	P14-C14	1.848(4)
Y1-O11	2.44(2)	P4-O4	1.498(16)	P21-O21	1.518(16)
Y1-O12	2.31(3)	P4-O5	1.522(16)	P21-O22	1.488(16)
Y2-O14	2.46(2)	P4-O6	1.529(17)	P21-O23	1.528(17)
Y2-O15	2.10(3)	P4-C4	1.850(4)	P21-C21	1.851(4)
Y2-O21	2.25(2)	P11-O11	1.524(16)	P24-O24	1.456(16)
Y2-O22	2.42(2)	P11-O12	1.459(17)	P24-O25	1.520(17)
Y2-O24	2.18(2)	P11-O13	1.496(17)	P24-O26	1.514(17)
Y2-O25	2.40(3)	P11-C11	1.847(4)	P24-C24	1.849(4)

Table 4.3: Selected bond distances in the dehydrated structure of $Y_2(\mathbf{L}H_2)_3$.

The disorder in the interlayer ligand was not removed, though with further cycles of refinement it would be possible to remove the disorder and leave a ligand with a chemically sensible geometry.

The structure of $Y_2(\mathbf{L}H_2)_3$-DH is very closely related to the as-prepared material (*Fig. 4.12*). The structure of the inorganic chains is retained, with three bridging PO_3C groups linking octahedral Y^{3+} cations in a chain along the *b*-axis. YO_6 octahedra again have a distorted geometry (*Table 4.3*). Two crystallographically distinct groups of ligands link chains together in the *a*-direction to form the structural layer in the *ab*-plane. These two ligand groups are tilted more relative to the *c*-direction than in the as-prepared material, probably to reduce the amount of free space within the structure following the removal of physisorbed water molecules. As a result of the tilting, the protonated piperazinyl groups are no-longer able to

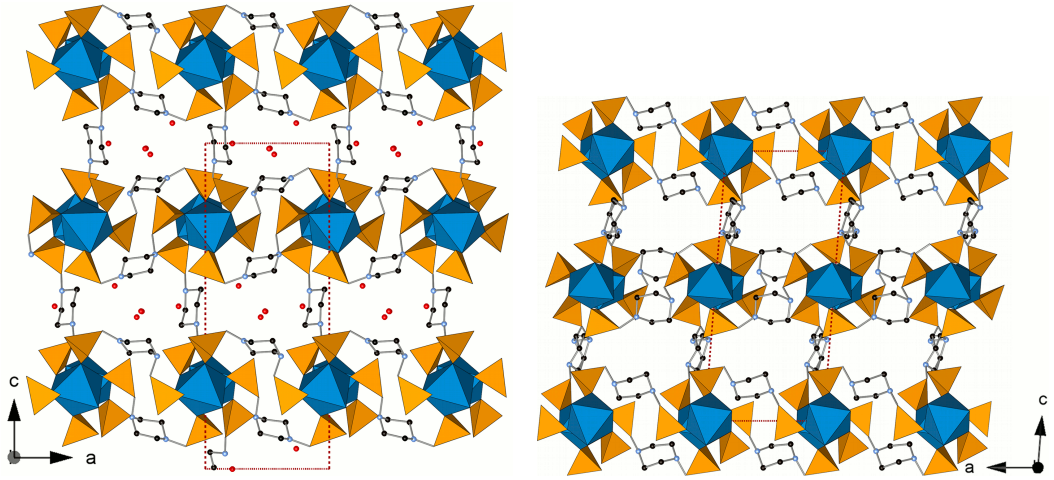

(a) As-prepared (b) Dehydrated

Figure 4.12: Structures of as-prepared (*left*) and dehydrated (*right*) $Y_2(\mathbf{L}H_2)_3$ viewed parallel to the *b*-axis. Dark red dashed lines show the unit cell. Pore space is minimised by the material on dehydration by the tilting of the ligands within the layer and by the shearing of the structural layers relative to one another.

engage in H-bonding with the pendant P=O groups. Structural layers are pillared in the *c*-direction by disordered piperazinyl ligands. In the as-prepared material, these ligands were approximately perpendicular to the *ab*-plane. However, in the dehydrated structure, the ligands are tilted by $\sim 15^{\circ}$ to the normal vector of the *ab*-plane. This tilt is accompanied by an offset of the structural layers (relative to neighbouring layers) of ~ 0.7 Å in the *a*-direction. This gives an overall shear effect compared to the as-prepared material, in which the layers stack directly above one another. The tilt and offset, combined with tilting of the piperazinyl rings within the layers minimises the free pore space in $Y_2(\mathbf{L}H_2)_3$-DH, present following the removal of physisorbed water from the structure.

4.4 $Y_2(L'H_2)_3 \cdot 7H_2O$ — STA-13(Y)

Using racemic $H_4\mathbf{L}'$ in place of $H_4\mathbf{L}$ in a reaction with conditions optimised to prepare structure $Y_2(\mathbf{L}H_2)_3$ yields an amorphous product. In the absence of base however a new phase was obtained with a diffraction pattern similar to that reported for the $Sc^{(III)}$ bisphosphonate, STA-13(Sc).[184] Labelled STA-13(Y), this phase was readily obtained with a high degree of phase purity as confirmed by laboratory powder diffraction. The effect of varying the $Y(AcO)_3$:$H_4\mathbf{L}'$ ratio was investigated, but showed no other phases in the system. Similarly reaction time and temperature had no effect, though at lower temperatures recrystallised ligand was also recovered (*Table 4.4*).

$Y(OAc)_3$: $H_4\mathbf{L}'$: KOH : H_2O	pH	Temp. / °C	Time	Phase
1.0 : 1.5 : 3.0 : 1000	5	190	190	Amorphous
1.0 : 1.0 : 0 : 1000	6	190	48	STA-13(Y)
1.0 : 1.5 : 0 : 1000	5	190	48	STA-13(Y)
1.0 : 2.0 : 0 : 1000	5	190	48	STA-13(Y)
1.0 : 3.0 : 0 : 1000	4	190	48	STA-13(Y)
1.0 : 1.5 : 0 : 1000	5	140	48	STA-13(Y) & $H_4\mathbf{L}'$
1.0 : 1.5 : 0 : 1000	5	220	48	Amorphous
1.0 : 1.5 : 0 : 1000	5	190	18	STA-13(Y)

Table 4.4: Selected reactions of $Y(AcO)_3$ with $H_4\mathbf{L}'$ showing the optimised synthesis conditions of STA-13(Y). Reactions were performed in 40 ml PTFE lined autoclaves, using 20 ml H_2O. No other phases were obtained in the $Y(AcO)_3$-$H_4\mathbf{L}'$ system. The most porous samples of STA-13(Y) were obtained with short reaction times.

The final optimised reaction conditions, to prepare the most porous samples of STA-13(Y), was a gel of composition 1.0 : 1.5 : 1000 ($Y(AcO)_3$: $H_4\mathbf{L}'$: H_2O) with no base and an initial pH of 5. The reaction was then heated at 190°C for 16–18 hrs. To obtain more porous material, samples were then sonicated, with the light fraction (consisting of fine, fibrous needles) kept and the heavy fraction discarded.

Other rare-earth cation forms of STA-13, in addition to the $Y^{(III)}$ and previously reported $Sc^{(III)}$ forms,[184] have also been prepared (see *Section 4.7*).

4.4.1 Characterisation of STA-13(Y)

STA-13(Y) was characterised by a combination of TGA, EDX and elemental analysis and found to have a composition consistent with a $Y^{(III)}$ analogue of the $Sc^{(III)}$ bisphosphonate STA-13(Sc). TGA data for STA-13(Y) were collected in the range 25–850°C under a flow of dry air (*Fig. 4.13*). As with $Y_2(\mathbf{L}H_2)_3$, the final solid is

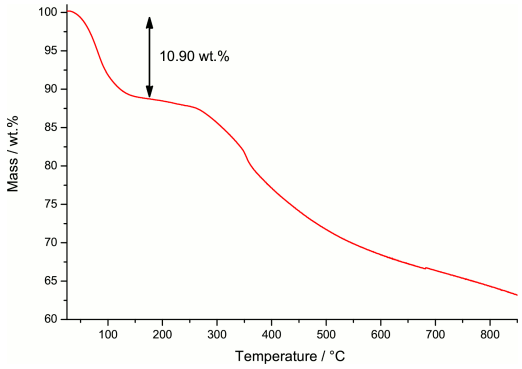

Figure 4.13: TGA of STA-13(Y) from 25–850°C under dry air showing principal weight loss events.

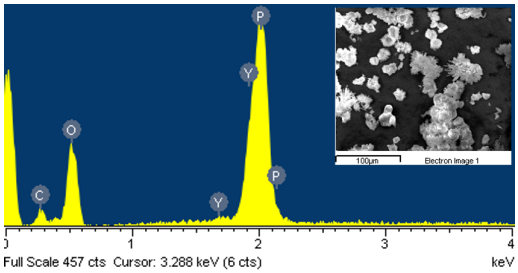

Figure 4.14: EDX spectrum of STA-13 indicating elements found. Y : P ratio of 1.0 : 3.13. Inset shows the area analysed.

assumed to be Y_2O_3. Two principal weight loss events occur; the first is in the range 25–120°C (10.90 wt.%) and indicates the loss of ~ 7 molecules of water per formula unit. Above 275°C, a second weight loss begins which continues to above 850°C, attributed to framework collapse. Again a plateau in the TGA following the loss of physisorbed water indicates a thermally stable dehydrated phase (see *Section 4.4.4*).

The $Sc^{(III)}$ bisphosphonate reported by Miller is thought to have a metal:ligand ratio of 2 : 3.[184] EDX data for the new $Y^{(III)}$ phase gave a Y : P ratio of 1.0 : 3.13, close to the 1 : 3 ratio expected for a metal:ligand ratio of 2 : 3 (*Fig. 4.14*). A composition was therefore proposed for this phase of $Y_2(\mathbf{L}'H_2)_3 \cdot 7H_2O$, which gave good agreement with with elemental analysis: expected — C 21.7 %, H 5.4 %, N 7.2 %; found — C 20.8 %, H 4.9 %, N 6.7 %.

4.4.2 Structure of As-Prepared STA-13(Y)

The structure of STA-13 was determined from synchrotron powder X-ray diffracton data collected at beamline ID31 of the ESRF (Grenoble, France),[144] using data collected on both the STA-13(Sc) (*vide infra*) and STA-13(Y) forms of the material. All data collection and initial model building for the Sc form of the material was carried out by S. R. Miller.[184] Data collection was performed at 100 K in a Debye-Scherrer geometry with the sample mounted in a sealed 0.7 mm quartz glass capillary tube. Data were collected over the range 0–46° 2θ using monochromated X-ray radiation of wavelength 0.800178(6) Å. To minimise the effect of beam damage, 25 two minute data collections were performed on freshly exposed portions of the sample. The final data set was the sum of all of these collections.

The $Sc^{(III)}$ material was indexed with a metrically trigonal or hexagonal unit cell $a = 16.0314(11)$ Å, $c = 9.6921(8)$ Å, V = 2157.2(3) Å^3.[184] Sixteen space groups are

Trigonal	**Hexagonal**
$P\,3$ $P\,\bar{3}$ $P\,321$ $P\,3m1$	$P\,6$ $P\,\bar{6}$ $P\,6/m$ $P\,622$
$P\,\bar{3}m1$ $P\,312$ $P\,31m$ $P\,\bar{3}1m$	$P\,6mm$ $P\,\bar{6}2m$ $P\,\bar{6}m2$ $P\,6/mmm$

Table 4.5: Space groups consistent with systematic absences in synchrotron powder X-ray diffraction patterns of STA-13.[184]

consistent with the pattern of systematic absences in the powder data (*Table 4.5*).

Using the EXPO2004 suite,[149] four different space groups were trialled to obtain a model ($P\,3$, $P\,\bar{3}$, $P\,6$ and $P\,\bar{6}$) as any additional symmetry present in the other twelve space groups would be obvious from the final model. The trigonal space group $P\,\bar{3}$ gave the most promising results, locating the Sc, P and O atoms of the inorganic chains. In parallel with this, laboratory single crystal X-ray diffraction data for a small single crystal of STA-13(Y) were obtained, using Cu K_α radiation. This gave a partial structure solution only in $P\,\bar{3}$, finding not only the heavy atoms (Y, P, O) but also the PO_3C C atom, though the piperazine ring could not be located. $P\,\bar{3}$ was therefore assumed to be the correct space group. Using the P$\cdots$P distance derived from the single crystal solution, a model for the structure of the $Sc^{(III)}$ material was developed by molecular modelling, using the Cerius program.[185]

For STA-13(Y), the synchrotron powder diffraction data were indexed using DICVOL[152] in a metrically trigonal or hexagonal space group with cell parameters a = 16.178(4) Å, c = 9.990(4) Å, V = 2264(1) Å^3 (F.O.M. M_{20}) = 53.7).[154] The STA-13(Sc) model was used as a starting point for Rietveld refinement using the GSAS suite of programs.[156, 157] During refinement, the lower limit of the data was set to 2.0° 2θ, due to the beamstop, whilst data above 38° 2θ were discarded due to the low relative intensity of peaks above this point. Restraints were applied to the octahedral Y-O (2.36 Å), tetrahedral P-O and P-C (1.49 Å and 1.88 Å, respectively), C-N, C- C and C-C(methyl) (1.50-1.51 Å, 1.52 Å and 1.50 Å). In order to ensure a chemically sensible geometry, certain non-bonding distances were also restrained: O$\cdots$O (Y octahedra) (3.32 Å), O$\cdots$O and O$\cdots$C (P tetrahedra) (2.44 Å and 2.75 Å, respectively), N$\cdots$N (diagonal, cross-ring) (2.866 Å), C$\cdots$C (diagonal, cross-ring) (2.892 Å), C$\cdots$C (2^{nd} neighbour, within ring) (2.466 Å) and C$\cdots$C (2^{nd} neighbour, outwith ring) (2.500 Å). Two methyl C atoms, included in the starting model, were initially allowed to refine freely, except for a C-C bonding restraint (1.50 Å). It was found that the fit was improved by the inclusion of only one methyl group (C8 in the final refinement) in a equatorial configuration.

Solid-state ^{13}C and ^{31}P MAS NMR spectra were collected for STA-13(Y) (*Fig. 4.15*) and assigned by reference to the solution phase NMR spectra of the

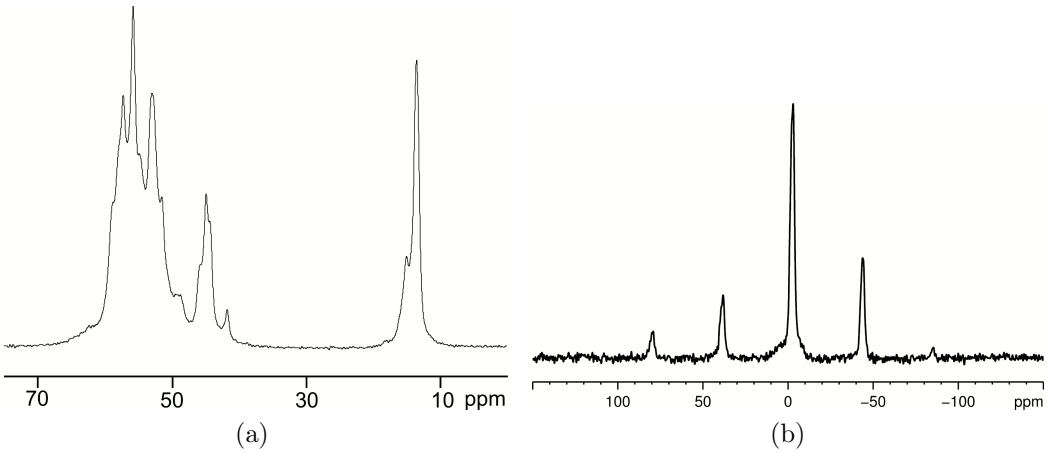

Figure 4.15: ^{13}C (*left*) and ^{31}P (*right*) MAS NMR spectrum of STA-13(Y).

ligand (see*Section 3.2.2*). The ^{31}P spectrum shows two overlapping resonances at -2.2 ppm and -2.9 ppm, as expected from the crystal structure. The ^{13}C spectrum shows a multiplet centred at 53 ppm assigned to methylene and ring C atoms and two distinct resonances in the methyl region (14.1 ppm and 14.9 ppm). The additional resonance in the methyl region cannot be accounted for by a reduction in symmetry as a lower symmetry space group would show extra peaks in the ^{31}P spectrum. The extra resonance is therefore a result of disorder in the methyl C environment.

A second lower occupancy methyl C atom (C7) was therefore added to the model, bonded to C2 in a equatorial geometry, projecting into the pore space, and the occupancy of the two methyl C atoms fixed (C7: 25 %; C8: 75 %). C7 was placed on the C2 site as this was the only other site in the piperazinyl ring which was sufficiently sterically unhindered. Restraints were applied to the methyl C atoms to ensure they remained in chemically sensible positions: $N\cdots C_{Me}$ and $C\cdots C_{Me}$ (2.39 Å and 2.41 Å). A good fit to the data was obtained after 5065 cycles (R_{wp} = 0.0523, R_p = 0.0409, $R(F^2)$ = 0.0452, χ^2 = 4.462) and the final Rietveld fit for STA-13(Y) is shown (*Fig. 4.16*).

As in the structure of $Y_2(\mathbf{L}H_2)_3$ (see *Section 4.3.3*) each Y cation has a slightly distorted octahedral (YO_6) coordination environment (*Table 4.6*). Each YO_6 is linked to two others by six bridging phosphonate groups (three to each neighbour), forming chains parallel to the *c*-direction (*Fig. 4.17a*). In STA-13(Y) chains are linear rather than undulating and are connected to three others, in the *a*- and *b*-directions, by crystallographically identical linkers, to form a honeycomb array of narrow 3 Å channels, lined with methyl groups, parallel to the *c*-direction and occupied by physisorbed water molecules (*Fig. 4.17c*). An extensive H-bonding network is developed between protonated piperazinyl moieties and pendant P=O

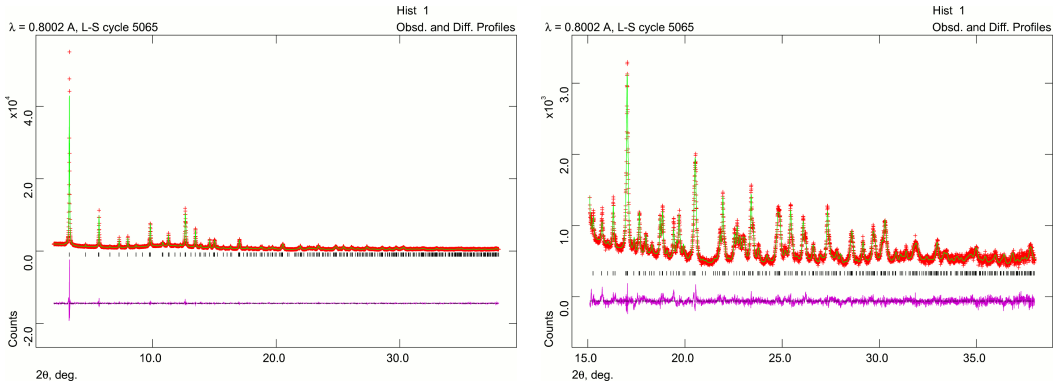

Figure 4.16: Final Rietveld fit for the refinement of STA-13(Y) in trigonal space group $P\bar{3}$. $R_{wp} = 0.0523$.

Bond	Distance / Å	Bond	Distance / Å
Y1-O1	2.261(9)	P1-O1	1.470(6)
Y1-O1	2.260(9)	P1-O2	1.481(5)
Y1-O1	2.260(9)	P1-O3	1.508(10)
Y1-O4	2.376(8)	P1-C1	1.880(8)
Y1-O4	2.377(8)	P4-O4	1.506(8)
Y1-O4	2.375(8)	P4-O5	1.463(7)
Y2-O2	2.316(7)	P4-O6	1.483(9)
Y2-O2	2.315(7)	P4-C4	1.887(8)
Y2-O2	2.315(7)		
Y2-O5	2.354(7)		
Y2-O5	2.354(7)		
Y2-O5	2.353(7)		

Table 4.6: Selected bond distances in the as-prepared structure of STA-13(Y).

bonds (short contacts: N1-O3, 2.771 Å; N4-O6, 2.757 Å) of neighbouring linkers along the *c*-direction (*Fig. 4.17b*), facilitated by the conformational locking provided by the Me groups and also driving crystallisation of the structure. Ligands arrange themselves along the *c*-direction with an alternating chiral ordering. Considering an individual ligand, even though the Me group may be placed in two positions, both configurations have the same chirality. Neighbouring ligands in the chain are related to one another across a crystallographic inversion centre, so both *R* and *S* enantiomers are incorporated into the structure of STA-13(Y) in equal numbers, suggesting that both enantiomers are necessary to develop the H-bonding network and so to crystallise STA-13(Y).

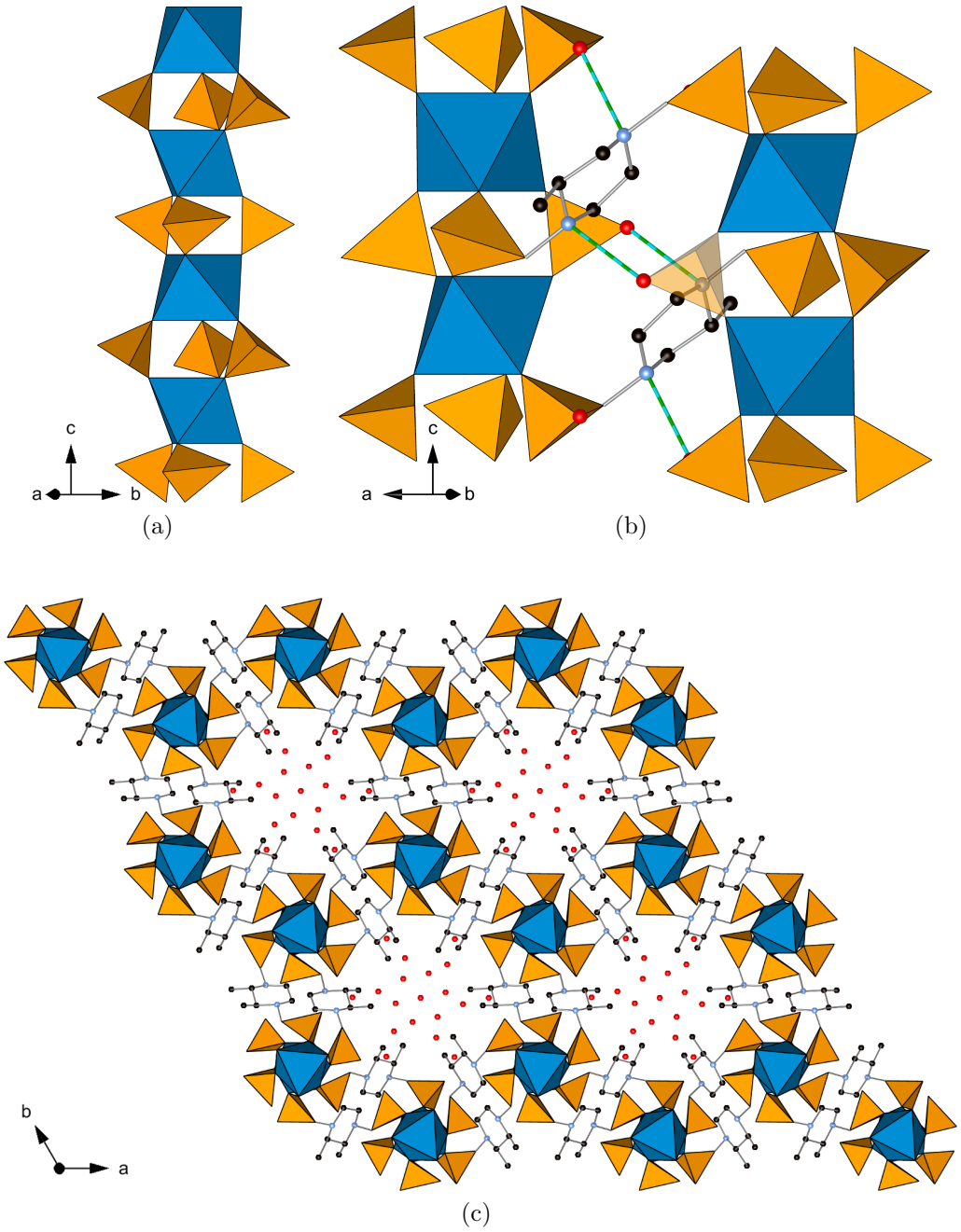

Figure 4.17: Structure of STA-13(Y). *Top Left:* Structure of inorganic yttrium phosphonate chain of STA-13(Y) showing linking PO_3C groups. *Top Right:* Detail of H-bonding between neighbouring protonated piperazinyl N atoms along the chains (blue-green bonds), thought to drive crystallisation of STA-13(Y). *Bottom:* View along the *c*-direction showing the linking of the chains to form a honeycomb array of 3 Å channels, occupied by physisorbed water molecules.

4.4.3 Dehydration Behaviour of Structure STA-13(Y)

TGA data (*Fig. 4.13*) indicate that physisorbed water may be removed from the structure of STA-13(Y) by heating to 120°C, whilst heating above 275°C leads to framework collapse. To investigate the structural behaviour of STA-13(Y) on dehydration, a sample of the material was dehydrated by heating (200°C) under vacuum (1×10^{-4} Torr) in a 0.7 mm quartz glass capillary tube. The tube was then sealed and a laboratory X-ray diffraction pattern collected (Cu K_α). The capillary was then broken open and allowed to rehydrate over five days and another diffraction pattern collected. Diffraction data indicate that STA-13(Y) retains its trigonal symmetry on dehydration and shows only a slight shift in the positions of the diffraction peaks, indicating little change in the unit cell dimensions (*Fig. 4.18*).

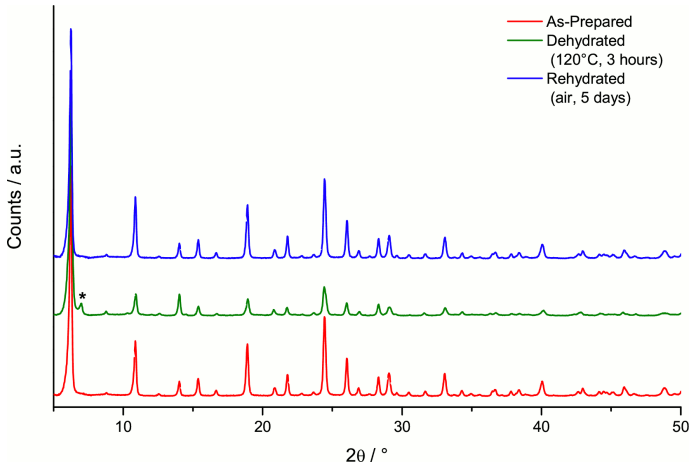

Figure 4.18: Comparison of the normalised laboratory diffraction patterns (Cu K_α) of as-prepared (red), dehydrated (dark green) and rehydrated (blue) structure STA-13(Y). Asterisk marks peak attributed to an unknown impurity phase (see *Section 4.4.4*).

The dehydrated structure of STA-13(Y), referred to as STA-13(Y)-DH, shows permanent porosity to N_2 at 77 K. The porosity of STA-13(Y)-DH has been investigated with a range of other gases (see *Section 4.8*)

4.4.4 Structure of Dehydrated STA-13(Y)

A second dehydrated sample was prepared by the method described (*Section 4.4.3*) and powder X-ray diffraction data collected on beamline ID31 at the ESRF (Grenoble, France).[144] Data were collected following the same data collection protocol as the as-prepared material (see *Section 4.4.2*). Indexing the synchrotron diffraction pattern using DICVOL[152] gave a metrically trigonal or hexagonal unit cell: a = 16.120(2) Å, c = 10.0302(17) Å, V = 2257.2(6) Å^3 (F.O.M M_{20} =

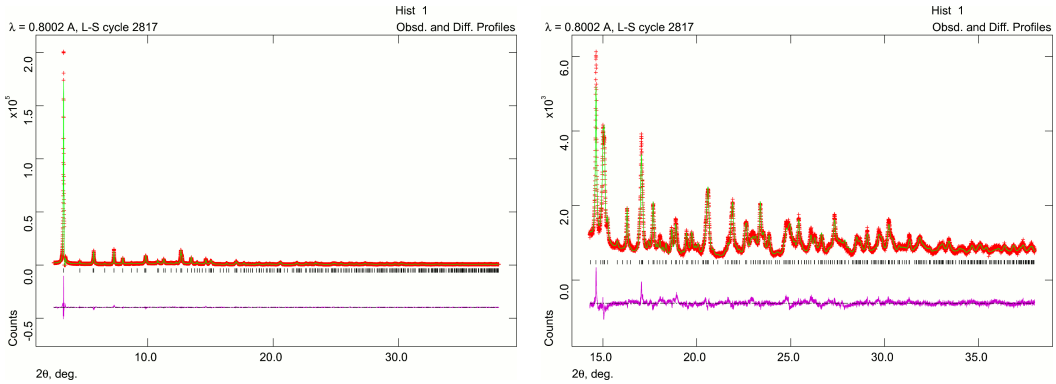

Figure 4.19: Final Rietveld fit for the refinement of STA-13(Y)-DH in trigonal space group $P\bar{3}$. $R_{wp} = 0.0677$.

55.1).[154] Two additional peaks were observed but not indexed by this cell (3.37° and 5.86° 2θ) and are thought to belong to an unidentified minor impurity phase. As the patterns and unit cells of the as-prepared and dehydrated forms of STA-13(Y) are similar, a Rietveld refinement using the GSAS suite of programs[156, 157] was attempted, using as the starting model the as-prepared material with physisorbed water molecules (O101–O104) removed. To prevent the larger of the impurity peaks from affecting the refinement, the region between 3.337–3.429° 2θ was excluded. The lower data limit was set to 2.5° 2θ, due to the beamstop, and the upper limit to 38° 2θ, as above this angle diffraction peak intensities were relatively low. To ensure that the structure remained chemically sensible during the refinement, restraints were applied to bonding distances: octahedral Y-O (2.36 Å), tetrahedral P-O and P-C (1.49–1.50 Å and 1.88 Å respectively), C-N, C-C and C-C(methyl) (1.50–1.51 Å, 1.52 Å and 1.50 Å). In addition, certain non-bonding distances were also restrained: O···O (Y octahedra) (3.338 Å), O···O and O···C (P tetrahedra) (2.434 Å and 2.761 Å respectively), N···N (diagonal, cross-ring) (2.855 Å), C···C (diagonal, cross-ring) (2.865 Å), C···N (2^{nd} neighbour, within ring) (2.400 Å), C···C (2^{nd} neighbour, within ring) (2.440 Å), C···C (2^{nd} neighbour, outwith ring) (2.460 Å) and N···C(methyl) and C···C(methyl) (2^{nd} neighbour) (2.450 Å and 2.465 Å). A reasonable fit to the data was obtained after 2817 cycles of refinement ($R_{wp} = 0.0677$, $R_p = 0.0540$, $R(F^2) = 0.0647$, $\chi^2 = 11.41$) and the final Rietveld fit for $Y_2(\mathbf{L}'H_2)_3$ — STA-13(Y)-DH — is shown (*Fig. 4.19*).

STA-13(Y)-DH has a nearly identical framework structure to the as-prepared form. The structure consists of a honeycomb array of unidirectional channels, parallel to the *c*-direction. Channels are delimited by chains of YO_6 octahedra, linked together by three bridging $PO3_3C$ groups; protonated piperazinyl moieties

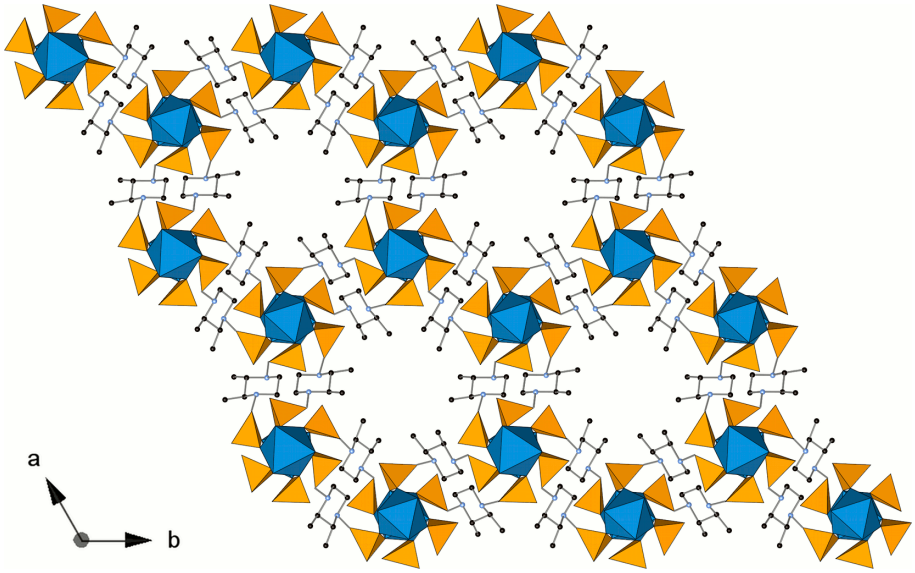

Figure 4.20: Structure of dehydrated STA-13(Y) viewed parallel to the *c*-direction, showing the 3 Å channels.

link the chains (*Fig. 4.20*). The extensive H-bonding network present in the as-prepared material is retained, even after heating to 200°C. The pore channels have a free diameter of $\sim$ 3 Å and the material is porous to N_2 at 77 K, CO_2 at 196 K and 273 K, and CH_4 and other alkanes at 273 K (see *Section 4.8*).

4.5 $Y_2(R\text{-}L'H_2)_3 \cdot 4H_2O$

The crystal structure of STA-13(Y) indicates that both R and S enantiomers are needed in the synthesis gel for the structure to crystallise. To investigate this, the enantiopure R form of $H_4\mathbf{L}'$ (R-$H_4\mathbf{L}'$) was prepared (*Section 3.2.2*) and used in place of racemic $H_4\mathbf{L}'$ in syntheses which had produced phase pure samples of STA-13(Y) (*Table 4.7*)

$Y(OAc)_3$: R-$H_4\mathbf{L}'$: H_2O	pH	Temp. / °C	Time / hrs	Phase
1.0 : 1.5 : 1000	5	160	48	$Y_2(R\text{-}\mathbf{L}H_2)_3$& Unknown
1.0 : 1.5 : 1000	6	190	48	$Y_2(R\text{-}\mathbf{L}H_2)_3$
1.0 : 1.5 : 1000	5	220	48	**Amorphous**
1.0 : 2.0 : 1000	5	190	170	$Y_2(R\text{-}\mathbf{L}H_2)_3$

Table 4.7: Selected reactions of $Y(AcO)_3$ with R-$H_4\mathbf{L}'$ showing the optimised synthesis conditions of $Y_2(R\text{-}\mathbf{L}H_2)_3$. Reactions were performed in 40 ml PTFE lined autoclaves, using 20 ml H_2O. No other phases were obtained in this system.

Rather than form structure STA-13(Y), reactions with R-$H_4\mathbf{L}'$ produced a material with a diffraction pattern similar to that of structure $Y_2(\mathbf{L}H_2)_3$. This new phase is referred to as structure $Y_2(R\text{-}\mathbf{L}H_2)_3$. No other phases were obtained during these investigations. The most crystalline samples of $Y_2(R\text{-}\mathbf{L}H_2)_3$ (identified by the having the smallest FWHM) were prepared from synthesis gels with the same composition as those producing the best samples of structure STA-13(Y): 1.0 : 1.5 : 1000 ($Y(AcO)_3$: R-$H_4\mathbf{L}'$: H_2O).

4.5.1 Characterisation of Structure $Y_2(R\text{-}\mathbf{L}H_2)_3$

Structures were characterised by TGA, EDX and elemental analysis. TGA analysis showed two weight loss events in the range 25–850°C (*Fig. 4.21* — the final solid is assumed to be Y_2O_3). The first weight loss, from 25–120°C (6.78 wt.%) corresponds to the loss of $\sim$ 4 molecules of physisorbed water, whilst the second, starting at 260°C and continuing to above 850°C, indicates the collapse of the framework. This pattern of weight losses is analogous to those observed for structure $Y_2(\mathbf{L}H_2)_3$. The plateau in the TGA following the loss of physisorbed water indicates the formation of a thermally stable dehydrated phase (see *Sections 4.3.4 & 4.5.4*).

EDX analysis gave a Y : P ratio of 1.0 : 3.32, which agrees resonably with the 2 : 3 metal:ligand ratio expected for an analogue of structure $Y_2(R\text{-}\mathbf{L}H_2)_3$ — the slightly high P content may indicate some unreacted ligand in the sample. A composition for this material of $Y_2(R\text{-}\mathbf{L}'H_2)_3 \cdot 4H_2O$ was proposed and found to be in reasonable

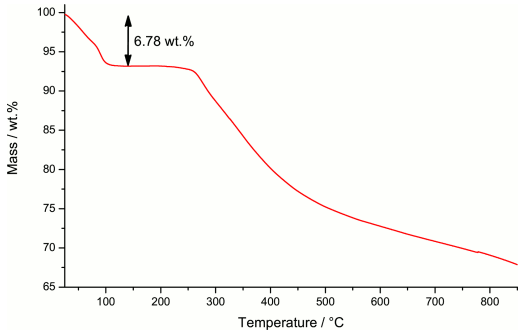

Figure 4.21: TGA of $Y_2(R\text{-}\mathbf{L}H_2)_3$ from 25–850°C under dry air showing principal weight loss events.

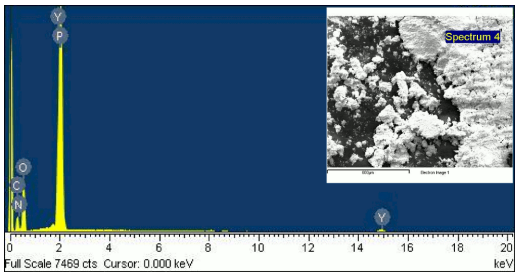

Figure 4.22: EDX spectrum of $Y_2(R\text{-}\mathbf{L}H_2)_3$ indicating elements found. Y : P ratio of 1.0 : 3.32. Inset shows the area analysed.

agreement with elemental analysis results: expected — C 22.6 %, H 5.1 %, N 7.6 %; found — C 21.5 %, H 4.8 %, N 7.2 %.

Structures of both the as-prepared and dehydrated forms of $Y_2(R\text{-}\mathbf{L}H_2)_3$ were confirmed by powder X-ray diffraction data. The structure of the fully dehydrated material was solved first, as the diffraction pattern only has contributions from the framework, making the problem of structure solution easier.

4.5.2 Structure of As-Prepared $Y_2(R\text{-}\mathbf{L}H_2)_3$

The structure of $Y_2(R\text{-}\mathbf{L}H_2)_3$ was obtained by Rietveld refinement of synchrotron powder X-ray diffraction data collected at beamline I11 of the Diamond Light Source (Harwell, Oxfordshire, UK).[145] Data were collected on a sample of as-prepared $Y_2(R\text{-}\mathbf{L}H_2)_3$ in a 0.5 mm glass capillary tube, mounted in a Debye-Scherrer geometry at 100 K. Eight three minute data sets were collected using monochromated X-ray radiation of wavelength 0.825028 Å over the range 1–140° 2θ, with each collection made on a fresh sample by translating the capillary between data collections. This protocol and the cooling of the sample were used to minimise the effect of beam damage on the material. Data sets were summed and initially binned with a step size of 0.002°. Prior to refinement, data at angles greater than 40° 2θ were discarded (as diffraction at high angle was relatively weak) and the remaining data were rebinned to a step size of 0.005°.

The structure was confirmed by Rietveld refinement using the GSAS suite of programs[147, 156, 157] with the starting model adapted from the fully dehydrated structure (see *Section 4.5.4*). The data were indexed using the TREOR routines of EXPO2009[153, 148] with an orthorhombic cell, a = 8.6932(11) Å, b = 9.910(3) Å, c = 23.291(5) Å, V = 2006.5(8) Å^3 (F.O.M. M_{20} = 24).[154] $Y_2(\mathbf{L}H_2)_3$ was also originally reported in an orthorhombic space group,[112] but shown by solid-state

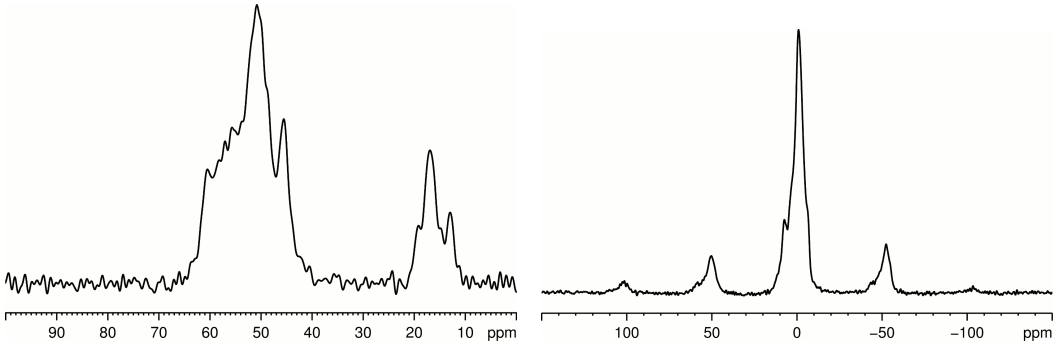

Figure 4.23: ^{13}C (*left*) and ^{31}P (*right*) MAS NMR spectrum of $Y_2(R\text{-}\mathbf{L}H_2)_3$.

MAS NMR to crystallise with a monoclinic cell (*Section 4.3.3*). Therefore MAS NMR ^{13}C and ^{31}P spectra were collected for an as-prepared sample of $Y_2(R\text{-}\mathbf{L}H_2)_3$. The ^{31}P spectra shows two distinct P environments (7.4 ppm and -1.0 ppm — *Fig. 4.23b*). Two shoulders are also observed on the lower field resonance (2.9 ppm and -5.9 ppm). Therefore we expect to observe four crystallographically distinct P sites, which would be consistent with an orthorhombic model, with one ligand disordered. The ^{13}C spectrum is slightly more ambiguous: a group of overlapped resonances centred at $\sim$ 53 ppm is assigned to ring and methylene C environments, whilst a second group of resonances centred at $\sim$ 15 ppm is assigned to methyl C environments (*Fig. 4.23a*). This second group shows two distinct resonances (17.0 ppm and 13.0 ppm) and two poorly defined shoulders (19.2 ppm and 14.9 ppm). Four methyl C environments might indicate a lower symmetry setting or could be attributed to disorder. As both ^{31}P and ^{13}C MAS NMR may be interpreted in terms of an orthorhombic crystal symmetry, a model for Rietveld refinement in the space group $P\,22_12_1$ (which $Y_2(\mathbf{L}H_2)_3$ was originally thought to crystallise in) was selected.

Unit cell background and profile parameters were refined until no further significant improvement in fit could be obtained. The positions of all framework atoms were constrained together and refined. Fourier maps were used to locate peaks in the electron density consistent with the position of physisorbed water molecules (O100, O101 and O102). This was repeated until no further chemically sensible or significant peaks were located in the difference maps. The constraint on the positions of all atoms was then removed and restraints on bonding distances were applied to the structure: Y-O (2.33 Å), P-O (1.50 Å), P-C (1.85 Å), C-N (1.51–1.53 Å) and C-C (1.53 Å). Restraints were also applied to non-bonding distances: O$\cdots$O (Y octahedron) (3.30 Å); O$\cdots$O and O$\cdots$C (P tetrahedra) (2.45 Å and

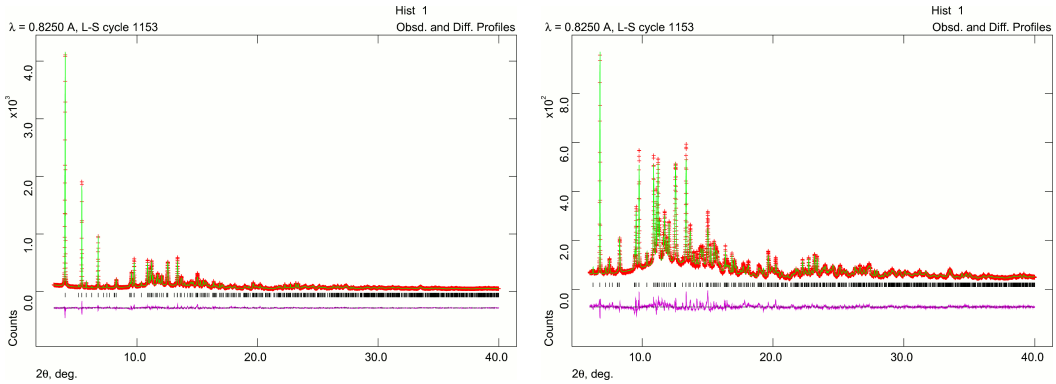

Figure 4.24: Final Rietveld fit for the refinement of the as-prepared structure of $Y_2(R\text{-}\mathbf{L}H_2)_3$ (R_{wp} = 0.0586).

2.74 Å respectively); N···N and C···C (diagonal, cross-ring) (2.90 Å and 2.90 Å); C···N and C···C (2nd neighbour, within ring) (2.50 Å and 2.50 Å); C···C (2nd neighbour, outwith ring) (2.50 Å); C···C_{Me} and N···C_{Me} (2nd neighbour, methyl C atom) (2.50 Å). No restraints were applied to the positions of the physisorbed water molecules. Positions of atoms within the structural layer (*vide infra* — *Fig. 4.25b*) and physisorbed water molecules were refined first, with cycles of refinement repeated until the ligand in the layer had a chemically sensible geometry. After this the atoms of the interlayer ligand and physisorbed water only were refined (*n.b.* the N···N cross-ring restraint and restraints on the position of the methyl C atom were not applied to this linker), with refinement again continued until a chemically sensible ring geometry was obtained. Finally the whole structure was refined together. U_{Iso} parameters were also refined and further cycles of refinement of the profile and background performed. Atomic positions and U_{Iso} values were refined further until convergence. The final fit after 1143 cycles was R_{wp} = 0.0586, R_p = 0.0468, $R(F^2)$ = 0.0684 and χ^2 = 90.17 (final fits are shown in *Fig. 4.24*).

The structure of as-prepared $Y_2(R\text{-}\mathbf{L}H_2)_3$ is very closely related to that of $Y_2(\mathbf{L}H_2)_3$. $Y_2(R\text{-}\mathbf{L}H_2)_3$ however was refined in an orthorhombic space group, whereas the final refinement of $Y_2(\mathbf{L}H_2)_3$ was in a monoclinic space group with a monoclinic (γ) angle close to 90°. In the final orthorhombic $P\,22_12_1$ model of $Y_2(R\text{-}\mathbf{L}H_2)_3$, there is one crystallographic Y site, coordinated in a slightly distorted octahedral geometry by six O atoms from three crystallographically distinct PO_3C groups, each with a regular tetrahedral coordination (*Table 4.8*). Three PO_3C groups from two distinct linkers connect each Y cation to two others in a bridging mode to form chains in the *b*-direction (*Fig. 4.25a*). The third PO_3C O atom does not engage in coordination, but projects into the pore space. Chains are linked

Bond	Distance / Å	Bond	Distance / Å
Y1-O1	2.210(12)	P4-O4	1.494(4)
Y1-O3	2.371(9)	P4-O5	1.493(4)
Y1-O4	2.369(10)	P4-O6	1.508(4)
Y1-O5	2.329(11)	P4-C4	1.853(4)
Y1-O11	2.230(11)	P11-O11	1.490(4)
Y1-O12	2.311(12)	P11-O12	1.490(4)
P1-O1	1.499(4)	P11-O13	1.510(4)
P1-O2	1.505(4)	P11-C11	1.853(4)
P1-O3	1.502(4)		
P1-C1	1.852(4)		

Table 4.8: Selected bond distances in the as-prepared structure of $Y_2(R\text{-}\mathbf{L}H_2)_3$.

in the *a*-direction by two crystallographically equivalent protonated piperazinyl moieties, each with one axial and one equatorial methylenephosphonate group to form a structural layer in the *ab*-plane (*Fig. 4.25b*). Piperazinyl rings have a chair conformation and the methyl group occupies an equatorial position consistent with the *R*-enantiomer. Short contacts are observed between the protonated N atoms of the piperazinyl ring and pendant P-O groups or physisorbed water molecules indicating H-bonding interactions (N$\cdots$O(P): 2.785(18) Å). A second group of crystallographically distinct, disordered linkers pillar the layers to form the framework (*Fig. 4.25c*). The pillaring protonated piperazinyl group was found to adopt a boat geometry with the methyl group in an axial geometry, which is also consistent with the *R*-enantiomer. During refinement it was noted that, due to the proximity of both pendant PO_3C O atoms and the presence of physisorbed water in the channels, the methyl group could not adopt an equatorial geometry. In this axial geometry with the boat conformation, the ligand is able to minimise the steric clashing between the methyl group and other parts of the framework. Physisorbed water in the channels are located on three sites closely related to those observed for water molecules in the channels of $Y_2(\mathbf{L}H_2)_3$. Physisorbed water molecules H-bond to protonated N atoms of both the pillaring piperazinyl ring and those rings within the structural layer (O$\cdots$N: 2.58(2)–2.95(3) Å) and also with pendant P-O groups (O(P)$\cdots$O: 2.591(18)–2.73(4) Å).

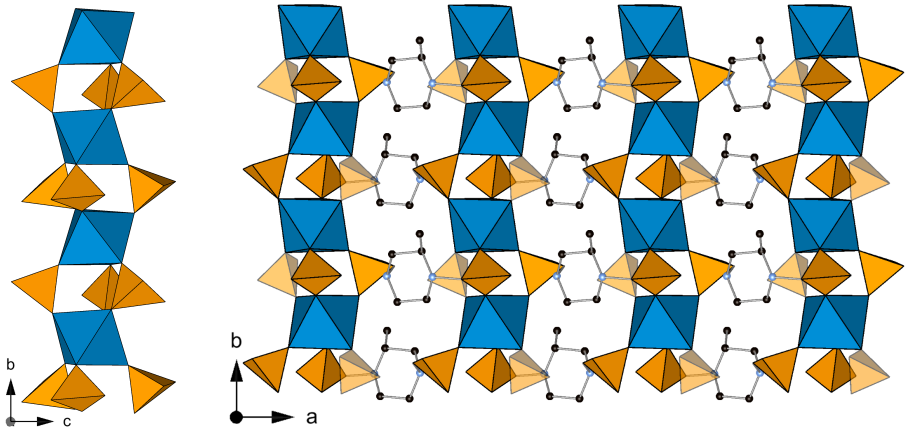

(a) (b)

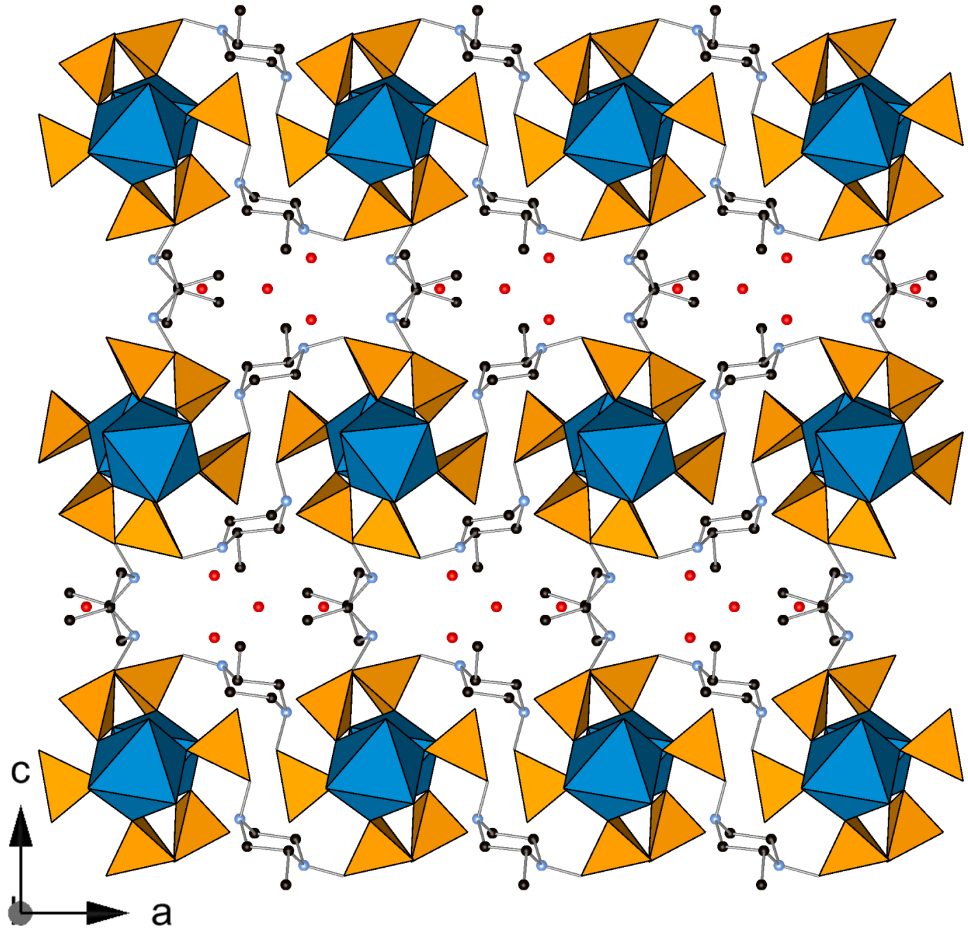

(c)

Figure 4.25: Structure of $Y_2(R\text{-}\mathbf{L}H_2)_3$. *Top Left:* Structure of the inorganic yttrium-phosphonate chain showing the linking PO_3C groups. *Top Right:* Chains link in the *c*-direction to form a layer. PO_3C groups involved in linking layers are transparent. *Bottom:* View along the *c*-direction, with chains linked into structural layers and linked in the third dimension to give small pores occupied by physisorbed water molecules.

4.5.3 Dehydration Behaviour of Structure $Y_2(R\text{-}LH_2)_3$

The plateau in the TGA plot (*Fig 4.21*), following loss of physisorbed water, indicates the formation of a thermally stable dehydrated phase. A sample of $Y_2(R\text{-}\mathbf{L}H_2)_3$ was loaded into a 0.7 mm quartz glass capillary tube and heated at 120°C under reduced pressure (1×10^{-4} Torr) for three hours. The capillary was then flame sealed and a laboratory powder X-ray diffractogram (Cu K_α) collected. The capillary was broken open and allowed to rehydrate in the air over 24 hours. A second diffractogram was then collected. Diffraction patterns for the as-prepared, dehydrated and rehydrated materials (*Fig. 4.26*) show no changes in the peak positions on dehydration and subsequent rehydration, though the peak intensities change, indicating the loss of water from the structure.

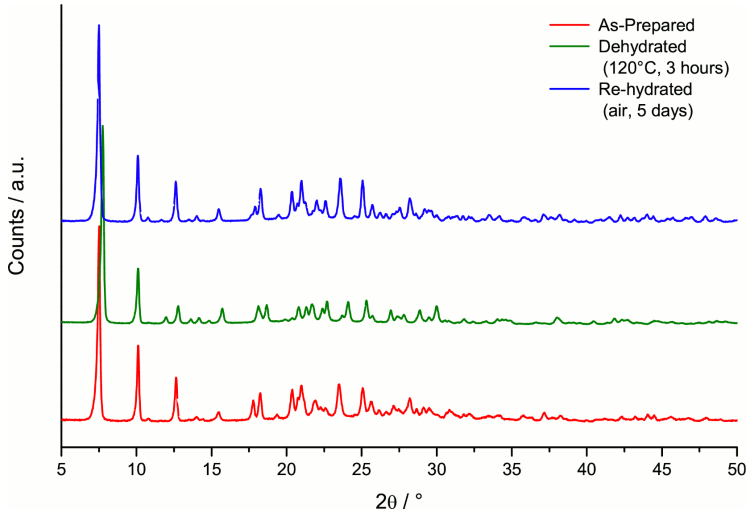

Figure 4.26: Diffraction patterns of as-prepared (red), dehydrated (green) and rehydrated (blue) samples of structure $Y_2(R\text{-}\mathbf{L}H_2)_3$.

To determine the structural changes occurring on dehydration, high-resolution synchrotron X-ray powder diffraction data were used to determine the structure of the dehydrated material. As discussed, the structure of the dehydrated material was solved first and used as a model in the refinement of as-prepared $Y_2(R\text{-}\mathbf{L}H_2)_3$ (*Section 4.5.2*).

4.5.4 Structure of Dehydrated $Y_2(R\text{-}LH_2)_3$

A sample of $Y_2(R\text{-}\mathbf{L}H_2)_3$-DH in a sealed 0.5 mm quartz glass capillary tube was prepared as described (see *Section 4.5.3*). Synchrotron powder X-ray diffraction data were collected at beamline I11 of Diamond Light Source (Harwell, Oxfordshire, UK)[145] using the sample protocol described for the as-prepared material (see

Section 4.5.2). For analysis, the data range 1.5–40° 2θ was used (below 1.5° is the beamstop; above 40° diffraction is weak) rebinned with a step size of 0.005°. Data were indexed using the TREOR routines of EXPO2009[153, 148] with an orthorhombic cell, a = 8.6979(16) Å, b = 9.6857(13) Å, c = 22.577(3) Å, V = 1902.0(5) Å^3 (F.O.M. M_{20} = 53).[154] A Le Bail fit of the structure was used to refine the cell and to obtain initial profile parameters for Rietveld refinement.[155]

Rietveld refinement, using the GSAS suite of programs,[147, 156, 157] used a starting model derived from the structure of as-prepared $Y_2(\mathbf{L}H_2)_3$, in orthorhombic space group $P\,22_12_1$. This model was selected as the space group is consistent with the MAS NMR spectra of the as-prepared material (*Section 4.5.2*) and since no peak splitting is observed on dehydration, which suggesting no change in symmetry occurs. Methyl C atoms were positioned geometrically, bonded 1.53 Å distance from C atoms to give linkers with *R*-chirality. The positions of the C atoms were confirmed by refinement of their occupancies. Bonding restraints were applied to the model before structural refinement: Y-O (2.33 Å), P-O (1.50 Å), P-C (1.85 Å), C-N (1.51–1.53 Å) and C-C (1.53 Å). Restraints were also applied to non-bonding distances: O$\cdots$O (Y octahedron) (3.30 Å); O$\cdots$O and O$\cdots$C (P tetrahedra) (2.45 Å and 2.74 Å respectively); N$\cdots$N and C$\cdots$C (diagonal, cross-ring) (2.90 Å and 2.90 Å); C$\cdots$N and C$\cdots$C (2$^{\text{nd}}$ neighbour, within ring) (2.50 Å and 2.50 Å); C$\cdots$C (2$^{\text{nd}}$ neighbour, outwith ring) (2.50 Å); C$\cdots$C$_{\text{Me}}$ and N$\cdots$C$_{\text{Me}}$ (2$^{\text{nd}}$ neighbour, methyl C atom) (2.50 Å). Positions of atoms within the structural layer (see *Section 4.5.2*) were refined first, with cycles of refinement repeated until the ligand in the layer had a chemically sensible geometry. Next, the atoms of the interlayer ligand only were refined. The ligand was found to adopt a slightly twisted conformation in which methyl C atoms had to be restrained apart (2.9 Å) to ensure a sensible geometry. In addition the N$\cdots$N restraint and the methyl C atom 2$^{\text{nd}}$ neighbour restraints were removed for this ligand. Cycles of refinement were continued until a satisfactory geometry for the ligand was obtained. The positions of all atoms were then refined and also the U_{Iso} parameters. Further cycles of profile and background parameters were also performed. Finally the positions of all atoms within the structure and their U_{Iso} parameters were refined until convergence was achieved. The final fit after 1768 cycles was R_{wp} = 0.0613, R_p = 0.0505, R(F^2) = 0.0747 and χ^2 = 104.3 (final fits are shown in *Fig. 4.24*).

The structure of dehydrated $Y_2(R\text{-}\mathbf{L}H_2)_3$ is very similar to that of the as-prepared material, although the unit cell has a shorter c-parameter (smaller by $\sim$ 0.7 Å — *Fig. 4.28*). Again the structure consists of chains parallel to the b-direction of YO_6 octahedra linked in a bridging mode by tetrahedral PO_3C groups (*Table 4.9*). Chains are linked in the a-direction to two others by two crystallographically equivalent

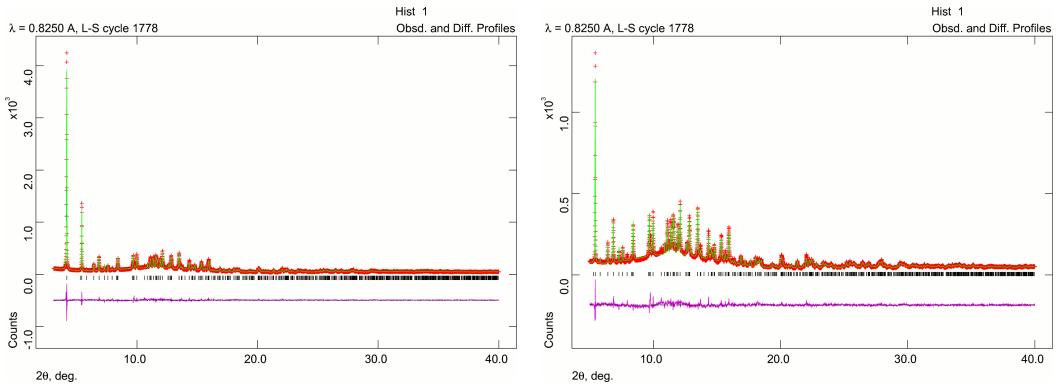

Figure 4.27: Final Rietveld fit for the refinement of the dehydrated structure of $Y_2(R\text{-}\mathbf{L}H_2)_3$ (R_{wp} = 0.0613).

Bond	Distance / Å	Bond	Distance / Å
Y1-O1	2.300(16)	P4-O4	1.468(14)
Y1-O3	2.345(15)	P4-O5	1.483(15)
Y1-O4	2.421(15)	P4-O6	1.674(15)
Y1-O5	2.426(16)	P4-C4	1.875(16)
Y1-O11	2.202(15)	P11-O11	1.439(14)
Y1-O12	2.273(15)	P11-O12	1.472(15)
P1-O1	1.427(15)	P11-O13	1.539(15)
P1-O2	1.566(16)	P11-C11	1.938(17)
P1-O3	1.550(15)		
P1-C1	1.851(17)		

Table 4.9: Selected bond distances in the dehydrated structure of $Y_2(R\text{-}\mathbf{L}H_2)_3$.

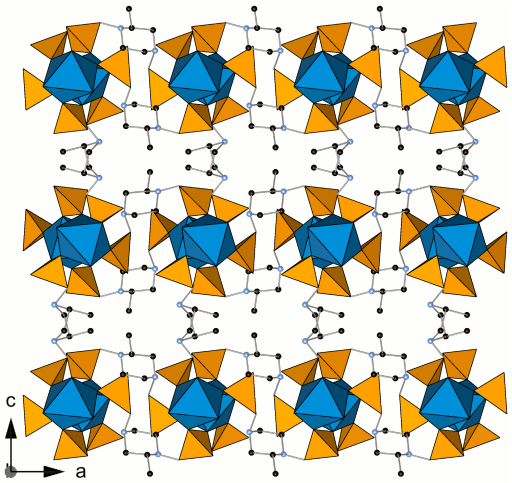

Figure 4.28: Structure of dehydrated $Y_2(R\text{-}\mathbf{L}H_2)_3$ viewed along the *b*-axis.

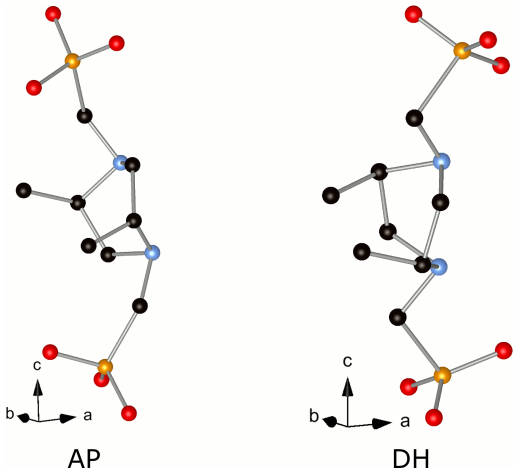

Figure 4.29: The conformation of the pillaring ligand in as-prepared (*left*) and dehydrated (*right*) $Y_2(R\text{-}\mathbf{L}H_2)_3$, showing the more twisted nature of the boat in the dehydrated material.

linkers, to form a structural layer in the *ab*-plane. These linkers have one axial and one equatorial methylenephosphonate group and the methyl C atom occupies a position consistent with an *R*-chiral ligand. In the dehydrated structure, only one protonated piperazinyl N atom is able to engage in H-bonding, although the N$\cdots$O distance is significantly greater than in the as-prepared material (3.17(3) Å (DH) *vs* 2.785(18) Å (AP)). Layers are pillared by a second crystallographically distinct group of linkers in the *c*-direction to form the framework. In the dehydrated structure, methyl groups in this linker again occupy an axial geometry, to avoid steric clashing with nearby framework atoms. Rather than a boat topology, the pillaring ligand has a topology more similar to the twist boat conformer, and it is this change in structure which results in the shortening of the *c*-parameter (*Fig. 4.29*). The shortening occurs to minimise the open space left in the structure by the removal of physisorbed water. Further shortening is precluded by the presence of the methyl C atom which would sterically clash with other parts of the framework if the ligand twisted further. It is also this steric clashing which prevents closure of the pores by tilting of the pillaring piperazinyl groups as is thought to occur in $Y_2(\mathbf{L}H_2)_3$.

4.6 Reactions of $Y(AcO)_3$ with H_4L''

The crystallisation of $Y_2(R\text{-}\mathbf{L}H_2)_3$ demonstrates that their is enough space in the $Y_2(\mathbf{L}H_2)_3$ network to support a linker with one Me group on the piperazinyl ring. Considering the structure of $Y_2(R\text{-}\mathbf{L}'H_2)_3 \cdot 4H_2O$, however, there was not thought to be enough space for a second Me group in the framework. Reactions of $Y(AcO)_3$ with the 2,5-*trans*-dimethyl linker ($H_4\mathbf{L}''$ — *Section 3.2.3*) were therefore undertaken to investigate this. In an initial investigation, a small array of high-throughput (HT) reactions probed the effect of varying the base and the metal:ligand ratio (*Table 4.10*).

$Y(AcO)_3$: $H_4\mathbf{L}''$: KOH : H2O	pH	Phase
1.5 : 1.5 : 0.0 : 800	5	Y-$H_4\mathbf{L}''$U1 & Y-$H_4\mathbf{L}''$U2
1.5 : 1.5 : 1.5 : 800	4	Amorphous
1.5 : 1.5 : 3.0 : 800	4	Amorphous
1.5 : 1.5 : 4.0 : 800	6	Amorphous
2.0 : 1.5 : 0.0 : 800	5	Y-$H_4\mathbf{L}''$U1
2.0 : 1.5 : 3.0 : 800	5	Amorphous

Table 4.10: Series of HT reactions of $Y(AcO)_3$ with $H_4\mathbf{L}''$, investigating the effect of varying the base and metal:ligand ratio. Reactions were performed in 3 ml PTFE liners in a 24 reactor block, using 1.5 ml H_2O. Reactions were heated to 190°C for 24 hours.

Following initial HT reactions, the 2.0 : 1.5 : 0 : 800 ($Y(AcO)_3 : H_4\mathbf{L}'' : KOH : H_2O$), which produced a phase pure unknown phase (Y-$H_4\mathbf{L}''$U1), was scaled up to a 7.5 ml reaction and found to yield the same phase (*Table 4.11*). Additional reactions probed the effect of varying the concentration and reaction temperature. Higher temperatures and more dilute reactions were found to strongly favour the crystallisation of Y-$H_4\mathbf{L}''$U1 at 2.0 : 1.5 and 1.0 : 1.5 ($Y(AcO)_3 : H_4\mathbf{L}''$) reaction ratio, the latter ratio producing the most crystalline sample. At higher concentration a third unknown phase co-crystallised with Y-$H_4\mathbf{L}''$U1.

4.6.1 Characterisation of Structure Y-H_4L''U1

The composition of structure Y-$H_4\mathbf{L}''$U1 was determined by a combination of TGA and elemental analysis. TGA of Y-$H_4\mathbf{L}''$U1 shows two weight loss events below 100°C, attributed to the dehydration of the structure. The first (20–46°C — 12.11 wt.%) corresponds to the loss of $1.59H_2O$ molecules per Y cation (assuming final solid Y_2O_3), whilst the second smaller step (73–86°C — 2.48 wt.%) is assigned to the loss of a further $0.33H_2O$ molecules per Y cation (*Fig. 4.30*). Above

$Y(AcO)_3$: $H_4\mathbf{L}''$: H2O	pH	Temp. / °C	Time / hrs	Phase
2.0 : 1.5 : 1000	6	190	17	Y-$H_4\mathbf{L}''$U1
2.0 : 1.5 : 1000	5	160	21	Y-$H_4\mathbf{L}''$U1
2.0 : 1.5 : 1000	5	220	21	Y-$H_4\mathbf{L}''$U1
2.0 : 1.5 : 500	5	190	71	Y-$H_4\mathbf{L}''$U1 & Y-$H_4\mathbf{L}''$U3
2.0 : 1.5 : 1000	5	220	71	Y-$H_4\mathbf{L}''$U1
1.0 : 1.5 : 1000	5	190	71	Y-$H_4\mathbf{L}''$U1

Table 4.11: Selected reactions of $Y(AcO)_3$ with $H_4\mathbf{L}''$, showing the optimised synthesis of Y-$H_4\mathbf{L}''$U1, following from the HT array. Reactions were performed in 15 ml PTFE lined autoclaves, using 7.5 ml H_2O.

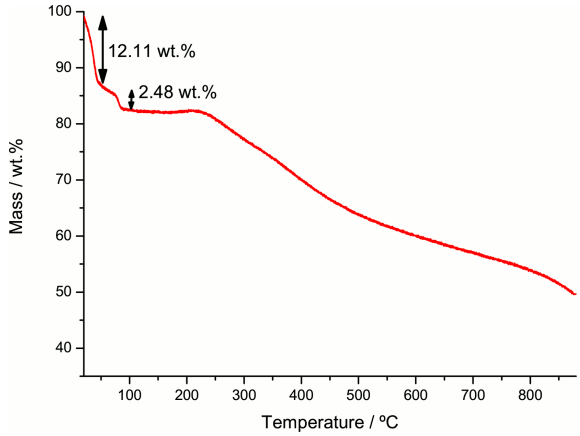

Figure 4.30: TGA of Y-$H_4\mathbf{L}''$U1 from 20–900°C under dry air showing principal weight loss events.

250°C a further series of weight losses occurs, attributed to the collapse of the framework. The two step weight loss below 100°C may indicate the presence of both physisorbed and chemisorbed water molecules in the structure. Alternatively, the second step might be attributed to a dehydroxylation of the structure. Further structural information is necessary to determine which process is occurring. From the initial gel composition used to prepare the most crystalline Y-$H_4\mathbf{L}''$U1 (1 : 1.5, $Y(AcO)_3$: $H_4\mathbf{L}''$) and considering the compositions of other structures in this series ($Y_2(\mathbf{L}H_2)_3$ and STA-13(Y)) a composition of $Y_2(\mathbf{L}''H_2)_3 \cdot 3.5H_2O$ is proposed for Y-$H_4\mathbf{L}''$U1. Elemental analysis gave reasonable agreement with the proposed structure and the experimentally determined values: expected — C 25.06 %, H 5.4 %, N 7.3 %; found — C 22.9 %, H 5.7 %, N 6.5 %. The relatively large difference between the expected and determined C and N composition may indicate that an amorphous second phase, with low organic content (e.g. Y_2O_3) is present. EDX spectra would confirm this hypothesis.

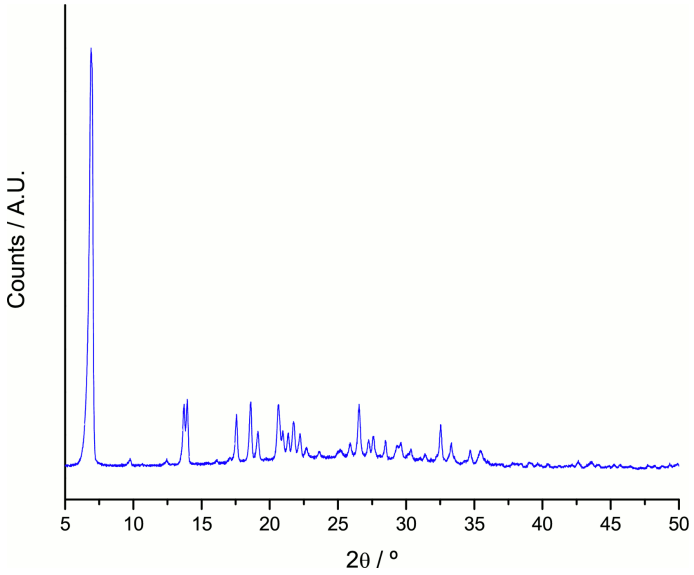

Figure 4.31: Powder X-ray diffraction pattern (Cu K_α) for the unknown phase Y-H_4**L**″U1, formed from reaction of $Y(AcO)_3$ and H_4**L**″.

4.6.2 Structure of As-Prepared Structure Y-H_4L″U1

Laboratory powder X-ray diffraction data (Cu K_α) were collected on a phase pure sample of Y-H_4**L**″U1 and successfully indexed (*Fig. 4.31*). Data were collected in a Debye-Scherrer at 298 K. The data was indexed using the TREOR routine of the EXPO2009 package[153, 148] with a monoclinic unit cell (a = 13.010(10) Å, b = 12.738(9) Å, c = 5.555(5) Å, β = 92.44(13)°, V = 919(5) Å^3, F.O.M. M_{20} = 12).[154] Data quality was too low to permit further analysis (e.g. by Le Bail analysis or Rietveld refinement).

4.7 Reactions of Other Rare Earth Trivalent Cations

Of the $Y^{(III)}$ bisphosphonates prepared, only STA-13(Y) is permanently porous, whilst STA-13(Sc),[184] the only other known form of STA-13, has been reported with variable porosity.[184] Permanently porous STA-13(Sc) is of interest as $Sc^{(III)}$ is a much lighter cation than $Y^{(III)}$ and so a greater weight-for-weight uptake would be expected for the material. Efforts have also been made to determine the range of cation radius over which the STA-13 network forms, to limit the search space for finding permanently porous STA-13 materials made with other trivalent cations. Reactions of Sc with the linker $H_4\mathbf{L}$ have also been investigated to determine whether an Sc form of $Y_2(\mathbf{L}H_2)_3$ is prepared or another (porous) phase (e.g. MIL-91 — see *Section 4.10*).

4.7.1 Reaction of $Sc^{(III)}$ with $H_4\mathbf{L}$

Hydrothermal reactions of $ScCl_3$ and $Sc(piv)_3$ (see *Appendix Section A.3* for details of synthesis) yielded at least two unknown products, though it was only possible to prepare one of them phase pure (*Table 4.12*).

Reaction	ScX_3 : $H_4\mathbf{L}$: KOH : H_2O	pH	Product
MTW812	1.0 : 1.0 : 2.85 : 1000	1	Amorphous
MTW813	1.0 : 1.0 : 0 : 1000	1	Mixed Unknowns
MTW814	1.0 : 1.0 : 2.0 : 1000	6	Sc-$H_4\mathbf{L}$U1

Table 4.12: Selected 7.5 ml scale reactions of ScX_3 (metal source used: MTW812 — $ScCl_3$; MTW813 & MTW814 — $Sc(piv)_3$). All reactions were heated at 190°C for 18 hrs.

A phase pure sample of Sc-$H_4\mathbf{L}$U1 was obtained from a gel of composition 1.0 : 1.0 : 2.0 : 1000 ($Sc(piv)_3$: $H_4\mathbf{L}$: KOH : H_2O). Sc-$H_4\mathbf{L}$U1 was characterised by both TGA and EDX analyses. The TGA plot of Sc-$H_4\mathbf{L}$U1 shows a single weight loss at low temperature (20–194°C — 5.00 wt.%) which is assigned to the loss of $0.78H_2O$ per $Sc^{(III)}$ cation (assuming final solid is Sc_2O_3) (*Fig. 4.32*). Above 260°C a further series of weight losses occur, assigned to the collapse of the framework. The EDX spectrum of Sc-$H_4\mathbf{L}$U1 gave a Sc : P ratio of 1.0 : 0.80 (*Fig. 4.33*), and also indicated the presence of variable amounts of both K and Br (from the base and the ligand respectively). The Sc : P ratio suggests that Sc-$H_4\mathbf{L}$U1 is a Sc rich material. However, the Sc source ($Sc(piv)_3$) is highly insoluble and therefore it is very likely that unreacted $Sc(piv)_3$ is present in the sample.

Laboratory powder X-ray diffraction data (Fe K_α) were collected on a sample of Sc-$H_4\mathbf{L}$U1 in a transmission geometry at 298 K. The data were indexed

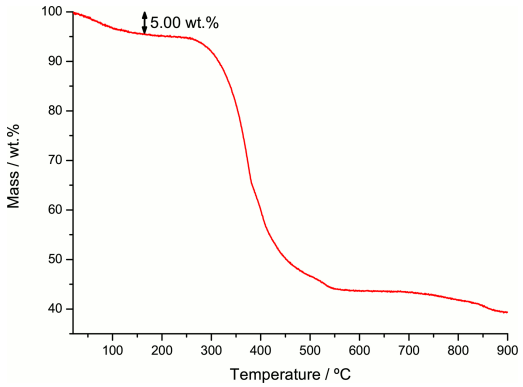

Figure 4.32: TGA of Sc-H_4**L**U1 from 25–900°C under dry air showing principal weight loss events.

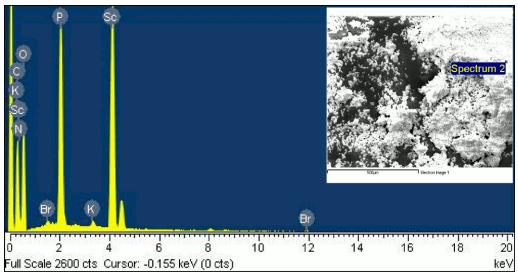

Figure 4.33: EDX spectrum of Sc-H_4**L**U1 indicating elements found. Y:P ratio of **1.0 : 0.80**. Inset shows the area analysed.

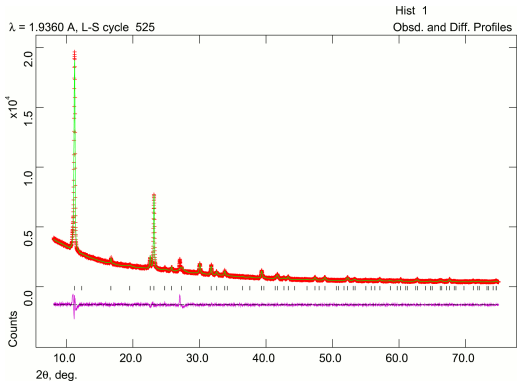

Figure 4.34: Final Le Bail fit of Sc-H_4**L**U1 with $R_{wp} = 0.0451$.

using TREOR[153] (F.O.M. $M_{12} = 92$)[154] with a metrically trigonal or hexagonal unit cell. This was then fitted using the Le Bail routines of the GSAS suite of programs.[155, 156, 157] Le Bail fit gave a unit cell with parameters $a = 11.3951(8)$ Å, $c = 9.0053(6)$ Å, $V = 1012.66(10)$ Å^3, with a final Le Bail fit of $R_{wp} = 0.0451$ (*Fig. 4.34*).

The c parameter of the unit cell is very similar to that of Zr_2H_4**L**$_3$·$9H_2O$ reported by Taddei *et al.*[101], whilst the a parameter is $\frac{1}{\sqrt{3}}$ of this structure. Using the model Taddei *et al.* a starting point, a model containing Sc, P and O sites was constructed in space group $P\bar{3}$ (*Fig. 4.35a*). The simulated powder X-ray diffraction pattern for this model and the experimental structure show reasonable agreement (*Fig. 4.35b*), suggesting this to be a good candidate starting point. Interestingly, due to the change in symmetry, the structure of this model and that of Taddei's Zr phase differ in the arrangement of the chains. Whereas neighbouring chains in Taddei's phase are offset from one another in the c direction, the primitive symmetry of the Sc model means that all chains are symmetry equivalent, so the connectivity of the chains will

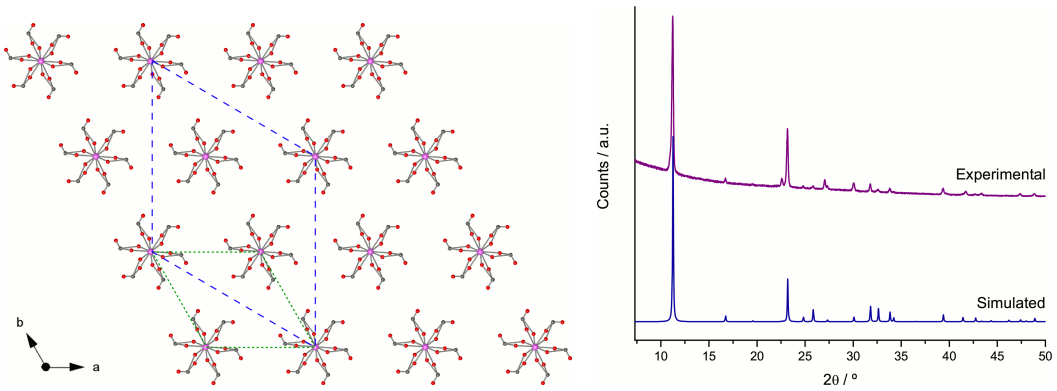

(a) Model viewed along [0 0 1] direction. (b) Powder X-ray diffraction patterns.

Figure 4.35: View of the model derived from $Zr_2H_4\mathbf{L}_3{\cdot}9H_2O$[101] in $P\bar{3}$, viewed along the [0 0 1] direction (*left*). Dashed lines show unit cells of $Zr_2H_4\mathbf{L}_3{\cdot}9H_2O$ (blue) and Sc-H_4**L**U1 (green). A comparison of simulated and experimental powder X-ray diffraction patterns is also shown of the phase (*right*).

also differ slightly. Channels within this material are, however, still likely to be very narrow (∼2–3 Å) and therefore this material is likely to show minimal porosity.

4.7.2 Synthesis of STA-13(Sc)

Previous syntheses of STA-13(Sc) used Sc_2O_3 as the metal source[184] Using a gel of composition 1.0 : 1.5 : 1000 (Sc_2O_3 : $H_4\mathbf{L}'$(racemic) : H_2O), heated at 190°C for 48 hours, a white solid was obtained. Powder X-ray diffraction showed that this was mostly STA-13(Sc) with an impurity of Sc_2O_3. Porosimetry measurements on this material indicate that it has a much lower permanent porosity to N_2 at 77 K than STA-13(Y) (STA-13(Sc): $\sim$ 0.5 mmol g^{-1}; STA-13(Y): $\sim$ 3.0 mmol g^{-1}) and therefore the use of other Sc sources was investigated (summarised in *Table 4.13*). $Sc(piv)_3$ was used rather than $Sc(AcO)_3$ as it may be readily synthesised in the laboratory from relatively inexpensive reagents (see *Appendix Section A.3* for details of preparation). piv^- is also expected to have similar counterion properties to AcO^-. The sample of structure STA-13(Sc) with the greatest porosity to N_2 at 77 K was prepared using $Sc(piv)_3$ ($\sim$ 0.5 mmol g^{-1}), though this is still considerably lower than the best sample of STA-13(Y). It might be possible to improve the porosity of structure STA-13(Sc) by sonication or by tuning the reaction times and temperature. (Full details of porosity measurements made on structure STA-13(Sc) are given in *Section 4.8*).

To determine the range of cation radius over which the STA-13 network will crystallise, a combined approach of high-throughput (HT) and 20 ml scale syntheses

Sc Source	Product	Porosity / mmol g^{-1}
Sc_2O_3	STA-13(Sc) & Sc_2O_3	0.42
$Sc(NO_3)_2$	STA-13(Sc)	0.43
$ScCl_3$	Amorphous	-
$Sc(piv)_3$	STA-13(Sc)	0.50

Table 4.13: Effect of changing the metal source on the porosity of samples of structure STA-13(Sc). All samples were prepared from gels of composition 1.0 : 1.5 : 1000 (Sc source : $H_4\mathbf{L}'$(racemic) : H_2O) heated at 190°C for 20 hours.

Metal Source	Cation Radius[186] / pm	M : $H_4\mathbf{L}'$: H_2O	Temp. / °C	Time
$Yb(AcO)_3$	86.8	1.0 : 1.5 : 1000	190	18 hrs
$Dy(AcO)_3$	91.2	1.0 : 1.5 : 1000	190	21 hrs
$Gd(AcO)_3$	93.8	1.0 : 1.5 : 1000	220	23 hrs

Table 4.14: Scaled-up (20 ml scale) synthesis of heavy lanthanide cation containing STA-13 networks.

were used. HT reactions of $Yb(AcO)_3$, $HoCl_3$ and $Gd(AcO)_3$ with $H_4\mathbf{L}'$ indicate that the STA-13 network is stable over the range of the larger radius lanthanide cations. Larger radius cations have been shown to form one of two other networks,[111] and therefore Gd^{3+} (93.8 pm)[186] represents the upper limit of cation radius for which STA-13 will crystallise. To investigate the lower limit of cation radius, HT reactions using $AlCl_3$ and $FeCl_3$ with $H_4\mathbf{L}'$ were performed. Rather than forming STA-13, these reactions yielded MIL-91[108] (MIL-91(Fe) — with $H_4\mathbf{L}'$ or $H_4\mathbf{L}$— is unknown and will be discussed in greater depth in *Section 4.10*). As MIL-91 crystallises with the small radius cations (Al^{3+}: 53.5 pm; Fe^{3+}: 64.5 pm)[186] Sc^{3+} (74.5 pm) represents the smallest cation for which the STA-13 network will crystallise. To investigate the porosity of the newly prepared STA-13 materials, selected reactions were scaled-up to the 20 ml scale and, at this stage, the reaction of $Dy(AcO)_3$ with $H_4\mathbf{L}'$ was also shown to form STA-13 (*Table 4.14*). In^{3+} (80.0 pm) was also investigated as a framework-forming cation for STA-13; however, syntheses yielded MIL-91. The reason for the crystallisation of MIL-91 is unclear.

The unit cell dimensions of the new forms of STA-13 were determined from laboratory powder X-ray diffraction (*Fig. 4.36*) and were found to increase with increasing cation radius (*Table 4.15*). The porosity of each form was also analysed by N_2 adsorption at 77 K. As sonicated samples of structure STA-13(Y) were found to yield more porous material than the as-prepared samples, all of these new materials were also sonicated prior to activation. Samples were all activated at 120°C for three hours at reduced pressure (1×10^{-4} Torr).

STA-13(Dy) and 1 were found to be significantly less porous to N_2 at 77 K,

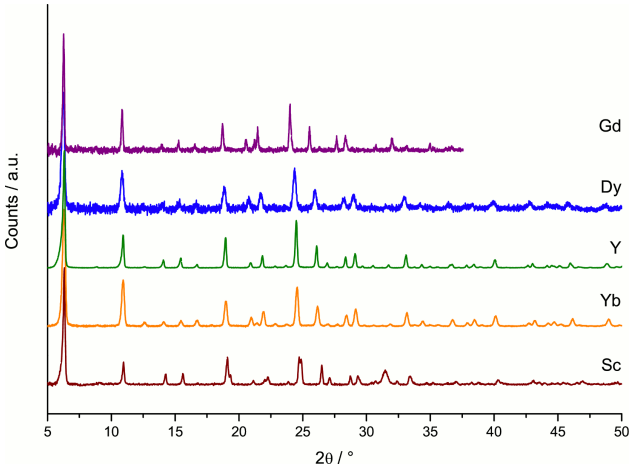

Figure 4.36: Laboratory powder diffraction patterns (Cu K_α) of the known forms of STA-13: Sc (maroon); Yb (orange); Y (green); Dy (blue); Gd (purple).

	Sc	Yb	Y	Dy	Gd
Cation Radius[186] / pm	74.5	86.8	90.0	91.2	93.8
Space Group	$P\bar{3}$	$P\bar{3}$	$P\bar{3}$	$P\bar{3}$	$P\bar{3}$
a / Å	16.05147(13)	16.1808(7)	16.1895(3)	16.224(2)	16.2420(16)
c / Å	9.69167(13)	9.9291(6)	10.00355(16)	10.0215(15)	10.0457(10)
V / Å^3	2162.51(3)	2251.35(14)	2270.64(4)	2284.5(5)	2295.0(4)

Table 4.15: Unit cell parameters for all of the known forms of STA-13. Values for Sc and Y forms have been determined by Rietveld refinement,[147] whereas cells for other forms were determined by Le Bail fitting.[155]

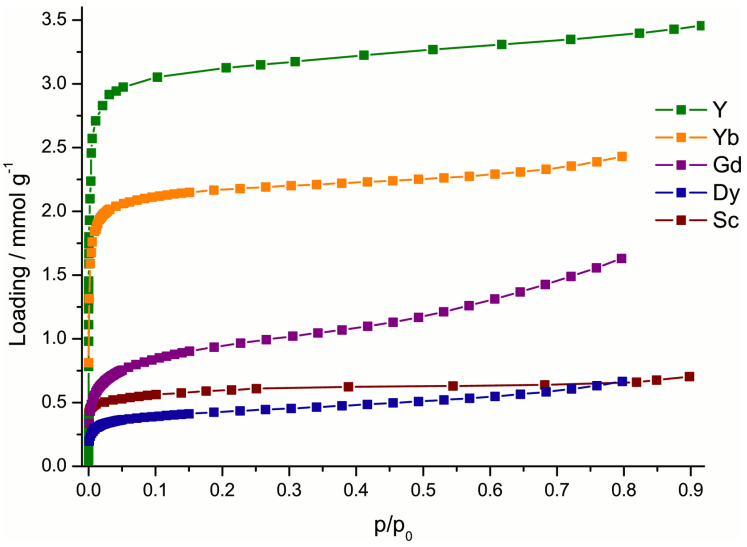

Figure 4.37: Comparison of the N_2 adsorption isotherm (77 K) for different forms of STA-13: Sc (maroon); Yb (orange); Y (green); Dy (blue); Gd (purple).

whereas STA-13(Yb) was found to have a similar porosity to STA-13(Y) (*Fig. 4.37*). The porosity of STA-13(Yb) will be investigated further and compared to the porosity of STA-13(Y) to a range of adsorbates (*Section 4.8*).

4.8 Porosity in STA-13

The adsorptive properties of activated samples of STA-13(Y) and STA-13(Yb) have been investigated by N_2 adsorption at 77 K, using a volumetric apparatus, and CH_4 adsorption at 196 K and 273 K using a gravimetric apparatus. The porosity of STA-13(Y) to CO_2 at 196 K using a gravimetric apparatus was investigated. Adsorption of CO_2 at 273 K was also investigated using a volumetric high-pressure apparatus. C_2H_6, C_3H_8 and C_4H_{10} (*n*-butane) adsorption at 273 K was also investigated using a high-pressure volumetric apparatus. Both STA-13(Y) and STA-13(Yb) were activated (*i.e.* dehydrated) for adsorption by heating to 120°C for three hours at reduced pressure (1×10^{-4} Torr). Simulated adsorption isotherms have been calculated, using the MUSIC code[171] for the adsorption of N_2 at 77 K and CH_4 at 196 K and 273 K in STA-13(Y) (*Section 4.8.2*).

4.8.1 Experimental Adsorption Isotherms for STA-13(Y) and STA-13(Yb)

Structures STA-13(Y) and STA-13(Yb) both show porosity to N_2 at 77 K (*Fig. 4.38*), exhibiting Type I isotherms typical of microporous materials.[163] No hysteresis is observed for STA-13(Y) and a slight hysteresis is observed for STA-13(Yb), probably due to the problems equilibrating the sample (a common problem of microporous unidirectional channel materials). Lack of hysteresis indicates reversibility of adsorption. Qualitatively, STA-13(Y) is more porous to N_2 than STA-13(Yb) and this result is also shown by the maximum micropore loading calculated from Dubinin-Radushkevich (D-R) analysis (*Table 4.16*). Similarly for BET surface areas (calculated using the consistency criteria described by Bae *et al.*)[175], STA-13(Y) shows a significantly larger surface area than STA-13(Yb) (*Table 4.16*). As both cations have a similar ionic radius (Yb: 86.8 pm; Y: 90 pm)[186] similar values for both the surface area and the pore volume would be expected. The lower maximum loading and surface area of STA-13(Yb) suggests a high degree of pore blocking in the material or the presence of a relatively large amount of a non-porous (amorphous) second phase.

Both materials are also porous to CH_4 at 196 K and 273 K showing Type I isotherms in each case (only the adsorption isotherm was collected at 273 K due

	STA-13(Y)	STA-13(Yb)
BET Surface Area / $m^2\ g^{-1}$	279(2)[a]	194.8(5)[b]
N_0 (D-R) / mmol g^{-1}	3.187(5)	2.202(1)
Pore Volume / $cm^3\ g^{-1}$	0.11	0.07

[a] $\frac{p}{p_0}$ linear range: 0.001–0.02
[b] $\frac{p}{p_0}$ linear range: 0.002–0.02

Table 4.16: Comparison of the BET surface area (calculated following the method of Bae *et al.*[175]) and maximum micropore loading (N_0) and pore volume (calculated using the Dubinin-Radushkevitch equation[163]) of STA-13(Y) and STA-13(Yb).

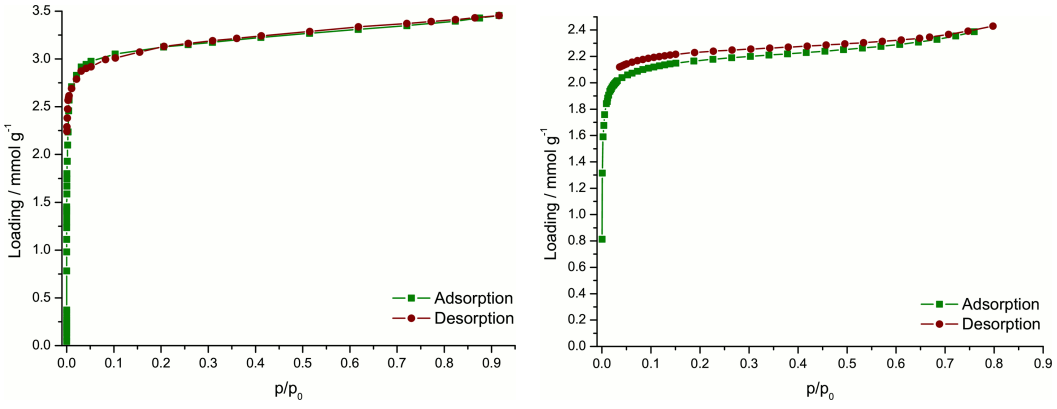

(a) STA-13(Y) (b) STA-13(Yb)

Figure 4.38: N_2 isotherms at 77 K for STA-13(Y) (*left*) and STA-13(Yb) (*right*). Isotherms are Type I. Adsorption — green; Desorption — red.

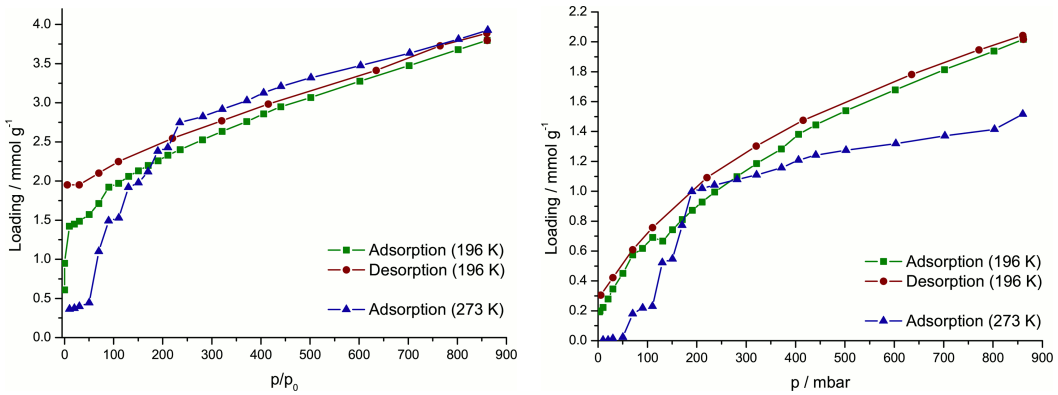

(a) STA-13(Y) (b) STA-13(Yb)

Figure 4.39: CH_4 isotherms at 196 K (red — adsorption; green — desorption) and 273 K (blue —adsorption) for STA-13(Y) (*left*) and STA-13(Yb) (*right*). Isotherms are Type I. The steps in the isotherm are due to artifacts of the experimental method. Only adsorption data were collected at 273 K.

to experimental difficulties). Loading of CH_4 at 196 K in STA-13(Y) increases steeply from 0–10 mbar, due to the initial micropore filling, followed by a shallower loading. This second loading is due to intercrystalline adsorption. A slight hysteresis loop is observed on desorption, attributed to an experimental artifact. At 273 K uptake increases more slowly in the range 0–170 mbar than the 196 K data, due to the higher thermal energy of the system overcoming the adsorbate-framework interactions. Above 170 mbar a shallow rising limb continues to the end of the experiment, attributed again to intercrystalline adsorption. Loading at 200 mbar at both temperatures is similar to that obtained with N_2, indicating that CH_4 is accessing a similar amount of pore space. STA-13(Yb) shows a more gradual loading of CH_4 increasing and becoming less rapid across the entire range of the isotherm at 196 K. No hysteresis was observed on desorption. Adsorption at 273 K shows a more well defined Type I profile, with loading complete at 190 mbar and a slight rising limb due to intercrystalline adsorption. The overall loadings in STA-13(Yb) are again lower than in STA-13(Y), as with N_2, providing further evidence of pore blocking in STA-13(Yb).

STA-13(Y) was also found to be porous to light alkanes (C_2H_6, C_3H_8 and C_4H_{10} (*n*-butane)) at 273 K using a high-pressure volumetric apparatus. Isotherms of each adsorbate showed a Type I profile (*Fig. 4.40*).[163] The maximum uptakes of each adsorbate decrease approximately with increasing molecular volume. Uptakes are slightly lower than expected by comparison with the maximum uptake of CH_4, though this is probably due to sample preparation for the high-pressure adsorption experiment, which required the sample to be pelletised.

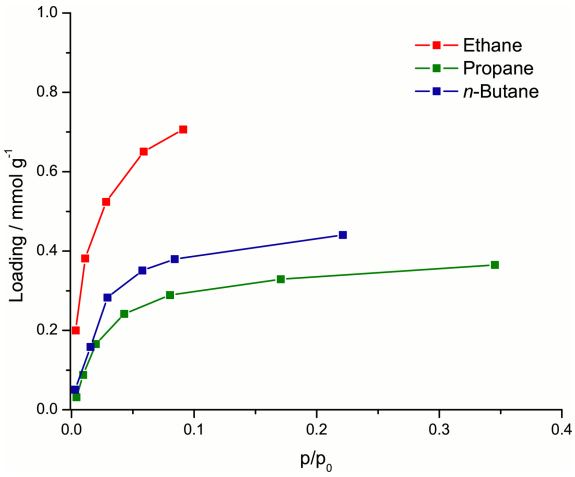

Figure 4.40: Adsorption isotherms of light alkanes (C_2H_6 — red; C_3H_8 — green; and C_4H_{10} — blue) in STA-13(Y).

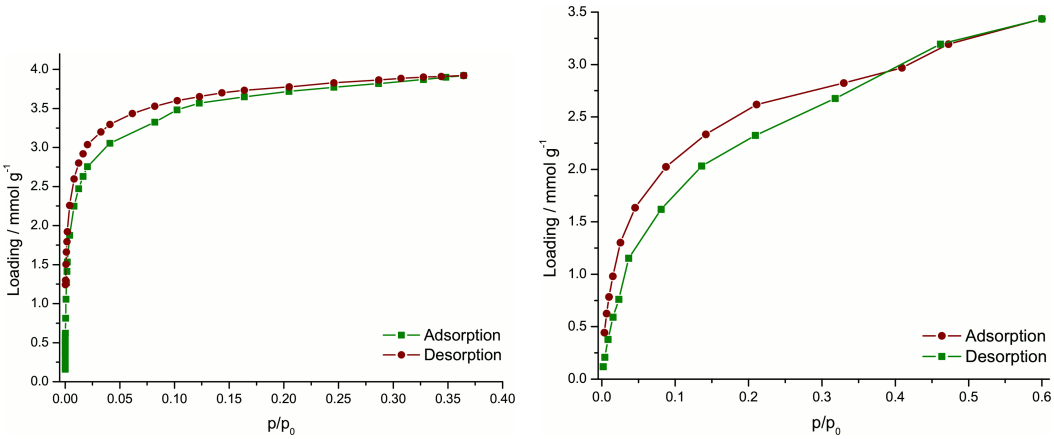

Figure 4.41: Isotherms for the adsorption of CO_2 by STA-13(Y) measured at 196 K using a gravimetric instrument (*left*) and at 273 K, using a volumetric high-pressure instrument (*right*). Isotherms have a Type I profile. Adsorption — green; Desorption — red.

	STA-13(Y)
N_0 (D-R) / mmol g^{-1}	3.978(7)
Pore Volume / cm^3 g^{-1}	0.14

Table 4.17: The maximum micropore loading of CO_2 (N_0) and pore volume (calculated using 196 K data with the Dubinin-Radushkevitch equation[163]) for STA-13(Y).

STA-13(Y) is also porous to CO_2 at 196 K and 273 K, with a maximum loading at 196 K of 3.978 mmol g^{-1} (calculated by the D-R equation[163]), higher than that of N_2. The isotherm is again Type I, as expected for a microporous material (*Fig. 4.41a*). Adsorption of CO_2 at 273 K show a slightly lower uptake with maximum at 3.43 mmol g^{-1} (*Fig. 4.41b*). Both isotherms show a slight hysteresis, the origin of which is not clear as the structure is not apparently flexible and does not seem to possess sites which would adsorb CO_2 very strongly at high temperature. This could be an experimental artifact originating from the long equilibration times for the material.

4.8.2 Simulated Adsorption of N_2 and CH_4 in STA-13(Y)

Adsorption isotherms for of N_2 at 77 K and CH_4 at 196 K and 273 K in STA-13(Y) were simulated using the MUSIC simulation code.[171] Grand Canonical Monte Carlo (GCMC) simulations modelled only the van der Waals interactions, as neither adsorbate is strongly polar, using Lennard-Jones potentials. Parameters for the framework and for adsorbate N_2 were taken from the UFF force field[167], whilst the potential for adsorbate CH_4 was taken from the TraPPE force field.[170]

The simulated N_2 adsorption isotherm has a Type I profile very similar to the experimental isotherm (*Fig. 4.42*).[163] However, the loading of the simulated material is significantly higher than the experimental sample (at $\frac{p}{p_0} = 0.10$: simulated — $\sim$ 4.0 mmol g^{-1}; experimental — $\sim$ 3.1 mmol g^{-1}). Similarly the BET surface area and maximum pore loading (D-R N_0) for the simulated data are significantly higher than the experimental values (*Table 4.18*). The overpredicted uptake of the material indicates either significant pore blocking of the sample or the presence of a non-porous (amorphous) second phase. Pore blocking is not taken into account by the simulation as the simulated sample is a perfect crystal and therefore adsorbates are able to access the complete pore network.

	Experimental	Simulated
BET Surface Area / m^2 g^{-1}	279(2)[a]	385.6(5)[b]
N_0 (D-R) / mmol g^{-1}	3.187(5)	4.086(7)
Pore Volume / cm^3 g^{-1}	0.11	0.14

[a] $\frac{p}{p_0}$ linear range: 0.001–0.02
[b] $\frac{p}{p_0}$ linear range: 1×10^{-5}–0.001

Table 4.18: Comparison of the BET surface area (calculated following the method of Bae *et al.*[175]) and maximum micropore loading (N_0) and pore volume (calculated using the Dubinin-Radushkevitch equation[163]) of experimental and simulated samples of STA-13(Yb).

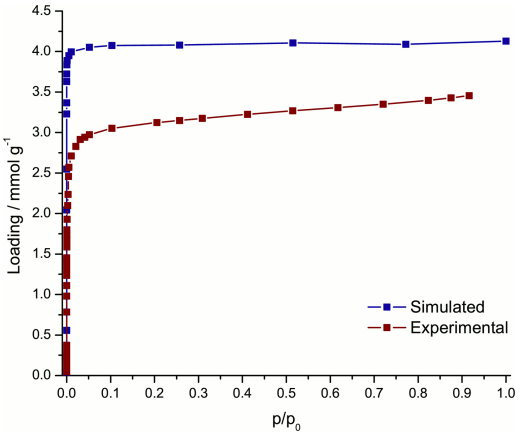

Figure 4.42: Experimental and simulated N_2 adsorption isotherms at 77 K. Both isotherms shown have a Type I profile.

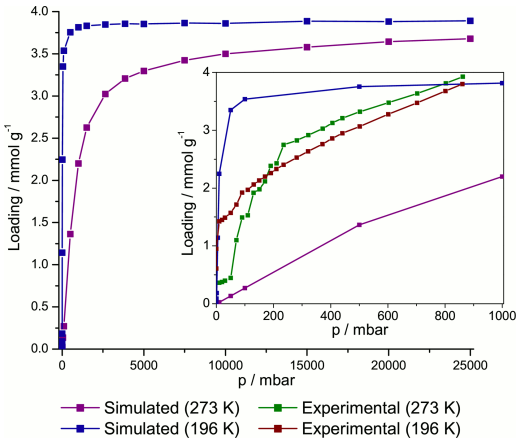

Figure 4.43: Simulated adsorption isotherms for adsorption of CH_4 at 196 K (blue) and 273 K (purple). Inset shows 0–1000 mbar region with the experimentally determined 196 K (red) and 273 K (green) isotherms marked.

Simulated isotherms for CH_4 over the range 0–25 bar are also both Type I.[163] Adsorption at 196 K rapidly reaches a maximum filling close to that observed for N_2 simulations (*Fig. 4.43*). The 273 K isotherm, by contrast, fills more slowly and even at 25 bar the pores are continuing to fill, resulting from the increased thermal energy overcoming the weak physisorption interaction between adsorbates and framework. The experimental isotherms are significantly different from the simulated ones at both temperatures. The initial loading of the experimental 196 K isotherm is similar to the simulated isotherm up to 10 mbar, though above this pressure experimental and simulated data diverge. This may indicate a high degree of pore blocking in the experimental sample. The simulated and experimental adsorption isotherms at 273 K are very different. Loading in the simulated data increases much more slowly than the experimental data. This could indicate that the interactions between the framework and the adsorbate have been significantly underpredicted. The origin of the discrepancies in both 196 K and 273 K isotherms is not understood.

4.9 Reactions of $Fe^{(III)}$ with $H_4\mathbf{L}$

Reaction of $FeCl_3$ with $H_4\mathbf{L}$ forms a structure with the MIL-91 network,[108] $Fe(OH)(H_4\mathbf{L}H_2)\cdot 2.6H_2O$ labelled MIL-91(Fe). Reactions using $H_4\mathbf{L}'$ in place of $H_4\mathbf{L}$yielded an isostructural phase (see *Section 4.7*). High-throughput (HT) syntheses investigated the reactions of $H_4\mathbf{L}$ with $FeCl_3$, $FeCl_2$, $Fe(AcO)_2$ and $Fe^{(III)}(AcO)$[1]. Both $FeCl_3$ and $Fe^{(III)}(AcO)$ produce structure MIL-91(Fe) phase pure in HT syntheses, whereas $FeCl_2$ and $Fe(AcO)_2$ produce mixtures of STA-12(Fe) (see *Section 5.3.1*) and $Fe(\mathbf{L}H_2)\cdot 1.5H_2O$[103, 105]. It was necessary to add base to syntheses with $FeCl_3$, which raised the pH slightly to 2, in order to obtain phase pure samples, whereas addition of base to $Fe^{(III)}(AcO)$ caused co-crystallisation of MIL-91(Fe) with STA-12(Fe). HT syntheses were scaled-up to 7.5 ml scale reactions, which allowed sufficient MIL-91(Fe) to be prepared for analysis (*Table 4.19*). The most crystalline samples of structure MIL-91(Fe) were obtained from gels of composition 1.0 : 1.0 : 2.5 : 1000 ($FeCl_3$: $H_4\mathbf{L}$: KOH : H_2O) or 0.23 : 1.0 : 1000 ($Fe^{(III)}(AcO)$:$H_4\mathbf{L}$:H_2O) heated at 160°C for 18 hours.

M : $H_4\mathbf{L}$: KOH : H_2O	pH	Temp. / °C	Time / hrs	Phase
M = $FeCl_3$				
1.0 : 1.5 : 2.5 : 500	2	190	18	Unknown Phase
1.0 : 1.0 : 2.0 : 1500	2	190	23	MIL-91(Fe)
1.0 : 1.0 : 2.5 : 1000	2	190	72	MIL-91(Fe)
1.0 : 1.0 : 2.5 : 1000	2	160	19	MIL-91(Fe)
M = $Fe^{(III)}(AcO)$				
0.33 : 1.5 : 0.0 : 500	2	190	18	MIL-91(Fe) & $H_4\mathbf{L}$
0.13 : 1.5 : 0.0 : 1000	1	160	20	MIL-91(Fe) & $H_4\mathbf{L}$
0.18 : 1.0 : 0.0 : 1000	2	160	18	MIL-91(Fe)
0.23 : 1.0 : 0.0 : 1000	2	160	20	MIL-91(Fe)

Table 4.19: Selected 7.5 ml scale syntheses used to prepare structure MIL-91(Fe).

Prior to HT experiments, a series of probe reactions with $Fe^{(III)}(AcO)$ were performed, using an $Fe^{(III)}(AcO)$: $H_4\mathbf{L}$ ratio of 1 : 1. These reactions produced a material related to the tetrameric Co cluster phase reported by Groves *et al.*[105] This new Fe material is also thought to contain tetramers of Fe cations and therefore is referred to as Fe-Tet.. Further syntheses showed that Fe-Tet. could be prepared over a range of stoichiometries and also with the ligand $H_4\mathbf{L}'$, forming a direct analogue of the previously reported Co structure. Reaction ratios of 1.33 : 1.0 : 500 ($Fe^{(III)}(AcO)$: $H_4\mathbf{L}$: H_2O) heated at 190°C for 70 hrs gave samples with good

[1]Exact composition unknown, but thought to be trimeric $Fe_3O(AcO)_6$ based clusters, *cf.* Orgel[187] or Figgis & Robertson[188], with AcO^- counter ions

$Fe^{(III)}(AcO) : H_4\mathbf{L} : H_2O$	pH	Phase
1.0 : 1.0 : 500	3	Fe-Tet.
1.33 : 1.0 : 500	3	Fe-Tet.
0.89 : 1.0 : 500	3	Fe-Tet.
1.0 : 1.0 : 250	2	Fe-Tet.
1.0 : 1.0[a] : 500	3	Fe-Tet.-Me

[a] $H_4\mathbf{L}'$ used in place of $H_4\mathbf{L}$

Table 4.20: Selected 7.5 ml scale reactions producing Fe-Tet.. All reactions were heated at 190°C for 70 hrs.

crystallinity (*Table 4.20*), whilst highly crystalline Fe-Tet. could be prepared through addition of NaAcO (1.0 : 1.0 : 2.0 : 500 — $Fe^{(III)}(AcO) : H_4\mathbf{L} : NaAcO : H_2O$).

4.10 Fe(OH)($\mathbf{LH_2}$)·2.6$\mathbf{H_2O}$ — MIL-91(Fe)

4.10.1 Characterisation of Structure MIL-91(Fe)

The composition of a sample of structure MIL-91(Fe) was determined by TGA, EDX and elemental analyses. TGA shows two weight loss events at less than 300°C (*Fig. 4.44*). The first at 25–144°C (11.55 wt.%) corresponds to the loss of ∼ 2.6 molecules of physisorbed water from the structure. Following the end of this weight loss, there is a short plateau (∼20°C) indicating the dehydrated from of MIL-91(Fe). With further heating a second weight loss 162–208°C (2.73 wt.%) occurs, which is assigned, by analogy to MIL-91(Al), as dehydroxylation of the Fe-(OH)-Fe chains (*vide infra*).[108] Above 280°C approximately three further weight losses are observed, assigned to the collapse of the framework.

EDX analysis gave an Fe : P ratio of 1.0 : 1.65. This is slightly low compared with the expected ratio of 1 : 2 (for the literature metal:ligand ratio of 1 : 1) and may indicate the presence of a second phase in the sample. SEM micrographs of the sample analysed by EDX also show that MIL-91(Fe) crystallises in clusters of large needle crystals (100 × 10 μm — *Fig. 4.45*). From the EDX spectra and TGA data, a composition of Fe(OH)($\mathbf{L}H_2$)·2.6H_2O was proposed for MIL-91(Fe). Elemental analysis showed good agreement between this proposed composition and the experimental values: expected — C 17.3 %, H 5.6 %, N 6.7 %; found — C 17.6 %, H 5.4 %, N 6.7 %.

The structure of MIL-91(Al) contains charge balancing μ_2-OH groups linking the metal centres to form M-(OH)-M chains.[108] Similar hydroxide groups would be expected in structure MIL-91(Fe) if Fe is present as Fe^{3+}. Fe^{3+} is indicated by

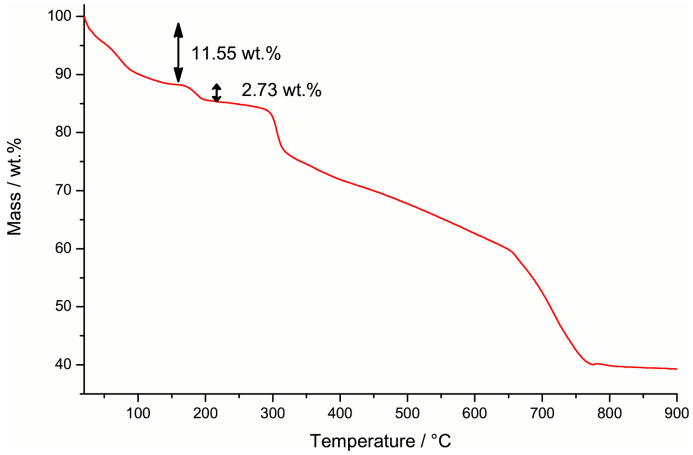

Figure 4.44: TGA of MIL-91(Fe) from 25–900°C under dry air showing principal weight loss events.

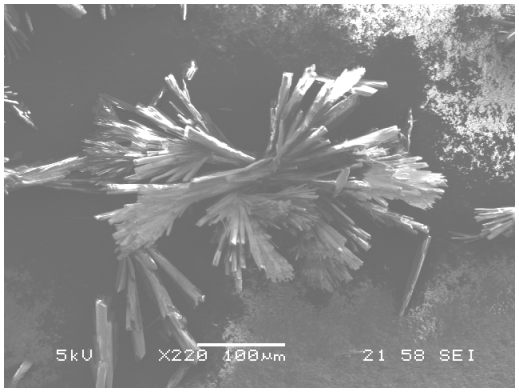

Figure 4.45: SEM micrograph showing crystals of MIL-91(Fe). Crystals have dimensions approx. 100 × 10 μm.

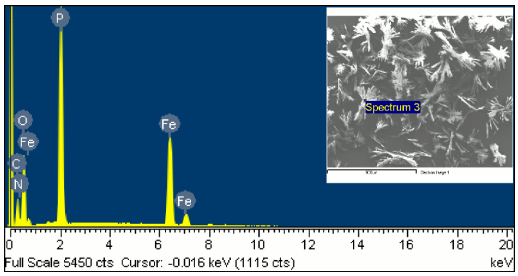

Figure 4.46: EDX spectrum of MIL-91(Fe) indicating elements found. Fe : P ratio of 1.0 : 1.64. Inset shows the area analysed.

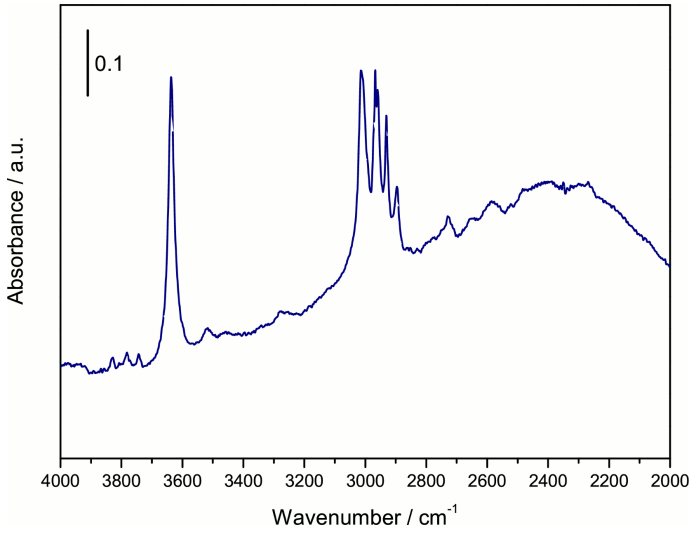

Figure 4.47: IR spectrum of structure MIL-91(Fe) dehydrated at 100°C for one hour. The region 4000–2000 cm^{-1} is shown. Peak at 3636 cm^{-1} corresponds to O-H stretch attributed to framework OH groups; peaks in region 3006–2901 cm^{-1} correspond to framework C-H stretches.[a]

[a]Collected by L. Picone, at LCS ENISCAEN, Caen

the pale yellow colour of samples of MIL-91(Fe): Fe^{3+} cations with a high-spin d^5 configuration would prevent electronic transitions. Therefore OH groups must be present to balance the charge of the structure, and their presence is implied by TGA data (*vide supra*). To confirm the presence of OH groups, IR spectra of a sample of dehydrated structure MIL-91(Fe) were collected. The spectra show a sharp peak in the O-H region at 3636 cm^{-1}, assigned to structural OH groups (*Fig. 4.47*).

4.10.2 As-Prepared Structure MIL-91(Fe)

To confirm the structure, powder X-ray diffraction data (Fe K_α) were collected on a sample of MIL-91(Fe) at 298 K using a Stoe Stadi P diffractometer. The data were indexed using the program DICVOL[152] in a monoclinic space group consistent with the previously reported MIL-91(Al) (a = 19.441(8) Å, b = 6.116(4) Å, c = 11.368(4) Å, β = 91.55(3)°, V = 1351.1(10) $Å^3$ (F.O.M. M_{14} = 21)).[154] The cell was then refined by Le Bail analysis using the GSAS suite of programs[155, 156, 157]. During the Le Bail refinement the b parameter of the unit cell changed significantly so that the final cell, in the space group $C\,2/m$ (as reported for MIL-91(Al))[108], was a = 19.444(3) Å, b = 7.1533(11) Å, c = 11.369(2) Å, β = 91.562(12)°, V = 1580.7(6) $Å^3$. It was also found that there are several peaks in the diffraction pattern which do not correspond to this unit cell and are believed to be due to a second, as yet unknown, phase co-crystallising with MIL-91(Fe). Peaks due to

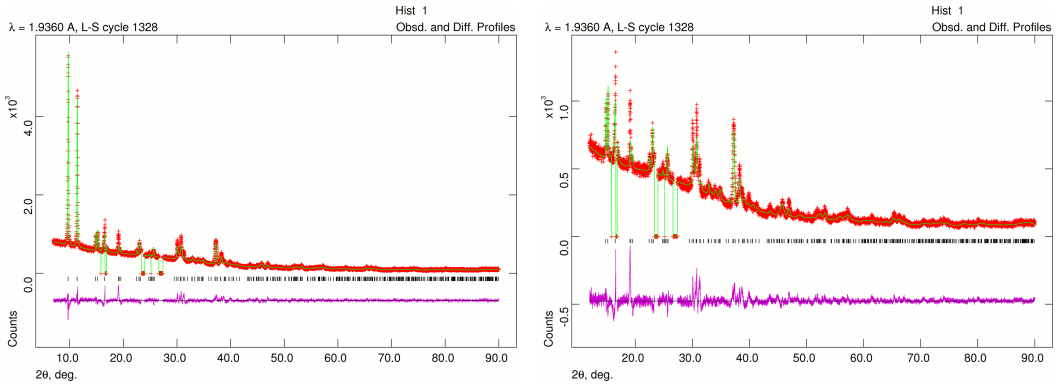

Figure 4.48: Final Rietveld fit for the refinement of MIL-91(Fe) (R_{wp} = 0.0868).

this second phase were excluded from the Le Bail and Rietveld refinements (16.59–16.85°; 23.39–23.98°; and 26.61–27.39°) A preliminary Rietveld refinement using the cell from the Le Bail fit and the structure of MIL-91(Al) as the starting model was also performed. Due to the presence of the second phase, the refinement was only performed to compare the structural intensities with the experimental intensities (rather than to change the model as in a full refinement). Therefore the positions of all atoms were constrained to move together to allow the structure to partially relax. After 1328 cycles the refinement gave a fit of R_{wp} = 0.0868, R_p = 0.0636, $R(F^2)$ = 0.2204 and χ^2 = 2.244 (*Fig. 4.48*).

The structure of MIL-91(Fe) consists of corner-sharing chains of octahedral Fe^{3+} cations parallel to the *b*-direction. The corner-sharing O atoms are protonated to form charge balancing hydroxide group (*Fig. 4.49a*). Four PO_3C groups provide the remaining four O atoms and bridge along the chains, two to each of the neighbouring Fe sites. Chains are linked in the *a*-direction by one group of linkers. A second disordered group of ligands link in the *c*-direction to form the framework, with half the ligands parallel to the [0 1 1] direction and half parallel to the $[0\,\bar{1}\,1]$ direction. Channels are $\sim$ 4 Å in free diameter and are occupied by physisorbed water molecules (*Fig. 4.49b*).

Although the literature report of MIL-91(Al) indicates that the structure is porous to N_2 at 77 K, it has not been possible to prepare a porous sample of MIL-91(Fe). Activation at 120°C under reduced pressure (1×10^{-4} Torr) for three hours did not give a porous material. Activation at higher temperature is thought to cause the structure to dehydroxylate, indicated by a change in colour from pale yellow to dark brown.

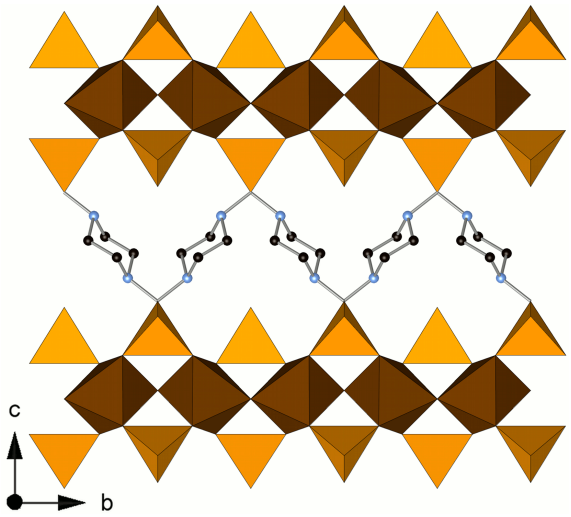

(a)

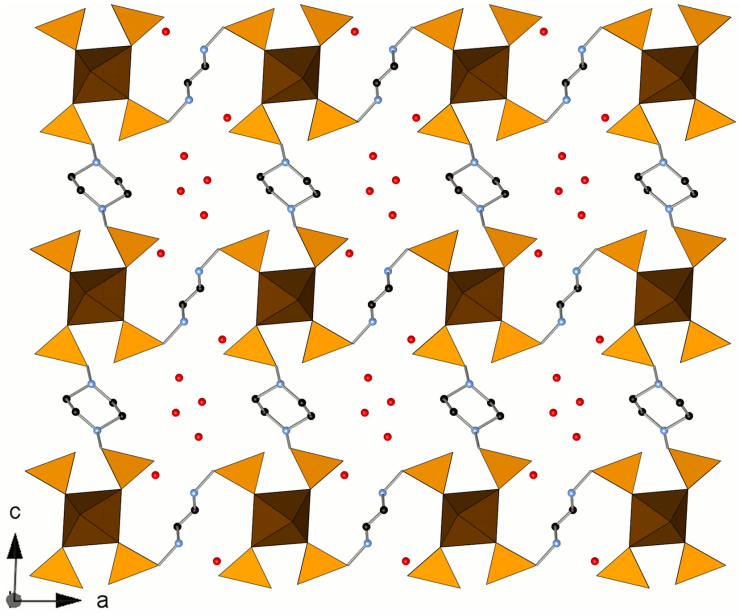

(b)

Figure 4.49: Structure of two chains in MIL-91(Fe) (*top*) showing the disordered piperazinyl ligands, only half of which are present in the actual structure, linking the chains together in the *c*-direction. The structure of the pores is also shown (*bottom*).

4.11 Fe-Tet. & Fe-Tet.-Me

The phases Fe-Tet. and Fe-Tet.-Me, $[Fe_4\mathbf{L}_{1.5}(AcO)_{1.5}(OH,H_2O)_3]\cdot 0.5NH_4 5.5H_2O$ ($\mathbf{L} = \mathbf{L}$ — Fe-Tet.; $\mathbf{L} = \mathbf{L}'$ — Fe-Tet.-Me), have a structure related to that of $[Co_4\mathbf{L}'_{1.5}(AcO)_{1.5}(OH,H_2O)_3]\cdot 0.5NH_4 5.5H_2O$ reported by Groves *et al.*[105] Both Fe-Tet. (made with $H_4\mathbf{L}$) and Fe-Tet.-Me (made with $H_4\mathbf{L}'$) were analysed by TGA, EDX and elemental analysis, with data analysed by analogy to the previously reported Co phase. Fe-Tet. is unusual in that it is formed with $H_4\mathbf{L}$ and therefore there are no Me groups projecting into the pore space. Thus there is a greater potential pore volume for gas adsorption.

TGA data for Fe-Tet. shows a nearly continuous weight loss from the material over the range 20–700°C. There are two poorly defined steps in the TGA plot (*Fig. 4.50a*): 20–130°C (6.63 wt.%) and 153–330°C (9.29 wt.%). The first weight loss is equivalent to the loss of $\sim 0.39H_2O$ molecules per Fe cation (assuming the final solid is Fe_2O_3). However, the pore space in the structure of the Co phase of Groves *et al.* was occupied by charge balancing NH_4^+ cations derived from the breakdown of the ligand, which might be expected to be lost as NH_3 leaving a proton to balance the charge. In this case we would expect $\sim 0.41NH_3$ molecules per Fe cation. It remains unclear what the nature of the physisorbed molecules in the pore are and further analysis (e.g. TG/MS) would be necessary to determine this. The second weight loss is ascribed to the collapse of the framework. Fe-Tet.-Me behaves in a very similar way under TGA to Fe-Tet. (*Fig. 4.50b*). Two weight losses are again observed: 17–106°C (6.82 wt.%) and 152–420°C (14.68 wt.%). The two events are assigned to the loss of either H_2O or NH_3 from the physisorbed molecules in the channels and the collapse of the framework respectively.

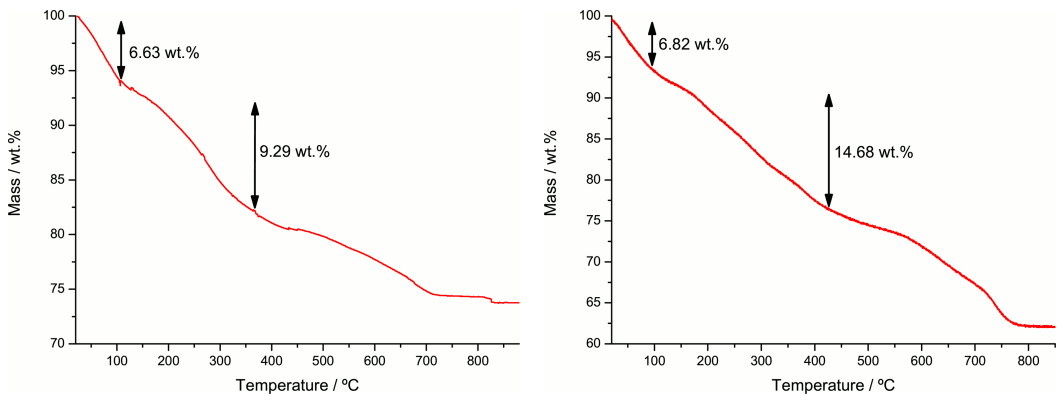

(a) Fe-Tet. (b) Fe-Tet.-Me

Figure 4.50: TGA plots of two Fe bisphosphonates constructed from Fe tetramers. Principal weight loss events are shown.

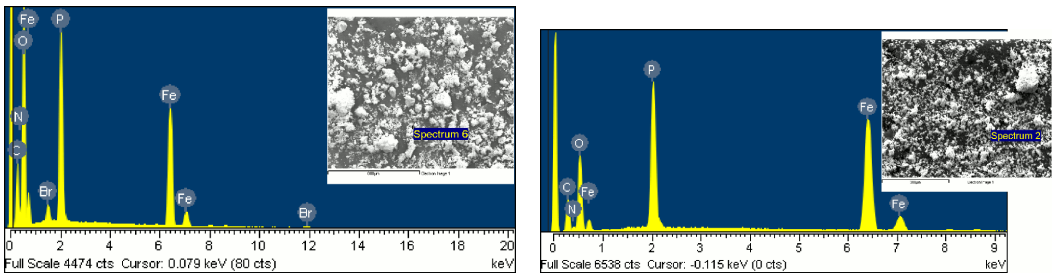

(a) Fe-Tet. — 1.0 : 0.73 (b) Fe-Tet.-Me — 1.0 : 0.72

Figure 4.51: EDX spectra of two Fe bisphosphonates constructed from Fe tetramers, with Fe:P ratios quoted. Insets show the area analysed for each sample.

	Fe-Tet.			Fe-Tet.-Me		
	C / %	H / %	N / %	C / %	H / %	N / %
Expected	14.6	4.1	5.0	16.1	4.3	4.9
Found	14.6	3.5	4.1	17.7	3.4	4.6

Table 4.21: Results of elemental analysis for Fe-Tet. and Fe-Tet.-Me.

EDX spectra of Fe-Tet. gave an Fe : P ratio of 1.0 : 0.73. This is in very good agreement with the expected metal:ligand ratio of 4 : 1.5 (Fe : P — 1.0 : 0.75) (*Fig. 4.51a*). Br was also found to be present at each of the analysed sites in the sample with an average Fe : Br ratio of 1.0 : 0.05. Although this is not a high concentration of Br, the fact that Br was observed in each spectrum suggests that it is somehow involved in the crystallisation of Fe-Tet.. Br comes from residual HBr within the ligand. The EDX spectra of Fe-Tet.-Me gave an Fe : P ratio of 1.0 : 0.72, again in good agreement with the expected metal:ligand ratio of 4 : 1.5. No Br was observed in the EDX spectra of Fe-Tet.-Me.

Elemental analysis results for Fe-Tet. shows good agreement between the expected composition of $[Fe_4\mathbf{L}_{1.5}(AcO)_{1.5}(OH,H_2O)_3]\cdot 0.5NH_4 5.5H_2O$ (*Table 4.21*). Fe-Tet.-Me shows a slightly larger difference between the expected and calculated values, though values still show some agreement.

4.11.1 Structural Characterisation of Fe-Tet. and Fe-Tet.-Me

Powder X-ray diffraction data (Cu K_α) were collected on a sample of Fe-Tet. using a Panalytical Empyrean diffractometer in a Bragg-Brentano geometry at 298 K. Data were analysed by Le Bail analysis using the GSAS suite of programs.[155, 156, 157] The cell of the reported Co phase[105] was used as a starting point for Le Bail fitting, in the space group $P\bar{3}c1$. After 353 cycles a final fit of $R_{wp} = 0.0204$, $R_p = 0.0152$ and $\chi^2 = 2.620$ was obtained (final Le Bail fits are given in *Fig. 4.52*). The final unit

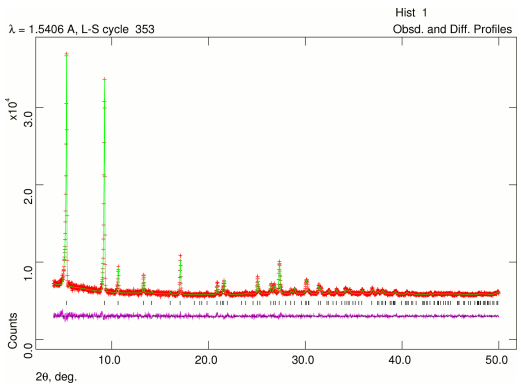

Figure 4.52: Final Le Bail fit for Fe-Tet. (R_{wp} = 0.0204).

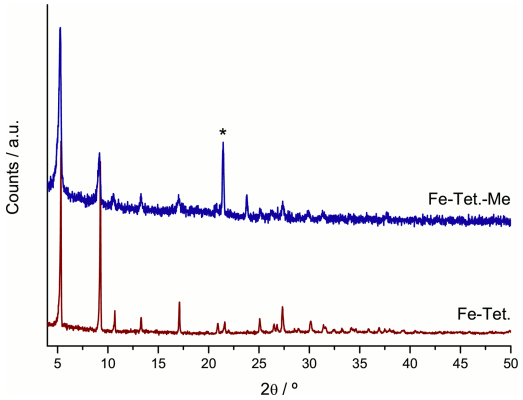

Figure 4.53: Comparison of the powder X-ray diffraction patterns of Fe-Tet. and Fe-Tet.-Me (Cu K_α). Peak marked * is an experimental artifact.

cell parameters were (in space group $P\bar{3}c1$) a = 19.1166(11) Å, c = 9.2817(7) Å, V = 2937.50(27) Å^3. The cell parameters are very similar to those of the Co phase and this therefore provides further evidence that Fe-Tet. is a structural analogue, with a potentially significantly enlarged accessible pore volume. The hypothetical structure of Fe-Tet., illustrating the enlarged pore volume (thanks to the absence of Me groups in this material) is given (*Fig. 4.54*).

Powder X-ray diffraction data (Cu K_α) were also collected for a sample of Fe-Tet.-Me, using an Panalytical Empyrean diffractometer in a transmission geometry. The diffraction peaks in the pattern of this material were significantly broader and of lower intensity than the peaks in the data for Fe-Tet. and it was therefore not possible to index the data. A comparison of the diffraction patterns of Fe-Tet. and Fe-Tet.-Me shows a strong similarity between the peak positions, indicating them to be structurally related (*Fig. 4.53*).

Although the absence of Me groups in the structure of Fe-Tet. gives a greater theoretical pore volume for gas sorption, samples of the material prepared have shown negligible porosity to N_2 at 77 K. To better understand this it will be necessary to determine the nature of the species in the pore channels of the as-prepared material.

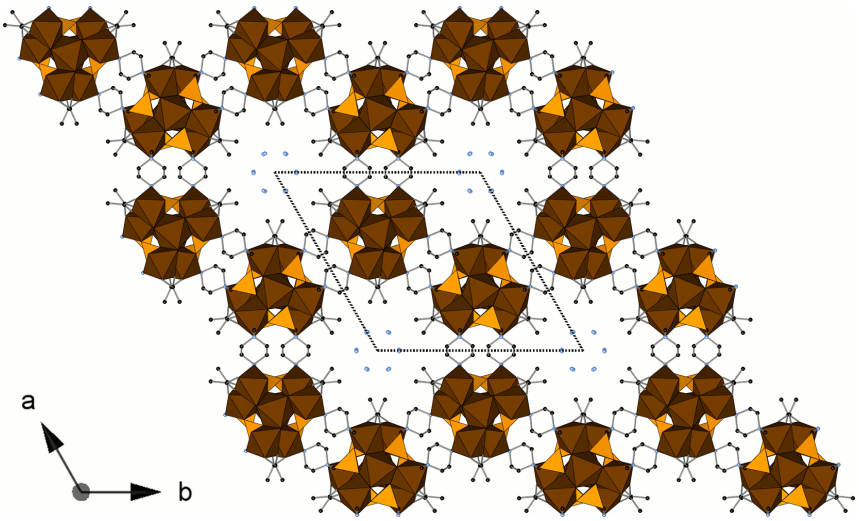

Figure 4.54: Structure of Fe-Tet. viewed along the *c*-direction. Note that the absence of the Me groups yields a theoretically greater accessible pore volume. The material is however non-porous.

4.12 Summary

4.12.1 Rare Earth Bisphosphonates

Four yttrium phosphonate materials have been hydrothermally synthesised using $H_4\mathbf{L}$, $H_4\mathbf{L}'$, *R*-$H_4\mathbf{L}'$ and $H_4\mathbf{L}''$, with $Y(AcO)_3$ as the metal source, in reactions with initial metal:ligand stoichiometry 1.0 : 1.5 (*Table 4.22*). $Y_2(\mathbf{L}H_2)_3$, obtained using $H_4\mathbf{L}$ as the ligand, was previously reported by Groves *et al.*[112] The synthesis of this phase was optimised and it was found that a two-fold excess of KOH base was necessary to obtain phase pure material. Using racemic $H_4\mathbf{L}'$, STA-13(Y) was obtained, a material previously observed by Miller with both Y and Sc.[184] STA-13(Y) was prepared over a range of temperatures and reaction times, but only in the absence of base. Similarly $Y_2(R\text{-}\mathbf{L}H_2)_3$, a structural analogue of $Y_2(\mathbf{L}H_2)_3$ (*vide infra*), could only be obtained in the absence of base, when using enantiopure *R*-$H_4\mathbf{L}'$. Using $H_4\mathbf{L}''$, the phase Y-$H_4\mathbf{L}''$U1 with a structure unrelated to either $Y_2(\mathbf{L}H_2)_3$ or STA-13(Y) was obtained.

Phase	Ligand	$Y(AcO)_3$: **L** : KOH	Time / hrs
$Y_2(\mathbf{L}H_2)_3$	$H_4\mathbf{L}$	1.0 : 1.5 : 3.15	168
STA-13(Y)	$H_4\mathbf{L}'$	1.0 : 1.5 : 0.0	18
$Y_2(R\text{-}\mathbf{L}H_2)_3$	*R*-$H_4\mathbf{L}'$	1.0 : 1.5 : 0.0	48
Y-$H_4\mathbf{L}''$U1	$H_4\mathbf{L}''$	1.0 : 1.5 : 0.0	71

Table 4.22: Optimised reaction ratios and reaction times for four principal Y phosphonate phases formed with the ligands $H_4\mathbf{L}$, $H_4\mathbf{L}'$, *R*-$H_4\mathbf{L}'$ and $H_4\mathbf{L}''$. 1000 eq. of water was used as the solvent in each reaction and all reactions were all heated at 190°C.

This dependence of the structure formed on the ligand used in the reaction is caused by both the number of Me groups on the piperazinyl ring and also on the ability of this group of ligands to engage in H-bonding. With no Me groups on the ring, the default structure for this system is that of $Y_2(\mathbf{L}H_2)_3$. Using the racemic $H_4\mathbf{L}'$ ligand, the Me group provides an energy barrier to ring flipping in solution, essentially providing a small degree of conformational locking. This preorganises the doubly protonated piperazinyl ring for H-bonding with neighbouring ligands. An extensive H-bonding network was observed in STA-13(Y), giving a large enthalpic gain to the crystallisation of this phase over that of $Y_2(\mathbf{L}H_2)_3$. There is some H-bonding in the structure of $Y_2(\mathbf{L}H_2)_3$, but it is not as extensive as in STA-13(Y).

A further factor favouring the crystallisation of STA-13(Y) over a $Y_2(\mathbf{L}H_2)_3$-like network is that there is not enough space to fit both *R* and *S* enantiomers into the crystal structure of $Y_2(\mathbf{L}H_2)_3$. C atoms located in positions consistent with

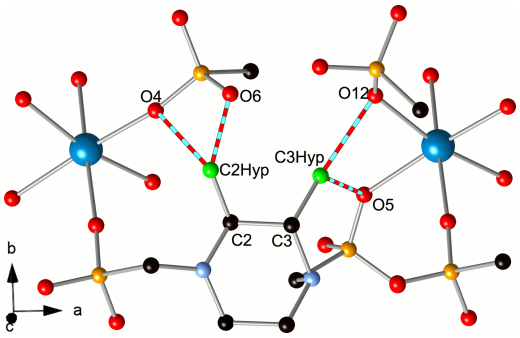

Figure 4.55: Part of the $Y_2(\mathbf{L}H_2)_3$ structure showing two Me group positions corresponding the *S* enantiomer. Short contacts are indicated (blue & red bonds).

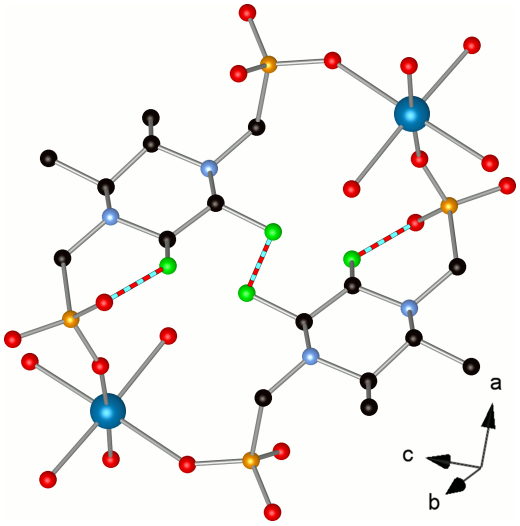

Figure 4.56: Part of the STA-13(Y) structure showing the hypothetical positions of Me groups (green) if an enantiopure ligand was used in the synthesis. Short contacts are indicated (blue & red bonds).

the *S* ligand Me group in $Y_2(\mathbf{L}H_2)_3$ sterically clash with other framework atoms ($C_{Me}\cdots$(P)O: 1.95–2.67 Å — *Fig. 4.55*). Thus a conglomerate might form instead. However, as STA-13(Y) crystallises under the same conditions, but is enthalpically favoured (*vide supra*) it forms in preference, as a true racemate.

A $Y_2(\mathbf{L}H_2)_3$-like network is, however, obtained using enantiopure *R*-$H_4\mathbf{L}'$. In this case STA-13(Y) does not crystallise as there would be significant steric clashing of the Me group of one ligand with Me groups belonging to neighbouring linkers or nearby PO_3C O atoms ($C_{Me}\cdots C_{Me}$: 1.63 Å; $C_{Me}\cdots$(P)O: 1.95 Å — *Fig. 4.56*).

An unrelated structure is thought to be obtained using $H_4\mathbf{L}''$ as it would be impossible to fit two Me groups in a *trans* configuration into either the $Y_2(\mathbf{L}H_2)_3$ or STA-13(Y) networks.

In addition to these principal structures, four unknown phases have been identified in the $Y(AcO)_3$–$H_4\mathbf{L}$ system. Two of these were prepared as single phase products, though only one of them was sufficiently crystalline to yield a cell. Reactions of $Sc(piv)_3$ with $H_4\mathbf{L}$ also yielded a previously unknown phase which is thought to have a structure related to that of the Zr phosphonate of Taddei *et al.*[101] Both the Zr and Sc phosphonates feature a similar chain motif to STA-13(Y) (*vide infra*).

The range of cation radii over which the STA-13 network may be crystallised was also investigated. STA-13 could be crystallised with cations as small as Sc^{3+} and as

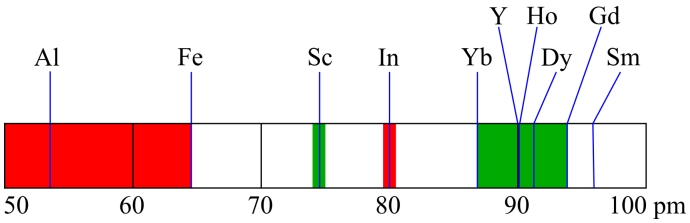

Figure 4.57: Plot of phase formed against cation radius (pm). Cations are labelled at their radii. Red band — MIL-91 network crystallised; green band — STA-13 network crystallised.

large as Gd^{3+} (*Fig. 4.57*). Cations smaller than Sc^{3+} formed the MIL-91 structure type (*vide infra*) whilst cations larger than Gd^{3+} form structures reported by Mowat *et al.*[111] The exception to this is In^{3+}, which is larger than Sc^{3+} but crystallises the MIL-91 structure. The reasons for this are not fully understood. Crystallisation of the MIL-91 network is disfavoured for larger radius cations as the M-(μ_2-OH)-M angles along the metal phosphonate chain would become less favourable. Instead, chains in the networks adopted by larger cations, such as STA-13, consist of isolated metal cations, which put fewer constraints on the cation size.

The structures of $Y_2(\mathbf{L}H_2)_3$, STA-13(Y) and $Y_2(R\text{-}\mathbf{L}H_2)_3$ were analysed by powder X-ray diffraction (*Table 4.23*). All three materials are constructed from chains of YO_6 octahedra bridged to neighbouring YO_6 units through three bridging PO_3C tetrahedra. The structures of the chains in $Y_2(\mathbf{L}H_2)_3$ and $Y_2(R\text{-}\mathbf{L}H_2)_3$ are essentially identical (the structures being analogous). In $Y_2(\mathbf{L}H_2)_3$, neighbouring YO_6 octahedra are offset from one another in the *ac*-plane by $\sim$ 0.7Å forming an undulating chain. In STA-13(Y), the Y^{3+} cations sit on the $\bar{3}$ axis, though the arrangement of coordinating O atoms results in a staggered configuration of neighbouring YO_6 octahedra along the chain. The chain repeat distance for both the $Y_2(\mathbf{L}H_2)_3$ and STA-13(Y) networks is approximately 10 Å, representing two YO_6 octahedra and associated bridging PO_3C groups. The chain motif is not thought to be present in the unknown structure of Y-$H_4\mathbf{L}''$U1 as none of the unit cell dimensions are approximately 10 Å in length.

The structures of each of the fully dehydrated materials were determined by powder X-ray diffraction (*Table 4.24*). $Y_2(\mathbf{L}H_2)_3$, STA-13(Y) and $Y_2(R\text{-}\mathbf{L}H_2)_3$ show very different dehydration behaviours. On dehydration, $Y_2(\mathbf{L}H_2)_3$ undergoes a $\sim$ 200 $Å^3$ decrease in cell volume, due to a shortening of the *c*-axis and changes to the monoclinic unit cell. The γ angle in as-prepared $Y_2(\mathbf{L}H_2)_3$ is close to but not exactly 90° (90.120(50°), whereas in 2-DH it was determined to be 90°. It is conceivable that in $Y_2(\mathbf{L}H_2)_3$-DH, γ is also non-90 (making the structure triclinic),

	$Y_2(\mathbf{L}H_2)_3$	STA-13(Y)	$Y_2(R\text{-}\mathbf{L}H_2)_3$
Formula	$Y_2(\mathbf{L}H_2)_3 \cdot 5H_2O$	$Y_2(\mathbf{L}'H_2)_3 \cdot 7H_2O$	$Y_2(R\text{-}\mathbf{L}'H_2)_3 \cdot 3H_2O$
Space Group	$P\,112_1$	$P\,\bar{3}$	$P\,22_12_1$
a / Å	8.6744(3)	16.18945(13)	8.70549(10)
b / Å	9.7820(3)		9.92067(28)
c / Å	22.7997(9)	10.00355(16)	23.31635(33)
α / °			
β / °			
γ / °	90.120(5)		
V / Å^3	1934.60(13)	2270.64(4)	2013.70(6)
Diffractometer	Lab/Stoe Stadi P	ESRF/ID31	DLS/I11
Temperature / K	298	100	100
λ / Å	1.54056	0.800178	0.825028
No. Reflections	1621	861	731
No. Atoms (non-H)	54.5	60.75	28
No. Restraints	134	67	82
R_{wp}	0.0380	0.0523	0.0586
R_p	0.0299	0.0409	0.0468
$R(F^2)$	0.1049	0.0452	0.0684
χ^2	1.711	4.462	90.17

Table 4.23: Crystallographic data for the as-prepared forms of the principal phases of the $Y(AcO)_3$– $H_4\mathbf{L}$, $H_4\mathbf{L}'$ and R-$H_4\mathbf{L}'$ systems.

but with a difference from 90° that is so small that it is difficult to observe (this has not been investigated). Structurally, $Y_2(\mathbf{L}H_2)_3$ minimises pore space in the dehydrated structure by a shearing of the structural layers in the *a*-direction and by tilting of the piperazinyl rings. $Y_2(R\text{-}\mathbf{L}H_2)_3$ has a much reduced pore space due to the additional Me groups in the structure. It shows very little distortion on dehydration as the Me groups lock the structure open. Pore volume is also effectively minimised by tilting of the ligand in the structural layer. The framework of STA-13(Y) shows almost no change on dehydration. The structure is not flexible and cannot distort due to H-bonding, thus leaving an open pore network for gas adsorption.

Of the three Y structures, only STA-13(Y) is porous. The porosities of STA-13 networks formed with other metals were also investigated and again STA-13(Y) was found to be the most porous, though STA-13(Yb) also showed significant porosity. STA-13(Y) was porous to N_2 at 77 K, CO_2 and CH_4 at 196 K and 273 K and a range of short chain alkanes at 273 K. THe small hysteresis loops in the CO_2 isotherm are not understood, but may hint at a novel behaviour. Further experiments are needed to determine the origin of the hysteresis. Simulated adsorption isotherms indicate significant pore blocking or the presence of a non-porous, amorphous secondary

	$Y_2(\mathbf{L}H_2)_3$-DH	STA-13(Y)-DH	$Y_2(R\text{-}\mathbf{L}H_2)_3$-DH
Composition	$Y_2(\mathbf{L}H_2)_3$	$Y_2(\mathbf{L}'H_2)_3$	$Y_2(R\text{-}\mathbf{L}'H_2)_3$
Space Group	$P\,12_11$	$P\,\bar{3}$	$P\,22_12_1$
a / Å	8.7651(3)	16.1352(2)	8.70047(16)
b / Å	9.9093(6)		9.6944(4)
c / Å	20.0013(5)	10.0296(2)	22.6032(4)
α / °			
β / °	94.479(7)		
γ / °			
V / Å^3	1731.92(12)	2261.32(6)	1906.48(7)
Diffractometer	DLS/I11	ESRF/ID31	DLS/I11
Temperature / K	100	100	100
λ / Å	0.825028	0.800178	0.825028
No. Reflections	1560	857	694
No. Atoms (non-H)	50	53	26.5
No. Restraints	168	73	85
R_{wp}	0.0778	0.0677	0.0613
R_p	0.0621	0.0540	0.0505
$R(F^2)$	0.2500	0.0647	0.0747
χ^2	142.2	11.41	104.3

Table 4.24: Crystallographic data for the fully dehydrated forms of the principal phases of the $Y(AcO)_3$– $H_4\mathbf{L}$, $H_4\mathbf{L}'$ and R-$H_4\mathbf{L}'$ systems.

phase in the experimental sample. Further tuning of the sample preparation (both synthesis and activation) may help in identifying the cause of the reduced porosity.

4.12.2 Iron Bisphosphonates

MIL-91(Fe) was synthesised for the first time, using either $Fe^{(III)}(AcO)$ or $FeCl_3$. MIL-91(Fe) was found to crystallise as clusters of large needle crystals ($100 \times 10\,\mu$m) from gels with initial Fe^{3+} cation:ligand ratios of 1 : 1, with pH modification with KOH necessary when using $FeCl_3$. Characterisation of the material gave a composition similar to the expected composition reported for MIL-91(Al).[108] TGA data show a second step after the loss of physisorbed water, assigned by analogy to MIL-91(Al), to dehydroxylation of the $\cdots MO_4(\mu_2\text{-OH})MO_4 \cdots$ chains. The presence of OH groups in the framework of MIL-91(Fe) was confirmed by *in situ* IR spectroscopy. Le Bail fits and the early stages of a Rietveld refinement confirm the unit cell is consistent with previously reported MIL-91 frameworks (*Table 4.25*).[108] Good fits to the unit cell were only achieved by excluding certain peaks from the diffraction pattern, indicating that a second phase is co-crystallised with MIL-91(Fe). The identity of this phase is unknown. In contrast to the reported Al^{3+} and Ti^{4+} forms of MIL-91, MIL-91(Fe) has shown no significant porosity to

	MIL-91(Fe)	Fe-Tet.
Formula	$Fe(OH)\mathbf{L} \cdot 3.1H_2O$	***F***
Space Group	$C\,2/m$	$P\,\bar{3}c1$
a / Å	19.4435(19)	19.1166(11)
b / Å	7.1876(7)	
c / Å	11.3997(13)	9.2817(7)
β / °	88.681(7)	
V / Å^3	1592.7(3)	2937.5(3)
Diffractometer	Lab/Stoe Stadi P	Lab/Panalytical Empyrean
Temperature / K	298	298
λ / Å	1.93604	1.54056
No. Reflections	374	176
R_{wp}	0.0868	0.0204
R_p	0.0636	0.0152
χ^2	2.244	2.620

Table 4.25: Crystallographic data for MIL-91(Fe) and Fe-Tet. from Le Bail analyses of powder X-ray diffraction data. ***F*** — Composition of Fe-Tet. is $[Fe_4\mathbf{L}_{1.5}(AcO)_{1.5}(OH,H_2O)_3]\cdot 0.5NH_4 5.5H_2O$.

small gas molecules. This is attributed to difficulties in activating the material (the materials is very sensitive to heating and readily dehydroxylates) and also to the crystal morphology, which reduces the number of pore-openings for a given volume of solid.

Using a higher concentration of $Fe^{(III)}(AcO)$ to yield an initial gel with Fe^{3+} cation:ligand ratio of $\sim 4:1$ gave the phase Fe-Tet. with $H_4\mathbf{L}$ and Fe-Tet.-Me with $H_4\mathbf{L}'$. Fe-Tet. has a very similar diffraction pattern to the previously reported Co phase composed of tetrameric metal clusters.[105] Le Bail fits gave a cell which is consistent with Fe-Tet. being a structural analogue of the Co phase. Samples of Fe-Tet. and Fe-Tet.-Me have shown minimal porosity to N_2 at 77 K, even though a larger free pore space than in the previously reported phase of Groves *et al.*[105] should be available in the activated materials. The single crystal structure of the Co phase indicated the presence of unidentified physisorbed molecules in the pore space. The nature of these has not been resolved. Elucidating the nature of these may help in developing an activation procedure for Fe-Tet., Fe-Tet.-Me and indeed the Co tetramer phase.

Chapter 5

Synthesis of STA-12(Mg) and Comparison with Other STA-12 Materials

Divalent metal bisphosphonates of $H_4\mathbf{L}$ make up the greater part of structures reported with this ligand (see *Section 1.4.2* for a more complete review). Many are non-porous owing to their layered[106, 107] or small pore[103] structures. The first porous large-pore phosphonate formed with $H_4\mathbf{L}$ was STA-12, reported with $Ni^{(II)}$.[105] As well as possessing large 9 Å unidirectional pore channels, which in the as-prepared material are occupied by physisorbed water molecules, each metal atom is also coordinated by a chemisorbed water molecule, which may be removed on dehydration to leave a potentially catalytically active coordinatively unsaturated site. Work by Miller *et al.* showed that STA-12(Ni) dehydrates in a three step process, with loss of the chemisorbed water causing a structural transition from $R\bar{3}$ to $P\bar{1}$.[114] The transition is fully reversible on rehydration. The dehydrated material has been shown to be porous to a range of gases including N_2, CO_2, CH_4 and H_2. Pearce demonstrated the synthesis and structures of the as-prepared forms of $Mn^{(II)}$, $Fe^{(II)}$ and $Co^{(II)}$ forms of STA-12 (STA-12(Mn), STA-12(Fe) and STA-12(Co) respectively). The dehydration behaviour of each was also investigated by a combination of TGA, IR, UV-Vis and powder X-ray diffraction studies.[113] STA-12(Co) shows a similar behaviour to STA-12(Ni), whereas STA-12(Mn) and STA-12(Fe) behave differently, retaining a rhombohedral symmetry in the fully dehydrated form. Of the $Mn^{(II)}$, $Fe^{(II)}$ and $Co^{(II)}$ forms of STA-12, Pearce reports that only STA-12(Co) was porous to small gas molecules.

This chapter reports the discovery and synthesis of the $Mg^{(II)}$ form of STA-12 ($Mg_2(H_2O)_2\mathbf{L}{\cdot}5.6H_2O$, STA-12(Mg)), the first porous group II bisphosphonate.

Metal	$M(AcO)_2$: $H_4\mathbf{L}$: H_2O	pH	Temp. / °C	Time / hrs
Mn	2 : 1 : 900	6	190	96
Fe	2 : 1 : 900	5	190	120
Co	2 : 1 : 900	7	190	120
Ni	2 : 1 : 900	5	220	72
Mg[a]	2 : 1 : 900	7	220	72

Table 5.1: Reaction conditions used by Pearce in the synthesis of different forms of STA-12, using KOH solution (1 mol dm^{-3}) to raise pH where necessary.[113]

[a]This reaction did not form STA-12 — *vide infra*

During synthetic studies of this material, four other $Mg^{(II)}$ containing frameworks were identified, one of which was previously observed by Pearce.[113] Of these materials, the structures of two were solved by single crystal X-ray diffraction. Syntheses of STA-12(Co) and STA-12(Fe) were optimised to improve synthesis reliability. STA-12(Mg) was prepared as needle crystals from single crystal X-ray diffraction, confirming the earlier structure of STA-12(Ni) which was solved from powder data. The as-prepared structures of STA-12(Mn), STA-12(Fe) and STA-12(Co) were re-refined to obtain better fits to the powder X-ray diffraction data and to allow comparison of their structures with STA-12(Mg). Dehydration behaviour of STA-12(Mg) was analysed by TGA, powder X-ray diffraction, IR and solid-state NMR spectroscopies, and compared with the behaviour of the other known phases of STA-12. To that end, the structure of fully dehydrated STA-12(Mn) (STA-12(Mn)-DH) was re-refined to obtain a better fit to the data and a more chemically sensible structure. The porosity of STA-12(Mg) to N_2 and CO_2 has also been investigated.

5.1 Syntheses of Reported STA-12(Fe) & STA-12(Co)

Pearce reports the syntheses of STA-12(Mn–Ni) (*Table 5.1*).[113] These conditions were found to prepare each form of STA-12, but in the case of STA-12(Fe) and STA-12(Co) with a second phase ($M(\mathbf{L}H_2)\cdot xH_2O$ — Co form, LaDuca *et al.*;[103] Fe form, Groves *et al.*[105]).

The synthesis of STA-12(Co) was improved by dropwise addition of a known volume of KOH solution, as the last component of the synthesis gel. An initial reaction ratio of 2.0 : 1.0 : 2.12 : 900 ($Co(AcO)_2$: $H_4\mathbf{L}$: KOH : H_2O). In a typical synthesis of structure STA-12(Co), $H_4\mathbf{L}$ (0.338 g, 1.11×10^{-3} mol) was placed in a 40 ml PTFE autoclave liner to which was added water (12.38 ml) and $Co(AcO)_2$

Metal	$M(AcO)_2$: $H_4\mathbf{L}$: KOH : H_2O	pH	Temp. / °C	Time / hrs
Fe	2.0 : 1.0 : 3.0 : 900	6	160	18
Co	2.0 : 1.0 : 2.12 : 900	6	160	18
Co	2.0 : 1.0 : 2.12 : 900	7	220	18
Ni	2.0 : 1.0 : 0 : 900	5	220	18

Table 5.2: Optimised reaction conditions producing phase pure STA-12(Co) and STA-12(Fe). Reaction at 160°C produced STA-12(Co) showing broader peaks in its X-ray diffraction pattern, thought to be due to smaller particle size. Reaction at 220°C produced highly crystalline material.

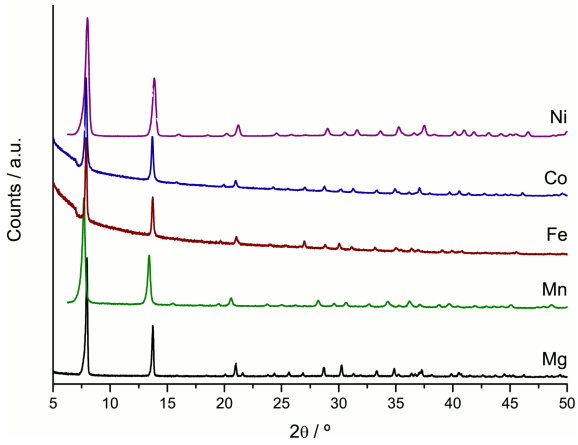

Figure 5.1: Laboratory powder X-ray diffraction patterns (Fe K_α) of the four previously reported forms of STA-12, STA-12(Mn) (dark green), STA-12(Fe) (maroon), STA-12(Co) (dark blue) and STA-12(Ni) (purple), and the newly synthesised STA-12(Mg) (black).

solution (6.15 ml, 0.1 g ml^{-1}, 2.22×10^{-3} mol). The reaction was stirred and KOH solution (1.47 ml, 0.1 g ml^{-1}, 2.35×10^{-3} mol) added dropwise, resulting in a total volume of 20 ml. The gel was then stirred at room temperature for 30 minutes and the pH recorded (6–7). The reaction was then heated at 160°C for 18 hours. Syntheses of the STA-12(Fe) were similarly optimised (*Table 5.2*, *Fig. 5.1*). A sample of STA-12(Ni) was also prepared with a shorter reaction time in order to compare its porosity with that of STA-12(Mg).

For all metal forms of STA-12 investigated, a short reaction time was found to yield crystalline samples of STA-12 and did not have any detrimental effect on the porosity of the material. In addition, for structures STA-12(Co) and STA-12(Fe) reactions at low temperature (160°C) were found to favour crystallisation of the STA-12 network. In the case of structure STA-12(Co), samples prepared at 160°C tended to be more porous than those prepared at higher temperature, but have diffraction patterns with broader peaks, due to smaller particle sizes in the lower temperature reactions (see *Section 5.7*).

5.2 Synthesis of STA-12(Mg)

STA-12(Mg) was first prepared in High-Throughput (HT) syntheses performed by L.-H. Schilling in the group of Prof. N. Stock (Christian-Albrechts-Universität zu Kiel, Kiel, Germany). An HT discovery array for the $MgCl_2$/H_4**L**/KOH system investigated $MgCl_2$: H_4**L** ratios of 1 : 1 and 2 : 1, varying the amount of base. Reactions were heated at 115–160°C for 24–52 hours. Mixtures of two phases were identified: STA-12(Mg) and an unknown phase, MgU1. Optimisation of reaction conditions was then performed using HT methods, with the best results obtained with a reaction ratio of 1 : 1 : 3.5 : 1700 ($MgCl_2$: H_4**L** : KOH : H_2O). However, phase pure structure STA-12(Mg) could not be prepared by conventional heating. Microwave syntheses were also found to yield STA-12(Mg), but again it could not be prepared in the absence of MgU1.

Pearce reports some syntheses with $Mg(AcO)_2$ (*Table 5.1*),[113] which yielded a second unknown phase, MgU2. Combining the approaches of Pearce and Schilling, hydrothermal reactions on a 20 ml scale were performed using $Mg(AcO)_2$ as the metal source and with relatively high base concentration to afford a gel composition of 2.0 : 1.0 : 3.27 : 1000 ($Mg(AcO)_2$: H_4**L** : KOH : H_2O). This gel was conventionally heated at 220°C for 72 hours and yielded large needle crystals of STA-12(Mg). Optimisation of this reaction showed that MgU2 forms under hydrothermal conditions when lower base concentrations are used in the reaction. Two other phases were identified during optimisation (*Table 5.3*): the previously unreported Mg form of M(**L**H_2)·xH_2O (known with M = $Mn^{(II)}$, $Co^{(II)}$; $Fe^{(II)}$, $Zn^{(II)}$ — LaDuca *et al.*[103] and Groves *et al.*[104, 105] respectively) labelled Mg(**L**H_2); and a Mg phosphate, $MgP_2O_7 \cdot 3.5H_2O$ labelled MgP_2O_7, produced by the breakdown of the ligand, and previously reported only as a powder by Kongshaug *et al.*[189] Single crystal diffraction data has been obtained and solved for both of these materials (*Section 5.9*).

$Mg(AcO)_2$: H_4**L** : KOH : H_2O	pH	Temp. / °C	Time / hrs	Phase
2.0 : 1.0 : 0 : 1500	5	220	44	MgU2
1.0 : 2.0 : 0 : 1500	4	220	50	MgP_2O_7 & Other
2.0 : 1.0 : 0 : 300	5	220	20	Mg(**L**H_2)
2.0 : 1.0 : 3.27 : 1000	7–8	220	72	STA-12(Mg)

Table 5.3: Reaction conditions preparing each of the phases identified in the $Mg(AcO)_2$-H_4**L** system, including optimised conditions for structure STA-12(Mg).

5.3 Structures of As-Prepared STA-12

The composition of as-prepared forms of STA-12(Mn), STA-12(Fe) and STA-12(Co) have been fully reported by Pearce.[113] In the following sections these structures are re-refined to obtain better fits to the data and more chemically sensible structural refinement results for comparison with the newly prepared STA-12(Mg). Details of the composition and structure of newly synthesised structure STA-12(Mg) will be given (see *Section 5.4*).

5.3.1 Structures of As-Prepared STA-12(Mn), STA-12(Fe) & STA-12(Co)

Laboratory powder X-ray diffraction data were collected on fresh samples of structures STA-12(Fe) and STA-12(Co) (Fe K_α); for structure STA-12(Mn) data collected by G. M. Pearce were used (Cu K_α). All data collections were made using Stoe Stadi P diffractometers at 298 K, using transmission geometry, over the range 5–90° 2θ with a step size of 0.1° step size. Data above 60° 2θ were discarded due to a decrease in the intensity of diffraction peaks. Structures were analysed using the GSAS suite of programs by first determining the unit cell parameters by Le Bail fitting and then using Rietveld refinement to confirm the structures.[147, 155, 156, 157] The starting unit cell for Le Bail analysis was taken from as-prepared STA-12(Ni) and the structure of this material was used as the starting model for Rietveld refinement.[114] Data below 7.2° 2θ were discarded due to the effect of the beamstop and, for structures STA-12(Fe) and STA-12(Co), an additional peak thought to be an artifact of the diffractometer was excluded (26.8–27.2° 2θ). Prior to refinement of the structure, restraints were applied to bonding distances of the octahedral M-O, M-O100[1] and M-N bonds (*Table 5.4*); tetrahedral P-O and P-C bonds (1.51 Å and 1.85 Å); and C-C and C-N bonds (1.53 Å and 1.51–1.53 Å). Additional restraints were also applied to selected non-bonding distances: O$\cdots$O, O$\cdots$O100, O$\cdots$N and O100$\cdots$N (M octahedra — *Table 5.4*); O$\cdots$O and O$\cdots$C (P tetrahedra) (2.47 Å and 2.58 Å); N$\cdots$N and C$\cdots$C (diagonal, cross-ring) (2.91 Å and 2.91 Å); and C$\cdots$C (methylene carbon-ring carbon) (2.50 Å).

The structures were refined and found to give a satisfactory fit to the data. However, certain O$\cdots$O distances of the physisorbed water molecules were found to be less than a chemically sensible H bonding distance. O$\cdots$O distances shorter than an H-bonding distance were restrained (2.50–2.60 Å) and further cycles of refinement performed, including of the occupancies of the physisorbed water O

[1] O100 is label given to chemisorbed water molecule.

	STA-12(Mn)	STA-12(Fe)	STA-12(Co)
M-O	2.25	2.20	2.15
M-O100	2.25	2.20	2.15
M-N	2.30	-	2.20
O$\cdots$O	-	3.11	3.04
O$\cdots$O100	-	3.11	3.00
O$\cdots$N	3.30	-	3.08
O100$\cdots$N	3.30	-	3.03

Table 5.4: Bond restraints applied about MO_5N octahedra in Rietveld refinements of structures STA-12(Mn), STA-12(Fe) and STA-12(Co). O100 is the chemisorbed water molecule. All distances in Å.

Structure	R_{wp}	R_p	$R(F^2)$	χ^2	Cycles
STA-12(Mn)	0.0214	0.0166	0.1056	1.690	3466
STA-12(Fe)	0.0371	0.0276	0.4959	1.434	5264
STA-12(Co)	0.0351	0.0245	0.1398	4.186	2842

Table 5.5: Final R_{wp}, R_p, $R(F^2)$, χ^2 and the number of cycles for the final refinements of as-prepared structures STA-12(Mn), STA-12(Fe) & STA-12(Co).

atoms. Isotropic thermal parameters were refined, constraining the framework, the physisorbed water O atoms and the chemisorbed water O atom parameters to vary together as separate groups. Fourier difference maps of the refined structure indicated no significant unaccounted electron density within the pores, indicating all water molecules have been located. R_{wp}, R_p, $R(F^2)$, χ^2 values for the final Rietveld fits of each of structure STA-12(Mn) (*Fig. 5.2*), STA-12(Fe) (*Fig. 5.3*) and STA-12(Co) (*Fig. 5.4*) are detailed in *Table 5.5*.

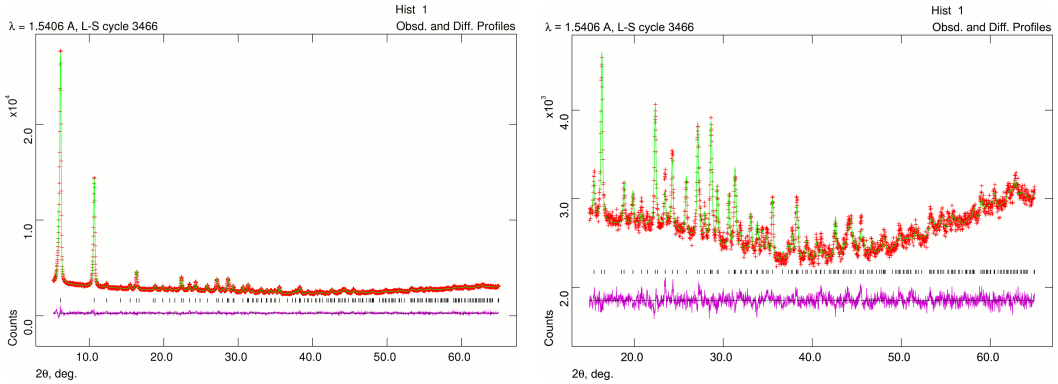

Figure 5.2: Final Rietveld fit for refinement of as-prepared structure STA-12(Mn) ($R_{wp} = 0.0214$).

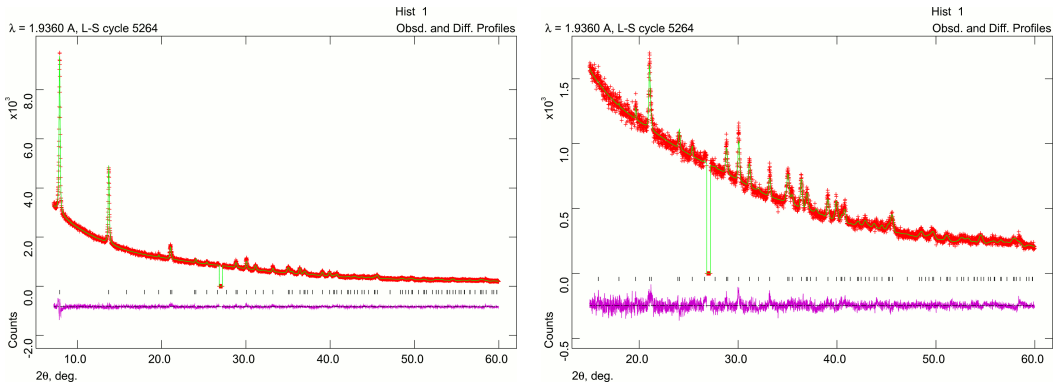

Figure 5.3: Final Rietveld fit for refinement of as-prepared structure STA-12(Fe) ($R_{wp} = 0.0371$).

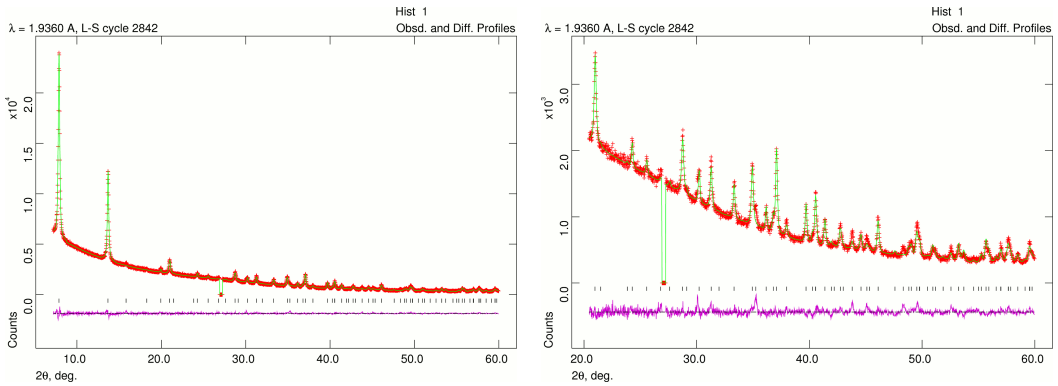

Figure 5.4: Final Rietveld fit for refinement of as-prepared structure STA-12(Co) ($R_{wp} = 0.0351$).

5.4 Characterisation of STA-12(Mg)

Previously reported forms of STA-12 were found to crystallise as microcrystalline powders. However, STA-12(Mg) was obtained as needle crystals of *ca.* 100 × 10 μm dimensions (*Fig. 5.5*).

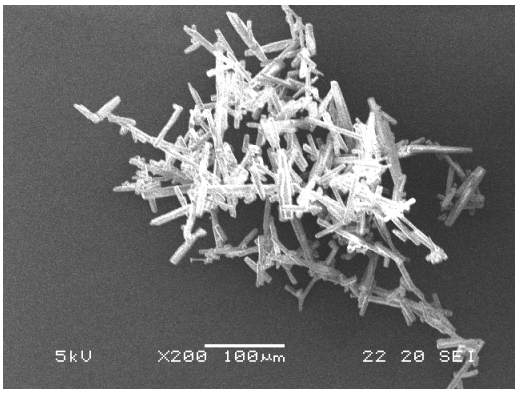

Figure 5.5: SEM micrograph of crystals of structure STA-12(Mg). Needle crystals have dimensions *ca.* 100 × 10 μm.

The composition of structure STA-12(Mg) was determined from TGA, EDX and elemental analyses. TGA analysis shows a sequence of weight loss events similar to those previously reported for STA-12(Ni)[114] (*Figs. 5.6 & 5.12*). From 20–107°C (weight loss of 22.66 wt.%) the material loses ∼ 5.6 molecules of physisorbed water per formula unit. There is then a definite plateau indicating the formation of the partially dehydrated structure ($Mg_2(H_2O)_2$**L**— STA-12(Mg)-PDH, *Section 5.6.4*), which extends to 128°C. This is a greater temperature range than the equivalent partially dehydrated material in structure STA-12(Ni), indicating STA-12(Mg)-PDH is more thermally stable. In the range 128–175°C the material loses ∼ 2 chemisorbed water molecules (7.46 wt.%) to leave the fully dehydrated structure, which is stable up to 325°C. Unlike STA-12(Ni), loss of chemisorbed water occurs in one step. Above 325°C, further weight loss events indicate the breakdown of the structure. EDX analysis gave an Mg : P ratio of 1.0 : 1.14 (*Fig. 5.7*), which is consistent with the metal:ligand ratio of 1 : 1 expected from the previously reported forms of STA-12.

From EDX and TGA results, a composition for structure STA-12(Mg) of $Mg_2(H_2O)_2(C_6H_12N_2O_6P_2)\cdot 5.6H_2O$ was proposed. This composition was confirmed by elemental analysis: expected — C 15.8 %, H 6.0 %, N 6.1 %; found — C 15.7 %, H 5.9 %, N 6.1 %.

The structure of STA-12(Mg) was determined by single crystal X-ray diffraction. Phase purity and unit cell were confirmed by Le Bail analyses (*Sections 5.4.1*

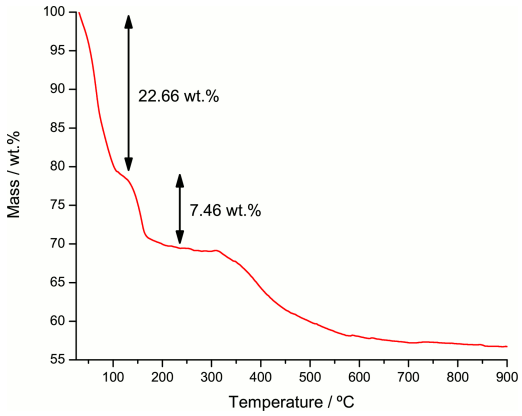

Figure 5.6: TGA of STA-12(Mg) from 20–900°C under dry air showing principal weight loss events.

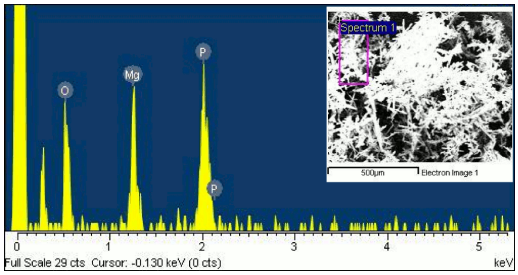

Figure 5.7: EDX spectrum of STA-12(Mg) indicating elements found. Mg : P ratio of 1.0 : 1.14.

& 5.4.2). The structure of STA-12(Mg)-PDH was also confirmed by Rietveld refinement (*Section 5.6.4*). The fully dehydrated structure, STA-12(Mg)-DH, was studied by a combined approach of TGA, powder X-ray diffraction, MAS NMR and IR spectroscopies (*Section 5.6.8*).

5.4.1 Single Crystal X-ray Diffraction Study of As-Prepared STA-12(Mg)

The structure of structure STA-12(Mg) was determined from single crystal X-ray diffraction by L.-H. Schilling & A. Lieb (Christian-Albrechts-Universität zu Kiel, Kiel, Germany) and found to be consistent with the previously reported structure of STA-12. STA-12(Mg) crystallises in space group $R\bar{3}$ (hexagonal setting, a = 28.1046(8)Å, c = 6.2967(3) Å, V = 4307.2(3) Å^3). The refined structure gave a fit to the data of R_1 = 0.0785 and R_{w2} = 0.2345. This large R_{w2} is due to disordered, partially occupied water molecules in the pore space. The fit could be improved by the use of the SQUEEZE routine of PLATON[190] (R_1 = 0.0511 and R_{w2} = 0.1357) although information on the location of physisorbed water molecules would then be lost.

The structure is very similar to the as-prepared structure of STA-12(Ni), which was solved from synchrotron powder X-ray diffraction data.[105] Mg is six-fold coordinated by four phosphonate O atoms, an O atom from a chemisorbed water molecule and a piperazinyl N atom in an octahedral geometry (*Table 5.6*). MgO_5N octahedra share edges, with phosphonate tetrahedra coordinating in a bridging mode, to form helical chains parallel to the c-direction (*Fig. 5.8a*). The remaining phosphonate O atom projects into the pore space (P-O1: 1.507(3) Å) and engages

Bond	Distance / Å	Bond	Distance / Å
Mg1-O2	2.093(3)	P1-O1	1.507(3)
Mg1-O2	2.114(3)	P1-O2	1.536(3)
Mg1-O3	2.079(3)	P1-O3	1.532(3)
Mg1-O3	2.080(3)	P1-C1	1.826(4)
Mg1-N1	2.283(3)		
Mg1-O100	2.049(3)		

Table 5.6: Selected bond distances in the structure of STA-12(Mg) determined from single crystal X-ray diffraction.

in H-bonding with physisorbed water molecules. Chains are linked together in the *a*- and *b*-directions by piperazinyl rings coordinating the Mg atoms through ring N atoms, to give a honeycomb array of unidirectional channels, occupied by physisorbed water molecules (H-bonding distances: 2.05(2)–2.80(2) Å) (*Fig. 5.8b*), which also interact with the framework through the chemisorbed water molecule and the pendant P-O group. Channels have an approximate free diameter in the as-prepared material of 10 Å.

5.4.2 Powder X-ray Diffraction Study of As-Prepared STA-12(Mg)

Unit cell and phase purity of a sample of STA-12(Mg) were confirmed by Le Bail analysis.[155] X-ray powder diffraction data were collected on an as-prepared sample of STA-12(Mg). The sample was loaded into a 0.7 mm glass capillary tube and data collected in a Debye-Scherrer geometry using a Stoe Stadi P diffractometer fitted with a Cu K_α source at 298 K over the range 5–90° 2θ. Data were analysed using the Le Bail routines of the GSAS suite of programs.[156, 157] The unit cell of STA-12(Mg) determined from single crystal X-ray diffraction was used as a starting point for Le Bail analysis. After 617 cycles a final fit of $R_{wp} = 0.1079$, $R_p = 0.0783$ and $\chi^2 = 0.9713$ was obtained (*Fig. 5.9*). Le Bail analysis was consistent with a unit cell with rhombohedral symmetry with unit cell parameters $a = 28.2331(8)$ Å, $c = 6.2648(2)$ Å, V = 4324.7(2) Å^3 (space group $R\bar{3}$). No peaks that could not be accounted for by this cell were observed, confirming the phase purity of the sample.

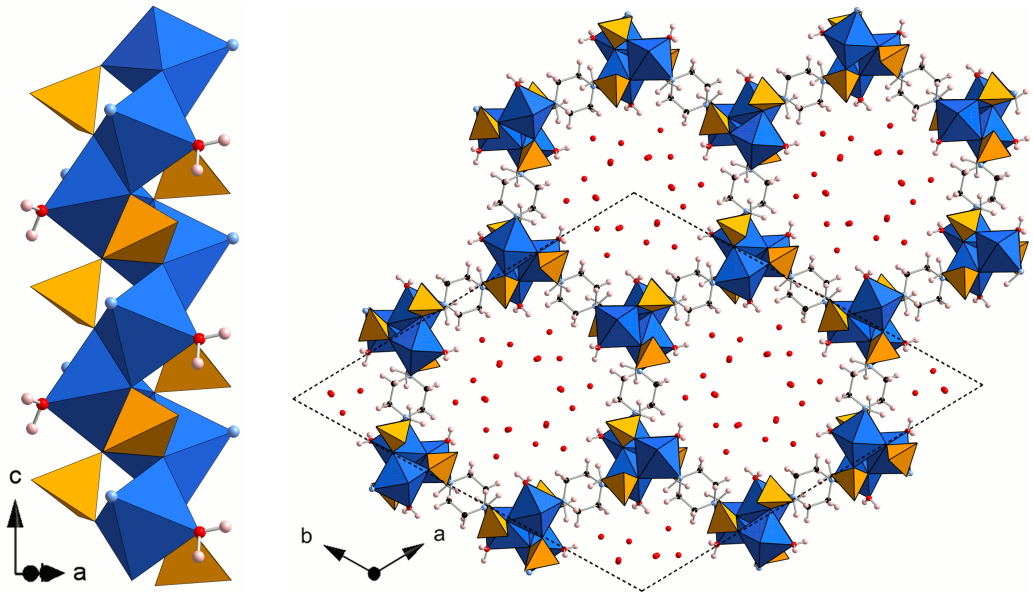

(a) (b)

Figure 5.8: Structure of STA-12(Mg) (STA-12(Mg)). *Top:* Helical chain of edge-sharing MgO_5N octahedra linked by phosphonate tetrahedra. *Bottom:* View along the *c*-axis showing honeycomb array of 10 Å channels occupied by physisorbed water molecules.

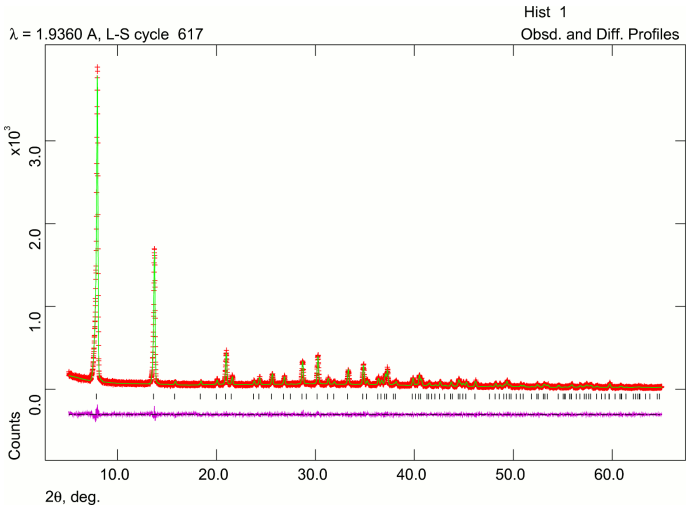

Figure 5.9: Final Le Bail fit for the unit cell of STA-12(Mg) (617 cycles, $R_{wp} = 0.1079$).

5.4.3 Solid-State MAS NMR of STA-12(Mg)

^{13}C and ^{31}P solid-state CP MAS NMR spectra of an as-prepared sample of structure STA-12(Mg) were collected and found to be consistent with the structure of STA-12(Mg) determined by X-ray diffraction. ^{13}C CP MAS NMR shows three resonances (*Fig. 5.10a*): a doublet centred at 48.91 ppm (peaks at 49.44 and 48.37 ppm, J = 161.2 Hz) assigned to the C1 resonance, which is split due to bonding to the P1 site, and two singlets at 48.03 ppm and 43.98 ppm assigned to the C2 and C3 environments. The ^{31}P MAS NMR spectrum (*Fig. 5.10b*) shows a single resonance at 17.76 ppm, assigned to the P1 site. A low intensity resonance at 2.18 ppm is attributed to the presence of a small amount of the structure MgU2.

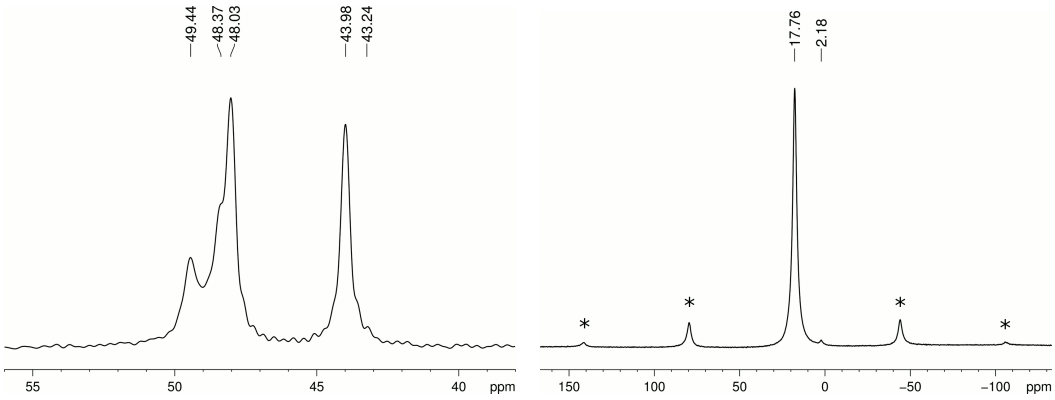

(a) ^{13}C MAS NMR spectrum (b) ^{31}P MAS NMR spectrum

Figure 5.10: MAS NMR spectra for as-prepared STA-12(Mg). Peaks marked * are spinning side bands.

5.5 Comparison of the Structures of As-Prepared STA-12

The different metal forms of STA-12 are all isostructural, with slight variation of unit cell parameters and specfic bond distances. Solution of the structure of STA-12(Mg) from single crystal diffraction data provides confirmation of the STA-12 network, which was originally solved from powder diffraction data collected on STA-12(Ni).[105, 114] All structures crystallise in space group $R\bar{3}$ and unit cell dimensions decrease with decreasing cation radius (*Table 5.7*).

	STA-12(Mg)	STA-12(Mn)	STA-12(Fe)
Cation Radius / pm	86	97	92
a / Å	28.2331(8)	28.5814(10)	28.0103(10)
c / Å	6.2648(2)	6.4264(4)	6.4044(5)
V / Å^3	4324.7(2)	4546.4(4)	4351(5)
M-O / Å	2.079(3)–2.114(3)	2.139(6)–2.265(7)	2.184(13)–2.308(12)
M-N / Å	2.283(3)	2.328(5)	2.260(10)
M-O100 / Å	2.049(3)	2.120(14)	2.315(18)

	STA-12(Co)	STA-12(Ni)
Cation Radius / pm	88.5	83
a / Å	28.0942(9)	27.83424(11)
c / Å	6.2846(3)	6.24208(3)
V / Å^3	4295.8(5)	4188.12(2)
M-O / Å	2.121(8)–2.181(9)	2.066(5)–1.233(6)
M-N / Å	2.236(13)	2.193(7)
M-O100 / Å	2.071(14)	2.044(5)

Table 5.7: Unit cell parameters and bonding distances in the MO_5N octahedra of each structure, showing variation of unit cell and bonding distances with cation radius. Values for STA-12(Ni) from work of Miller *et al.*;[114] cation radii from Shannon;[186] O100 is the chemisorbed water molecule.

In each structure the piperazine ring adopts a chair conformation with the methylenephosphonate groups in an axial conformation. The biggest structural variation is in the MO_5N octahedron. Typical M-O distances increase with increasing cation radius. The greatest variation is in the M-O100 (chemisorbed water) bonding distance. The M-N distance is also significantly longer than the M-O (phosphonate O atom) bonding distances in each structure, due to the slightly larger radius of N compared to O atoms. There are very few other structural differences between the different forms of STA-12.

5.6 Comparison of Dehydration Behaviour of Different Metal Forms of STA-12

In-depth studies of the dehydration behaviour of structures STA-12(Ni), STA-12(Mn), STA-12(Fe) and STA-12(Co) have been reported previously.[113, 114] This section will limit itself to a brief review of results reported by Miller *et al.* and Pearce[113, 114], beginning with a description of the reported dehydration behaviour of STA-12(Ni). New findings on the dehydration behaviour of STA-12(Mg) will be reported and compared with the known behaviours of STA-12 materials. Dehydration behaviour has been analysed using a combined approach of TGA, powder X-ray diffraction, MAS NMR and IR spectroscopies.

5.6.1 Reported Dehydration Behaviour of STA-12(Ni)

Miller *et al.* report that structure STA-12(Ni) dehydrates in a three-step process. The material initially loses physisorbed water in a single step to form a partially dehydrated structure ($Ni_2(H_2O)_2$**L**— STA-12(Ni)-PDH).[114] This material has a framework structure nearly identical to that of the as-prepared material, retaining the circular cross-section ~ 10 Å channels. With further heating, the material loses chemisorbed water in a two-step process, losing first $\frac{2}{3}$ and then $\frac{1}{3}$ of the coordinating water molecules. In a concerted change with the first chemisorbed water loss, $\frac{2}{3}$ of the PO_3C groups become fully coordinated, causing a structural transition from $R\bar{3}$ to $P\bar{1}$ and causing a distortion of the channels to a more elliptical cross-section (*Fig. 5.11*).

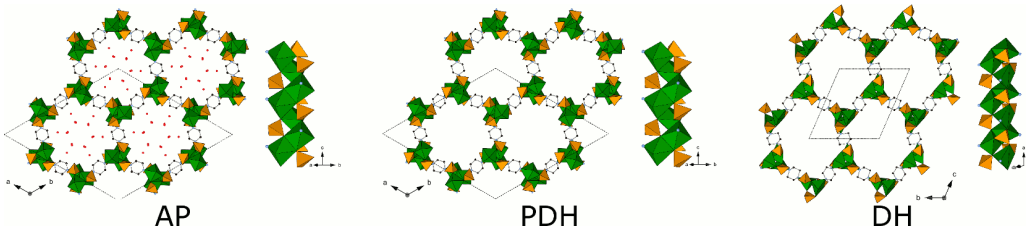

Figure 5.11: Structures reported by Miller *et al.* for the dehydration of structure STA-12(Ni).[114] AP — As-Prepared STA-12(Ni); PDH — STA-12(Ni)-PDH; DH — fully dehydrated STA-12(Ni), showing structural transition to $P\bar{1}$.

5.6.2 Dehydration of STA-12 Studied By TGA

TGA data for the dehydration of the other forms of STA-12 show that, depending on the framework forming metal, a different dehydration behaviour is observed

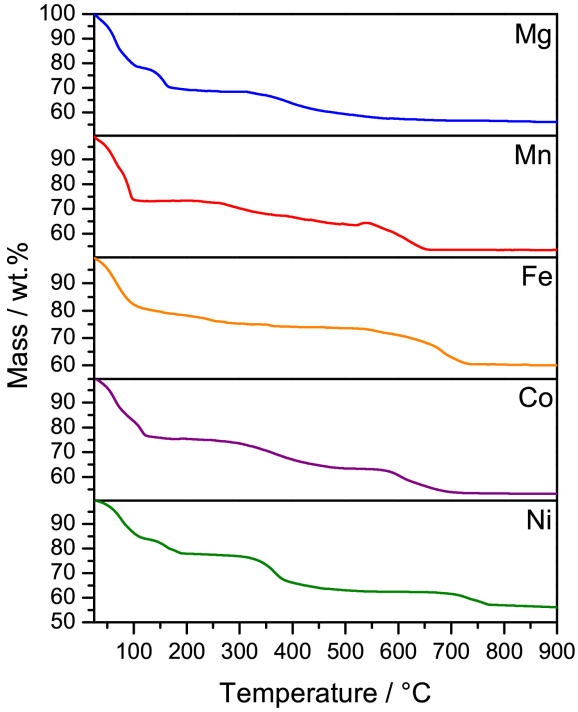

Figure 5.12: TGA plots of each of the forms of STA-12: blue — STA-12(Mg); red — STA-12(Mn); orange — STA-12(Fe); purple — STA-12(Co); and greem — STA-12(Ni). Only STA-12(Mg) and STA-12(Ni) show intermediate partially dehydrated structures. STA-12(Fe) does not have a well defined plateau, indicating the fully dehydrated material has poor thermal stability.

(*Fig. 5.12*). The thermal stabilities of the partially dehydrated $M_2(H_2O)_2(\mathbf{L})$ structure (**STA-12(M)**-PDH) of each form show the clearest differences. STA-12(Mg) and STA-12(Ni) show a well defined plateau for this phase, whereas only a knee is observed in the TGA of STA-12(Co). STA-12(Ni) loses chemisorbed water in a two step process, shown in TGA by a weight loss with a slight change in gradient followed by a further weight loss. A similar two stage process is just visible for TGA of STA-12(Co). STA-12(Mg) does not show a step in the loss of chemisorbed water, indicating a different dehydration process is occurring (full analysis of TGA data of STA-12(Mg) is given in *Section 5.4*). STA-12(Mn) and STA-12(Fe) show a single step for the loss of both physisorbed and chemisorbed water, indicating a strongly different dehydration process to the other forms of STA-12. A full analysis of the TGA data of STA-12(Mn), STA-12(Fe) and STA-12(Co) is reported by Pearce.[113]

5.6.3 Dehydration of STA-12 Studied By Powder X-ray Diffraction

Powder X-ray diffraction patterns for samples of STA-12(Mg) dehydrated at a range of different temperatures were collected. Samples were loaded into 0.7 mm glass capillary tubes and heated at the respective temperatures at reduced pressure (1×10^{-4} Torr) for three hours. Data were collected in a Debye-Scherrer geometry using Stoe Stadi P diffractometers at 298 K fitted with either Cu K_α or Fe K_α radiation sources. Capillaries were then broken open and allowed to rehydrated over 24 hours and another diffraction pattern collected on the rehydrated sample. Powder diffraction data for dehydrated and rehydrated STA-12(Mn) (Cu K_α), STA-12(Fe) (Fe K_α) and STA-12(Co) (Fe K_α) collected by G. M. Pearce were also re-analysed to improve the quality of the reported fits for comparison with STA-12(Mg) data (Cu K_α).

Pearce reports the dehydration behaviour of STA-12(Co) is closely related to that of STA-12(Ni),[113] showing a structural transition from $R\bar{3}$ to $P\bar{1}$ but with some loss of long-range order, indicated by the broading of the peaks. Re-refinement of the unit cell parameters by Le Bail fitting,[155] using the cell parameters reported for STA-12(Ni) as a starting model,[114] confirm this result (*Table 5.8*).

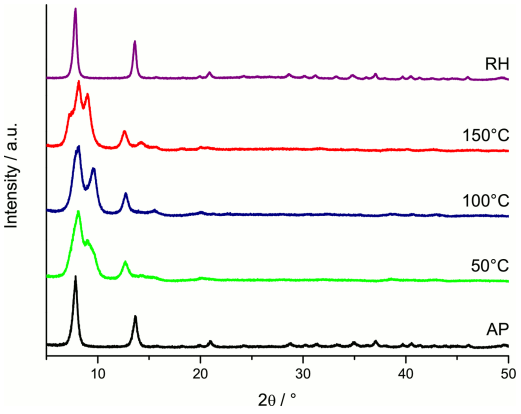

Figure 5.13: Powder X-ray diffraction patterns (Cu K_α) of STA-12(Co) showing the structural transitions on dehydration and their reversibility on rehydration.

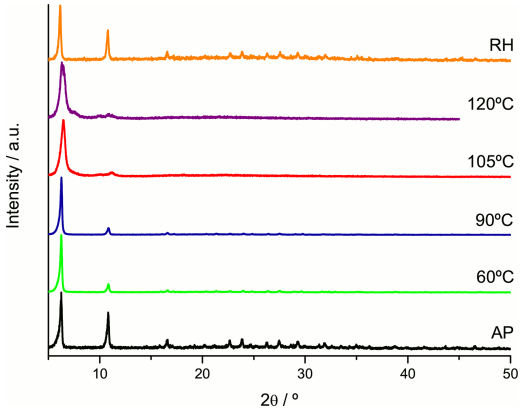

Figure 5.14: Powder X-ray diffraction patterns (Cu K_α) of STA-12(Mg) showing the structural transitions on dehydration and their reversibility on rehydration.

STA-12(Mn) and STA-12(Fe) were reported to retain rhombohedral symmetry on dehydration.[113] Data were re-analysed by indexing the pattern with DICVOL,[152] which gave a unit cell consistent with space group $R\bar{3}$, but with a lower volume than the as-prepared materials. The unit cells were then refined by Le Bail fitting.[155]

	STA-12(Mn)-DH	STA-12(Fe)-DH	STA-12(Co)-DH	STA-12(Ni)-DH
Space Group	$R\bar{3}$	$R\bar{3}$	$P\bar{1}$	$P\bar{1}$
a / Å	26.0701(18)	26.283(18)	6.073(6)	6.03475(5)
b / Å			14.539(8)	14.9156(2)
c / Å	5.9630(6)	5.91(3)	16.053(9)	16.1572(2)
α / °			108.879(17)	112.5721(7)
β / °			92.14(7)	95.7025(11)
γ / °			96.77(8)	96.4950(11)
V / Å^3	3509.8(5)	3540(18)	1330(19)	1318.06(3)
R_{wp}	0.0144 (R)	0.0617	0.0660	-

Table 5.8: Refined unit cells determined from Le Bail analysis[155] of the diffraction patterns of fully dehydrated forms of STA-12. Data for STA-12(Ni)-DH taken from Miller *et al.*[114] (R, Rietveld method used to refine cell of STA-12(Mn)).[147]

The structure of fully dehydrated STA-12(Mn) (STA-12(Mn)-DH) was also re-refined by the Rietveld method[147] to obtain a more chemically sensible structural model (*Section 5.6.5*). The unit cell of STA-12(Mn)-DH is smaller than the unit cell of the as-prepared material in both the a and c directions by 2.51 Å and 0.46 Å respectively, giving a decrease in unit cell volume of $\sim$ 1000 Å^3 (*Table 5.8*).

As reported by Pearce, STA-12(Fe) shows a similar dehydration behaviour to STA-12(Mn), though the magnitude of the unit cell shrinkage is smaller, decreasing by $\sim$ 800 Å^3 (*Table 5.8*).

Diffraction data for STA-12(Mg) show the step-wise dehydration consistent with TGA results (*Sections 5.4 & 5.6.2*). STA-12(Mg) loses physisorbed water at relatively low temperature (60°C) to form the partially dehydrated structure (STA-12(Mg)-PDH). STA-12(Mg)-PDH retains rhombohedral symmetry with little change in the peak positions. The structure has been fully refined by the Rietveld method (*Section 5.6.4*).[147] Further heating results in the removal of coordinated water and leads to peak broadening, indicating a loss in periodicity in the fully dehydrated structure (STA-12(Mg)-DH). Peaks do not split on dehydration, suggesting that STA-12(Mg)-DH retains rhombohedral symmetry, like STA-12(Mn). Unlike STA-12(Mn), there seems to be little change in the unit cell dimensions on dehydration: the (1 1 0) reflection shows only a very small shift (in terms of d-spacing: as-prepared, 13.93 Å; dehydrated, 13.67 Å). The loss of periodicity was fully reversed on exposure to atmospheric moisture. As periodicity is lost on dehydration of STA-12(Mg), it is not possible to determine the structure of the fully dehydrated material. Therefore spectroscopic methods (IR — *Section 5.6.6*; MAS NMR — *Section 5.6.7*) will be used to probe the local structural features and analogies will be made with other STA-12 materials where possible.

5.6.4 Structure of STA-12(Mg)-PDH

A sample of as-prepared STA-12(Mg) was loaded into a 0.7 mm glass capillary tube and heated to 60°C under reduced pressure (1×10^{-4} Torr) for three hours. The capillary was then flame sealed. Powder X-ray diffraction data were collected at 298 K in a Debye-Scherrer geometry using a Stoe Stadi P diffractometer fitted with a Cu K_α source over the range 5–90° 2θ. Data above 65° 2θ were discarded due to the low intensity of diffraction peaks in this region. The structure was refined by Rietveld refinement routines of the GSAS suite of programs,[156, 157] using the structure of as-prepared STA-12(Mg) with physisorbed water molecules removed as a starting point. Profile parameters and background were refined first. Before refinement of the structure, restraints were applied to the bonding distances of the Mg octahedra, Mg-O (2.14 Å); P tetrahedra, P-O and P-C (1.50 Å and 1.85 Å respectively); and C-C and C-N bonds (1.53 Å and 1.51–1.53 Å). The Mg-N distance was not restrained. Restraints were also applied to selected non-bonding distances of the Mg octahedra O···N (3.10 Å respectively); P tetrahedra O···O and O···C (2.45 Å and 2.74 Å); and N···N (diagonal, cross-ring) (2.90 Å), C···N (2^{nd} neighbour) (2.50 Å) and C···C (diagonal, cross-ring; 2^{nd} neighbour outwith ring) (2.90 Å, 2.50 Å). The final Rietveld fit of the data after 1563 cycles was R_{wp} = 0.0558, R_p = 0.0406, $R(F^2)$ = 0.0478 and χ^2 = 1.435 (fit shown in *Fig. 5.15*).

The structure of STA-12(Mg)-PDH is very similar to that of the as-prepared STA-12(Mg), though without physisorbed water in the unidirectional channels (*Fig. 5.16*). Mg is coordinated by four phosphonate O atoms, a piperazinyl N atom and an O atom from a chemisorbed water molecule in a distorted octahedral geometry (*Table 5.9*). Neighbouring MgO_5N octahedra share edges to form helical

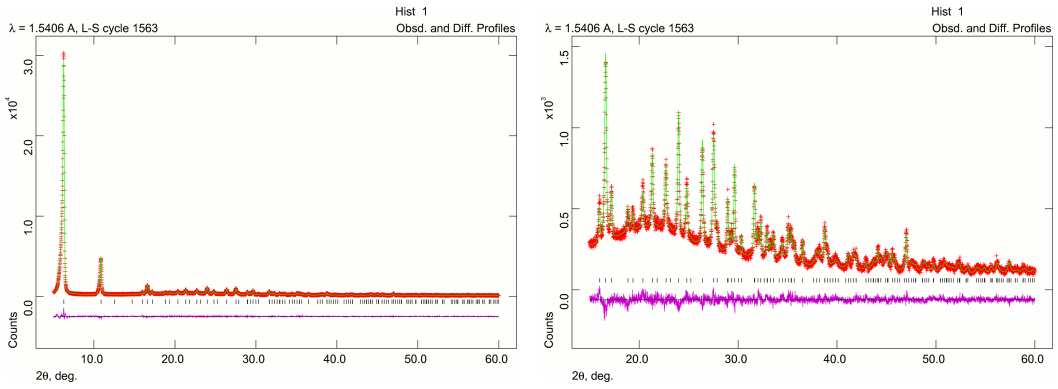

Figure 5.15: Final Rietveld fit for refinement of partially dehydrated structure STA-12(Mg) (R_{wp} = 0.0558).

Bond	Distance / Å	Bond	Distance / Å
Mg1-O2	2.138(8)	P1-O1	1.507(5)
Mg1-O2	2.151(8)	P1-O2	1.523(5)
Mg1-O3	2.058(8)	P1-O3	1.513(5)
Mg1-O3	2.225(8)	P1-C1	1.861(5)
Mg1-N1	2.333(8)		
Mg1-O100	2.155(11)		

Table 5.9: Selected bond distances in the structure of STA-12(Mg)-PDH determined from final Rietveld refinement.

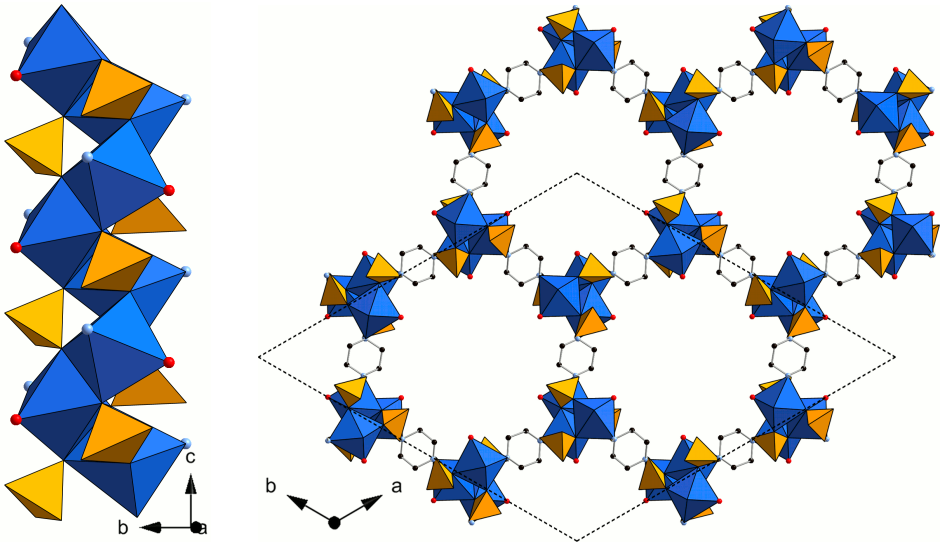

(a) (b)

Figure 5.16: Structure of STA-12(Mg)-PDH. *Left:* Helical chain of edge-sharing MgO_5N octahedra linked by phosphonate tetrahedra. *Right:* View along the *c*-axis showing honeycomb array of 10 Å channels.

chains parallel to the *c*-direction, with PO_3C groups coordinating to the outside of this chain in a bridging mode, leaving a pendant P=O group projecting into the pore channel (P-O1: 1.507(3) Å). Chains are linked in the *a*- and *b*-directions by piperazinyl rings, coordinated to Mg sites through the piperazinyl N atoms, to give a hexagonal array of unidirectional channels parallel to the *c*-direction with an approximate free diameter of 10 Å.

5.6.5 Structure of STA-12(Mn)-DH

A fresh sample of structure STA-12(Mn) was dehydrated in a 0.7 mm quartz glass capillary tube at 150°C under vacuum (1×10^{-4} Torr) for three hours. Laboratory powder diffraction data were collected on this sample using a Stoe Stadi P diffractometer fitted with a Cu K_α source at 298 K in a Debye-Scherrer geometry. Data were collected by G. M. Pearce over the range 5–90° 2θ. Data above 60° were discarded due to low intensity of diffraction peaks. Data were indexed using DICVOL[152] and refined by Le Bail analysis in space group $R\bar{3}$ (hexagonal setting, a = 26.031(7) Å, c = 5.953(3) Å, V = 3493.6(2) Å^3). The structure was then refined by the Rietveld method using the GSAS suite of programs,[156, 157] using the structure of as-prepared structure STA-12(Mn) (with chemisorbed and physisorbed water molecules removed) as a starting point. Profile parameters and background were refined first. Before refinement of the structure, restraints were applied to the bonding distances of the Mn octahedra, Mn-O (2.25 Å); P tetrahedra, P-O and P-C (1.50 Å and 1.85 Å respectively); and C-C and C-N bonds (1.53 Å and 1.51–1.53 Å). The Mn-N distance was not restrained nor, initially, was the Mn-O1 distance. Restraints were also applied to selected non-bonding distances of the Mn octahedra O$\cdots$O and O$\cdots$N (3.00 Å and 3.20 Å respectively); P tetrahedra O$\cdots$O and O$\cdots$C (2.50 Å and 2.74 Å); and N$\cdots$N (diagonal, cross-ring) (2.90 Å), C$\cdots$N (2$^{\text{nd}}$ neighbour) (2.50) and C$\cdots$C (diagonal, cross-ring; 2$^{\text{nd}}$ neighbour, within ring; 2$^{\text{nd}}$ neighbour, outwith ring) (2.90 Å, 2.50 Å, 2.48 Å). After several cycles of refinement, the PO_3C tetrahedron was found to rotate to bring O1 within the coordination sphere of Mn, whilst the piperazinyl ring also rotates. A restraint from Mn-O1 was added (2.25 Å) and further cycles of refinement performed after which the Mn-N distance was found to increase. The distance O3$\cdots$N across the Mn1 site was then restrained (4.44 Å). Little further movement occurred in subsequent cycles of refinement. Profile and background parameters were re-refined and isotropic displacement parameters (U_{Iso}) were then refined, with U_{Iso}s of all atoms constrained to change together. Restraints were gradually reduced and further structural refinements performed to allow the framework to relax. Fourier difference maps showed no additional/excess electron density. Final cycles of refinement were performed with both atomic positions and U_{Iso} parameters refined. A final Rietveld fit of the data after 4338 cycles was R_{wp} = 0.0144, R_p = 0.0110, R(F^2) = 0.0807 and χ^2 = 1.918 (fit shown in *Fig. 5.17*).

As discussed, the dehydrated form of structure STA-12(Mn) shows a large reduction in unit cell volume ($\sim$ 1000 Å^3) due to a contraction of the a and c parameters (*Section 5.6.3*). The origin of this contraction is the coordination of

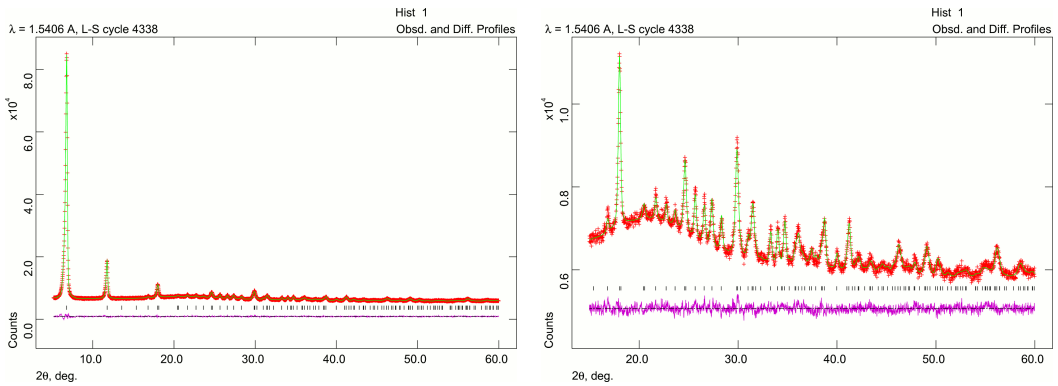

Figure 5.17: Final Rietveld fit for refinement of dehydrated structure STA-12(Mn) (R_{wp} = 0.0144).

Bond	Distance / Å	Bond	Distance / Å
Mn1-O1	2.25(2)	P1-O1	1.500(6)
Mn1-O2	2.212(9)	P1-O2	1.517(6)
Mn1-O2	2.312(12)	P1-O3	1.510(6)
Mn1-O3	2.280(12)	P1-C1	1.859(6)
Mn1-O3	2.331(11)		
Mn1-N1	2.338(14)		

Table 5.10: Selected bond distances in the structure of STA-12(Mn)-DH determined from final Rietveld refinement.

the Mn1 site by O1 (Mn1-O1: 2.25(2) Å) to retain an octahedral coordination environment, achieved by the concerted rotation of the PO_3C group and the piperazinyl ring. These rotations lead to a change in the conformation of the methylenephosphonate groups from axial, with respect to the piperazinyl ring (in the as-prepared material), to equatorial. The combined effect of these structural changes is the contraction of the unit cell. After the structural transition, the material retains rhombohedral symmetry (space group $R\bar{3}$). The heavily distorted octahedral coordination environment about Mn is provided by five PO_3C O atoms and a piperazinyl N atom (*Table 5.10*). Each PO_3C group coordinates four Mn sites: O2 is shared between two sites in a monodentate coordination mode, whilst O3 coordinates one Mn site in a monodentate mode and with O1, coordinates the fourth site in a bidentate coordination mode. Surprisingly the phosphonate tetrahedron shows little distortion as a result of this unprecedented coordination mode (*Table 5.10*). The final structure retains open 10 Å channels, but Pearce reports it to be non-porous to N_2 and with minimal porosity for CO_2.[113] This low porosity is thought to be caused by changes to the surface of individual crystallites, as a result of the bulk structural transition, which lead to the blocking or closure of pore openings.

5.6.6 Dehydration of STA-12 Studied by IR

Reported results of *in situ* IR spectroscopic studies on the dehydration of STA-12(Mn) and STA-12(Co) will be reviewed[113] and compared against new data collected on STA-12(Mg).

IR spectra for the dehydration and fully dehydrated structures of STA-12(Ni) and STA-12(Co) are closely related (*Fig. 5.18*) and confirm the model of dehydration reported by Pearce from TGA and powder X-ray diffraction data.[114] Substantial changes occur in the region 4000–1500 cm^{-1}: bands due to physisorbed water (ν(O-H): 3250 cm^{-1} and δ(O-H): 1650 cm^{-1}) decrease in intensity, accompanied by the growth of a sharp peak due to chemisorbed water coordinated to Co sites, which is no longer engaged in H-bonding (ν(O-H): 3690 cm^{-1}). An additional sharp peak at 1185 cm^{-1} is also observed, assigned to the formation of P=O groups (ν(P=O)) projecting into the pores.

STA-12(Mn) shows a very different evolution of the IR spectra. Bands due to physisorbed water (ν(O-H): 3450 cm^{-1} and δ(O-H): 1620 cm^{-1}) are retained in the fully dehydrated structure, albeit of much lower intensity. In the partially dehydrated structure a complex band is present for chemisorbed water no longer engaged in H-bonding (ν(O-H): 3609 cm^{-1}), though it is of much weaker intensity

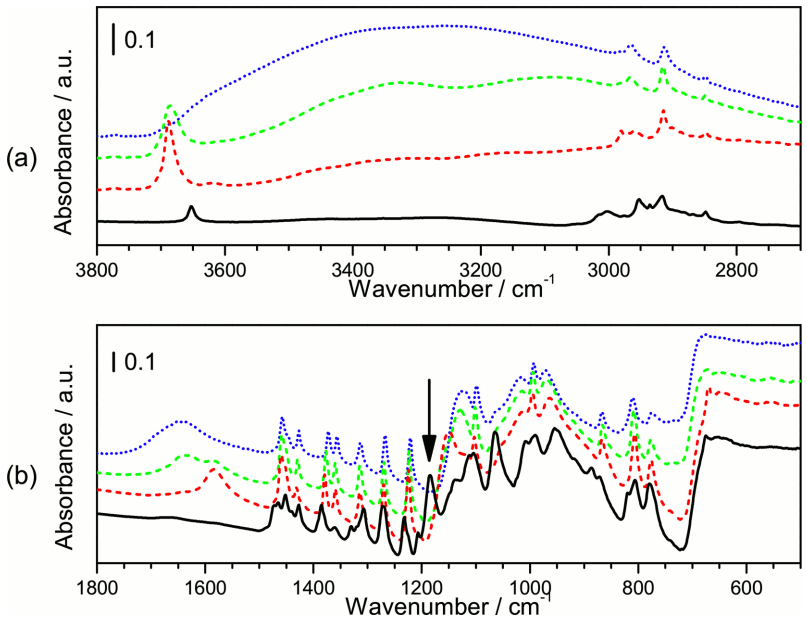

Figure 5.18: IR spectra showing the progressive dehydration of structure STA-12(Co) in the regions 3800–2700 cm^{-1} (*top*) and 1800–500 cm^{-1} (*bottom*), from as-prepared (blue) through partially dehydrated (green, red) to fully dehydrated (black). Arrow indicates peak at 1185 cm^{-1} due to P=O groups.

than in structure STA-12(Co). This band disappears in the fully dehydrated material. No ν(P=O) peak is observed, indicating that, unlike STA-12(Ni)-DH and STA-12(Co)-DH PO_3C, groups are fully coordinating (in agreement with the structure of STA-12(Mn)-DH — *Section 5.6.5*).

IR spectra of STA-12(Mg) (*Fig. 5.20*) show a more complex evolution of the ν(O-H) chemisorbed water peak on dehydration than structure STA-12(Co), with possible similarity to STA-12(Mn) (peak intensity in STA-12(Mn) is too weak to be certain). The peak in the as-prepared material (3680 cm^{-1}) shifts to 3708 cm^{-1} and a shoulder develops at 3692 cm^{-1}. On further dehydration, a third peak develops at 3672 cm^{-1}, whilst the intensity of the peaks at 3708 cm^{-1} and 3692 cm^{-1} erode to leave only this newly developed peak in the fully dehydrated material, albeit of significantly reduced intensity. In contrast, the δ(O-H) peak evolves in much the same way as the structure STA-12(Co). This sequence of changes of the ν(O-H) peak is caused by changes of the H-bonding environment of the chemisorbed water and changes to the local crystallographic environment which occur on dehydration and result in the loss of periodicity in the material. Bands due to the framework evolve in a similar way to STA-12(Mn), with the same splitting of peaks observed in the ν(C-H) (3100–2800 cm^{-1}), CH_2 bending (1470–1350 cm^{-1}) and phosphonate tetrahedron stretching mode (1160–950 cm^{-1}) regions. A slight

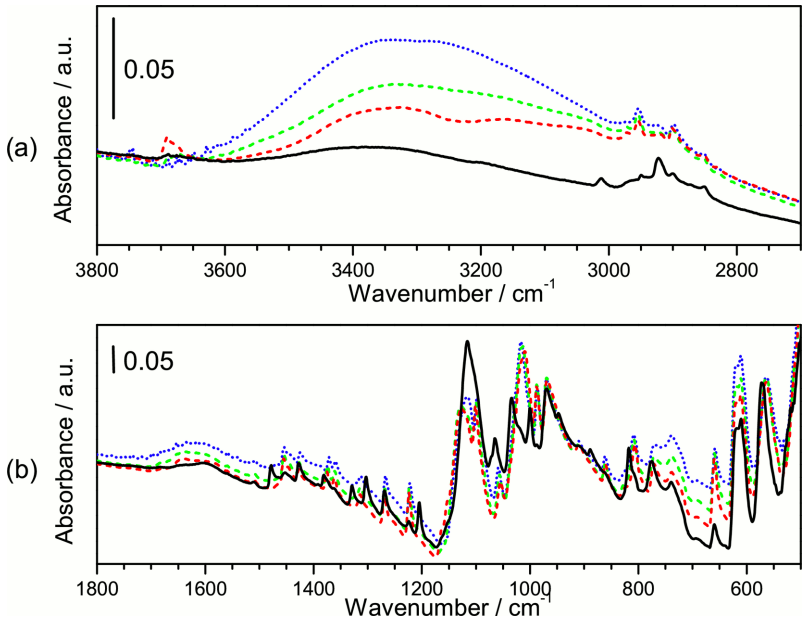

Figure 5.19: IR spectra showing the progressive dehydration of structure STA-12(Mn) in the regions 3800–2700 cm^{-1} (*top*) and 1800–500 cm^{-1} (*bottom*), from as-prepared (blue) through partially dehydrated (green, red) to fully dehydrated (black).

blue shift (+40 cm^{-1}) of the ν(C-H) band is also observed. The growth of a band at 1193 cm^{-1} indicates the presence of P=O groups in the structure, as observed for both structures STA-12(Ni) and STA-12(Co). It seems likely from these features that structure STA-12(Mg) retains a similar local symmetry in its framework to the as-prepared material, as did structure STA-12(Mn), but retaining uncoordinated P=O bonds, similar to STA-12(Co) and STA-12(Ni).

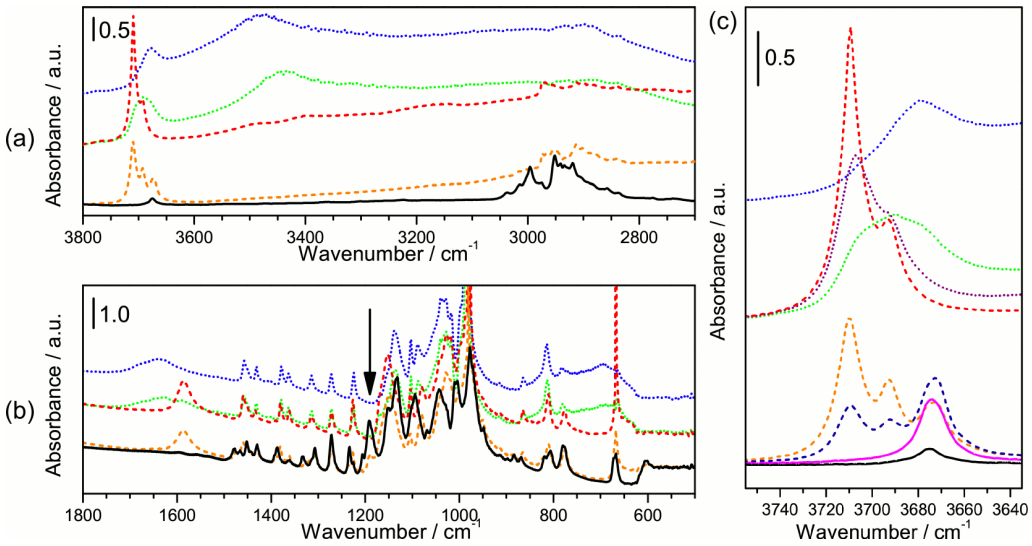

Figure 5.20: IR spectra showing the progressive dehydration of structure STA-12(Mg) in the regions 3800–2700 cm^{-1} (*top left*), 1800–500 cm^{-1} (*bottom left*) and the OH stretching region (*right*), from as-prepared (blue) through partially dehydrated (green, purple, red, orange, dark blue, pink) to fully dehydrated (black).

5.6.7 MAS NMR Study of Fully Dehydrated STA-12(Mg)

A sample of as-prepared STA-12(Mg) was loaded into a 4 mm NMR rotor and placed in an oven at 160°C for 36 hours to ensure complete dehydration. Solid-state MAS NMR spectra of the dehydrated material are consistent with short-range retention of the crystal structure of the as-prepared material. Three resonances are observed in the ^{13}C CP MAS NMR spectrum of the dehydrated material (*Fig. 5.21a*) and these are assigned by analogy to the spectrum of the as-prepared material (*Section 5.4.3*). A doublet (centred at 48.89 ppm, peaks at 49.38 & 48.39 ppm, J = 149.8 Hz) is assigned to the C1 site, split by coupling to P1, to which it is directly bonded. Resonances at 47.30 ppm and 43.22 ppm are assigned to C2 and C3. The ^{31}P MAS NMR spectrum (*Fig. 5.21b*) shows a single resonance at 18.26 ppm, similar to that observed for the as-prepared rhombohedral structure (*Section 5.4.3*).

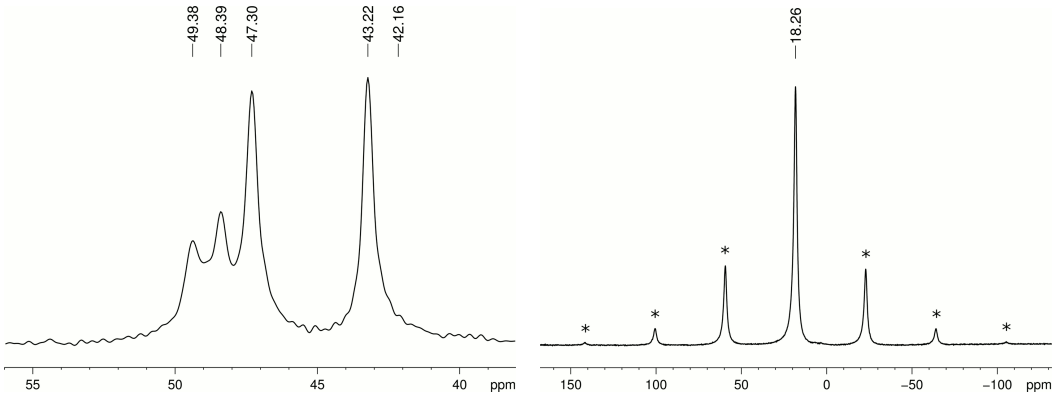

(a) ^{13}C MAS NMR spectrum (b) ^{31}P MAS NMR spectrum

Figure 5.21: MAS NMR spectra of dehydrated STA-12(Mg) prepared by heating a sample of the as-prepared material at 160°C for 36 hours.

5.6.8 Structure of Fully Dehydrated Structure STA-12(Mg)

Evidence from TGA and IR spectroscopy indicates that STA-12(Mg) dehydrates by a similar process to STA-12(Co) and STA-12(Ni). All three materials (STA-12(Mg), STA-12(Co) & STA-12(Ni)) form a partially dehydrated $M_2(H_2O)_2(\mathbf{L})$ phase in which chemisorbed H_2O molecules remain bound to metal cations. Differences between the dehydration of STA-12(Mg) and STA-12(Ni) are observed in the loss of the chemisorbed water molecules to form the fully dehydrated form, with H_2O lost in a single step by STA-12(Mg) rather than in a two step process as the other materials do.

Powder X-ray diffraction and solid-state MAS NMR spectroscopy indicate

STA-12(Mg)-DH is more similar to STA-12(Mn)-DH. Powder X-ray diffraction shows a broadening of diffraction peaks due to a loss of long range order. No splitting of peaks is observed in the dehydrated material, indicating the retention of rhombohedral symmetry, but unlike STA-12(Mn), peaks do not shift relative to the as-prepared material. MAS NMR spectra show no additional resonances for STA-12(Mg)-DH, which is also consistent with a retention of rhombohedral symmetry.

IR spectra show features of both STA-12(Ni)-DH and STA-12(Mn)-DH. A similar evolution of the chemisorbed H_2O peaks to STA-12(Mn) indicates a similarity between the processes of loss of these molecules. However, STA-12(Mg)-DH shows a peak for ν(P=O) similar to STA-12(Ni)-DH.

STA-12(Mg)-DH retains an open structure (as indicated by the porosity of the material — *see Section 5.7*) with local $R\bar{3}$ symmetry. As Mg^{2+} cations possess no d-electrons, there can be no gain in crystal field stabilisation energy from re-organising the coordination environment about the cation on loss of chemisorbed water. Pendant P=O groups therefore remain uncoordinated, as in STA-12(Ni). There is also no driving force for a concerted structural distortion on dehydration, and domains form where different regions of the crystal distort in slightly different ways to reduce the pore volume. It is likely that STA-12(Mg)-DH is closely related to STA-12(Mg)-PDH (*Section 5.6.4*).

5.7 Porosity of Different Forms of STA-12

The porosity to N_2 at 77 K and CO_2 at 196 K of samples of the newly synthesised STA-12(Mg) has been investigated. Porosities of STA-12(Co) and STA-12(Ni) prepared using the modified syntheses (*Section 5.1*) have also been determined and compared to STA-12(Mg). Materials were activated (*i.e.* dehydrated) by heating as-prepared samples of each solid to 180°C for three hours under vacuum (1×10^{-4} Torr). The porosity of the materials is compared using surface area (calculated using the BET method, described by Bae *et al.*)[175], micropore volume and maximum total uptake (both calculated using the Dubinin-Radushkevitch — D-R — equation[163]). *In situ* IR spectra have also been obtained for the adsorption of both CO at 77 K and CO_2 at 196 K on structure STA-12(Mg).

5.7.1 N_2 and CO_2 Adsorption Isotherms

All three structures (STA-12(Ni), STA-12(Co) and STA-12(Mg)) are porous to N_2 and CO_2 (*Figs. 5.22, 5.23 & 5.24*), showing Type I isotherms which are characteristic of microporous materials.[4] STA-12(Co) shows a slight gradient in the isotherm above the micropore region and hysteresis at the highest pressures ($\frac{p}{p_0} > 0.95$) (*Fig. 5.23*), attributed to surface and inter-crystallite adsorption, due to the small particle size. Of the three materials, STA-12(Ni) shows the greatest uptake of N_2, whereas STA-12(Mg) shows the greatest uptake for CO_2. The greater porosity of STA-12(Ni) to N_2 is a result of its smaller particle size, making channels shorter in length and therefore less susceptible to pore blocking. STA-12(Mg) shows a higher uptake of CO_2 because of a slightly higher affinity for CO_2 compared with STA-12(Ni). At higher pressure it is expected that STA-12(Ni) would show an equally high loading of CO_2. The low porosity of STA-12(Co) is attributed to the lower crystallinity of dehydrated structure STA-12(Co), leading to more blocked pores. This material has a higher maximum uptake than previously reported samples of STA-12(Co),[113] thanks to the smaller overall particle size.

	STA-12(Mg)	STA-12(Co)	STA-12(Ni)
BET Surface Area / $m^2\ g^{-1}$	506.0(8)[a]	355(1)[b]	675(1)[c]
Pore Volume / $cm^3\ g^{-1}$	0.20	0.14	0.26
N_0 (N_2) (D-R) / mmol g^{-1}	5.72	4.10	7.63
N_0 (CO_2) (D-R) / mmol g^{-1}	8.54	6.00	8.05

Table 5.11: Comparison of the BET surface area (calculated following the method of Bae *et al.*[175]) and pore volume, calculated from N_2 adsorption, and maximum micropore loadings (N_0) for N_2 and CO_2 (calculated using the Dubinin-Radushkevitch equation[163])

[a] $\frac{p}{p_0}$ linear range: 0.002–0.011
[b] $\frac{p}{p_0}$ linear range:0.001–0.010
[c] $\frac{p}{p_0}$ linear range: 0.001–0.010

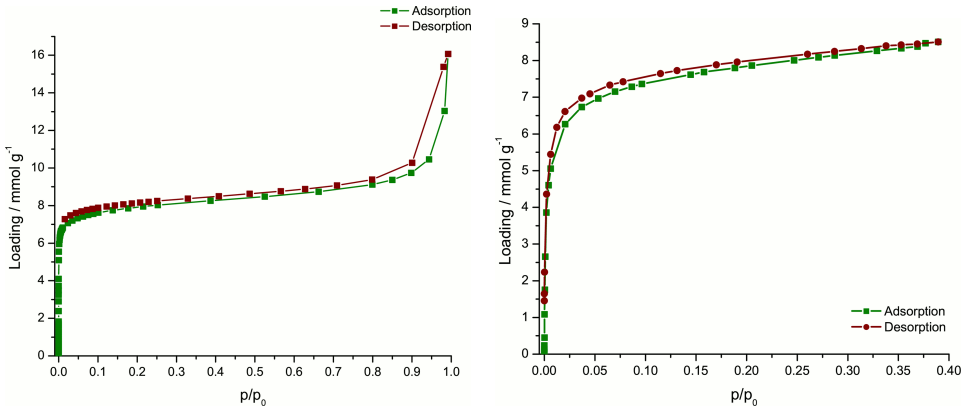

(a) N_2 isotherm at 77 K (b) CO_2 isotherm at 196 K

Figure 5.22: N_2 isotherm at 77 K (*left*) and CO_2 isotherm at 196 K (*right*) for adsorption by STA-12(Ni).

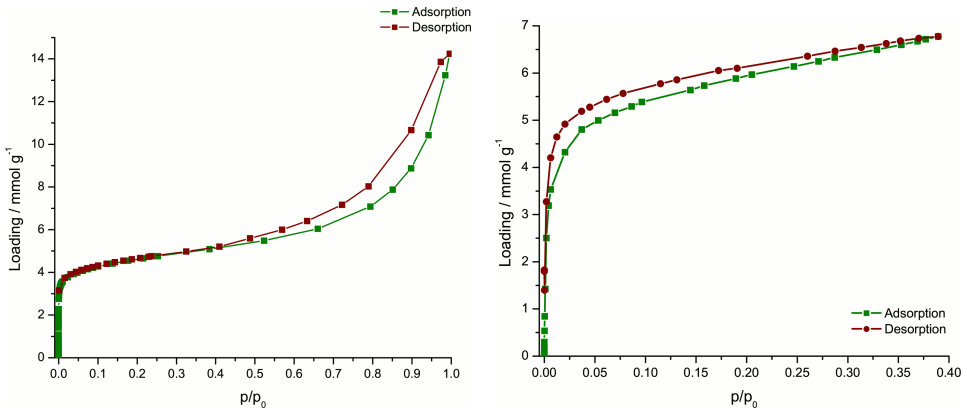

(a) N_2 isotherm at 77 K (b) CO_2 isotherm at 196 K

Figure 5.23: N_2 isotherm at 77 K (*left*) and CO_2 isotherm at 196 K (*right*) for adsorption by STA-12(Co).

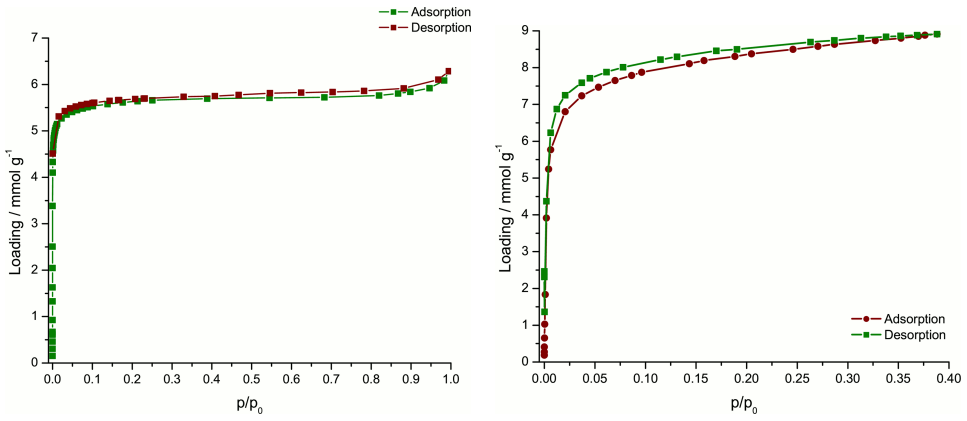

(a) N_2 isotherm at 77 K (b) CO_2 isotherm at 196 K

Figure 5.24: N_2 isotherm at 77 K (*left*) and CO_2 isotherm at 196 K (*right*) for adsorption by STA-12(Mg).

5.7.2 IR Spectroscopic Study of the Adsorption of CO_2 & CO By Structure STA-12(Mg)

In addition to the porosimetry measurements, the adsorption of CO_2 at 303 K and CO at 77 K have been studied by *in situ* IR spectroscopy. Similar experimental results have been reported prevously for STA-12(Ni) and STA-12(Co).[113, 114] A pelletised, fresh sample of STA-12(Mg) was activated at 180°C for three hours under vacuum (1×10^{-4} Torr). The adsorbate species was then progressively dosed on and spectra recorded with increasing coverage (*Fig. 5.25*). The CO_2 spectrum shows a central peak with maximum at 2339 cm^{-1}, attributed to the ν_3 band of physisorbed CO_2, and two shoulders on the high (2357 cm^{-1}) and low (2328 cm^{-1}) frequency sides, which can be assigned to frustrated rotations of CO_2 molecules. The frequency of these bands and the fact that they are easily removed under vacuum suggests the principal species is weakly physisorbed CO_2. The red-shift of the main band is attributed to confinement effects, as observed for silicalite.[191] A strongly chemisorbed species would be expected to show a band at 2353 cm^{-1}, as reported for the $Mg\cdots CO_2$ complex formed in CPO-27(Mg), which is structurally similar to STA-12(Mg).[192] The behaviour of structure STA-12(Mg) is very similar to that previously reported for STA-12(Ni).[114]

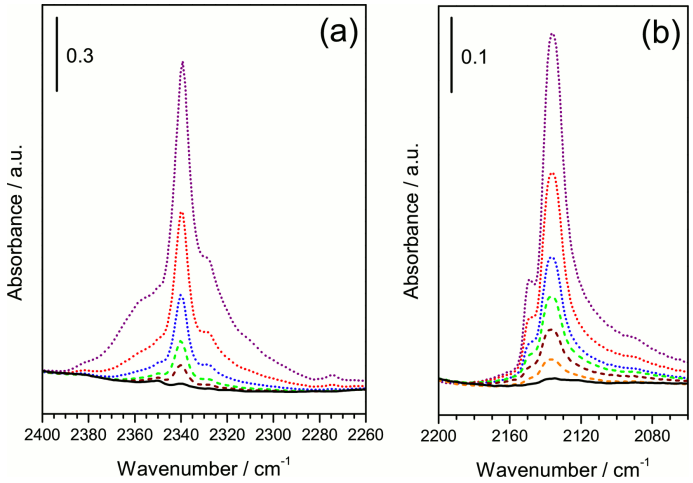

Figure 5.25: IR spectra for increasing loadings of CO_2 at 303 K (*left*) and CO at 77 K (*right*) adsorbed in STA-12(Mg).

IR spectra for the adsorption of CO show a similarly weak interaction (*Fig. 5.25*). The main absorption band at 2135 cm^{-1} corresponds to physically adsorbed CO, whilst a minor component at 2148 cm^{-1} is attributed to CO interacting with open Mg sites. This weak signal and only slightly blue shifted value indicates a weak affinity of the Mg sites for the adsorbate CO.[192]

5.8 Magnetic Measurements on Different Forms of STA-12

Measurements of the magnetic susceptibility have been made on three forms of STA-12 (STA-12(Mn), STA-12(Co) & STA-12(Ni)). Field cooled and zero-field cooled data were collected in the range 4–300 K using field strengths of 1 kOe and 40 kOe (*Fig. 5.26*).

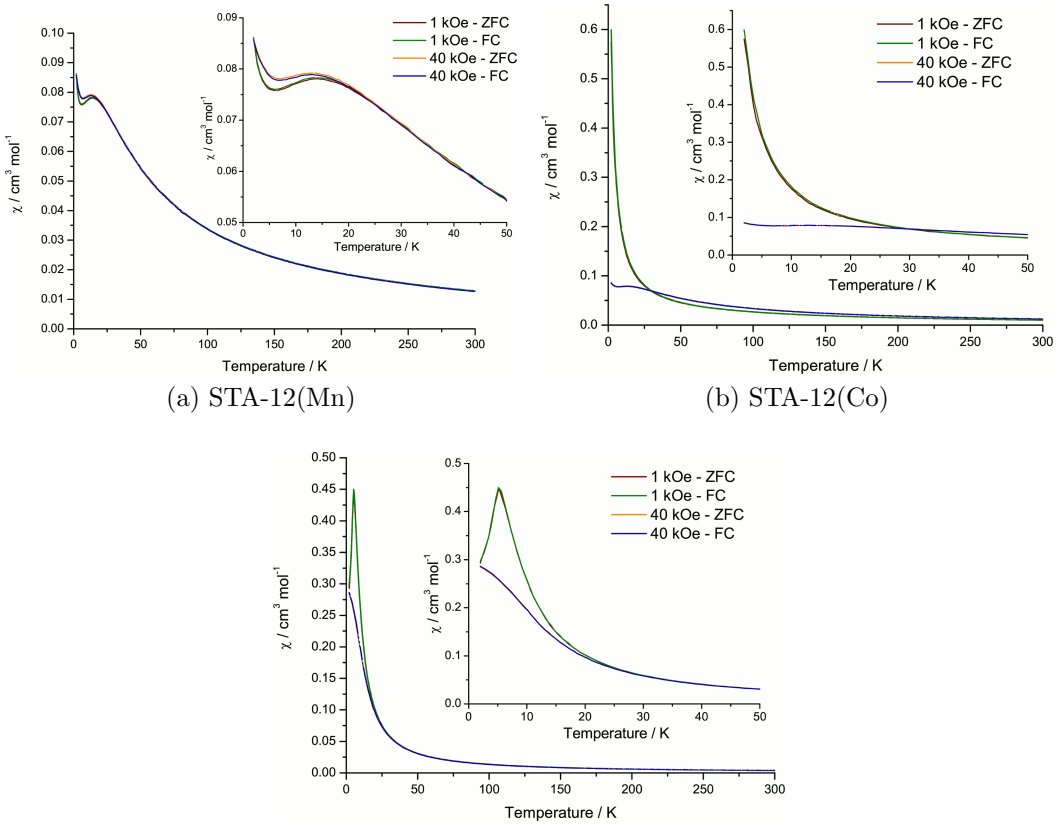

(a) STA-12(Mn)

(b) STA-12(Co)

(c) STA-12(Ni)

Figure 5.26: χ versus T plots for STA-12(Mn) (*top left*), STA-12(Co) (*top right*) and STA-12(Ni) (*bottom*).

$1/\chi$ versus T plots (*Fig. 5.27*) confirm the 2+ oxidation state for STA-12(Mn) and STA-12(Ni). Spin-only effective magnetic moments were calculated by fitting the Curie-Weiss paramagnetic region of the plot. STA-12(Mn) and STA-12(Ni) gave $\mu_{eff}(SO)$ values at 1 kOe of 5.79 B.M. (S = 2.44, five unpaired e^-) and 3.07 B.M. (S = 1.11, two unpaired e^-) respectively. The magnetic moment of STA-12(Co) was not consistent with a 2+ oxidation state ($\mu_{eff}(SO)$ = 5.16B.M.; S = 2.13, four unpaired electrons. This discrepancy is attributed to spin-orbit coupling.

χ versus T plots (*Fig. 5.26a*) show STA-12(Mn) has a significantly weaker

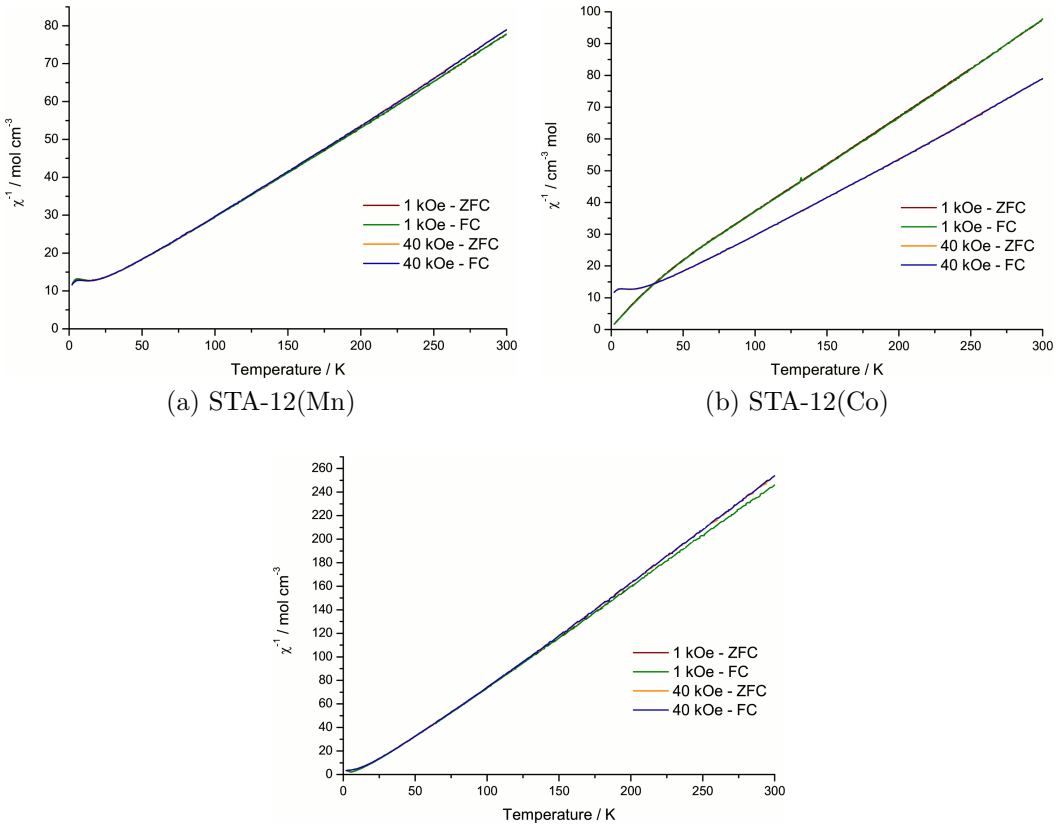

(a) STA-12(Mn)

(b) STA-12(Co)

(c) STA-12(Ni)

Figure 5.27: $1/\chi$ versus T plots for STA-12(Mn) (*top left*), STA-12(Co) (*top right*) and STA-12(Ni) (*bottom*).

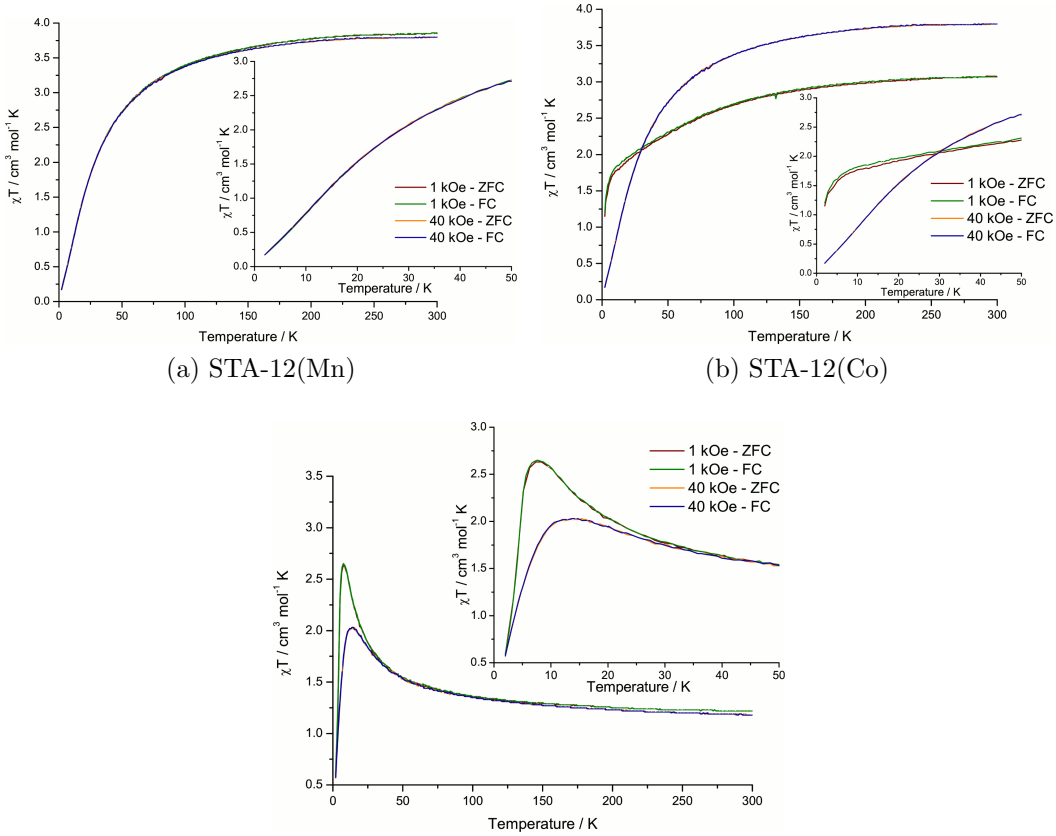

(a) STA-12(Mn)

(b) STA-12(Co)

(c) STA-12(Ni)

Figure 5.28: χT versus T plots for STA-12(Mn) (*top left*), STA-12(Co) (*top right*) and STA-12(Ni) (*bottom*).

magnetic susceptibility than STA-12(Co) or STA-12(Ni). At $\sim$ 15 K STA-12(Mn) shows a magnetic phase transition. The negative gradient of the χT versus T plot indicates that the phase transition is to an anti-ferromagnetic phase (*Fig. 5.28a*).

STA-12(Co) shows a similar anti-ferromagnetic phase transition in its χT versus T plots (*Fig. 5.28b*). χ versus T plots show only increasing magnetic susceptibility with decreasing temperature (*Fig. 5.26b*). The $1/\chi$ versus T plot gives a Néel temperature for STA-12(Co) of -2.15 K.

The magnetic behaviour of STA-12(Ni) is most similar to that of the reported CPO-27(Co).[193] At 1 kOe, STA-12(Ni) shows a transition to an anti-ferromagnetic phase, indicated by both decreasing χ below $\sim$ 7 K (*Fig. 5.26c*) and by the decreasing χT versus T plot at low temperature (*Fig. 5.28c*).

5.9 Other Structures Formed During Optimisation of Syntheses of STA-12(Mg)

5.9.1 Structure of Mg(**L**H$_2$)·1.5H$_2$O — Mg(**L**H$_2$)

Mg(**L**H$_2$) was obtained from reactions with the initial composition 2.0 : 1.0 : 300 (Mg(AcO)$_2$: H$_4$**L** : H$_2$O). Although not obtained phase pure, it was possible to obtain a crystal of the material suitable for single crystal diffraction. The structure of Mg(**L**H$_2$) was solved using the Sir2008 package[141] in space group $P\bar{1}$ (a = 8.250(2) Å, b = 9.0925(18) Å, c = 9.174(2) Å, α = 63.208(10)°, β = 86.871(18)°, γ = 79.121(16)°, V = 602.9(2) Å^3). The structure was refined using the SHELXL routine of SHELX-97.[140] All framework non-hydrogen atoms were located from the initial structure solution and solvent water O atoms were located in the first cycles of refinement by Fourier difference maps. Protons bound to piperazinyl N atoms were also located by Fourier mapping, whilst those attached to C atoms were placed geometrically with position and U$_{Iso}$ constrained to ride on the bonded C atom. The structure was refined further until all significant electron density had been accounted for and the structural shift had reduced to zero. A fit of R$_1$ = 0.0496 (R$_{w2}$ = 0.1142) was obtained.

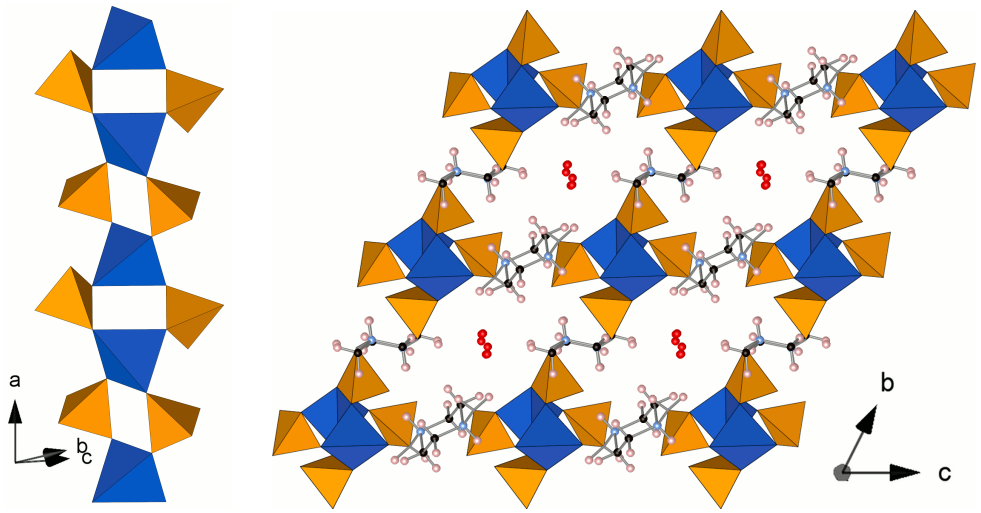

(a) (b)

Figure 5.29: Structure of Mg(**L**H$_2$). *Left:* Chain of linked [Mg$_2$P$_2$O$_4$] rings. *Right:* View along the a-axis showing narrow channels occupied by physisorbed water molecules.

Structure Mg(**L**H$_2$) is isostructural with the Mn$^{(II)}$, Co$^{(II)}$, Fe$^{(II)}$ and Zn$^{(II)}$ materials reported by LaDuca *et al.*[103] and Groves *et al.*[104, 105] respectively. The formula unit of the structure is Mg(**L**H$_2$)·1.5H$_2$O, with two formula units per unit

Bond	Distance / Å	Bond	Distance / Å	Bond	Distance / Å
Mg1-O1	1.909(3)	P1-O1	1.516(3)	P11-O11	1.533(3)
Mg1-O2	1.955(3)	P1-O2	1.535(3)	P11-O12	1.518(3)
Mg1-O11	1.940(3)	P1-O3	1.509(3)	P11-O13	1.508(3)
Mg1-O12	1.926(3)	P1-C1	1.831(4)	P11-C11	1.834(4)

Table 5.12: Selected bond distances and angles for MgP_2O_7.

cell. Each Mg^{2+} cation is tetrahedrally coordinated by four PO_3C groups with Mg-O distances in the range 1.909(3)–1.955(3) (*Table 5.12*). The two crystallographically independent PO_3C groups coordinate Mg through two O atoms (P1: O1, O2; P11: O11, O12) leaving two O atoms, with shorter P-O distances (O3 and O13 — *Table 5.12*) projecting into the pore space which may engage in H-bonding. Two Mg cations and two PO_3C groups link to form $[Mg_2P_2O_4]$ rings which are polymerised into chains parallel to the *a*-axis (*Fig. 5.29a*). Chains are linked in the *b*- and *c*-directions by piperazinyl moieties with a chair conformation and with methylenephosphonate groups equatorial, to form an array or rhombic channels (*Fig. 5.29b*). Piperazinyl N atoms are protonated and engage in H-bonding with pendant P=O groups of the PO_3C groups (N1-H1$\cdots$O13: 1.65(5) Å; N11-H11$\cdots$O3: 1.73(4) Å), acting to direct crystallisation of this structure. Channels within the framework are occupied by physisorbed water molecules, which have short contacts with the framework (O2-O100: 2.78(2) Å; O2-O101: 2.81(3) Å; O11-O102: 2.79(2) Å) and with one another (O101-O102: 2.78(2) Å), indicating an H-bonding network. No further characterisation of this material has been performed.

5.9.2 Structure of $MgP_2O_7 \cdot 3.5H_2O$ — MgP_2O_7

A reaction of composition 1.0 : 2.0 : 1500 ($Mg(AcO)_2$: $H_4\mathbf{L}$: H_2O) yielded a mixture of plate-like crystals of $MgP_2O_7 \cdot 3.5H_2O$ (MgP_2O_7) and fans of needles of another unidentified phase. The structure of MgP_2O_7 was previously solved from powder diffraction data and its properties reported by Kongshaug *et al.*[189] In Kongshaug's synthesis, $Mg(AcO)_2$ was mixed with phosphoric acid and DABCO (or another amine such as ethylenediamine), which acts to adjust the pH, to yield a phase pure powder of MgP_2O_7. Breakdown of $H_4\mathbf{L}$ will yield a similar composition to this synthesis gel and so it is unsurprising that MgP_2O_7 was obtained.

Crystals of MgP_2O_7 suitable for single crystal X-ray diffraction were obtained and the structure determined was found to be very similar to the structure reported from powder diffraction data.[189] The structure was solved using the Sir2008 package[141] in space group $P\,2_1/a$ (a = 9.229(3) Å, b = 8.029(3) Å,

c = 10.940(4) Å, β = 90.175(6)°, V = 810.6(5) Å^3). Structure solution located all ordered non-H atoms. During cycles of refinement, using the SHELXL routine of SHELX-97,[140] Fourier difference maps indicated that O101 and O103 were disordered over two sites (O101 with O102 at a distance of 0.854(8) Å; O103 with O104 at 0.793(9) Å). After modelling this disorder, only peaks corresponding to H atoms remained in the Fourier difference maps. The positions of H atoms were restrained to ensure a chemically sensible geometry for the water molecules. It was not possible to refine the U_{Iso} values of all of the water protons and therefore, where necessary, these were fixed 0.025. H atoms for all water molecules were located. Further cycles of refinement were then performed to allow the structure to relax. A final fit of R_1 = 0.0400 (R_{w2} = 0.1070) was achieved.

MgP_2O_7 consists of layers of Mg-P_2O_7 pillared by $MgO_2(OH_2)_4$ groups (*Fig. 5.30*). Selected bond distances and angles are given (*Table 5.13*). There are three crystallographically distinct Mg sites in the crystal structure, all with slightly distorted octahedral coordination environments. Mg1 and Mg2 form edge-sharing chains of Mg^{2+} cations parallel to the *b*-direction, which are linked by P_2O_7 groups to form layers in the *ab*-plane. Mg1 has an axially elongated octahedral coordination environment, with four equatorial O atoms provided by two P_2O_7 groups coordinating in a bidentate chelating mode (Mg-O: 2.011(4)–2.0589(19) Å). Two axial O atoms from two monodentate P_2O_7 groups (Mg-O: 2.267(6) Å). Mg2 is coordinated by three monodentate and one bidentate P_2O_7 groups (Mg-O: 2.013(6)–2.119(3) Å) and a water molecule (Mg-O: 2.072(6) Å) which projects into the interlayer region. P_2O_7 groups are comprised of two distorted corner-sharing PO_4 tetrahedra, which use all six available O atoms to coordinate Mg cations. P-O bonding distances to the shared O atom (O4) are longer than to those involved in coordinating Mg sites (P-O4: 1.622(3)–1.625(3) Å vs P-O: 1.510(3)–1.528(5) Å). O6 coordinates to Mg3 (P-O6: 1.493(4) Å), forming the structural pillar between layers. Mg3 has an axially contracted octahedral coordination environment, with short Mg-O6 contacts from the layers (Mg-O6: 1.952(6) Å) and longer equatorial Mg-OH_2 bonds to disordered water molecules (Mg-OH_2: 2.060(5)–2.136(5) Å). Within the pillared layered structure there are small cavities with narrow windows between them ($\sim$ 1 Å) containing physisorbed water molecules which H-bond with water molecules coordinated to Mg3.

The structure is found to be in good agreement with that reported by Kongshaug, showing the same distortions of the Mg octahedra. No further characterisation of this material has been performed.

Bond	Distance / Å	Bond	Distance / Å	Bond	Distance / Å
Mg1-O7	2.011(4)	Mg2-O2	2.085(6)	Mg3-O103	2.136(5)
Mg1-O7	2.011(4)	Mg2-O7	2.119(3)	Mg3-O103	2.136(5)
Mg1-O3	2.0589(19)	Mg3-O6	1.952(6)	P1-O1	1.510(3)
Mg1-O3	2.0589(19)	Mg3-O6	1.952(6)	P1-O3	1.516(5)
Mg1-O1	2.267(6)	Mg3-O101	2.060(5)	P1-O2	1.518(3)
Mg1-O1	2.267(6)	Mg3-O101	2.060(5)	P1-O4	1.622(3)
Mg2-O5	2.013(6)	Mg3-O104	2.078(9)	P2-O6	1.493(4)
Mg2-O3	2.065(4)	Mg3-O104	2.078(9)	P2-O5	1.518(2)
Mg2-O100	2.072(6)	Mg3-O102	2.124(7)	P2-O7	1.528(5)
Mg2-O2	2.080(3)	Mg3-O102	2.124(7)	P2-O4	1.625(3)

Table 5.13: Selected bond distances and angles for MgP_2O_7.

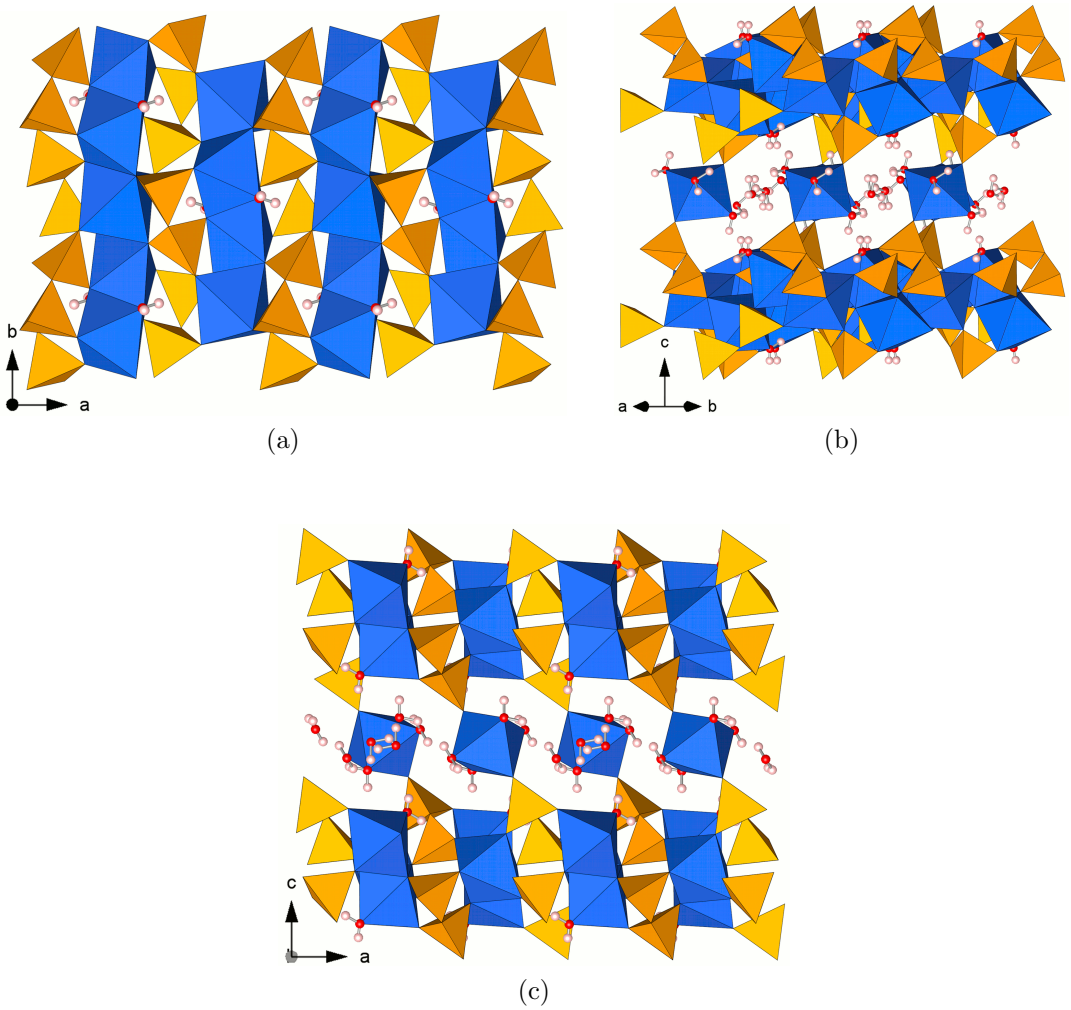

Figure 5.30: Structure of MgP_2O_7. *Top left:* Layer structure showing the edge-sharing MgO_6 chains. *Top right:* View along the [1 1 0] direction showing the narrow windows and the cavities occupied by H-bonding physisorbed water. *Bottom:* View along the *b*-axis showing the pillaring of the layers by MgO_6 octahedra, which are themselves coordinated by chemisorbed water molecules.

5.10 Summary

The first synthesis of STA-12(Mg) has been reported from high-throughput hydrothermal methods using both conventional and microwave heating. The synthesis was successfully scaled-up and found to yield large needle crystals. The structure of STA-12(Mg) was solved from single crystal X-ray diffraction data (*Table 5.14*) and found to be consistent with the structure of STA-12(Ni) reported from powder X-ray diffraction data. During the optimisation of the synthesis of STA-12(Mg), four other phases were identified. The structures of two of these, Mg($\mathbf{L}H_2$) and MgP_2O_7, crystallised as crystals suitable for single crystal X-ray diffraction and their structures were solved (*Table 5.14*).

	STA-12(Mg)	Mg($\mathbf{L}H_2$)	MgP_2O_7
Formula	$Mg_2(H_2O)_2\mathbf{L} \cdot 4.0H_2O$	Mg($\mathbf{L}H_2$) $\cdot$ $1.5H_2O$	$MgP_2O_7 \cdot 3.5H_2O$
Space Group	$R\bar{3}$	$P\bar{1}$	$P2_1/a$
a / Å	28.1046(8)	8.250(2)	9.229(3)
b / Å		9.0925(18)	8.029(3)
c / Å	6.2967(3)	9.174(2)	10.940(4)
α / °		63.208(10)	
β / °		86.871(18)	90.175(6)
γ / °		79.121(16)	
V / Å^3	4307.2(3)	602.9(2)	810.6(5)
Z	18	2	4
Crystal Morphology	Needle, colourless	Platelet, colourless	Platelet, colourless
Temperature / K	120(2)	93(2)	93(2)
Wavelength	Mo K_α	Mo K_α	Mo K_α
Reflections: Total / $[I > 2\sigma(I)]$	2794/2278	2189/2095	1495/1465
R_1 $[I > 2\sigma(I)]$	0.0783	0.0496	0.0400
R_{w2}	0.2345	0.1142	0.1070

Table 5.14: Crystallographic data from single crystal X-ray diffraction experiments for STA-12(Mg), Mg($\mathbf{L}H_2$) and MgP_2O_7.

The structures of STA-12(Mn), STA-12(Fe) and STA-12(Co) were re-refined by the Rietveld method. Structures were consistent with those previously reported[113] and gave a better fit to the data with more chemically sensible bonding distances (*Table 5.15*). All STA-12 materials crystallise in the space group $R\bar{3}$, with unit cell parameters and M-O/M-N bonding distances decreasing with cation radius (*Section 5.5*).

	STA-12(Mg)	STA-12(Mn)	STA-12(Fe)	STA-12(Co)
Formula	$Mg_2(H_2O)_2\mathbf{L}\cdot xH_2O$	$Mn_2(H_2O)_2\mathbf{L}\cdot 5.7H_2O$	$Fe_2(H_2O)_2\mathbf{L}\cdot 5.1H_2O$	$Co_2(H_2O)_2\mathbf{L}\cdot 5.1H_2O$
Space Group	$R\bar{3}$	$R\bar{3}$	$R\bar{3}$	$R\bar{3}$
a / Å	28.2331(8)	28.5814(10)	28.0103(10)	28.0942(9)
c / Å	6.2648(2)	6.4264(4)	6.4044(5)	6.2846(3)
V / Å^3	4324.7(2)	4546.4(4)	4351(5)	4295.8(5)
Diffractometer	Lab/Stoe Stadi P	Lab/Stoe Stadi P	Lab/Stoe Stadi P	Lab/Stoe Stadi P
Temperature / K	298	298	298	298
λ / Å	1.54056	1.54056	1.93604	1.93604
No. Reflections	182	359	144	142
No. Atoms (non-H)	-	12.87	12.53	12.55
No. Restraints	-	36	36	43
R_{wp}	0.1079*(L)*	0.0214	0.0371	0.0351
R_p	0.0783*(L)*	0.0166	0.0276	0.0245
R(F^2)	-	0.1056	0.4959	0.1398
χ^2	1.711	1.690	1.434	4.186

Table 5.15: Crystallographic data for the re-refined structures of as-prepared STA-12(Mg), STA-12(Mn), STA-12(Fe) and STA-12(Co). Formula quoted is that determined from diffraction. Data for STA-12(Mg) were only analysed by Le Bail fitting, *(L)*.

	STA-12(Mn)	STA-12(Fe)	STA-12(Co)
Space Group	$R\bar{3}$	$R\bar{3}$	$P\bar{1}$
a / Å	26.0701(18)	26.283(18)	6.073(6)
b / Å			14.539(8)
c / Å	5.9630(6)	5.91(3)	16.063(9)
α / °			108.879(17)
β / °			92.14(7)
γ / °			96.77(8)
V / Å^3	3510.2(5)	3540(18)	1330(19)
Diffractometer	Lab/Stoe Stadi P	Lab/Stoe Stadi P	Lab/Stoe Stadi P
Temperature / K	298	298	298
λ / Å	1.54056	1.93604	1.93604
No. Reflections	223	33	233
R_{wp}	0.0144 *(R)*	0.0617	0.0660
R_p	0.0110 *(R)*	0.0478	0.0489
χ^2	1.918	0.9264	1.091

Table 5.16: Crystallographic data from the Le Bail fits of STA-12(Fe) and STA-12(Co). Data for STA-12(Mn) were obtained by Rietveld refinement, *(R)*.

The dehydration behaviour of STA-12(Mg) was investigated by a combined approach of TGA, powder X-ray diffraction, solid-state MAS NMR and IR spectroscopies. Powder X-ray diffraction shows that STA-12(Mg)-DH loses long range order, showing broader diffraction peaks, and therefore it was not possible to determine a crystal structure. To gain some insight into the structure of STA-12(Mg)-DH, data were compared against data for the other dehydrated forms of STA-12. Powder X-ray diffraction data for a dehydrated sample of STA-12(Mn) was re-refined by the Rietveld method whilst data for dehydrated samples of STA-12(Fe) and STA-12(Co) were re-analysed by Le Bail fitting (*Table 5.17*). STA-12(Mn) and STA-12(Fe) both retain the rhombohedral symmetry on dehydration, whereas STA-12(Co) undergoes a structural transition to a triclinic space group, as reported by Pearce.[113]

Structural refinements of two structures formed on dehydration were undertaken. The structure of STA-12(Mn) was re-refined by the Rietveld method and found to dehydrate with no change of symmetry, but with a reduction in unit cell volume. This change in unit cell volume was explained by changes in the coordination environment about the Mn^{2+} cation, with all PO_3C tetrahedra becoming fully coordinating retain the octahedral coordination environment about Mn in the fully dehydrated material. STA-12(Mg) loses water in a two step process, forming a partially dehydrated STA-12(Mg)-PDH ($Mg_2(H_2O)_2\mathbf{L}$) following the loss of physisorbed water. The structure of this material was refined by the Rietveld

	STA-12(Mg)-PDH	STA-12(Mn)-DH
Formula	$Mg_2(H_2O)_2\mathbf{L}$	$Mn_2\mathbf{L}$
Space Group	$R\bar{3}$	$R\bar{3}$
a / Å	28.2453(10)	26.0701(18)
c / Å	6.22022(17)	5.9630(6)
V / Å^3	4297.6(3)	3509.8(5)
Diffractometer	Lab/Stoe Stadi P	Lab/Stoe Stadi P
Temperature / K	298	298
λ / Å	1.54056	1.54056
No. Reflections	342	223
No. Atoms (non-H)	10	9
No. Restraints	30	37
R_{wp}	0.0558	0.0144
R_p	0.0406	0.0110
R(F^2)	0.0476	0.0807
χ^2	1.453	1.918

Table 5.17: Crystallographic data for the Rietveld refinements of STA-12(Mg)-PDH and STA-12(Mn)-DH. Formulae quoted are determined from refinement.

method. The framework of STA-12(Mg)-PDH is very similar to the as-prepared material.

Comparing STA-12(Mg) to the other forms of STA-12, an explanation for the behaviour observed was developed. Dehydration of STA-12(Mg) is fully reversible and therefore connectivity in STA-12(Mg)-DH must be the same as in the as-prepared material. STA-12(Mg)-DH retains local rhombohedral symmetry (as does STA-12(Mn)) as evidenced by powder X-ray diffraction and solid-state MAS NMR data. Unlike STA-12(Mn), P=O groups remain uncoordinated (shown by IR spectroscopy — similar to the behaviour of STA-12(Co)/STA-12(Ni)) as there is no gain in crystal field stabilisation energy for reorganising the coordination environment about the Mg^{2+} cations. Instead the structure reduces pore volume by different regions of crystal distorting in slightly different ways, each retaining local rhombohedral symmetry but the structure losing long-range order, resulting in the broadening of peaks in the X-ray diffraction pattern.

STA-12(Mg) has shown significant porosity to both N_2 and CO_2 at 77 K and 196 K respectively. STA-12(Mg) crystallises as large needle crystals which are susceptible to pore blocking due to the low relative number of pore-openings to the volume of the crystal. As a result, STA-12(Mg) has a lower porosity to small gas molecules than STA-12(Ni). STA-12(Mg) is more porous than STA-12(Co) as dehydration of STA-12(Mg) forms fewer defect sites. *In situ* IR spectra for the adsorption of CO and CO_2 by STA-12(Mg) indicate a weak interaction, probably

due to the absence of available *d*-orbitals in Mg^{2+} cations for synergic back bonding by the adsorbates.

Finally, magnetic susceptibility data have been reported for the first time for STA-12(Mn), STA-12(Co) and STA-12(Ni). All forms of STA-12 undergo a transition to an anti-ferromagnetically coupled phase at low temperature. Quantitative analysis of the magnetic superexchange interactions within this structure is yet to be undertaken.

Chapter 6

Extending the Pore Size of Metal Bisphosphonates and Isoreticular Chemistry

H_4**L** has been demonstrated to be a versatile framework-forming ligand, similar in some respects to H_2BDC in carboxylate MOF chemistry. In order to increase the porosity of carboxylate MOFs, new frameworks have been been designed by the application of *isoreticular synthesis*[39] and the related *scale chemistry.*[42, 43] Eddaoudi *et al.* have reported the preparation of a series of carboxylate MOFs with identical network topology, but different pore sizes and functionalities on the pore walls, using a series of linkers with identical connectivity.[38] Similar ideas have been applied to MIL-88[45] and MIL-101.[194] Isoreticular chemistry has not however been reported before for porous bisphosphonate MOFs.

Mowat demonstrated the synthesis of the linker H_4**LL**,[182] whilst the structure was fully characterised in this work (*Section 3.2.4*). This ligand is topologically identical to H_4**L**, but approximately one half longer (H_4**L**: 0.83 nm; H_4**LL**: 1.25 nm) (*Fig. 6.1*). Using H_4**LL** it should be possible to prepare frameworks with identical networks to those prepared with H_4**L**, but with larger pores. A specific target for such synthesis is an isoreticular, larger pore analogue of STA-12 (*Chapter 5*).

This chapter reports efforts to synthesise the first porous bisphosphonate framework using an isoreticular approach. Using divalent metal cations Co^{2+} and Ni^{2+} the material STA-16 was obtained and its structure and dehydration behaviour are reported. The material shows porosity to N_2 and CO_2, and the results of these experiments are also reported. In addition, a range of other frameworks have been prepared with divalent metal cations and their structures and properties are discussed. Early attempts to extend the isoreticular approach to trivalent cations,

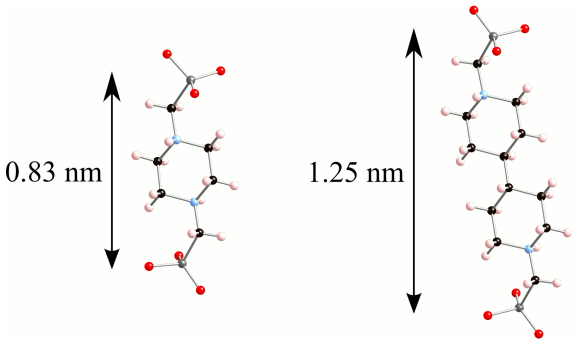

Figure 6.1: Comparison of the topologies and lengths of H_4**L** and H_4**LL**. Structures determined by X-ray diffraction (*Sections 3.2.1* and *3.2.4*)

using high-throughput (HT) methods are also presented.

6.1 Syntheses Using H_4LL and Co^{2+} or Ni^{2+} Cations

Initial syntheses with H_4**LL** used similar reaction conditions to those reported in this work for the synthesis of STA-12(Co): a gel of composition 2.0 : 1.0 : 2.1 : 1500 ($Co(AcO)_2$: H_4**LL** : KOH : H_2O) (pH 6–7), heated at 190°C for 48 hours (*Section 5.1*]. This yielded a purple microcrystalline powder mixed with an amorphous black solid assumed to be a product of the ligand breaking down. The purple phase has a characteristic diffraction pattern and has been labelled STA-16(Co) (*Fig. 6.2*). Synthesis of STA-16(Co) was optimised (*Table 6.1*). Phase pure structure STA-16(Co) was obtained from reactions where base was added dropwise to a stirred gel of $Co(AcO)_2$ and H_4**LL**(final gel composition 2.0 : 1.0 : 2.0 : 1000), reacted at lower temperature (160°C) and for a shorter time (18 hours).

During optimisation, high metal:ligand ratios (4 : 1, $Co(AcO)_2$: H_4**LL**) were investigated and found to form a non-porous Co-H_4**LL** phase, $Co_4(O)_2$**LL**$(AcO)_2$, which had previously been observed by Mowat.[182] Syntheses using $CoCl_2$ in place of $Co(AcO)_2$ were found to yield a new layered Co-H_4**LL** phase, Co_2X_2**LL**H_2. Synthesis conditions (*Table 6.1*) and full characterisation of both phases have been reported (*Section 6.6*).

Syntheses using a range of other divalent metal cations were attempted, but only $Ni^{(II)}$ yielded STA-16. Syntheses and structures obtained with other divalent metals will be discussed later (see *Section 6.7*). Initial syntheses with $Ni(AcO)_2$ used the same conditions used to prepare STA-16(Co), yielding a pale green microcrystalline powder with a very similar charcteristic diffraction pattern to STA-16(Co), labelled STA-16(Ni) (*Fig. 6.2*). Using two equivalents of base in the reaction, diffraction

Co^{2+}:H_4**LL**:KOH:H_2O	pH	Temp. / °C	Time / hrs	Phase
Metal source: $Co(AcO)_2$				
2.0 : 1.0 : 2.08 : 1500	7	190	48	STA-16(Co)
2.0 : 1.0 : 0 : 1500	6	190	60	H_4**LL**
2.0 : 1.0 : 2.05 : 1000	8	220	62	STA-16(Co)
2.0 : 1.0 : 2.01 : 1000	7	220	81	STA-16(Co)
4.0 : 1.0 : 2.01 : 500	8	190	64	$Co_4(O)_2$**LL**$(AcO)_2$
2.0 : 1.0 : 2.0 : 1000	6	160	18	STA-16(Co)
Metal source: $CoCl_2$				
2.0 : 1.0 : 2.0 : 1000	6	190	18	Co_2X_2**LL**H_2
2.0 : 1.0 : 2.4 : 300	5	190	173	Co_2X_2**LL**H_2

Table 6.1: Examples of conditions used in the preparation of three phases obtained in the Co^{2+}-H_4**LL**system, STA-16(Co) (STA-16(Co)), $Co_4(O)_2$**LL**$(AcO)_2$ and Co_2X_2**LL**H_2.

patterns had broad peaks indicating lower crystallinity. Without base, more crystalline STA-16(Ni) was obtained, but co-crystallised with H_4**LL**. Following synthesis optimisation (*Table 6.2*), phase pure STA-16(Ni) could be obtained from reactions with no base (gel composition 2.0 : 1.0 : 1000, $Ni(AcO)_2$: H_4**LL** : H_2O) heated at 220°C for only 18 hours. Reactions had to be filtered as soon as they were cool, as otherwise H_4**LL** co-crystallised with STA-16(Ni).

Attempts were also made to crystallise $Ni^{(II)}$ analogues of $Co_4(O)_2$**LL**$(AcO)_2$ (using high $Ni(AcO)_2$:H_4**LL** ratios) and Co_2X_2**LL**H_2 (using $NiCl_2$) (*Table 6.2*). Neither material has been obtained from reactions using a 7.5 ml or larger scale — phase pure STA-16(Ni) was obtained instead. A $Ni^{(II)}$ form of Co_2X_2**LL**H_2 was observed in high-throughput syntheses, but it was not possible to prepare phase pure.

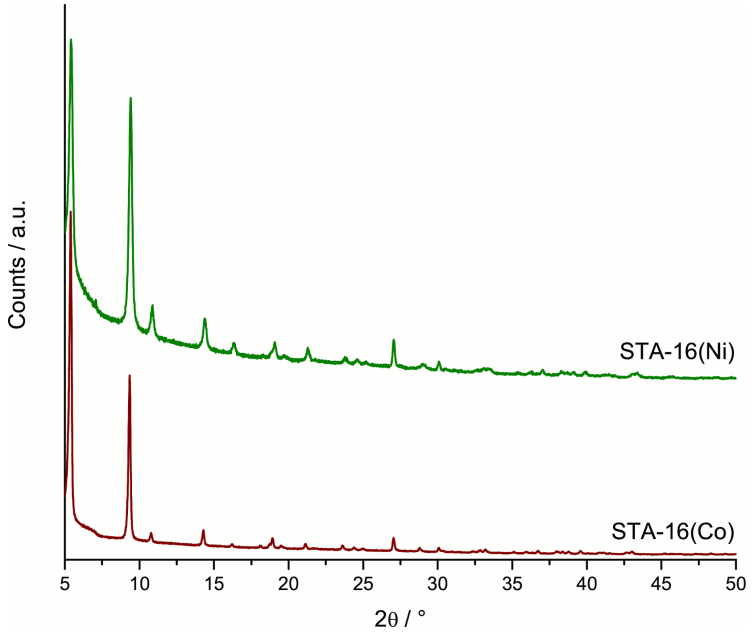

Figure 6.2: Characteristic powder X-ray diffraction patterns (Fe K_α) of STA-16(Co) (red) and STA-16(Ni) (green).

Ni^{2+}:H_4**LL**:KOH:H_2O	pH	Temp. / °C	Time / hrs	Phase
Metal source: $Ni(AcO)_2$				
2.0 : 1.0 : 2.03 : 1500	7	190	60	STA-16(Ni)[a]
2.0 : 1.0 : 0 : 1500	6	190	60	STA-16(Ni) & H_4**LL**
2.0 : 1.0 : 1.08 : 1500	7	190	46	STA-16(Ni) & H_4**LL**
2.0 : 1.0 : 0 : 1000	6	220	18	STA-16(Ni)
2.0 : 1.0 : 0 : 1000	7	160	72	STA-16(Ni)
2.0 : 1.0 : 0 : 1000	5	220	18	STA-16(Ni)
4.0 : 1.0 : 0 : 500	6	220	15	STA-16(Ni)[b]
Metal source: $NiCl_2$				
2.0 : 1.0 : 0 : 500	1	220	18	H_4**LL**
2.0 : 1.0 : 2.0 : 300	6	220	18	Amorphous

Table 6.2: Examples of conditions used in the preparation of STA-16(Ni).

[a]Sample is poorly crystalline.
[b]Sample is poorly crystalline.

6.2 Characterisation of STA-16(Co) & STA-16(Ni)

Both STA-16(Co) and STA-16(Ni) have been characterised by a combined approach of TGA, EDX and elemental analysis. TGAs of both materials were obtained by heating as-prepared samples of the material at a rate of 1.5°C min^{-1} in flowing air. TGA plots of both STA-16(Co) and STA-16(Ni) show features also observed in the related STA-12(Co) and STA-12(Ni) materials (*Section 5.6.2*), as would be expected from isoreticular forms of these materials. STA-16(Co) shows two weight losses below 120°C, followed by a plateau indicating the formation of a thermally stable dehydrated phase (*Figure 6.3a*). The first weight loss (17–52°C: 26.19 wt.%) is attributed to the loss of ∼ 11 molecules of physisorbed water per formula unit. The second weight loss begins at 52°C (52–120°C: 6.93 wt.%), indicated by a change in gradient of the TGA curve. The elevated temperature of onset of this second weight loss suggests a stronger interaction between the water and the framework, therefore the weight loss is assigned to to the loss of ∼ 2 molecules of chemisorbed water per formula unit (expected loss, 5.1 wt.%). The difference in expected and observed losses is attributed to the continuing loss of physisorbed water after the start of the loss of chemisorbed water. The dehydrated phase of the material is stable up to 228°C, at which point a series of weight loss events occur, assigned to the collapse of the framework.

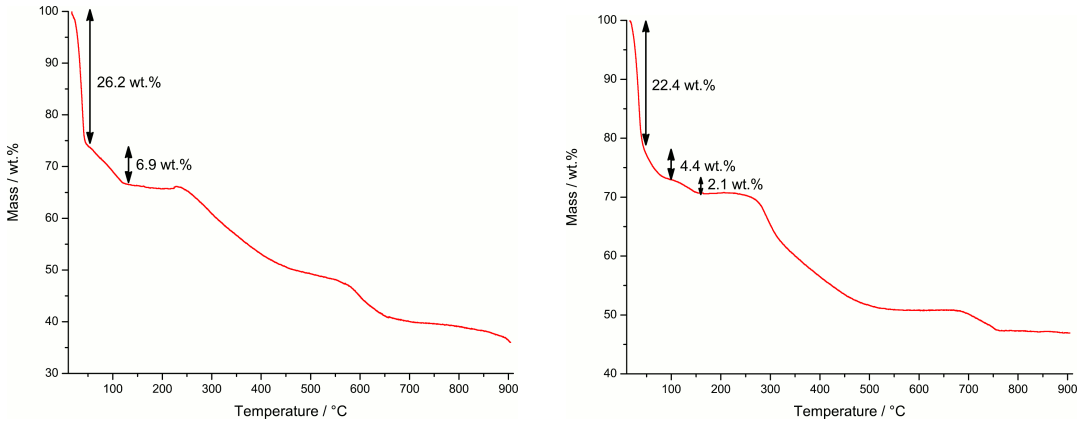

(a) (b)

Figure 6.3: TGA plots for STA-16(Co) (*left*) and STA-16(Ni) (*right*). The principal weight loss events occurring on dehydration of each structure are indicated.

For STA-16(Ni), a similar TGA behaviour is observed (*Fig. 6.3b*), except the material loses chemisorbed water in two steps (*c.f.* STA-12(Ni)). An initial weight loss (17–48°C: 22.35 wt.%) is attributed to the loss of ∼ 8.5 molecules of physisorbed water per formula unit. A change in gradient at 48°C indicates the

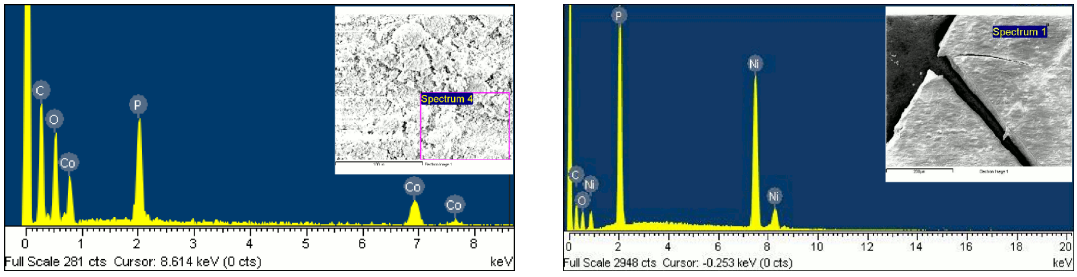

(a) (b)

Figure 6.4: EDX spectra of STA-16(Co) (*left*), with a Co : P ratio of 1.0 : 1.0, and STA-16(Ni) (*right*), showing a Ni : P ratio of 1.0 : 1.21. Insets show the sample area analysed.

onset of loss of chemisorbed water (as for STA-16(Co)) and the structure loses $\frac{2}{3}$ of the chemisorbed water molecules (48–93°C: 4.42 wt.%; expected for loss of 1.3 molecules H_2O, 3.6 wt.%). The difference in the observed and expected weight losses is again attributed to continued loss of physisorbed water after the structure starts to lose chemisorbed water. From 93–99°C, a plateau is observed thought to be (by analogy to STA-12(Ni)) a partially dehydrated phase retaining 0.66 chemisorbed water molecules. With further heating, these water molecules are also lost (99–148°C: 2.08 wt.%; expected 1.8 wt.%). The slight difference here is assigned to residual chemisorbed water from the previous weight loss. The dehydrated form of the material is stable up to 256°C, before a series of weight loss events indicate the collapse of the framework.

EDX data for structure STA-16(Co) gave a Co : P ratio of 1.0 : 1.0 showing excellent agreement with the expected 1 : 1 metal:P ratio of an isoreticular form of STA-12. Structure STA-16(Ni) also showed reasonable agreement with the expected 1 : 1 ratio, with a metal:P ratio of 1.0 : 1.21. The small discrepancy is attributed to a small amount of unreacted ligand present in samples analysed. Using the TGA and EDX results, hypothetical compositions of both structures STA-16(Co) and STA-16(Ni) were proposed and found to be in good agreement with the results of elemental analysis (*Table 6.3*). Differences in the elemental composition of structure STA-16(Ni) are thought to be due to small amounts of re-crystallised ligand in the analysed sample.

Structure	Proposed Composition	C / %		H / %		N / %	
STA-16(Co)	$Co_2(H_2O)_2(C_{12}H_{22}N_2O_6P_2)\cdot 11H_2O$	20.6	(21.6)	6.8	(6.6)	4.0	(4.2)
STA-16(Ni)	$Ni_2(H_2O)_2(C_{12}H_{22}N_2O_6P_2)\cdot 8.5H_2O$	26.6	(22.2)	5.4	(6.5)	5.0	(4.3)

Table 6.3: Elemental analysis results for structures STA-16(Co) and STA-16(Ni). Values in parentheses are values expected from the proposed compositions.

6.3 As-Prepared Structures of STA-16(Co) & STA-16(Ni)

The structure of STA-16 was determined from powder X-ray diffraction using data collected at beamline I11 of the Diamond Light Source synchrotron (Harwell, Oxfordshire, UK).[145] Diffraction patterns were collected for as-prepared forms of STA-16(Co) and STA-16(Ni), with samples mounted in 0.5 mm quartz glass capillary tubes, in Debye-Scherrer geometry using monochromated X-ray radiation of wavelength 0.825028 Å. The effect of beam damage was minimised by cooling samples to 100 K and by collecting eight short (3 minute) data sets, each on a freshly exposed portion of sample, with the capillary translated between data collections. Each data set was collected over the range 1–140° 2θ. After data collection all eight data sets were summed with a step size of 0.002°. Data at 2θ angles greater than 40° were discarded, as the intensity of the peaks strongly decreased. Finally, the data were re-binned to a step size of 0.003°.

Data for structures STA-16(Co) and STA-16(Ni) were indexed and found to have metrically trigonal or hexagonal cells using the TREOR routine of the EXPO2009 package[153, 148] (*Table 6.4*). Cells were then refined using Le Bail analysis routines[155] within the GSAS suite of programs.[156, 157] During refinement, the lower limit of the data was set to 1.7° 2θ due to the beamstop.

	STA-16(Co)	STA-16(Ni)
Crystal System	Trigonal/Hexagonal	Trigonal/Hexagonal
a / Å	41.173(4)	40.962(8)
c / Å	6.2433(9)	6.1922(15)
$\alpha = \beta$ / °	90	90
γ / °	120	120
F.O.M. (M_{20})[154]	39	27

Table 6.4: Unit cells determined by indexing diffraction patterns of structures STA-16(Co) and STA-16(Ni), using using the TREOR routine of the EXPO2009 package[153, 148].

A model for Rietveld refinement[147] was constructed geometrically from the

structure of as-prepared STA-12(Ni).[114] The centres of the metal phosphonate helices were assumed to have the same coordinates in the *ab*-plane in both STA-12 and the STA-16 (*i.e.* 0.3333,0.3333). STA-16 was also assumed to crystallise in the same space group as STA-12 ($R\bar{3}$) — systematic absence conditions from the indexed cells were consistent with this assumption. The absolute position (in Å) of each atom in the asymmetric unit of STA-12 relative to the centre of a metal phosphonate helix was determined, with *c* coordinates assumed to be the same in both STA-12 and STA-16 (due to the similarity of the *c* parameters of the indexed cells and of STA-12). Atoms were then placed in the enlarged unit cell of STA-16 using vectors calculated from STA-12. The positions of C3, C4, C5 (not present in STA-12) were determined from a complete piperazinyl ring in the STA-12 structure, using the positions of the symmetry-generated C1, N1 and C2 respectively. Water molecules were placed with fractional coordinates related to those present in the STA-12 structure.[114]

The structures of both STA-16(Co) and STA-16(Ni) were refined by the Rietveld method, using the GSAS suite of programs,[156, 157] using the refined unit cells from Le Bail analysis and the model derived from STA-12 (*vide supra*). Profile parameters were also taken from the Le Bail fits. The background was refined, and further cycles of refinement of the cell and profile were performed to ensure a good starting fit to the profile. Before refinement of the structure, restraints were applied to the octahedral M-O, M-O100[1] and M-N bonds (*Table 6.5*); tetrahedral P-O and P-C bonds (1.51 Å and 1.85 Å); and C-C and C-N bonds (1.53 Å and 1.51–1.53 Å). Non-bonding distance restraints were also applied to O$\cdots$O, O$\cdots$O100, O$\cdots$N and O100$\cdots$N (M octahedra — *Table 6.5*); O$\cdots$O and O$\cdots$C (P tetrahedra) (2.47 Å and 2.58 Å); N$\cdots$C and C$\cdots$C (diagonal, cross-ring) (2.91 Å and 2.91 Å); C$\cdots$C

[1]O100 is label given to chemisorbed water molecule.

	STA-16(Co)	STA-16(Ni)
M-O	2.15	2.10
M-O100	2.15	2.10
M-N	2.20	2.15
O$\cdots$O	3.04	2.97
O$\cdots$O100	3.00	2.97
O$\cdots$N	3.08	3.01
O100$\cdots$N	3.03	3.01

Table 6.5: Bond restraints applied about MO_5N octahedra in Rietveld refinements of structures STA-16(Co) and STA-12(Ni). O100 is a chemisorbed water molecule. All distances in Å.

(2^{nd} neighbour, across ring-bridging bond) and C$\cdots$C (3^{rd} neighbour, across ring-bridging bond) (2.55 Å and 3.00 Å). Applying restraints to 2^{nd} neighbours in the same ring (e.g. N1$\cdots$C3) was found to be detrimental to the geometry of the ring. Instead, angle restraints were applied to each of the 2nd neighbour pairs around the ring (i.e. C6-N1-C2, N1-C2-C3, C2-C3-C4, C3-C4-C5, C4-C5-C6 and C5-C6-N1: 109.5°).

The structure was refined and found to give a satisfactory fit to the data. Restraint were then gradually relaxed. Fourier difference maps were used to locate additional electron density in the pores. Fourier peaks in positions chemically-sensible for H-bonded water were identified and added to the refinement, refining alternately the occupancy of all of the water molecules and their positions. R_{wp}, R_p, $R(F^2)$ and χ^2 values for the final Rietveld fits of each of structure STA-16(Co) (*Fig. 6.5*) and STA-16(Ni) (*Fig. 6.6*) are detailed in *Table 6.6*).

Structure	R_{wp}	R_p	$R(F^2)$	χ^2	Cycles
STA-16(Co)	0.0467	0.0338	0.0532	45.17	2891
STA-16(Ni)	0.0446	0.0345	0.1318	138.3	1117

Table 6.6: Final R_{wp}, R_p, $R(F^2)$, χ^2 and the number of cycles for the final refinements of as-prepared structures STA-16(Co) & STA-16(Ni).

As expected for isostructural materials, the structural features of STA-16 are closely related to those of STA-12 (*Chapter 5*). Coordination of the M site is provided by four phosphonate O atoms, a piperidinyl N atom and the O atom of a chemisorbed water molecule (*Table 6.7* lists specific bonding distances for both structures). MO_5N octahedra are arranged in edge-sharing helical chains parallel to the *c*-axis with PO_3C groups coordinating M sites in a bridging mode along the chains, leaving one P=O group uncoordinated (*Fig. 6.7a*). Each chain is linked to three others through N-coordinating bipiperidinyl moieties, forming a hexagonal, honeycomb array of unidirectional channels, each approximately 1.8 nm in free diameter (*Fig. 6.7b*). Channels are occupied by physisorbed water molecules, with fractional occupancies in the range 0.40–0.79. The physisorbed water molecules form an H-bonding network and also engage in H-bonding with the uncoordinated P=O group and chemisorbed water molecule. The refinement of STA-16(Co) gave a structural compositon of $Co_2(H_2O)_2\mathbf{LL}\cdot 7.5H_2O$, suggesting that not all the water molecules have been located, though no significant unaccounted electron density was indicated by Fourier maps of the final refinement.

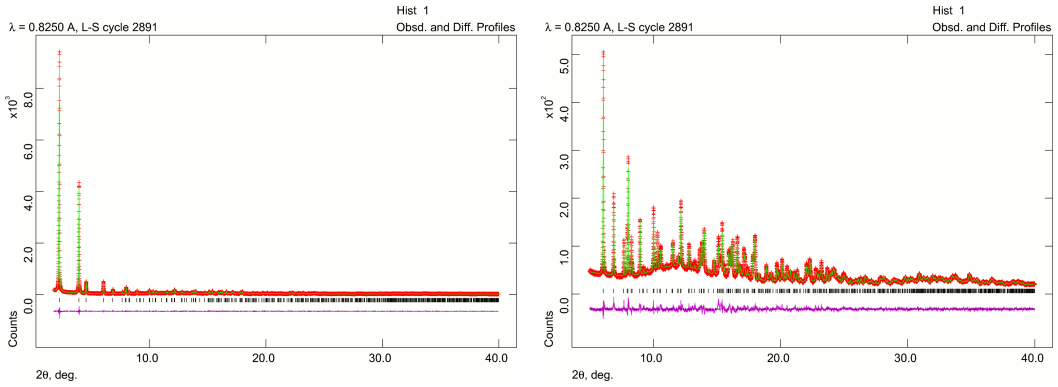

Figure 6.5: Final Rietveld fit for refinement of as-prepared STA-16(Co) ($R_{wp} = 0.0467$).

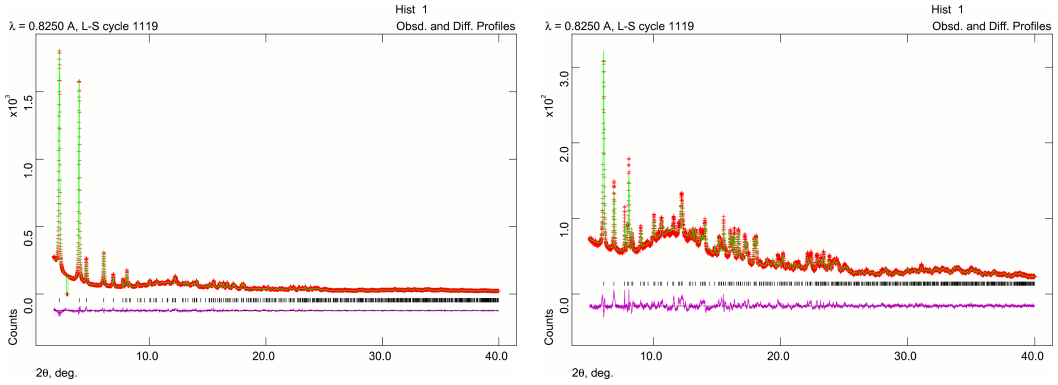

Figure 6.6: Final Rietveld fit for refinement of as-prepared STA-16(Ni) ($R_{wp} = 0.0446$).

Bond	STA-16(Co)	STA-16(Ni)
M1-O2	2.015(10)	2.071(15)
M1-O2	2.240(10)	2.164(15)
M1-O3	2.137(9)	2.050(14)
M1-O3	1.942(9)	1.838(14)
M1-O100	2.041(9)	1.780(19)
M1-N1	2.244(9)	2.124(16)
P1-O1	1.593(9)	1.559(13)
P1-O2	1.594(11)	1.479(12)
P1-O3	1.599(10)	1.477(12)
P1-C1	1.740(12)	1.843(10)

Table 6.7: Selected bond distances from the Rietveld refinements of STA-16(Co) and STA-16(Ni).

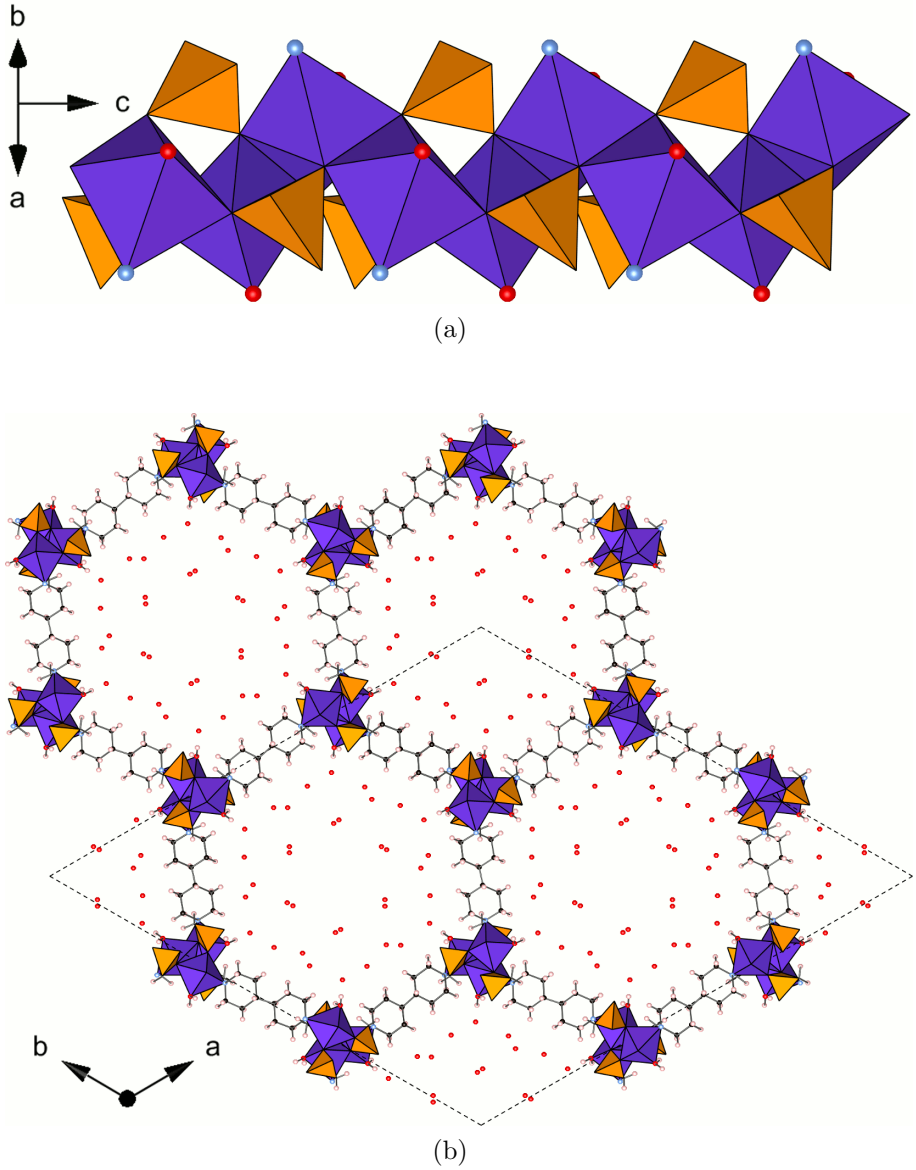

Figure 6.7: Structure of STA-16 determined from synchrotron powder X-ray diffraction data (STA-16(Co) shown). *Top:* Helical chain of edge-sharing MO_5N octahedra linked by phosphonate tetrahedra. *Bottom:* View along the *c*-axis showing honeycomb array of 18 Å channels occupied by physisorbed water molecules; protons shown in this view have been added geometrically after refinement.

6.4 Dehydration Behaviour of STA-16(Co) & STA-16(Ni)

TGA data indicated that both forms of STA-16 will form thermally stable, fully dehydrated materials (M_2**LL**). The processes by which the materials lose water is however different. STA-16(Co) begins to lose physisorbed water as soon as flowing gas is passed over the sample. Both physisorbed and chemisorbed water are lost in a single continuous step, a change in gradient indicating removal of chemisorbed water. Fully dehydrated STA-16(Co) (STA-16(Co)-DH) is formed at a temperature of 120°C and this is stable to 228°C. Likewise, STA-16(Ni) loses physisorbed water at low temperature and the onset of chemisorbed water loss is only marked by a subtle change in the gradient of the TGA curve. Initially however, STA-16(Ni) loses only $\frac{2}{3}$ of its chemisorbed water to form a partially dehydrated material (indicated by a short plateau in the TGA), before losing the remaining $\frac{1}{3}$ of the chemisorbed water to form the fully dehydrated material (STA-16(Ni)-DH). To confirm the analysis of TGA data and to try to understand the structure of the fully dehydrated material, powder diffraction studies of both materials have been undertaken. STA-16(Ni)-DH has also been analysed by *in situ* IR spectroscopy.

For powder diffraction studies of the dehydration, a diffraction pattern of the as-prepared form of each material was collected (STA-16(Co) — Fe K_α; STA-16(Ni) — Cu K_α). Fully dehydrated forms of STA-16 were prepared by heating as-prepared samples of the materials, loaded into a 0.7 mm quartz glass capillary tubes, at 180°C under vacuum (1×10^{-4} Torr) for three hours. A second powder diffraction pattern was then collected and the capillary was then broken open to allow the material to fully rehydrate. After 24 hours or more, a further diffraction pattern of the rehydrated material was collected.

6.4.1 Dehydration of Structure STA-16(Co)

Dehydration of structure STA-16(Co) is accompanied by a colour change of the sample from purple to blue and back to purple on rehydration (*Fig. 6.8*), suggesting that dehydration is reversible. The colour change indicates a change in the coordination environment of the Co^{2+} cations, due to the loss of coordinated water on dehydration, and a similar colour change has also been observed for the dehydration of STA-12(Co).[113] Powder diffraction confirms the reversibility of this change, with little difference between the as-prepared and rehydrated diffraction patterns (*Fig. 6.9*). The diffraction pattern of the dehydrated structure indicates a major structural transition occurs on dehydration, possibly similar to that observed

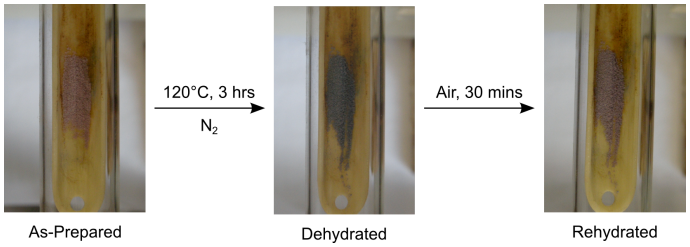

Figure 6.8: Photographs of colour changes going from the as-prepared (*left*), dehydrated (*middle*) and rehydrated (*right*) forms of STA-16(Co). Dehydrated sample was heated in a tube furnace at 120°C for three hours under flowing N_2.

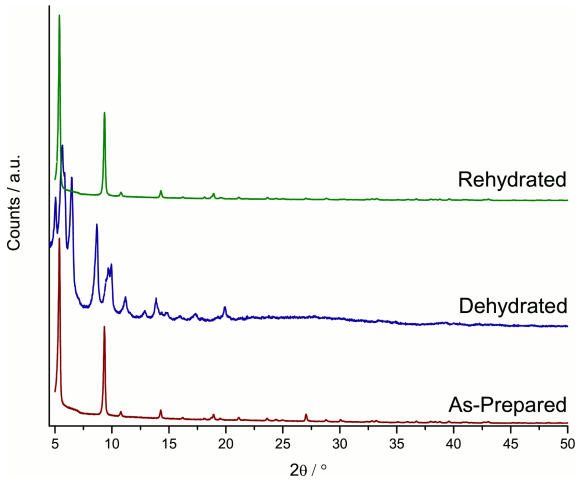

Figure 6.9: Powder X-ray diffraction patterns of as-prepared, dehydrated and rehydrated structure STA-16(Co). The diffraction pattern of the STA-16(Co)-DH indicates a symmetry change on dehydration, which is shown to be reversible upon rehydration.

for STA-12(Ni) or 3 (*Section 5.6.3*). It has so far proven impossible to index the diffraction pattern of this material and the structure remains unknown, though as dehydration is reversible, connectivity of the framework must be retained in the dehydrated material.

6.4.2 Dehydration of Structure STA-16(Ni)

Structure STA-16(Ni) also shows a colour change on dehydration, the green as-prepared material becoming orange-brown in the dehydrated form and returning to green on rehydration (*Fig. 6.10*). As for structure STA-16(Co), the colour change is indicative of the change in the coordination environment of the Ni^{2+} cations caused by the loss of chemisorbed water from the structure. Surprisingly however, there is no change in symmetry on dehydration of the material (*Fig. 6.11*). Peak positions also show only a small shift from the as-prepared material, suggesting the framework

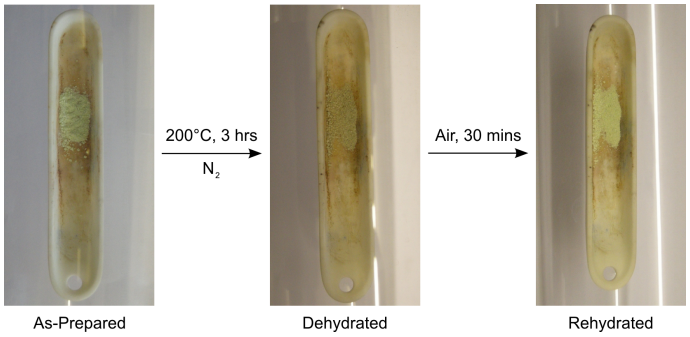

Figure 6.10: Photographs in colours of the as-prepared, dehydrated and rehydrated structure STA-16(Ni). Dehyrated sample was heated in a tube furnace at 180°C for three hours under flowing N_2.

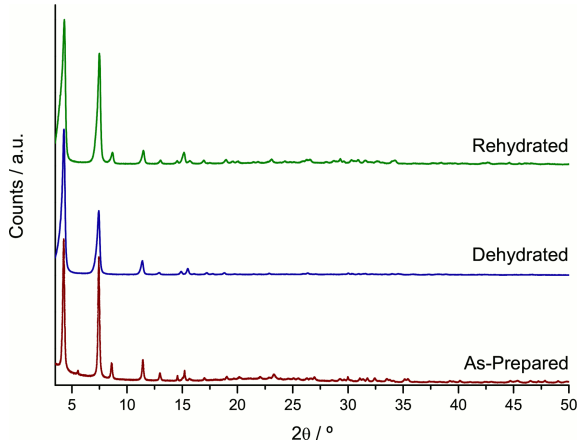

Figure 6.11: Powder X-ray diffraction patterns (Cu K_α) of as-prepared, dehydrated and rehydrated structure STA-16(Ni). As-prepared data were collected at beamline I11 of the Diamond synchrotron and has been re-scaled to Cu K_α wavelength; other data sets were collected using a laboratory diffractometer. All three diffraction patterns show the same peak positions, indicating a consistent framework structure regardless of hydration state.

structure is retained with few changes in the STA-16(Ni)-DH. Such behaviour has not been observed with structures of the STA-12 family before. It might also suggest that coordinatively unsaturated sites are more accessible than in any of the other materials. IR spectroscopy will be used to probe these features (*vide infra* and see *Section 6.5.2*). As the framework of the as-prepared material is thought to be retained in STA-16(Ni)-DH, Rietveld refinement of this structure has also been attempted (*Section 6.4.3*).

In situ IR spectra were collected by S. M. Chavan (Università di Torino, Turin, Italy) on as-prepared and dehydrated samples of structure STA-16(Ni). Dehydrated samples were prepared by subjecting the as-prepared material to vacuum at either room temperature or 150°C. The IR spectrum of the as-prepared

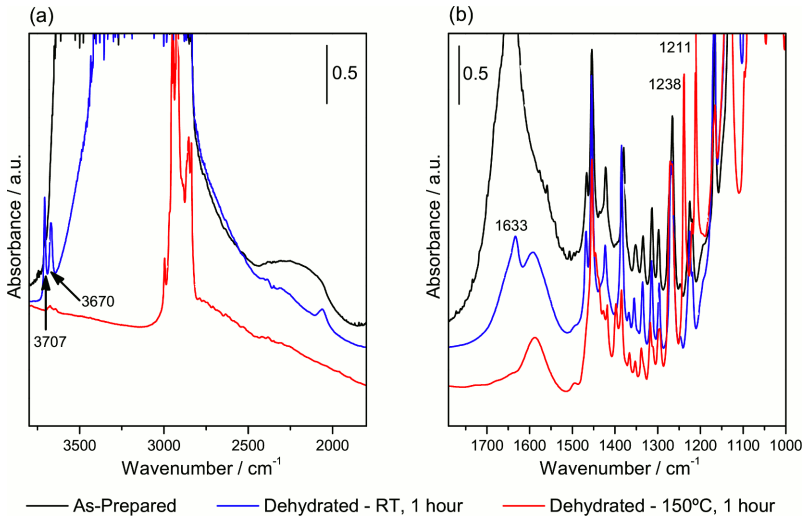

Figure 6.12: *In situ* IR spectra in the regions 3800–1800 cm^{-1} (a) and 1790–1000 cm^{-1} (b) of as-prepared (black) structure STA-16(Ni) and two samples of STA-16(Ni) dehydrated under vacuum (1×10^{-4} Torr) at room temperature (blue) and 150°C (red).

material shows similar features to the previously reported spectra of STA-12(Ni) (*Fig. 6.12*).[113, 114] A very broad band in the 3600–2800 cm^{-1} and a band centred at 1750 cm^{-1} are due to the ν(O-H) and δ(O-H) modes of physisorbed water molecules. Framework vibrations are observed in the region 1500–500 cm^{-1}. The principal vibrations in this region are due to bending modes of the CH_2 groups of the ligand (1470–1350 cm^{-1}) and combinations of ν(C-C) and ν(C-N) modes and stretching modes of the phosphonate tetrahedron (1160–950 cm^{-1}).[114, 195]

Dehydration of STA-16(Ni) at room temperature causes significant changes in the 3600–2800 cm^{-1} and 1700–1500 cm^{-1} regions: bands due to the physisorbed water narrow but are still present. Two sharp peaks are observed, (3707 and 3670 cm^{-1}) assigned to ν(O-H) stretching modes of chemisorbed water, and a δ(O-H) bending mode band is also observed (1633 cm^{-1}). Framework resonances are mostly unchanged.

When dehydrated at high temperature (to remove all physisorbed water and chemisorbed water) more significant changes to peaks attributed to the framework are observed — specifically the growth of two peaks (1238 and 1211 cm^{-1}). Similar peaks were observed in the IR spectra of dehydrated Ni^{2+}, Co^{2+} and Mg^{2+} forms of STA-12 and assigned to the ν(P-O) stretch of uncoordinated P=O groups (*Section 5.6.6*). It seems likely that this is also the origin of the peaks in structure STA-16(Ni)-DH. The IR spectrum of STA-16(Ni)-DH also shows significant changes in the 3600–2800 cm^{-1} region, with the band due to physisorbed water (3500–2800 cm^{-1}) and peaks assigned to the ν(O-H) mode of chemisorbed water (3707

and 3670 cm^{-1}) disappearing, indicating the complete removal of water from the structure. The absence of the broad band due to physisorbed water allow the observation of the ν(C-H) stretching band (2900–2750 cm^{-1}).

6.4.3 Structure of STA-16(Ni)-DH

Powder X-ray diffraction of the dehydrated form of STA-16(Ni)-DH suggests that it retains the same symmetry and structure as the as-prepared material. To confirm this, high-resolution powder X-ray diffraction data were collected at beamline I11 of Diamond Light Source synchrotron (Harwell, Oxfordshire, UK)[145] on a sample of STA-16(Ni)-DH, dehydrated in a 0.5 mm quartz glass capillary tube at 180°C for three hours. Data were collected in Debye-Scherrer geometry using monochromated X-ray radiation of wavelength 0.825028 Å. The effect of beam damage was minimised by cooling samples to 100 K and by collecting eight three minute data sets, each on a freshly exposed portion of sample, with the capillary translated between data collections. Each data set was collected over the range 1–140° 2θ. After data collection, all eight data sets were summed with a step size of 0.002°. Data at angles greater than 40° 2θ were discarded, as the intensity of the peaks strongly decreased. Finally, the data were re-binned to a step size of 0.005°.

The unit cell of as-prepared STA-16(Ni) was used as the starting cell for Le Bail analysis, using the GSAS suite of programs.[155, 156, 157] A good fit to the data was obtained, with a slight increase in the unit cell parameters of the dehydrated material (final Rietveld refined cells are given in *Table 6.8*). Rietveld refinement of the structure used the model determined for the as-prepared material (*Section 6.3*), but with physisorbed and chemisorbed water molecules removed. Profile and unit cell parameters were taken from the Le Bail analysis and background parameters derived by several cycles of refinement. Before refinement of the structure, restraints were applied to the bonding octahedral Ni-O and and Ni-N distances (2.10 Å and 2.15 Å); tetrahedral P-O and P-C bonds (1.51 Å and 1.85 Å); and C-C and C-N bonds (1.53 Å and 1.51–1.53 Å). Non-bonding distances were also restrained between O$\cdots$O and O$\cdots$N (Ni polyhedra) (2.10 Å and 2.15 Å respectively); O$\cdots$O and O$\cdots$C (P tetrahedra) (2.47 Å and 2.74 Å); N$\cdots$C and C$\cdots$C (diagonal, cross-ring) (2.90 Å and 2.90 Å); C$\cdots$C (2^{nd} neighbour within ring, 2^{nd} neighbour, outwith ring, across N) (2.50 Å and 2.50 Å); C$\cdots$C (2^{nd} neighbour, outwith ring, across ring-bridging bond) and C$\cdots$C (3^{rd} neighbour, across ring-bridging bond) (2.55 Å and 3.00 Å). As with the as-prepared structure, applying restraints to 2^{nd} neighbours in the same ring (e.g. N1$\cdots$C3) was found to be detrimental to the geometry of the ring. Instead, angle restraints were applied to each of the 2nd neighbour pairs

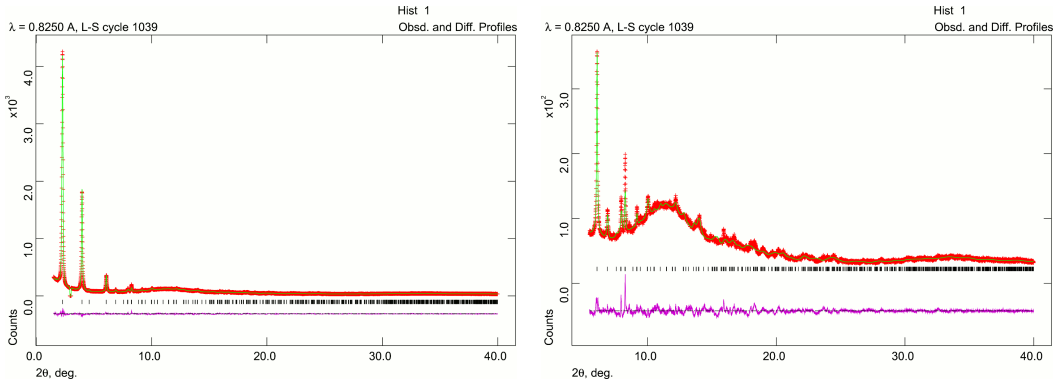

Figure 6.13: Final Rietveld fit for refinement of dehydrated STA-16(Ni) (STA-16(Ni)-DH) (R_{wp} = 0.0445).

	As-Prepared	Dehydrated
Space group	$R\bar{3}$	$R\bar{3}$
a / Å	41.0540(8)	41.2136(16)
c / Å	6.2056(2)	6.340(2)

Table 6.8: Comparison of the unit cell parameters obtained from Rietveld refinement of as-prepared and dehydrated structure STA-16(Ni).

around the ring (i.e. C6-N1-C2, N1-C2-C3, C2-C3-C4, C3-C4-C5, C4-C5-C6 and C5-C6-N1: 109.5°).

The structure was refined and found to give a good fit to the data. The final fit of the refinement was R_{wp} = 0.0445, R_p = 0.0327, R(F^2) = 0.0370 and χ^2 = 137.8 (*Fig. 6.13*).

The structure of STA-16(Ni)-DH is very closely related to the as-prepared form of the material, though with one key difference. Rather than an octahedral coordination environment, each Ni centre has an approximately square-based pyramidal five-fold coordination environment. Coordination is slightly distorted as upon dehydration the PO_3C groups 'rock' on their site, increasing the Ni1-O2

Bond	Distance / Å	Bond	Distance / Å
Ni1-O2	2.129(9)	P1-O1	1.504(5)
Ni1-O2	2.345(11)	P1-O2	1.508(5)
Ni1-O3	2.083(9)	P1-O3	1.509(5)
Ni1-O3	2.040(11)	P1-C1	1.849(3)
Ni1-N1	2.274(9)		

Table 6.9: Selected bond distances from the Rietveld refinement of fully dehydrated STA-16(Ni).

distance (2.345(14) Å) (*Table 6.9*, *Fig. 6.14a*). To accommodate this rocking, the bipiperidine group readjusts its position between the chains, aligning almost parallel to the crystallographic a and b directions. This in turn causes the slight increase in unit cell dimensions and leaves slightly larger channels in the dehydrated material (∼1.9 nm — *Fig. 6.14b*) than in the as-prepared material (∼1.8 nm).

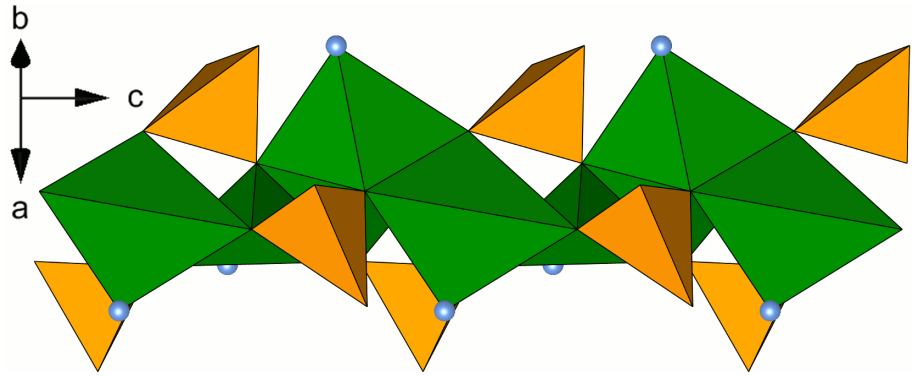

(a)

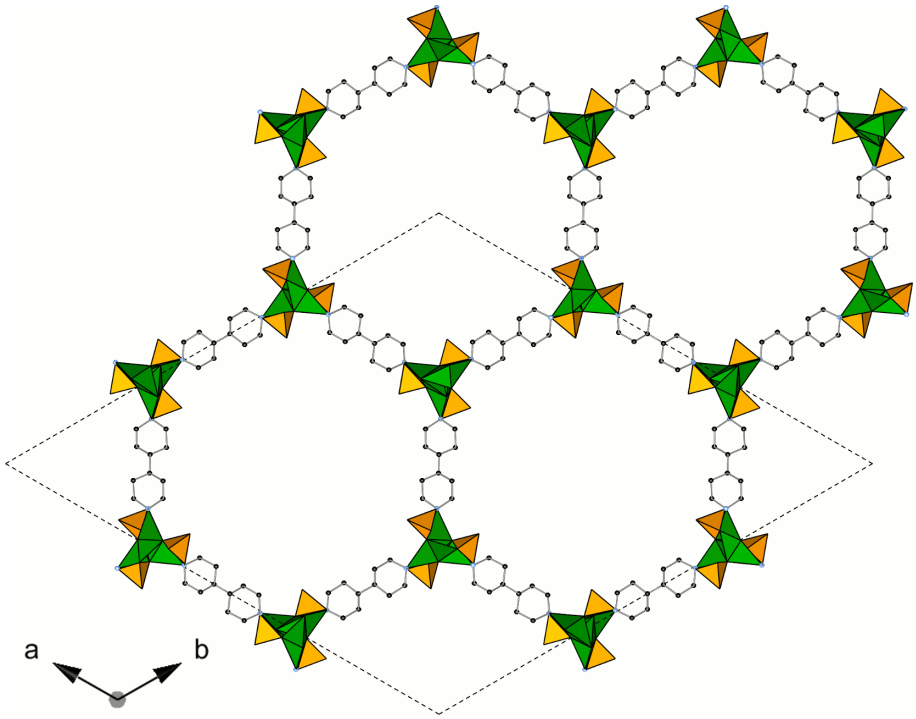

(b)

Figure 6.14: Structure of dehydrated STA-16(Ni), determined from synchrotron powder X-ray diffraction data. *Top*: Helical chain of edge-sharing MO_5N octahedra linked by phosphonate tetrahedra. *Bottom*: View along the *c*-axis showing honeycomb array of 19 Å channels occupied by physisorbed water molecules; protons shown in this view have been added geometrically after refinement.

6.5 Porosity of STA-16(Co) & STA-16(Ni)

The porosity of activated samples of both STA-16(Co) and STA-16(Ni) to N_2 at 77 K and CO_2 at 196 and 273 K have been investigated. Samples of STA-16 were activated (*i.e.* dehydrated) by heating as-prepared samples of the material under vacuum (1×10^{-4} Torr) at 180°C for three hours. Porosity measurements were made both volumetrically (N_2) and gravimetrically (CO_2). The porosity of the two forms of STA-16 is compared by measurement of the surface area (using the BET method, described by Bae *et al.*)[175], micropore volume and maximum total uptake (both calculated using the Dubinin-Radushkevitch — D-R — equation)[163]. The pore size distributions for both STA-16(Co) and STA-16(Ni) have been calculated using non-local density functional theory (NLDFT) models implemented in the Micromeritics ASAP 2020 software.[196, 197, 198] The adsorption of CO and CO_2 at room temperature and low temperature (77 K and 196 K respectively) by STA-16(Ni) have also been investigated by *in situ* IR spectroscopy (data collected collected by S. M. Chavan — Università di Torino, Turin, Italy).

6.5.1 Adsorption Isotherms for N_2 and CO_2 in STA-16

Structures STA-16(Co) and STA-16(Ni) are porous to N_2 at 77 K showing a Type IVc isotherm (*Fig. 6.15*). In a classic Type IVc isotherm, an initial uptake profile similar to a Type II isotherm is followed by a near vertical riser associated with the filling of approximately cylindrical pores. No hysteresis loop is observed at this riser indicating the reversibility of pore filling/emptying.[163] The riser in the N_2 isotherm of STA-16(Co) is inclined rather than vertical, occurring over the range $\frac{p}{p_0}$ 0.01–0.03, and shows no hysteresis. For STA-16(Ni), the riser, observed over the range 0.03–0.06, has a more vertical profile and again shows no hysteresis. The more inclined nature of the riser and the slightly larger BET surface area of STA-16(Co) (+137 $m^2\ g^{-1}$ — *Table 6.10*) are thought to be due to a distortion of the channels on dehydration, caused by the structural transition observed in the powder X-ray diffraction pattern. NLDFT analysis of the N_2 isotherms of both materials was used to calculate pore size distributions (PSDs). NLDFT models assumed a cylindrical pore structure with silica/alumina walls as models specific to MOFs were not available. Despite the inappropriate surface potential of this model, PSDs for both materials gave values in good agreement with the crystal structures (STA-16(Co): 1.66 nm; STA-16(Ni): 1.84 nm — *Fig. 6.16*). Isotherms were also calculated using the derived PSD for the region of mesoporous pore filling and show good agreement with experimental data

	STA-16(Co)	STA-16(Ni)
BET Surface Area / $m^2\ g^{-1}$	1365(11)[a]	1228(15)[b]
Pore Volume / $cm^3\ g^{-1}$	0.67	0.76
N_0 (N_2) (D-R) / mmol g^{-1}	19.35(3)	22.20(2)
N_0 (CO_2) (D-R) / mmol g^{-1}	21.74(1)	17.93(7)

Table 6.10: Comparison of the BET surface area (calculated following the method of Bae *et al.*;[175] linear $\frac{p}{p_0}$ ranges determined from consistency criteria quoted in footnotes), and pore volume, calculated from N_2 adsorption, and maximum micropore loadings (N_0) for N_2 and CO_2 (calculated using the D-R equation[163]). *N.B.* N_2 and CO_2 isotherms for STA-16(Co) were measured on different samples.

[a] $\frac{p}{p_0}$ linear range: 0.005–0.017
[b] $\frac{p}{p_0}$ linear range: 0.006–0.024

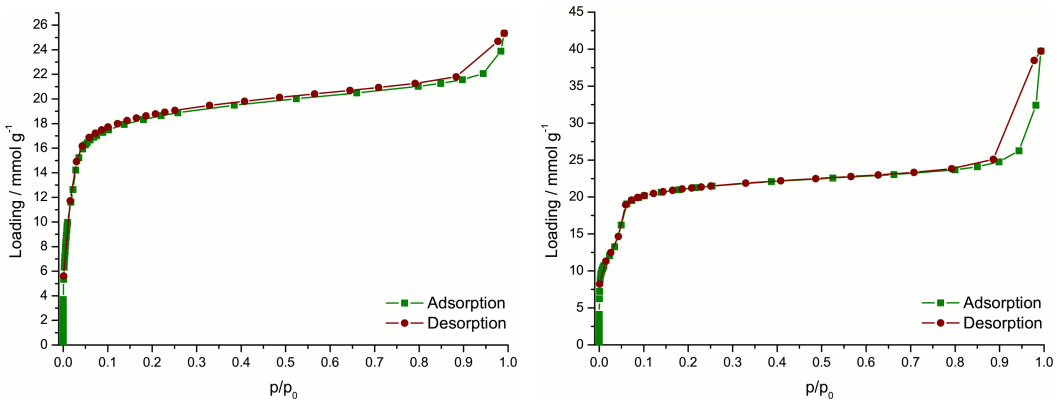

(a) (b)

Figure 6.15: N_2 isotherms at 77 K with Type IVc profiles for STA-16(Co) (*left* — riser at $\frac{p}{p_0}$ = 0.01–0.03) and STA-16(Ni) (*right* — riser at $\frac{p}{p_0}$ = 0.03–0.06).

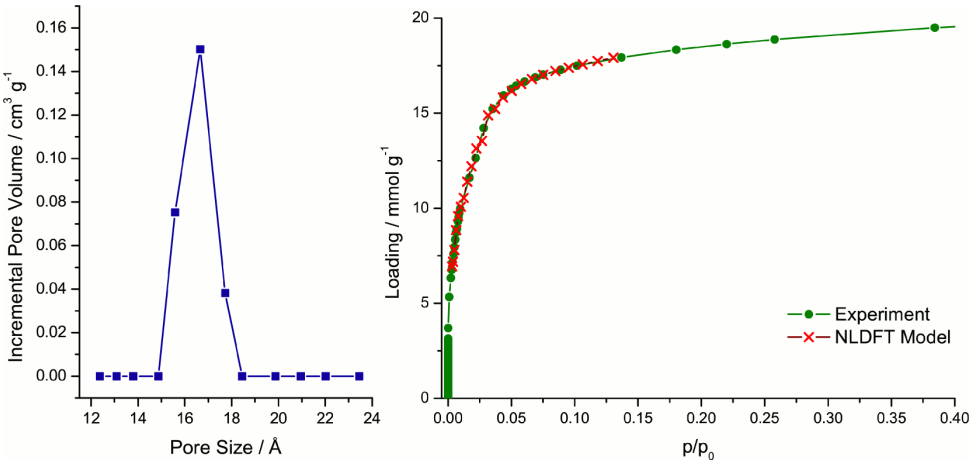

(a) STA-16(Co)

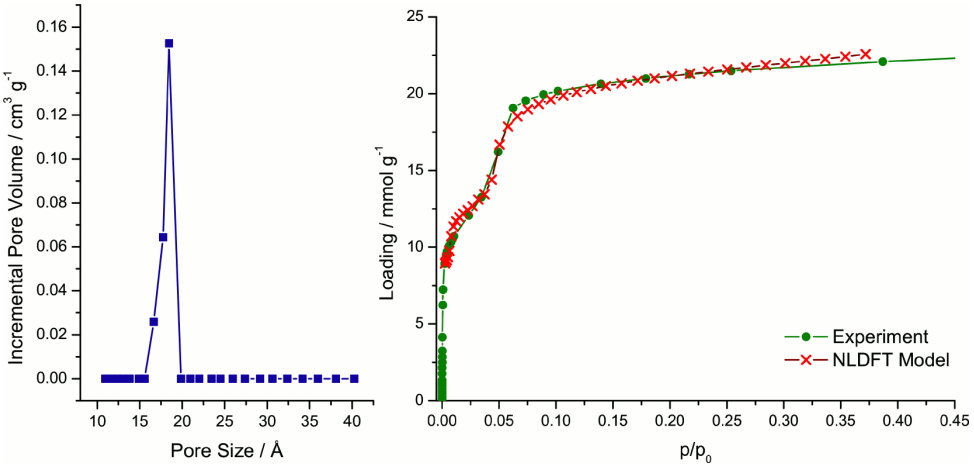

(b) STA-16(Ni)

Figure 6.16: Pore Size Distribution (PSD) calculated using NLDFT models within Micromeritics ASAP 2020 software[196, 197, 198] (*left*) and plots in the region of the mesoporous riser of the experimental and NLDFT model derived isotherm (*right*). Modal pore sizes of 16.6 Å and 18.4 Å for STA-16(Co) (*top*) and STA-16(Ni) (*bottom*) are in good agreement with crystallographic results and modelled data show good fits to the experimental isotherms.

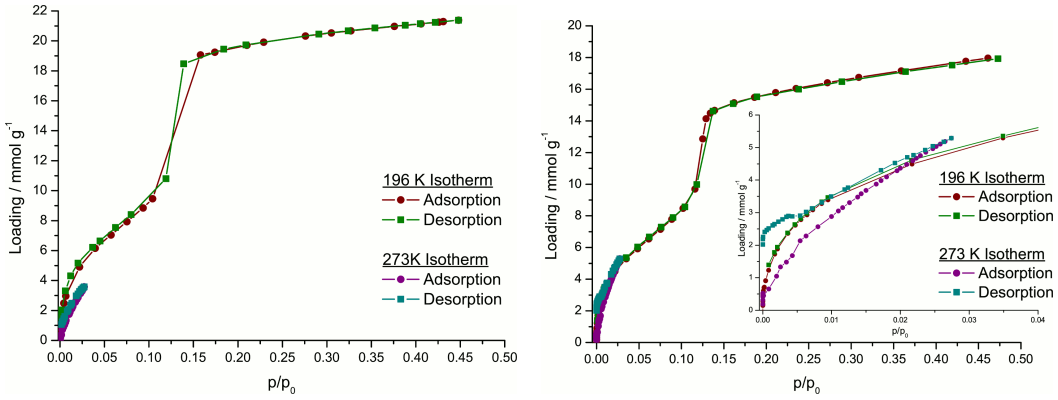

Figure 6.17: CO_2 isotherms at 77 K amd 196 K for STA-16(Co) (*left*) and STA-16(Ni) (*right*). Insets show detail of the $\frac{p}{p_0}$ 0–0.04 region. Both isotherms have a Type IVc profile.

D-R analysis of N_2 data indicates STA-16(Ni) has a greater maximum total loading, and hence pore volume, than STA-16(Co) (STA-16(Co): 0.67 cm^3 g^{-1}; STA-16(Ni): 0.76 cm^3 g^{-1}) due to the greater diameter of the pore channels (*Fig. 6.16*). Pore channels in STA-16(Ni) are larger as they retain their circular cross-section on dehydration and in fact increase in diameter on dehydration due to the slight structural rearrangement (*Section 6.4.3*), whereas those in STA-16(Co) are thought to distort.

Both materials are also porous to CO_2 at 196 and 273 K (*Fig. 6.17*).[2] Isotherms collected at 196 K show the same Type IVc profile as the N_2 isotherms. The 273 K isotherms, however, do not access a great enough range of $\frac{p}{p_0}$ to show the mesoporous riser. For structure STA-16(Co) the riser occurs in the range $\frac{p}{p_0}$ 0.12–0.16, whilst for STA-16(Ni) it was observed over $\frac{p}{p_0}$ 0.12–0.14. In both materials the riser is observed at significantly higher $\frac{p}{p_0}$ than for N_2.

Structure STA-16(Co) shows a lower uptake of CO_2 at 273 K (∼3.5 mmol g^{-1}, $\frac{p}{p_0} = 0.27$) than STA-16(Ni) (∼5.3 mmol g^{-1}, $\frac{p}{p_0} = 0.27$), whereas at 196 K both materials show a similar loading of CO_2 (∼4.8 mmol g^{-1}, $\frac{p}{p_0} = 0.22$). The cause of this difference is not clear as it would be expected that any effects due to diffusion or structural changes would be lessened at higher temperature. Further isotherms need to be collected to determine the cause of this.

D-R analysis was used to determine the maximum uptake of both materials. Analysis of the 273 K data found that they do not access sufficiently high $\frac{p}{p_0}$ values to quantify the maximum loading of the material, therefore only results from 196 K data will be discussed. Structure STA-16(Co) shows a significantly higher maximum

[2] *N.B.* CO_2 and N_2 adsorption data presented for STA-16(Co) were collected on different samples therefore results cannot be compared.

uptake of CO_2 than STA-16(Ni). The cause of this is currently unclear, but it may be related to changes in the structure of STA-16(Co) on adsorption. STA-16(Ni) shows a lower maximum uptake of CO_2 than N_2, partly due to the larger molecular volume of CO_2 compared to N_2. This cannot however explain such a big difference and the origin of this is also currently unknown. Maximum loadings of CO_2 and N_2 in STA-16(Co) have not been compared as adsorption data was collected on different samples of the material.

6.5.2 *In Situ* IR Spectroscopic Study of the Adsorption of CO and CO_2 by STA-16(Ni)

In situ IR spectra were collected for increasing coverages of CO_2 on STA-16(Ni) at 196 K and room temperature. Data collected at 196 K show a peak with a maximum at 2341 cm^{-1} assigned to physisorbed CO_2. With increasing coverage, two shoulders develop on the high (2357 cm^{-1}) and low (2312 cm^{-1}) frequency sides of the main peak (*Fig. 6.18*), assigned (by analogy to STA-12 — *Section 5.7.2*) to frustrated modes of CO_2. The main band, like that observed for CO_2 adsorbed in STA-12, shows a red-shift attributed to confinement effects.[191] No evidence of a chemisorbed species was observed. A similar behaviour was also observed for CO_2 adsorption at room temperature, with IR spectra showing only the presence of physisorbed CO_2.

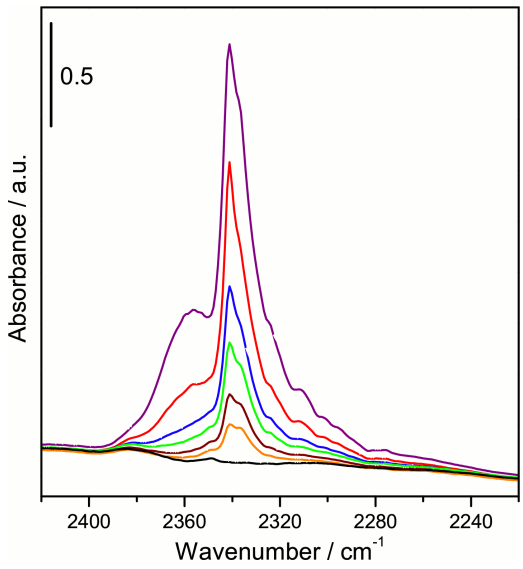

Figure 6.18: *In situ* IR spectra for the adsorption of CO_2 at 196 K in STA-16(Ni), from the activated material (black) to high CO_2 coverage (purple). Main peak (2341 cm^{-1}) assigned to physisorbed CO_2.

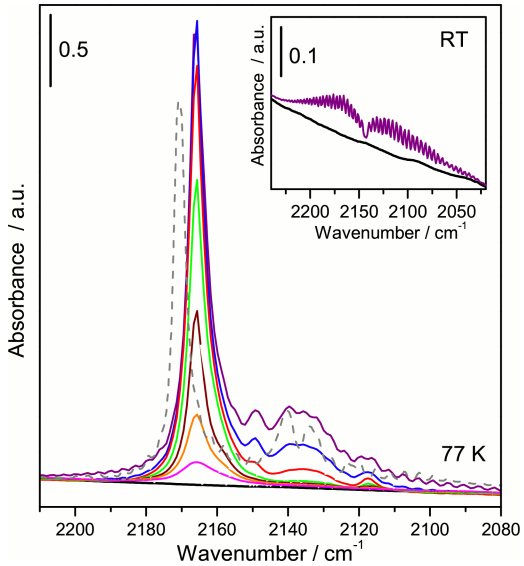

Figure 6.19: *In situ* IR spectra for the adsorption of CO at 77 K in STA-16(Ni), from the activated material (black) to high CO coverage (purple). Main peak (2166 cm^{-1}) assigned to chemisorbed CO. IR spectrum of CO_2 adsorbed by STA-12(Ni) shown for comparison (dashed grey). Inset shows spectrum for CO adsorption experiment at room temperature.

In situ IR spectra for the adsorption of CO by STA-16(Ni) were collected at 77 K and room temperature. Data collected at 77 K show the appearance of a peak at 2166 cm^{-1} and a second lower intensity peak at 2117 cm^{-1} (*Fig. 6.19*). These two peaks are assigned by analogy to STA-12(Ni) as ^{12}CO and ^{13}CO molecules, respectively, linearly bound to coordinatively unsaturated Ni^{2+} sites, through the C atom.[114] With increasing coverage additional bands develop on the low frequency side of the main band. At intermediate coverages, a band at 2135 cm^{-1} is observed, again assigned by analogy to STA-12(Ni), as CO adsorbed on P=O sites.[114], whilst at higher coverages a band centred at 2149 cm^{-1} is observed, assigned to liquid-like CO in the pores. The frequency shift from free CO (2143 cm^{-1})[199] is lower than that observed for STA-12(Ni) (STA-16(Ni): 2166 cm^{-1}; STA-12(Ni): 2170 cm^{-1} — *Fig. 6.19*). This smaller perturbation is due to the more sterically hindered environment about the coordinatively unsaturated Ni^{2+} site in STA-16(Ni)-DH. The C6 site in STA-16(Ni)-DH is only ∼2.8 Å from where the CO adsorbate would sit and thus the protons on this C atom will shield the Ni^{2+} cation from adsorbates. This is a surprising result since STA-16(Ni) does not undergo a structural transition on dehydration and therefore the coordinatively unsaturated sites were expected to be more available than in STA-12, whereas in fact they are slightly more hindered. At room temperature, IR spectra indicate CO is not chemisorbed by STA-16(Ni) (*Fig. 6.19 (inset)*).

6.6 Other Structures Formed with Co^{2+} Cations

6.6.1 Structure & Characterisation of $CoCl_{1.8}Br_{0.2}(\mathbf{LLH_2})$

Reactions using $CoCl_2$ in place of $Co(AcO)_2$ have been found to yield a new phase with a diffraction pattern very different to that of STA-16(Co). This new phase (labelled structure $Co_2X_2\mathbf{LL}H_2$ of this work) is obtained as a pure phase of large prismatic dark blue crystals from reactions with similar stoichiometry to that known to produce phase pure STA-16(Co), 2.0 : 1.0 : 2.0 : 1000 ($CoCl_2$: $H_4\mathbf{LL}$: KOH : H2O — *Table 6.1*).

The composition of this phase has been analysed by a combination of TGA, EDX and elemental analysis. TGA indicates a small weight loss at lower temperature (25–80°C: 2.9 wt.%) ascribed to the loss of water from the surface of the solid (*Fig. 6.20*). No significant weight losses are then observed until 395°C, above which temperature a sequence of weight losses is assigned to the collapse of the framework. This result suggests neither physisorbed nor chemisorbed water are present in the structure of $Co_2X_2\mathbf{LL}H_2$.

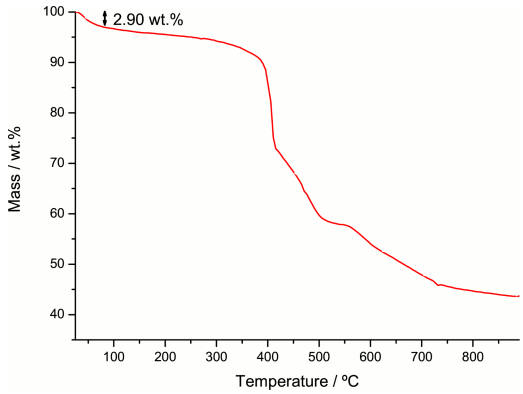

Figure 6.20: TGA plot for structure $Co_2X_2\mathbf{LL}H_2$. Initial weight loss is due to loss of water from the surface of the crystals. No weight losses due to dehydration are observed.

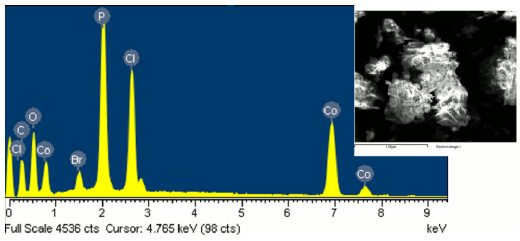

Figure 6.21: EDX spectrum of structure $Co_2X_2\mathbf{LL}H_2$ with Co : P ratio of 1.0 : 1.12 and Cl : Br ratio of 8.82 : 1.0. Inset shows area analysed.

EDX data gave a Co : P ratio of 1.0 : 1.12, suggesting a metal:ligand ratio of 2 : 1 (*Fig. 6.21*). As well as Co and P, EDX spectra also indicated the presence of both Cl and, at lower concentration, Br in the structure, in a ratio of 8.82 : 1.0. Combining these results, a composition of $Co_2Cl_{1.8}Br_{0.2}(\mathbf{LL}H_2)$ ($Co_2Cl_{1.8}Br_{0.2}(C_12H_24N_2O_6P_2)$) was proposed. Elemental analysis were found to be in reasonable agreement with this composition: expected — C 26.11 %, H 4.38 %, N 5.08 %; found — C 24.48 %, H 4.38 %, N 4.69 %.

Structure of $Co_2Cl_{1.8}Br_{0.2}(LLH_2)$

$Co_2X_2\mathbf{LL}H_2$ is obtained as large blue prismatic crystals suitable for measurement by single crystal X-ray diffraction. The structure of $Co_2X_2\mathbf{LL}H_2$ was solved using Sir2004[142] in space group $P\,2_1/c$ (a = 10.198(5) Å, b = 9.611(5) Å, c = 10.220(5) Å, β = 90.040(15)°, V = 1001.7(9) Å^3) and refined using the SHELXL routine of SHELX-97.[140] All non-H atoms were located in the initial structure solution, though the electron density due to the halide ion was assigned to Cl. A Br atom was placed on the same position as the Cl atom, with occupancy of the Cl set at 0.9 and Br at 0.1 (in agreement with EDX results — *vide supra*). Fractional coordinates and U_{Iso} parameters of both Cl1 and Br1 were restrained to vary together. Protons attached to N atoms were located from Fourier difference maps with positions and U_{Iso} parameters fully refined, whilst protons bonded to C atoms were positioned geometrically with coordinates and U_{Iso} values restrained to ride on the C atoms they were bound to. Refinement was continued until Fourier difference maps indicated no significant residual electron density. A final fit of R_1 = 0.0783 (R_{w2} = 0.1814) was obtained.

The structure crystallises with a β angle of nearly 90°and with very similar a and c parameters. This, and the R_{w2} may indicate that the structure might alternatively be solved in an orthorhombic or indeed tetragonal space group.

Bond	Distance / Å	Bond	Distance / Å
Co1-O3	1.962(6)	P1-O1	1.509(5)
Co1-O1	1.965(5)	P1-O2	1.534(5)
Co1-O2	1.975(5)	P1-O3	1.514(5)
Co1-Cl1	2.250(2)	P1-C6	1.825(8)

Table 6.11: Selected bond distances in the structure of $Co_2X_2\mathbf{LL}H_2$.

Structure $Co_2X_2\mathbf{LL}H_2$ has a pillared layered structure. Three PO_3C O atoms and a halide ion (either Cl^- or Br^-) coordinate every Co^{2+} in a distorted (due to the longer Co-X bond) tetrahedral geometry (*Table 6.11*). Cl^- and Br^- occupy the same site in a 9 : 1 ratio, capping the apex of the CoO_3X (X = Cl^- or Br^-) tetrahedron, projecting into the inter-layer region. PO_3C groups use all three O atoms in coordinating Co, forming $[Co_4P_4O_8]$ rings which are polymerised into layers in the *bc*-plane. Layers are pillared by bipiperidinyl moieties, bonded through the PO_3C groups and alternating in the [0 1 0] and [0 0 1] directions with the apical halide ions. Bipiperidinyl moieties engage in H-bonding through protonated N atoms with the PO_3C O atoms within the layers, the axial geometry of the methylenephosphonate groups permitting the development of these interactions.

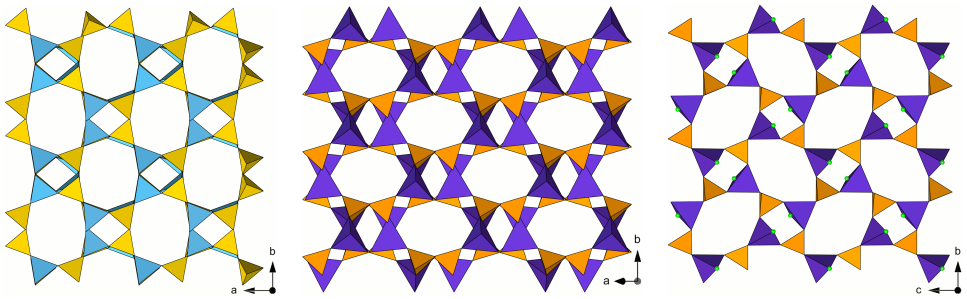

(a) (b) (c)

Figure 6.22: Comparison of the eight-rings in different forms of gismondine: natural gismondine (left) and a Co phosphate analogue (centre), with the layers of structure $Co_2X_2\mathbf{LL}H_2$ (right)

Narrow channels (1.0×1.2 Å) are delimited by the pillaring groups in the [1 1 0] direction, though these are too small to be accessible to adsorbates (*Fig. 6.23*).

The inorganic layer has a structure similar to that of the naturally occurring zeolite gismondine ($Ca_4[Al_8Si_8O_{31.9}]\cdot 18H_2O$).[200] In gismondine, [$AlO_4$] or [$SiO_4$] tetrahedra ($TO_4$) form eight-rings ([$T_8O_8$]), analogous to the [$Co_4P_4O_8$] rings observed in structure $Co_2X_2\mathbf{LL}H_2$. Rings delimit slightly elliptical channels parallel to the [1 0 0] and [0 0 1] directions (5.2×3.8 Å) which are occupied by Ca^{2+} and H_2O molecules. An analogous Co phosphate has also been prepared,[201] with eight-ring channels in the [0 0 1] and [1 0 1] directions with diameters (6.6×3.9 Å and 7.5×2.8 Å respectively). The eight-rings in structure $Co_2X_2\mathbf{LL}H_2$ have a similar diameter (6.6×4.0 Å) to the eight-rings of the Co phosphate gisomondine analogue. However in contrast to the other forms of gismondine, the long axes of neighbouring elliptical eight-rings are perpendicular to one another and are inaccessible to adsorbates due to the pillaring bipiperidinyl groups (*Fig. 6.22*).

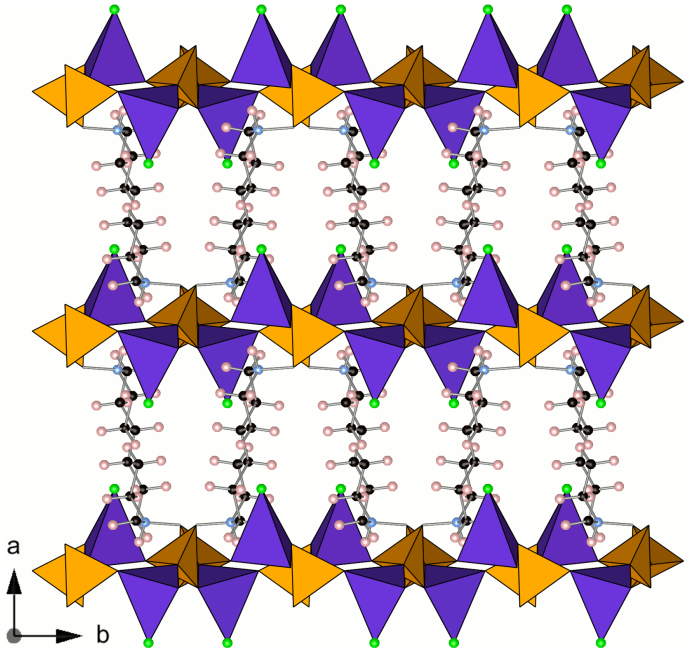

(a)

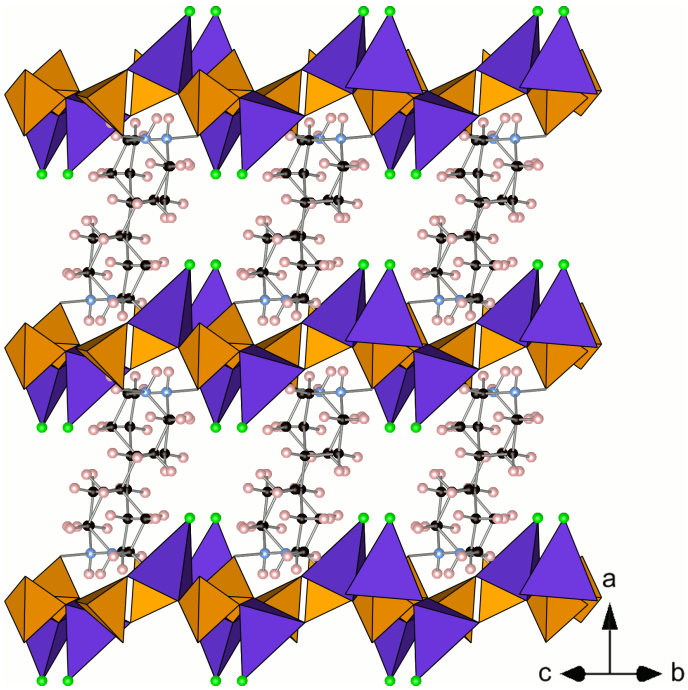

(b)

Figure 6.23: Structure of $Co_2X_2\mathbf{LL}H_2$ showing the pillaring of the inorganic layers by the bipiperidine groups (*top*) and the narrow channels delimited by the pillars in the [0 1 1] direction (*bottom*).

6.6.2 Structure & Characterisation of $Co_4(O)_2$**LL**$(AcO)_2 \cdot 1.8H_2O$

Reactions using a high $Co(AcO)_2$: H_4**LL** ratios (4 : 1) were found to give $Co_4(O)_2$**LL**$(AcO)_2 \cdot 1.8H_2O$ a pillared layered Co phase, $Co_4(O)_2$**LL**$(AcO)_2$. This phase was originally prepared by Mowat.[182] $Co_4(O)_2$**LL**$(AcO)_2$ is obtained over a range of reaction conditions (though a metal:ligand ratio of 4 : 1 is prerequsite for its formation) as a pink-red crystalline powder. Crystals are commonly large enough for single crystal X-ray diffraction. Structure $Co_4(O)_2$**LL**$(AcO)_2$ was analysed by TGA and single crystal diffraction. The TGA indicates a weight loss 20–160°C (4.22 wt.%) assigned to the loss of physisorbed water from the structure (*Fig. 6.24*). Assuming that on dehydration the composition of the material is $Co_4(O)_2$**LL**$(AcO)_2$, this weight loss corresponds to 1.8 molecules of water per formula unit. The dehydrated form of the material is stable to approximately 250°C.

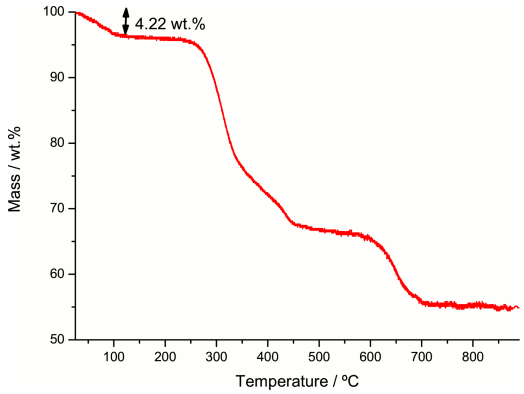

Figure 6.24: TGA plot for structure $Co_4(O)_2$**LL**$(AcO)_2$, showing a single weight loss 20–160°C (4.22 wt.%) corresponding to the loss of 1.8 molecules of water per formula unit from the structure.

Structure of $Co_4(O)_2$**LL**$(AcO)_2$

Single crystal diffraction data were collected for a sample of $Co_4(O)_2$**LL**$(AcO)_2$. Data were solved in space group $C2$ (a = 24.25(2) Å, b = 6.258(6) Å, c = 8.531(6) Å, β = 95.69(2)°, V = 1288.3(19) Å^3) using the Sir2008 package[141] and refined using the SHELXL routine of the SHELX-97 suite.[140] All non-H atoms were located from the initial structure solution. Not all electron density could be assigned to the structure, possibly indicating that the data were collected on a twinned crystal. Protons were placed geometrically on C atoms of the bipiperidine ring, with riding coordinates and U_{Iso} values. Due to the difficulty in assigning electron density it was not possible to refine thermal parameters anisotropically.

Bond	Distance / Å	Bond	Distance / Å	Bond	Distance / Å
Co1-O4	2.01(2)	Co2-O2	1.94(2)	P1-O1	1.53(3)
Co1-O4	2.01(2)	Co2-O2	1.94(2)	P1-O2	1.51(2)
Co1-O10	2.14(2)	Co2-O1	2.03(3)	P1-O2	1.51(2)
Co1-O10	2.14(2)	Co2-O4	2.07(4)	P1-C1	1.91(9)
Co1-O2	2.20(2)	Co2-N1	2.12(5)		
Co1-O2	2.20(2)				

Table 6.12: Selected bond distances in the structure of $Co_4(O)_2\mathbf{LL}(AcO)_2$.

The ADDSYM routine of PLATON[190] indicated the space group to be $C\,2/m$ and the structure was adapted to fit this new symmetry. Further cycles of refinement were undertaken and a final fit to the data of $R_1 = 0.2595$ ($R_{w2} = 0.5252$) was obtained. The high R_1 and R_{w2} values are attributed to the possible twinned nature of the crystal.

The structure of $Co_4(O)_2\mathbf{LL}(AcO)_2$ is composed of chains of edge-sharing distorted octahedrally coordinated Co ions (*Table 6.12*), parallel to the *b*-direction. Octahedral coordination is provided by two O atoms from PO_3C groups, two O atoms from acetate anions and two μ_3-O atoms. Chains are decorated with edge-sharing pseudo-square-based pyramidal coordinated Co ions on alternating sides of the chain, forming a zigzag ribbon (*Fig. 6.25a*). Coordination for this second Co site is provided by three PO_3C O atoms, a μ_3 O atom and a piperidinyl N atom. Co ribbons are linked in the *c*-direction, through the five-fold coordinate CoO_4N units by PO_3C groups, forming structural layers. Layers are pillared by N-coordinating bipiperidinyl units which alternate with monodentate AcO^- groups in the *c*-direction to leave $\sim 5 \times 2.8$ Å channels, which are occupied by physisorbed water molecules (*Figs. 6.25b & 6.25c*).

Considering the charges of the ions in this structure, in order for the framework to be charge neutral, the Co ions must have a 3+ charge. Co^{3+} is a stable oxidation state for Co, however for Ni^{3+} is not a common oxidation state and this may explain why it was not possible to form an Ni analogue of this material.

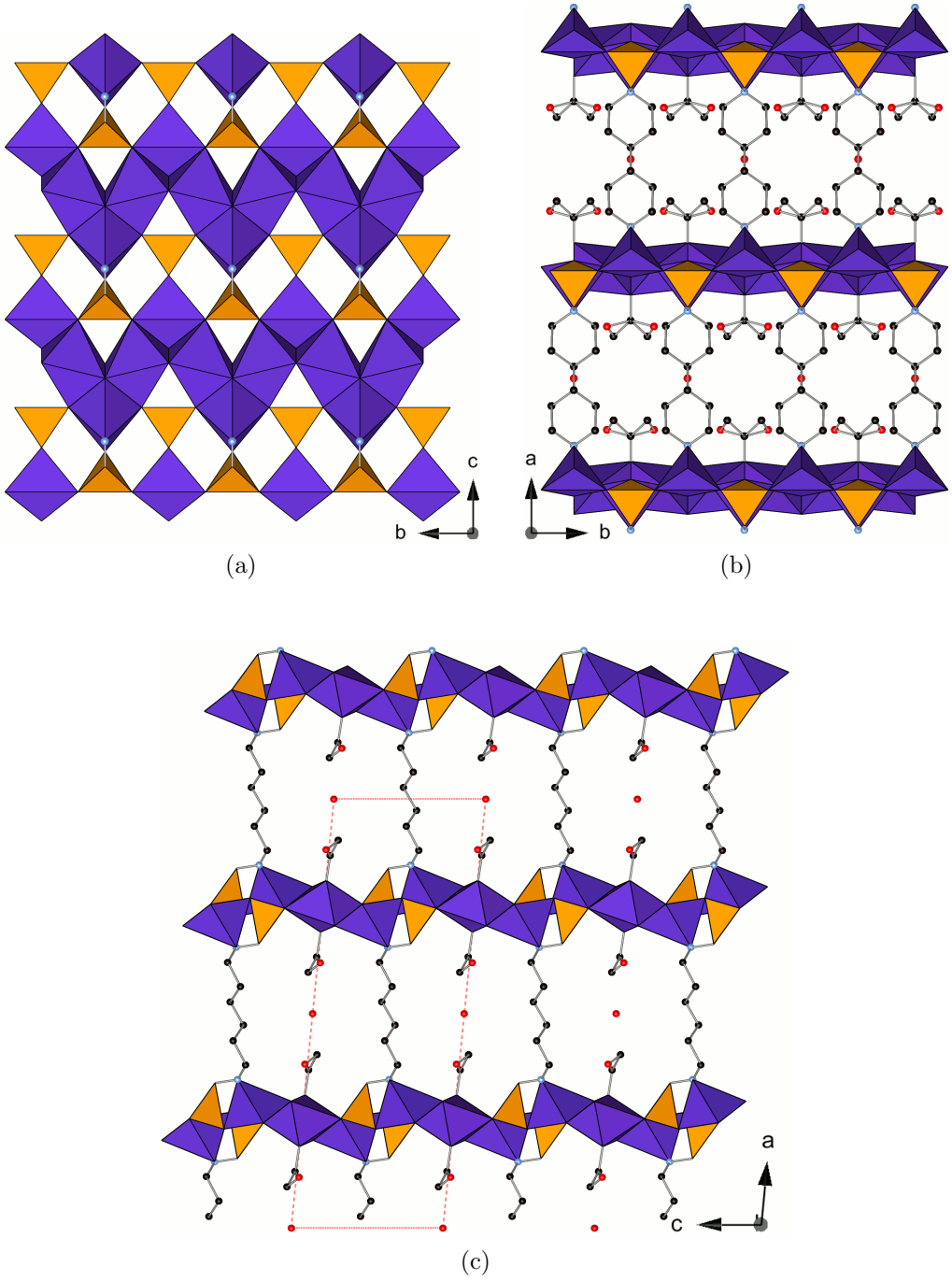

(a) (b)

(c)

Figure 6.25: Structure of $Co_4(O)_2$**LL**$(AcO)_2$ showing the structure of the *bc*-layers (*top left*) and the arrangement of the pillaring H_4**LL** groups and acetate groups capping the layers viewed along the *c*- (*top right*) and *b*-directions (*bottom*). Pink dashed lines in the *b*-direction view indicate unit cell — previously reported unit cell was twice as long as that shown in the *c* direction. The *b*-direction view also shows the narrow channels between the layers.

6.7 Reactions of Other Divalent Cations with H_4**LL**

In addition to $Co^{(II)}$ and $Ni^{(II)}$, reactions have been performed with a range of divalent metal cations including $Mg^{(II)}$, $Mn^{(II)}$, $Fe^{(II)}$, $Cu^{(II)}$ and $Zn^{(II)}$. Each cation was initially investigated using high-throughput (HT) syntheses to identify the phases formed. All HT syntheses used were performed using 1.5 ml of water.

Phase pure materials were obtained with all metals. However, to date it has only been possible to determine the structures for two formed with $Mn^{(II)}$. Characterisations of phases formed with $Mg^{(II)}$, $Fe^{(II)}$, $Cu^{(II)}$ and $Zn^{(II)}$ are reported in *Appendix C*.

6.7.1 Reaction of $Mn^{(II)}$ with H_4**LL**

Both $Mn(AcO)_2$ and $MnCl_2$ have been investigated as metal sources for $Mn^{(II)}$-H_4**LL** frameworks. HT reactions indicated that only one phase forms during hydrothermal reactions in the $Mn(AcO)_2$/H_4**LL**/KOH system (*Fig. 6.26*), $Mn_2(H_2O)_3$**LL** (labelled structure Mn_2**LL** of this work — *Section 6.7.2*). In the $MnCl_2$/H_4**LL**/KOH system, structure Mn_2**LL** was again observed and under very specific conditions a second phase, structure Mn_2X_2**LL**H_2, with composition determined as $Mn_2(H_2O)_4(Cl_{1.8}Br_{0.2})$**LL**$H_2$ (*Section 6.7.3*) was also obtained (*Fig. 6.27*).

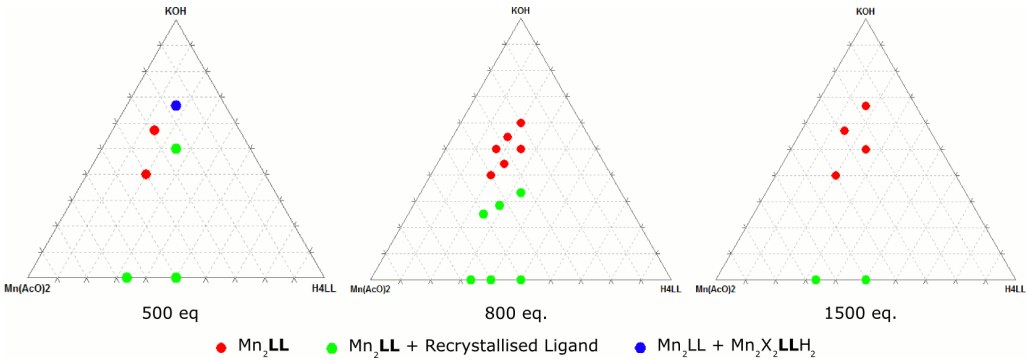

Figure 6.26: Triplots summarising HT reactions investigating phases formed in the $Mn(AcO)_2$/H_4**LL**/KOH system. The number of equivalents of water used in each series is given below each plot. All reactions were performed at 190°C for 24 hours.

In both the $MnCl_2$ and $Mn(AcO)_2$ systems, structure Mn_2**LL** was obtained with the greatest phase purity from reactions with high KOH concentrations (typically two or four equivalents of KOH for every ligand equivalent). At intermediate KOH concentrations, structure Mn_2**LL** was co-crystaliised with unreacted H_4**LL** and at the lowest base concentrations either recrystallised ligand or amorphous products

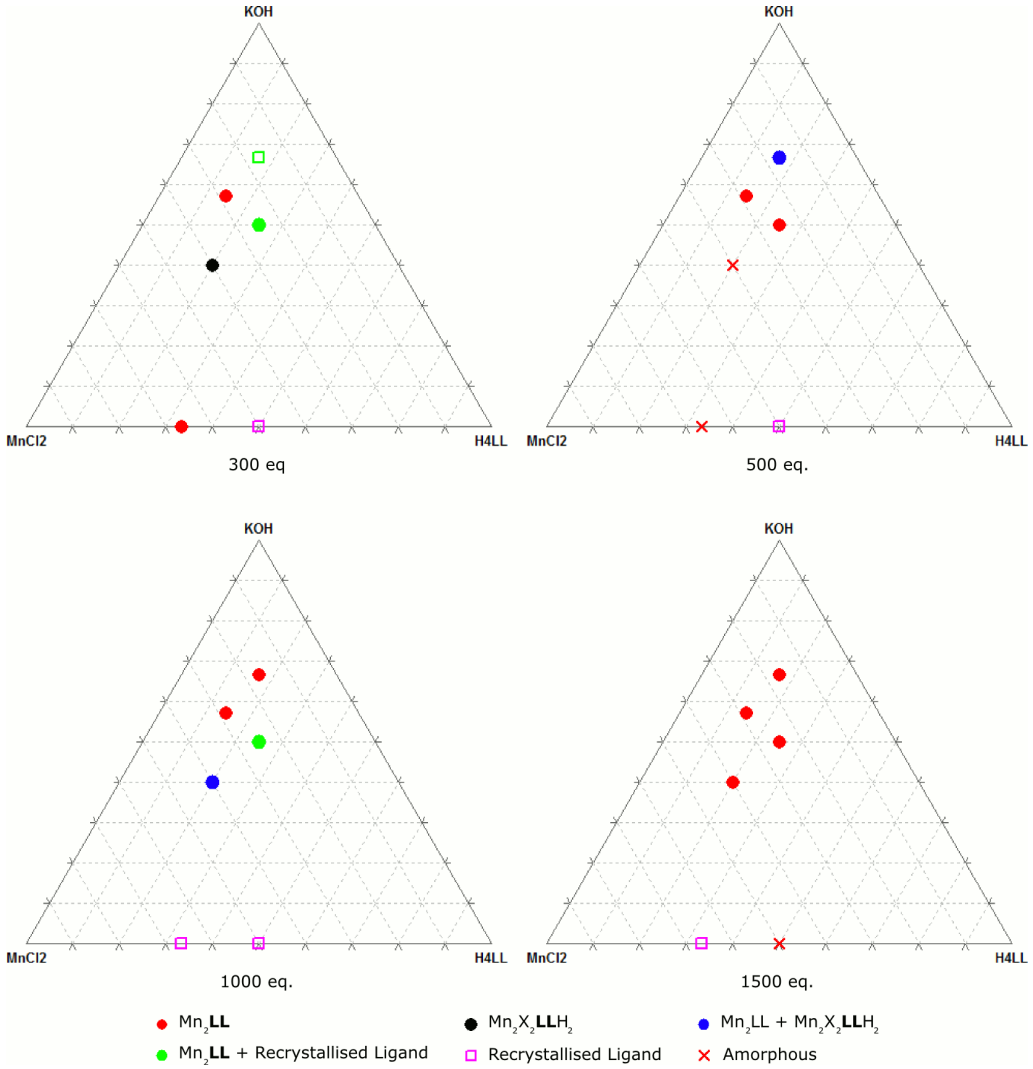

Figure 6.27: Triplots summarising HT reactions investigating phases formed in the $MnCl_2/H_4$**LL**/KOH system. The number of equivalents of water used in each series is given below the each plot. All reactions were performed at 190°C for 24 hours.

were obtained. More dilute reactions (1000 or 1500 equivalents of solvent) were found to favour the crystallisation of structure Mn_2**LL**, whilst the metal:ligand ratio was found to have little effect — ratios of 1 : 1 and 2 : 1 both successfully crystallised the material. Scaling HT preps up to 7 ml scale, it was impossible to obtain phase pure structure Mn_2**LL** and thus a full characterisation is not possible. However a single crystal of the material was obtain and its has been structure determined (*Section 6.7.2*).

Structure Mn_2X_2**LL**H_2 was obtained phase pure only in reactions using $MnCl_2$ as the metal source, indicating for crystallisation to occur halide ions must be present (*c.f.* structure Co_2X_2**LL**H_2 — *Section 6.6*). Most pure samples of structure Mn_2X_2**LL**H_2 were obtained from gel composition 2.0 : 1.0 : 2.0 : 300

Bond	Distance / Å	Bond	Distance / Å
Mn1-O11	2.116(6)	Mn2-O1	2.132(6)
Mn1-O10	2.117(6)	Mn2-O12	2.162(7)
Mn1-O3	2.132(6)	Mn2-O3	2.190(6)
Mn1-O100	2.205(7)	Mn2-O102	2.246(8)
Mn1-O101	2.233(8)	Mn2-O10	2.259(6)
Mn1-O11	2.251(7)	Mn2-N1	2.467(8)
P1-O1	1.522(7)	P10-O10	1.541(7)
P1-O2	1.529(7)	P10-O11	1.525(6)
P1-O3	1.557(7)	P10-O12	1.550(7)
P1-C1	1.806(10)	P10-C10	1.800(11)

Table 6.13: Selected bond distances about the Mn and P sites in structure Mn_2**LL**.

($MnCl_2$: H_4**LL** : KOH : H_2O). The phase was also observed as a minor impurity in the $Mn(AcO)_2$ system (gel composition: 1.0 : 1.0 : 4.0 : 500 — $Mn(AcO)_2$: H_4**LL** : KOH : H_2O), in which case the halide required to crystallise the phase would have come from residual HBr used as a catalyst in the preparation of H_4**LL**. In scaled up reactions of $MnCl_2$ and H_4**LL** (7 ml scale), phase pure structure Mn_2X_2**LL**H_2 was obtained allowing full characterisation of the material. Single crystals were also obtained and the structure determined (*Section 6.7.3*).

6.7.2 Structure of Mn_2LL

The structure of $Mn_2(H_2O)_3$**LL**, Mn_2**LL** of this work, was solved using the Sir2004 package[142] and refined using the SHELXL routine of the SHELX-97 suite.[140] The proposed composition is derived from the unit cell composition of the final refinement. The structure was solved in the triclinic space group $P\,1$ (a = 6.463(3) Å, b = 11.700(6) Å, c = 12.782(6) Å, α = 88.39(3)°, β = 79.76(3)°, γ = 79.28(2)°, V = 934.5(8) Å^3), with approximately half the non-H atoms located in the initial solution. Remaining non-H atoms were located by a series of Fourier difference maps. Protons were placed on C atoms geometrically with riding coordinates and U_{Iso} values. Cycles of refinement gave an adequate fit to the data. The ADDSYM routine of PLATON[190] suggested the space group should be changed to $P\,\bar{1}$ and the model thus adapted. Further cycles of refinement allowed location of protons on the three water molecules. The distances between the water O atoms and the protons were fixed at 0.9 Å. A final fit of R_1 = 0.0772 (R_{w2} = 0.149) was obtained.

Octahedrally coordinated Mn cations edge-share to form tetrameric clusters, composed of two Mn1 and two Mn2 sites. Mn1 is coordinated by four O atoms from

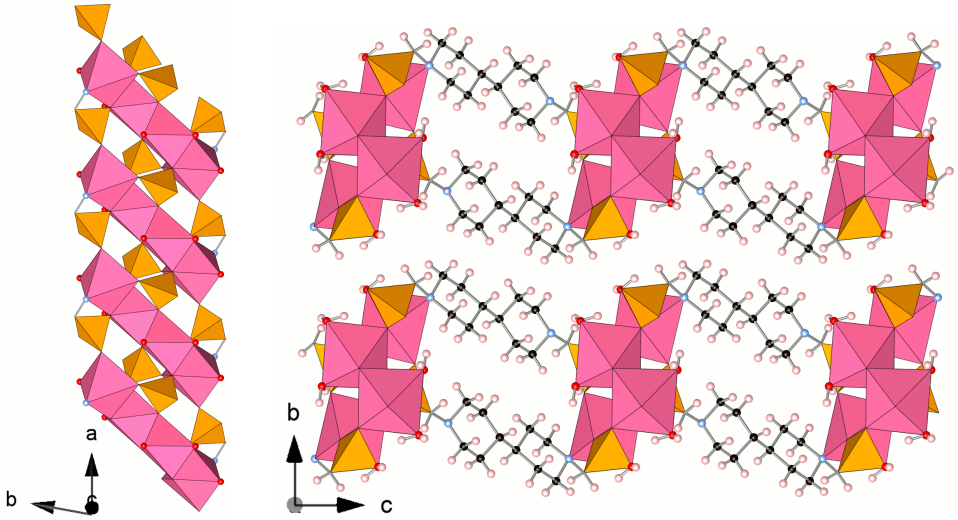

(a) (b)

Figure 6.28: Structure Mn_2**LL** showing the structure of the inorganic ribbons running parallel to the *a*-direction (*top*). Ribbons are linked to neighbours in the *b*-direction by bipiperidine moieties, forming sheets (*bottom*). Hydrogen bonding interactions hold the sheets together.

PO_3C groups and two O atoms from water molecules (*Fig. 6.13*). The distorted coordination environment about Mn2 is provided by four PO_3C O atoms, an O atom from a water molecule and completed by a long Mn-N contacts from a piperidinyl N atom (Mn2-N1: 2.467(8) Å) (*Fig. 6.13*). Coordination by the N atoms acts to terminate the Mn chain, limiting the length of the inorganic building block. Mn tetramers are linked together in the *a*-direction to form ribbons, by fully coordinating PO_3C units (P10) along the middle of the ribbon and bridging PO_3C units (P1) along the edge of the ribbon. The pendant P=O group of P10 forms an extensive H-bonding network with water molecules coordinating Mn sites in the same ribbon (H$\cdots$O: 1.94(4)–2.4(1) Å) and the neighbouring ribbon (O2$\cdots$H104: 2.14(7) Å). Ribbons are linked through two bipiperidinyl moieties to neighbouring ribbons above and below in the *c*-direction. There is no framework in this material, rather sheets are held together by H-bonding interactions between the inorganic portions of the structure.

6.7.3 Characterisation and Structure of $Mn_2X_2LLH_2$

The composition of $Mn_2(H_2O)_4(Cl_{1.8}Br_{0.2})(\mathbf{LL}H_2)$, $Mn_2X_2\mathbf{LL}H_2$ of this work, was analysed by EDX and elemental analysis. EDX spectra gave a Mn : P ratio of 1.0 : 1.13, indicating a metal:ligand ratio of 2 : 1. Both bromine and chlorine were found to be present in a consistent ratio of 10.40 : 1.0 (Cl : Br). Br is derived from the HBr catalyst used in preparation of $H_4\mathbf{LL}$. A composition of $Mn_2(H_2O)_4(Cl_{1.8}Br_{0.2})(\mathbf{LL}H_2)$ was proposed (H_2O was identified in the structure determination — *vide infra*) and found to be in good agreement with elemental analysis results: expected — C 23.40 %, H 5.24 %, N 4.55 %; found — C 23.82 %, H 5.57 %, N 4.53 %.

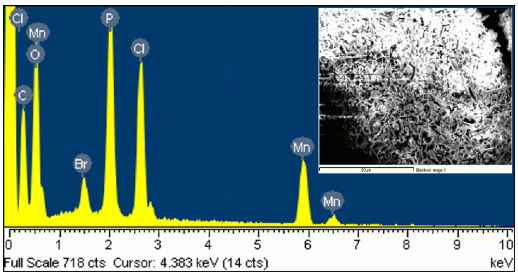

Figure 6.29: EDX spectrum of $Mn_2X_2\mathbf{LL}H_2$ showing the principal elements present in the material. Mn : P ratio 1.00 : 1.13; Cl : Br ratio 10.40 : 1.00. Inset shows area analysed.

The structure of $Mn_2X_2\mathbf{LL}H_2$ was solved using the Sir2004 package[142] and refined using the SHELXL routine of the SHELX-97 suite.[140] The structure was solved in monoclinic space group $P\,2_1/a$ (a = 10.064(6) Å, b = 7.618(4) Å, c = 14.377(8) Å, β = 91.521(6)°, V = 1102.0(11)Å^3) with all non-H atoms located in the initial structure solution, though the Cl/Br site was assigned as Cl only. Cycles of refinement indicated additional electron density was located at this site and following from the EDX results, a Br ion was placed on this site, with fractional occupancy of the Cl and Br atoms 0.9 and 0.1 respectively. Protons were placed geometrically on C atoms, with riding coordinates and U_{Iso} values, whilst the amino proton was located from Fourier difference maps. Additional cycles of refinement were performed until no significant movement was observed in the structure. A final fit of R_1 = 0.0398 (R_{w2} = 0.1685) was achieved.

Mn cations are coordinated in a distorted octahedral geometry by three O atoms from PO_3C groups, two O atoms from water molecules and a halide ion (*Table 6.14*). PO_3C groups are fully coordinating, linking three Mn sites together and forming a structural layer in the *ab*-plane. Water molecules coordinated to Mn cations project into small cavities within this layer; halide ions cap the faces of the layers. The layers may also be considered as polymerised $[Mn_4P_4O_8]$ rings, with rings inclined

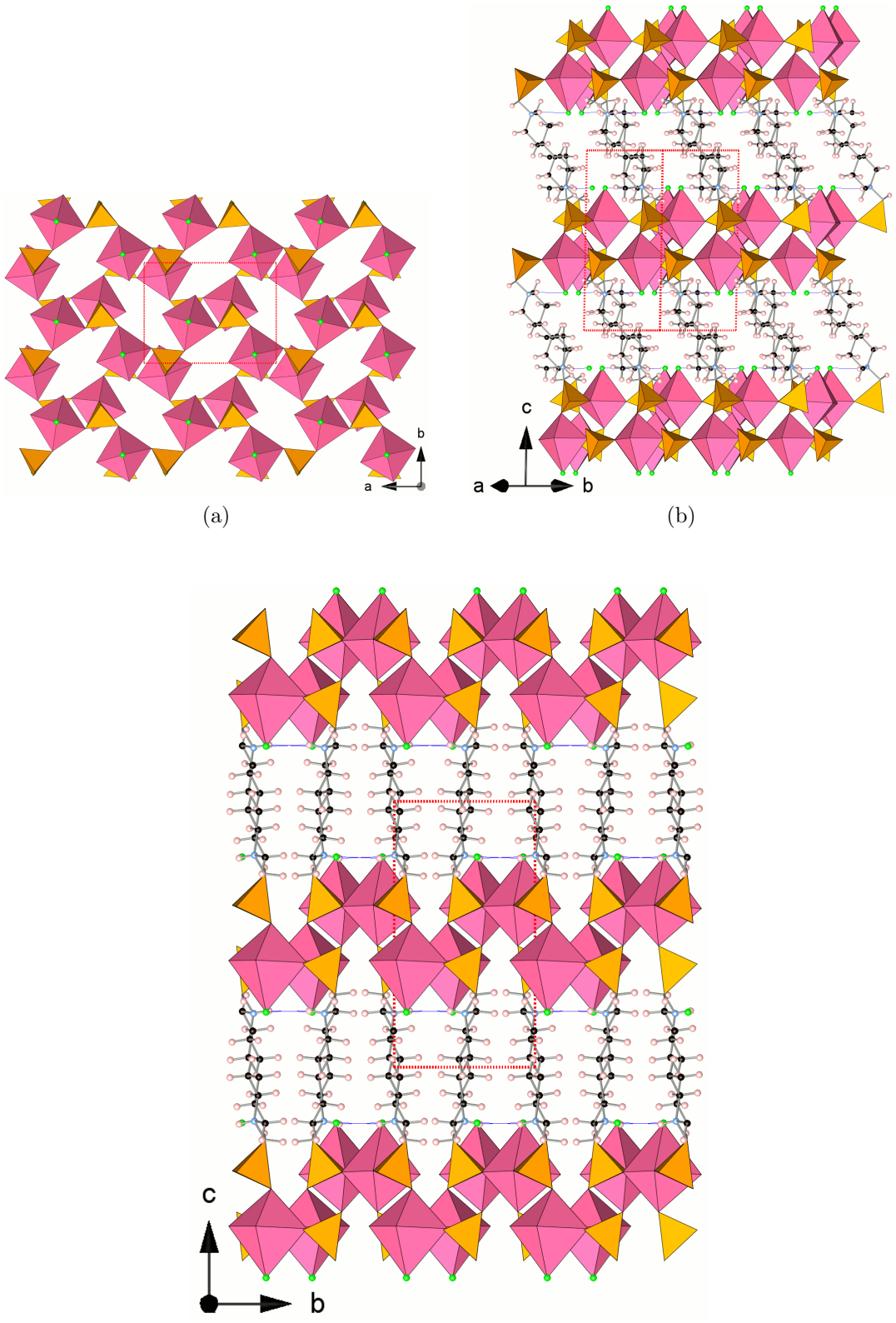

(a) (b)

(c)

Figure 6.30: Structure $Mn_2X_2\mathbf{LL}H_2$ showing the structure of the *ab*-layers (*top left*) and the arrangement of the pillaring bipiperidine moieties, viewed in the [1 1 0] direction (*top right*) and along the *a*-direction (*bottom*). Hydrogen bonding interactions between protonated bipiperidinyl N atoms and halide cations are shown (blue lines); unit cell also shown (red dashed lines).

Bond	Distance / Å	Bond	Distance / Å
Mn1-O2	2.112(3)	P1-O2	1.516(3)
Mn1-O3	2.114(3)	P1-O4	1.521(3)
Mn1-O4	2.215(3)	P1-O3	1.523(2)
Mn1-O1	2.227(3)	P1-C1	1.842(4)
Mn1-O5	2.251(3)		
Mn1-Cl1	2.6133(17)		

Table 6.14: Selected bond distances about the Mn and P sites of structure $Mn_2X_2\mathbf{LL}H_2$.

with respect to the layer plane. Such $[M_4P_4O_8]$ rings are also found in both structure $Co_2X_2\mathbf{LL}H_2$ (*Section 6.6*) and in the Sn^{2+} containing pillared layered material, $Sn(\mathbf{L}H_2)$[107] (see *Section 1.4.2*). The rings in $Mn_2X_2\mathbf{LL}H_2$ are most similar to the rings in $Sn(\mathbf{L}H_2)$, where instead of a Cl ion a lone-pair caps the surface of the layer. Layers are linked in the *c*-direction by protonated bipiperidinyl moieties. The amino protons of these groups engage in H-bonding with the capping halide ions (H7$\cdots$Cl1: 2.47(5) Å). Due to the density of pillaring, there are no accessible pores in the structure and the material is non-porous.

6.8 Initial Hydrothermal Syntheses Using Trivalent Cations with $H_4\mathbf{LL}$

The high-thoughput (HT) synthesis method has been used to determine whether it is possible to prepare isoreticular forms of either porous frameworks, such MIL-91 or STA-13, from reactions of trivalent metal cations $Al^{(III)}$, $Y^{(III)}$ or $Yb^{(III)}$ with $H_4\mathbf{LL}$. In each system, at least three previously unknown phases have been identified. Thus far it has not been possible to determine the structures of the new phases formed from these reactions, though initial analyses of powder X-ray diffraction patterns indicate that they are not isoreticular forms of known network. Results of high-throughput experiments detailing the synthetic conditions determined for the preparation of each phase are given in *Appendix D*.

6.9 Summary

6.9.1 STA-16 & Isoreticular Synthesis

The use of the longer linker H_4**LL** has led to the synthesis of the first isoreticular, permanently porous metal phosphonate materials: STA-16(Co) and STA-16(Ni). *Isoreticular synthesis*[39] or *scale chemistry*[42, 43] relies on the use of topologically identical building blocks to generate materials with the identical network connectivities. In previous examples, octahedral Zn_4O metal clusters were linked together by rigid linear dicarboxylate linkers.[38] In the current work, the linkers H_4**L** and H_4**LL** are topologically identical, yet also significantly more flexible than the rigid carboxylates previously used. Both ligands have the same α-aminomethylenephosphonate group, which coordinates the metal cations. The topologically identical nature of the two ligands is confirmed by the centrosymmetric structures of both linkers: H_4**L** has a centre of symmetry at the centre of the piperazine ring; H_4**L** has a centre of symmetry halfway between the bridging C-C bond (*Fig. 6.31*).

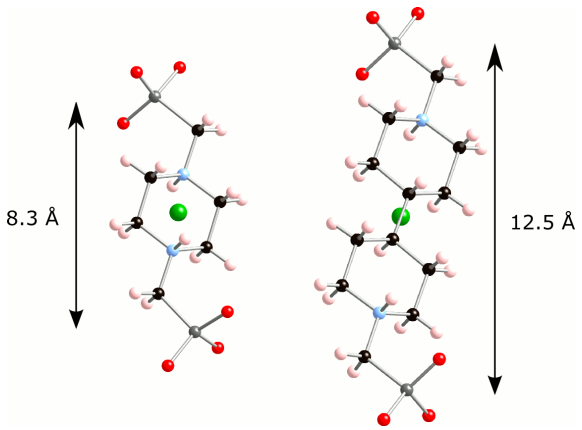

Figure 6.31: Comparison of the topology of the ligands H_4**L** and H_4**LL**. Both ligands possess the same groups to coordinate metal cations and both have a centre of symmetry (green sphere). H_4**LL** is approx. one third longer than H_4**L**. As ligands are topolgically identical, they should form isoreticular structures.

Using reaction conditions identical to those used in the preparation of STA-12(Co), but replacing H_4**L** with H_4**LL**, STA-16(Co) was prepared. Similarly, using H_4**LL** in a reaction which would prepare STA-12(Ni), STA-16(Ni) was synthesised. STA-16(Co) and STA-16(Ni) have been shown to be isostructural. Attempts to synthesise STA-16 with divalent metals other than Co and Ni have so far been unsuccessful. The structures of STA-12 and STA-16 are isoreticular, having identical helical chains of MO_5N octahedra which run parallel to the *c*-direction. Metal cations

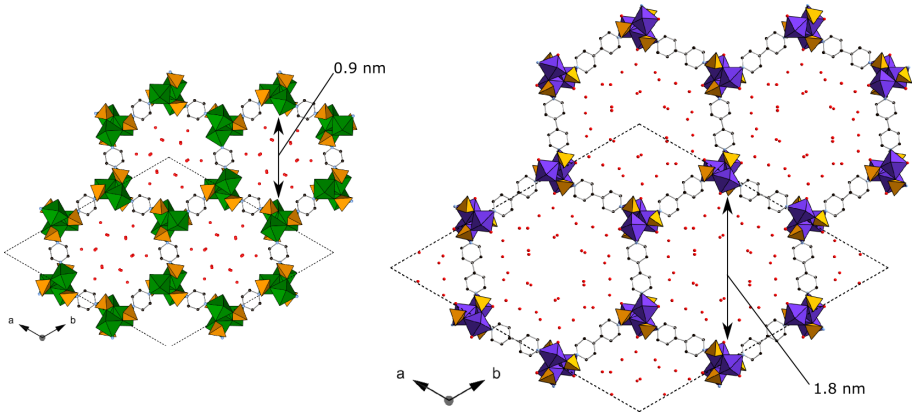

Figure 6.32: The as-prepared structures of STA-12(Ni) (*left*), formed with H_4**L**, and STA-16(Co) (*right*), prepared using H_4**LL**, viewed along the *c*-axis. Channels are occupied by physisorbed water molecules. Channels in the STA-12 structure have a free diameter of $\sim$ 0.9 nm whereas the longer linker in STA-16 gives the channels approx twice the free diameter ($\sim$ 1.8 nm).

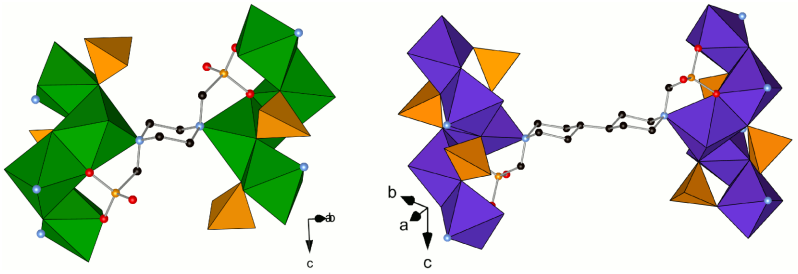

Figure 6.33: Comparison of the coordination modes of the linker **L** in STA-12(Ni) (*left*) and **LL** in STA-16(Co) (*right*). Both ligands have rings in chair conformation with ring N atoms engaged in coordinative bonding to the metal cation. α-methylenephosphonate groups are axial and coordinate three metal cations in a bridging mode with a pendant P=O bond.

in both structures are coordinated through the N atom of the ligand ring, whilst the PO_3C groups coordinate in a bridging mode to leave a pendant P=O group projecting into the pore space (*Fig. 6.33*). The coordination environment of metal cations in the as-prepared structures of both materials is completed by a chemisorbed water molecule. Chains are linked in the *ab*-plane by linkers, coordinated through the ring N atom, to form a honeycomb array of unidirectional channels. Clearly the diameter of the channels is entirely dependent on the distance between the 'terminal' N atoms of the linker. Using H_4**L** channels with a diameter of $\sim$ 9 Å are formed in the STA-12 family of materials, whereas using the longer H_4**LL** linker, in the STA-16 materials channel have a free diameter of $\sim$ 18 Å (*Fig. 6.32*).

The structure of STA-16 has been confirmed by synchrotron powder X-ray diffraction data (*Table 6.15*). The dehydration behaviour of both STA-16(Co) and

	STA-16(Co)	STA-16(Ni)	STA-16(Ni)-DH
Formula	$Co_2(H_2O)_2\mathbf{LL} \cdot 7.46H_2O$	$Ni_2(H_2O)2\mathbf{LL} \cdot 10.18H_2O$	$Ni_2(H_2O)_2\mathbf{LL}$
Space Group	$R\bar{3}$	$R\bar{3}$	$R\bar{3}$
a / Å	41.2870(2)	41.0540(8)	41.2136(16)
c / Å	6.26296(7)	6.2056(2)	6.340(2)
V / Å^3	9245.63(13)	9057.9(4)	9326(3)
Diffractometer	DLS/I11	DLS/I11	DLS/I11
Temperature / K	100	100	100
λ / Å	0.825028	0.825028	0.825028
No. Reflections	1213	1192	1223
No. Atoms (non-H)	16.73	18.09	12
No. Restraints	49	51	48
R_{wp}	0.0467	0.0446	0.0445
R_p	0.0338	0.0345	0.0327
$R(F^2)$	0.0532	0.1318	0.0370
χ^2	45.17	138.3	137.8

Table 6.15: Crystallographic data for the re-refined structures of as-prepared STA-16(Co) and STA-16(Ni) and dehydrated STA-16(Ni). Formula quoted is that determined from diffraction.

STA-16(Ni) were analysed by a combination of TGA and powder X-ray diffraction (and for STA-16(Ni), *in situ* IR spectroscopy). STA-16(Co) undergoes a structural transition on dehydration from $R\bar{3}$ to a lower symmetry material. The nature of this structure has not yet been determined, but the transition is reversed on dehydration, which shows the connectivity of the framework is retained. By contrast, STA-16(Ni) shows no significant changes in peak positions on dehydration, indicating the retension of rhombohedral symmetry. The structure of STA-16(Ni)-DH has been confirmed by synchrotron powder X-ray diffraction (*Table 6.15*). Channels retain a free diameter of $\sim$ 19 Å and each Ni^{2+} cation is five-fold coordinated, with a coordinatively unsaturated site (CUS). Pendant P=O groups are retained in the fully dehydrated material, as evidenced by *in situ* IR spectroscopy. CUS in STA-16(Ni) are less accessible than in STA-12(Ni) due to crowding of the site by piperidine methylene groups of the linker.

STA-16(Co) and STA-16(Ni) are porous to both N_2 at 77 K and CO_2 at 196 and 273 K. Isotherms of both materials are classified as Type IVc,[163] with a step typical of mesoporous materials. Both materials show significant porosity to both N_2 and CO_2. NLDFT analysis of the N_2 adsorption isotherms at 77 K gave a pore size distribution with peaks consistent with the pore sizes determined from crystallographic measurements (STA-16(Co): 1.66 nm; STA-16(Ni): 1.84 nm). *In situ* IR spectroscopic measurements for the adsorption of CO and CO_2 by

STA-16(Ni) show STA-16(Ni) behaves in a similar way to STA-12(Ni), though with weaker interactions between the adsorbate and the CUS. This is attributed to the greater steric crowding of the CUS in STA-16(Ni)-DH.

Although a wide range of divalent metal phosphonates have been reported by various groups using the linker $H_4\mathbf{L}$ (see *Section 1.4.2*), it has so far not proven possible to synthesise isoreticular forms of any structures other than STA-12. Similarly for trivalent cations, it has so far not been possible to form isoreticular forms of any of the reported frameworks (*Section 6.9.3* and *Appendix Section D*). The reasons for this are not entirely clear, though from a review of the reported structures it is clear that H-bonding plays an important role in directing the crystallisation of many phosphonate frameworks. Increasing the length of the linker (using $H_4\mathbf{LL}$) may mean that H-bonding arrangements do not develop in the same way and thus a network different to that formed under the same reaction conditions with $H_4\mathbf{L}$ is favoured. Further work is necessary to determine if this is the case.

6.9.2 Other Structures Formed with Divalent Cations & H_4LL

Reaction of $CoCl_2$ with $H_4\mathbf{LL}$, under the same conditions found to prepare STA-16(Co), yielded a different structure, $Co_2X_2\mathbf{LL}H_2$ (*Table 6.16*). $Co_2X_2\mathbf{LL}H_2$ has a pillared layered structure, with layers capped by halide anions. The layers have a structure related to that of the zeolite gismondine (which has also been prepared as a Co-phosphate) constructed from polymerised $[Co_4P_4O_8]$ rings. The structure is non-porous.

Using a higher concentration of $Co(AcO)_2$ with $H_4\mathbf{LL}$ under similar conditions to those forming STA-16(Co), a phase previously reported by Mowat was obtained, $Co_4(O)_2\mathbf{LL}(AcO)_2$.[182] $Co_4(O)_2\mathbf{LL}(AcO)_2$ is also a pillared layered compound. Layers are composed of edge-sharing zig-zag chains of Co ions in a distorted octahedral coordination linked into layers by fully coordinating PO_3C groups. Coordination is also provided by linker N atoms. Every other Co cation is coordinated by a monodenate AcO^- anion. AcO^- anions line the $\sim 5 \times 2.8$ Å channels parallel to the *c*-direction, which are also occupied by physisorbed H_2O molecules. Physisorbed water may be removed but the structure is non-porous.

Structure have also been prepared using $Mg^{(II)}$, $Mn^{(II)}$, $Fe^{(II)}$, $Cu^{(II)}$ and $Zn^{(II)}$ as the framework forming cation (see also *Appendix Section C*). Only structures of two $Mn^{(II)}$ phases were determined, whilst only cells for the $Mg^{(II)}$ and $Cu^{(II)}$ materials have been determined (*Table C.1*). Although the $Fe^{(II)}$ and $Zn^{(II)}$ structures were obtained phase pure, it was not possible to determine unit cells for the materials

(*Appendix Sections C.2 & C.4*). Of the two $Mn^{(II)}$ phases, only one has a framework structure. $Mn_2X_2\mathbf{LL}H_2$, formed from the reaction of $MnCl_2$ and $H_4\mathbf{LL}$, has a pillared layered structure. Like the layers in $Co_2X_2\mathbf{LL}H_2$, layers in $Mn_2X_2\mathbf{LL}H_2$ are formed from polymerised $[Mn_4P_4O_8]$ rings. Coordination of the Mn sites is completed by a halide anion and two H_2O molecules, with halide capping the layers, as in $Co_2X_2\mathbf{LL}H_2$. The structure is non-porous. The second $Mn^{(II)}$ phase has a layered structure of ribbons of tetrameric $Mn^{(II)}$ clusters and bridging PO_3C groups, parallel to the *a*-direction. Ribbons are linked by bipiperidinyl groups in the *c*-direction, whereas in the *b*-direction ribbons are linked only by H-bonding.

6.9.3 Structures Formed with Trivalent Cations & H_4LL

Reactions of $Al^{(III)}$, $Y^{(III)}$ and $Yb^{(III)}$ with $H_4\mathbf{LL}$ were investigated (*Appendix Section D*). With $Al^{(III)}$, three phases were identified by powder X-ray diffraction and the conditions favouring their synthesis were identified. Five phases were identified with $Y^{(III)}$ and analogues of three of these phases have been identified using $Yb^{(III)}$. High-throughput synthesis was used to determine synthetic conditions favouring each phase.

	$Co_2X_2\mathbf{LL}H_2$	$Co_4(O)_2\mathbf{LL}(AcO)_2$	$Mn_2X_2\mathbf{LL}H_2$	$Mn_2\mathbf{LL}$
Formula	$Co_2(Cl_{1.8}Br_{0.9})\mathbf{LL}H_2$		$Mn_2(Cl_{1.8}Br_{0.9})(H_2O)_4\mathbf{LL}$	
Space Group	$P\,2_1/c$	$C\,2/m$	$P\,2_1/a$	$P\,\bar{1}$
a / Å	10.198(5)	24.25(2)	10.064(6)	6.463(3)
b / Å	9.611(5)	6.258(6)	7.618(4)	11.700(6)
c / Å	10.220(5)	8.531(7)	14.377(8)	12.782(6)
α / °				88.39(3)
β / °	90.040(15)	95.69(2)	91.521(6)	79.76(3)
γ / °				79.28(2)
V / Å^3	1001.7(9)	1288.3(19)	1102.0(11)	934.5(8)
Z	4	2	4	2
Crystal Morphology	Prism, blue	Platelet, purple	Platelet, colourless	Prism, colourless
Temperature / K	93(2)	93(2)	93(2)	93(2)
Wavelength	Mo K_α	Mo K_α	Mo K_α	Mo K_α
Total / $[I > 2\sigma(I)]$ Reflections	1797/1367	1253/1176	1825/1733	3314/1457
R_1 $[I > 2\sigma(I)]$	0.0783	0.2595	0.0398	0.0772
R_{w2}	0.1814	0.5252	0.1685	0.1492

Table 6.16: Crystallographic data from single crystal X-ray diffraction experiments for $Co_2X_2\mathbf{LL}H_2$, $Co_4(O)_2\mathbf{LL}(AcO)_2$, $Mn_2X_2\mathbf{LL}H_2$ and $Mn_2\mathbf{LL}$. $Co_4(O)_2\mathbf{LL}(AcO)_2$ has a smaller unit cell than previously reported — this may account for the poor fit to the data.

Chapter 7

Conclusions & Further Work

Reactions of $Y^{(III)}$ with $H_4\mathbf{L}$, $H_4\mathbf{L}'$, *R*-$H_4\mathbf{L}'$ and $H_4\mathbf{L}''$ have been investigated and four principal phases identified from reactions. Initial work focussed on the re-investigation of the structure reported by Groves *et al.*, $Y_2(\mathbf{L}H_2)_3$ ($Y_2(\mathbf{L}H_2)_3 \cdot 5H_2O$).[112] Reported reaction stoichiometric ratios did not prepare $Y_2(\mathbf{L}H_2)_3$ but instead a new unknown $Y^{(III)}$ phase was obtained. Correct synthesis conditions were determined and optimised to an initial gel composition of 1.0 : 1.5 : 3.0 : 1000 ($Y(AcO)_3$: $H_4\mathbf{L}$: KOH : H_2O). During optimisation, a further three $Y^{(III)}$ phases were identified. The as-prepared structure of $Y_2(\mathbf{L}H_2)_3$ was determined by Rietveld refinement of powder X-ray diffraction data against a model of a related $Gd^{(III)}$ material.[112] The structure was initially solved in orthorhombic space group $P\,22_12_1$. However, solid state MAS NMR data indicated a lower symmetry for $Y_2(\mathbf{L}H_2)_3$ (due to the number of resonances in the ^{31}P spectrum). The final structure was refined in $P\,112_1$, with a γ angle close to 90°, as this space group was consistent with systematic absences and removed disorder from one of the ligands in the structure. $Y_2(\mathbf{L}H_2)_3$ has a pillared layered structure. Chains of Y^{3+} cations linked to neighbours by three bridging PO_3C groups parallel to the *b*-direction are linked in the *a*-direction by piperazine ligands to form a structural layer. Layers are then pillared in the *c*-direction to form the framework, with narrow channels between the layers occupied by physisorbed water molecules. The structure of dehydrated $Y_2(\mathbf{L}H_2)_3$ was also obtained from Rietveld refinement. The structure was refined in $P\,12_11$ and shows a large decrease in the *c* parameter of the unit cell ($\sim$ 12 %) and an increase in the β angle to 94.5°. Removal of the physisorbed water from the narrow channels results in a shearing motion of the structural layers as the structure attempts to reduce its free pore volume.

Miller had previously reported the preparation of STA-13(Sc) ($Sc_2(\mathbf{L}'H_2)_3{\cdot}H_2O$) using the racemic ligand $H_4\mathbf{L}'$ and also reported that synthesis of STA-13(Y)

($Y_2(\mathbf{L}'H_2)_3 \cdot 7H_2O$) was possible.[184] STA-13(Y) was successfully synthesised from gels with initial composition 1.0 : 1.5 : 1000 ($Y(AcO)_3$: $H_4\mathbf{L}'$: H_2O). The reaction stoichiometry is very similar to that preparing $Y_2(\mathbf{L}H_2)_3$, but no base is used in the preparation of STA-13(Y) — with base amorphous products were obtained. The structure of STA-13(Y) was determined from synchrotron powder X-ray diffraction data. Miller reports a nearly complete structure from synchrotron powder X-ray diffraction for the $Sc^{(III)}$ form of STA-13 with some uncertainty over the location of Me groups in the structure.[184] This model was used as the starting point for Rietveld refinement and was found to be in good agreement with the data. Solid state MAS NMR indicated disorder of the Me C atom over two positions on the piperazine ring. The dehydrated structure of STA-13(Y) was also confirmed by Rietveld refinement of synchrotron powder X-ray diffraction data. The framework was observed to undergo few changes on dehydration. The stoichiometry of the structure, $Y_2(\mathbf{L}'H_2)_3 \cdot 7H_2O$, is the same as $Y_2(\mathbf{L}H_2)_3 \cdot 5H_2O$ and the structure of the chains in both material is closely related, with isolated Y^{3+} cations linked to neighbours by three bridging PO_3C groups. In STA-13(Y), however, Y^{3+} cations are not staggered relative to neighbouring cations along the chain axis. Although sharing stoichiometries and similar chain structures, the two frameworks, $Y_2(\mathbf{L}H_2)_3 \cdot 5H_2O$ and STA-13(Y), are vastly different. Chains in STA-13(Y) are linked to three others to form a rigid honeycomb array of unidirectional channels which are retained on dehydration. These channels are large enough to take up adsorbates (*vide infra*) and the material may be described as permanently porous.

To try to understand why STA-13(Y) forms with racemic $H_4\mathbf{L}'$ whilst $Y_2(\mathbf{L}H_2)_3$ is obtained from reactions with $H_4\mathbf{L}$, reactions of $Y^{(III)}$ with enantiopure *R*-$H_4\mathbf{L}'$ and $H_4\mathbf{L}''$ using stoichiometric ratios of 1.0 : 1.5 : 1000 ($Y(AcO)_3$: $H_4\mathbf{L}$: H_2O) were investigated. With *R*-$H_4\mathbf{L}'$ a structural analogue of $Y_2(\mathbf{L}H_2)_3$, $Y_2(R\text{-}\mathbf{L}H_2)_3$ ($Y_2(R\text{-}\mathbf{L}'H_2)_3 \cdot 4H_2O$), was obtained, whilst with $H_4\mathbf{L}''$ a different phase with an unknown structure was obtained.

The structure of as-prepared $Y_2(R\text{-}\mathbf{L}H_2)_3$ was determined from synchrotron powder X-ray diffraction data. A starting model for Rietveld refinement of $Y_2(R\text{-}\mathbf{L}H_2)_3$ was obtained by placing Me C atoms geometrically in positions consistent with the *R* enantiomer of ligand $H_4\mathbf{L}'$ within the orthorhombic structure of $Y_2(\mathbf{L}H_2)_3$. The structure of dehydrated $Y_2(R\text{-}\mathbf{L}H_2)_3$ was also obtained from Rietveld refinement, using the same starting model as the as-prepared material. Dehydrated $Y_2(R\text{-}\mathbf{L}H_2)_3$ does not show the same unit cell contraction observed for $Y_2(\mathbf{L}H_2)_3$. This is because the Me groups effectively lock the structure open. Although larger voids are present in $Y_2(R\text{-}\mathbf{L}H_2)_3$, the structure is still non-porous, attributed to a rotation of the piperazinyl rings to reduce the free pore volume in the material

Two factors control which phase is obtained: the steric bulk of the ligand and the favourability of forming an H-bonding network. $Y_2(\mathbf{L}H_2)_3$ is thought to be a low energy configuration and therefore in the absence of any other effects, this structure is crystallised. Using racemic $H_4\mathbf{L}'$, the structure of $Y_2(\mathbf{L}H_2)_3$ is not able to accommodate both *R* and *S* in one crystal structure due to the steric clashing of the Me groups with other parts of the framework. Instead a conglomerate of *R* and *S* handed crystals would have to form. Crystallisation of STA-13(Y) is favoured enthalpically by the extensive H-bonding network present in the structure. The Me group on the piperazine ring hinders ring flipping, effectively preorganising the ligand to H-bond with neighbours. However, crystallisation of the STA-13 network requires both *R* and *S* enantiomers — enantiopure STA-13 cannot crystallise due to steric clashing of neighbouring ligands. Therefore when using enantiopure *R*-$H_4\mathbf{L}'$, the $Y_2(R\text{-}\mathbf{L}H_2)_3$ network was obtained. Using $H_4\mathbf{L}''$, however, a new unknown network crystallises as there is not sufficient space to accommodate two *trans* Me groups on the piperazine ring in either the STA-13 or $Y_2(\mathbf{L}H_2)_3$ networks.

Of these frameworks, only STA-13(Y) was found to be porous to N_2, CO_2, CH_4 and short alkanes, showing loadings of up to 4 mmol g^{-1} with CO_2 at 196 K. CO_2 isotherms collected at 196 K showed a small hysteresis loop. The origin of this was not clear and further adsorption measurements should be made to clarify nature of this hysteresis. CH_4 isotherms indicate similar loadings to the CO_2 isotherms. CH_4 isotherms show an approximately Type I form, apparently showing some intracrystalline adsorption which was not observed with other adsorbates. Further CH_4 adsorption data should be collected to confirm that this is intercrystalline adsorption. The use of STA-13(Y) in mixed gas adsorptions has not been investigated. This might initially be undertaken through the use of GCMC molecular simulations of adsorption isotherms.

In addition to $Y^{(III)}$, the STA-13 network has been prepared with $Sc^{(III)}$ and lanthanide cations $Gd^{(III)}$–$Yb^{(III)}$. Of these, only $Yb^{(III)}$ is consistently porous, showing approximately two thirds the porosity of STA-13(Y). The reasons for the variable porosity of the different forms of STA-13 has not been investigated. Understanding the cause of the lower porosity of these materials might help to improve either synthesis of the materials or activation condtions prior to adsorption.

Reactions of the the smaller trivalent cation Fe^{3+} with $H_4\mathbf{L}$ and $H_4\mathbf{L}'$ have also been investigated. Using either $Fe^{(III)}AcO$ or $FeCl_3$ in reactions with $H_4\mathbf{L}$ (1 : 1 metal : ligand ratio) the structure MIL-91(Fe) was obtained. Like the $Al^{(III)}$ analogue of this material, charge balance is maintained in the framework through protonation of O atoms, which are corner-shared along metal phosphonate chains. Although the $Al^{(III)}$ form of this structure is porous to N_2, it has not been possible

to prepare porous MIL-91(Fe). The lack of porosity is thought to be due to the dehydroxylation of the structure during activation, whilst heating the structure to a lower temperature did not remove physisorbed water molecules. Further modifications to the synthesis or the activation procedure may provide insights into how the structure might be made porous.

Using a higher metal:ligand ratio (4 : 1) with $Fe^{(III)}AcO$ as the metal source and either $H_4\mathbf{L}$ or $H_4\mathbf{L}'$, analogues of the Co tetramer containing structure, $[Co_4\mathbf{L}'_{1.5}(AcO)_{1.5}(OH,H_2O)_3]\cdot 0.5NH_4 5.5H_2O$, reported by Groves *et al.* were obtained.[105] The unit cells determined by indexing powder diffraction patterns of these structure were found to be consistent with the reported unit cell for the Co material. Elemental analysis results also gave good agreement, confirming the synthesis of the structure. A full structural characterisation of this material is necessary. The material should be porous, though Groves *et al.* were unable to make porous forms of the Co material. The nature of the molecules in the pores is an open question and needs to be resolved in order to determine how to make this material porous. The oxidation state of the cations in this structure is also not clear. Magnetic studies of the material might be used to determine this. It is also expected that, due to the structure of the clusters, this material may exhibit novel magnetic properties.

Reaction of the divalent metal cation Mg^{2+} with $H_4\mathbf{L}$ led to the preparation of STA-12(Mg), the first permanently porous alkaline metal phosphonate framework formed with piperazine derived ligands. The material was originally obtained from high-throughput hydrothermal synthesis. Using the results of high-throughput syntheses as a starting point, reactions were scaled up to obtain STA-12(Mg) in good yield. During the optimisation of the synthesis, the structures of two non-porous phases were identified: $Mg(\mathbf{L}H_2)$ ($Mg(\mathbf{L}H_2)\cdot 1.5H_2O$), the Mg analogue of the phase reported by LaDuca *et al.*;[103] and MgP_2O_7 ($MgP_2O_7 \cdot 3.5H_2O$), the structure of which was previously reported by Kongshaug *et al.* from powder X-ray diffraction data.[189] STA-12(Mg) crystallises as large (100×10 μm) needle crystals from which the structure was solved by single crystal X-ray diffraction. This provided conformation of the structure of STA-12 determined previously only from powder X-ray diffraction data. To allow comparison of the structure of STA-12(Mg) with the known forms of STA-12, as-prepared structures of STA-12(Mn), STA-12(Fe)) and STA-12(Co) were re-refined. STA-12(Mg) shows a very different dehydration behaviour to previously reported forms of STA-12, losing long-range order on dehydration. To determine the structural changes occuring in STA-12(Mg) on dehydration, the dehydration behaviours of known forms of STA-12 were re-analysed. Fully dehydrated STA-12 shows one of two behaviours on dehydration,

either undergoing a structural transition from $R\bar{3}$ to $P\bar{1}$ with $\frac{2}{3}$ of the PO_3C groups becoming fully coordinated (Ni & Co), or retaining the $R\bar{3}$ symmetry with all PO_3C groups fully coordinated (Mn & Fe).[113] This latter behaviour was not fully characterised before and therefore the structure of fully dehydrated STA-12(Mn) was re-refined. The powder diffraction pattern of fully dehydrated STA-12(Mg) does not show a shift in the peak positions or any splitting of peaks, indicating a retension $R\bar{3}$ symmetry. This analysis was confirmed by solid-state MAS NMR. IR spectra indicated that PO_3C groups are not fully coordinated. Fully dehydrated STA-12(Mg) is thought to retain local rhombohedral symmetry on dehydration, with little change to the unit cell. Pendant P=O groups remain uncoordinated, as there is no crystal field stabilisation energy gain in their engaging in coordinative bonding to the metal. The reduction of long range order is caused by the formation of domains within the structure, which exhibit different distortions to reduce the free pore volume. The material showed significant porosity to both N_2 at 77 K (5.72 mmol g^{-1}) and CO_2 at 196 K (5.72 mmol g^{-1}). The related structure CPO-27(Mg) (also known as MOF-74(Mg)), formed with dihydroxyterephthalic acid, shows strong selectivity for the adsorption of CO_2 over CH_4.[202] The porosity of STA-12(Mg) to CH_4 is currently unknown and therefore it was not possible in the scope of this work to assess the selectivity of STA-12(Mg) for CO_2 over CH_4. The porosity of STA-12(Mg) to CH_4, as well as other small alkanes and H_2 should be investigated to evaluate whether STA-12(Mg) would also be a good selective adsorbent.

Re-refinement of the as-prepared structure of STA-12(Fe) gave a very high $R(F^2)$ value (0.4959), indicating a poor structural fit, though a good fit to the profile was achieved. In addition, TGA plots show no plateau for the fully dehydrated structure and poor porosity has been achieved for the material. In recent work, Bloch *et al.* prepared the structural analogue CPO-27(Fe) under inert atmosphere conditions.[203] The material had a much lighter colour more typical of $Fe^{(II)}$ coordination compounds, in contrast to the dark brown colour of CPO-27(Fe) prepared without an inert atmosphere. Bloch *et al.* attribute this to the coordination of the Fe sites by O_2 molecules. CPO-27(Fe) prepared by this route was found to be porous and also a selective adsorber of O_2 over N_2. As STA-12(Fe) is a structural analogue it would be interesting to try to prepare the material under inert conditions to determine whether porous STA-12(Fe) may be obtained.

STA-12 has proven to be a very versatile adsorbent material, showing some selectivity for the adsorption of CO_2 over CH_4. The synthesis of a material with a similar structure, but larger pore size might lead to an even more versatile adsorbent with properties suitable for separations of other larger gas molecules or alternatively for the storage of gases. To extend the synthesis of porous metal bisphosphonates

from the microporous into near mesoporous region, the ideas of isoreticular chemistry were applied. H_4**LL** is topologically identical to H_4**L**, but has a backbone that is one half longer. Reaction of $Co^{(II)}$ or $Ni^{(II)}$ with H_4**LL** yielded materials with the STA-16 network, which is topologically identical to the STA-12 network. To date, only $Co^{(II)}$ and $Ni^{(II)}$ forms of STA-16 have been obtained. STA-12 has been reported to form with $Mn^{(II)}$, $Fe^{(II)}$, $Co^{(II)}$ and $Ni^{(II)}$ as the framework-forming cation,[113] whilst in this work STA-12(Mg) was reported for the first time. Early work by Mitchell on doping $Mg^{(II)}$ and $Mn^{(II)}$ into the structure of STA-16(Co) has shown that the doped cations may be accommodated within the framework and therefore that the preparation of other metal forms of STA-16 should be possible.[204]

The as-prepared structure of STA-16(Co) and STA-16(Ni) were determined by model building from the STA-12 network followed by Rietveld refinement of this model against synchrotron X-ray diffraction data. Data for both structures showed a good fit to the profile (R_{wp}: 0.0467 (Co); 0.0446 (Ni)) and good structural fit ($R(F^2)$: 0.0532 (Co); 0.1318 (Ni)). The material consists of helical chains of octahedrally coordinated MO_5N octahedra coordinated by PO_3C groups in a bridging mode. Chains are linked in two directions through coordinating N atoms of bipiperidinyl moieties to neighbouring chains to form a honeycomb network of unidirectional channels with free diameters of nearly 2 nm, occupied by physisorbed water molecules. Dehydration was shown to be reversible. On dehydration STA-16(Co) undergoes a structural transition. The structure of this material remains unknown, though as dehydration is reversible connectivity within the structure must be retained. Determination of the structure of dehydrated STA-16(Co) is an important target for future work. The structure of dehydrated STA-16(Ni), also obtained by Rietveld refinement of synchrotron powder X-ray diffraction data, is closely related to the structure of the as-prepared material.

Both STA-16(Co) and STA-16(Ni) are porous to N_2 at 77 K and CO_2 at 196 K and 273 K, showing loadings of up to 22 mmol g^{-1} for both N_2 and CO_2. Analysis of the N_2 adsorption isotherm using NLDFT gave pore size distributions for both STA-16(Co) and STA-16(Ni) which indicate that the dehydrated materials retain pores of radius 16.6 Å and 18.4 Å respectively. This is in very good agreement with pore radii determined for the structure of dehydrated STA-16(Ni) and is similar to the pore radii determined for as-prepared STA-16(Co). This indicates that STA-16(Co) also retains mesoporosity in its dehydrated form. The porosity of either material to gases other than N_2 and CO_2 remains unknown, but it is likely to be significant. To investigate the possibility of using STA-16 as a selective adsorbent, studies of the adsorption of gases such as H_2, CH_4 and other light alkanes should be undertaken and calorimetric data should also be obtained. The adsorption of

chemisorbing gases, such as CO and NO could also be studied and this may lead to other possible separations. Quantum mechanical studies might also be used to model the coordinatively unsaturated site, formed by the removal of chemisorbed water, to simulate adsorption isotherms for the materials. The large free diameters of the pores in dehydrated STA-16 and the presence of coordinatively unsaturated sites suggests applications for the materials in catalysis or, provided the material may be prepared with biocompatible framework-forming cations, as drug delivery agents.

As well as STA-16, two other phases were identified in the $Co^{(II)}$-H_4**LL** system. Using the same $Co^{(II)}$ source as used to prepare STA-16(Co) ($Co(AcO)_2$), but at a higher metal:ligand ratio (4 : 1, *c.f.* 2 : 1 in STA-16(Co) synthesis) the phase $Co_4(O)_2$**LL**$(AcO)_2$ ($Co_4(O)_2$**LL**$(AcO)_2 \cdot 2H_2O$), previously reported by Mowat was obtained.[182] Using $CoCl_2$ in place of $Co(AcO)_2$ in a reaction known to prepare STA-16(Co) results in the synthesis of unreported phase Co_2X_2**LL**H_2 ($Co_2Cl_{1.8}Br_{0.2}$(**LL**H_2)). This material has a pillared layered structure. Layers consist of tetrahedral CoO_3X (X = 0.9Cl, 0.1Br) units linked by fully coordinated PO_3C groups. Layers have a structure related to that of the naturally occurring zeolite gismondine. Pillaring is too dense for the structure to have any permanent porosity. Similar reactions were also attempted with $Ni^{(II)}$; however, only STA-16 was obtained.

Reactions of other divalent cations were also probed. Two new phases were identified using $Mn^{(II)}$ as the framework-forming cation. Using $MnCl_2$ as the metal source, Mn_2X_2**LL**H_2 ($Mn_2(H_2O)_4(Cl_{1.8}Br_{0.2})$(**LL**$H_2$)) was obtained. This material has a pillared layered structure of octahedral MnO_5X, coordinated by three fully coordinated PO_3C groups, two water molecules and a halide anion (X = 0.9Cl, 0.1Br), forming a bilayer-like structure. Layers are densely pillared by **LL**H_2 moieties. Using $Mn(AcO)_2$ as the metal source, a layered structure is formed. Layers are constructed from tetrameric Mn cluster/PO_3C ribbons linked together by **LL** moieties. Only intermolecular H-bonds hold the structure of the layers together. Preliminary reactions of $Mg^{(II)}$, $Fe^{(II)}$, $Cu^{(II)}$ and $Zn^{(II)}$ have prepared a range of unknown phases, the structures of which are yet to be determined.

Isoreticular synthesis has also been applied to reactions of trivalent cations, such as $Al^{(III)}$ and $Y^{(III)}$, in an attempt to prepare isoreticular analogues of the known porous frameworks MIL-91 and STA-13 (*vide supra*). To date, isoreticular analogues of these frameworks have not been obtained. The reasons for this remain unclear though it may be that the longer linker precludes the formation of the H-bonding networks necessary for the crystallisation of the networks. Whilst no other isoreticular structures have been found, a large number of new phases have

been identified by high-throughput synthesis. Scaling up the synthesis of these phases and determining their structures may provide evidence for why isoreticular networks are not formed or may yield new porous frameworks. The identification of the structures of these unknown phases is therefore a high priority.

Four new porous metal phosphonate framework materials have been reported from solvothermal reactions using divalent or trivalent metal cations and ligands $H_4\mathbf{L}$, $H_4\mathbf{L}'$ and $H_4\mathbf{LL}$, and their structures characterised. The new STA-16 materials show significant porosity, making them potentially useful as gas storage materials. The other narrower pore materials also show significant porosity for small molecules. To investigate the use of any of these materials as a selective adsorbent in pressure swing adsorption, the adsorptive properties of a range of other adsorbents need to be investigated. The structures formed with bisphosphonate ligands tend to adopt either layered structures or structures based on unidirectional channels, with porous materials adopting this latter structural motif. A simple way to increase porosity to improve the usefulness of bisphosphonates as gas storage media is to increase the free diameter of the channels. This can be achieved by using a longer linker. A linker longer than $H_4\mathbf{LL}$ was prepared in this work: $H_4\mathbf{LC}_3\mathbf{L}$; however, initial syntheses using divalent cations gave no solid products. The use of tri- or tetravalent cations with this linker might, however, produce new solid materials. Other more rigid bipiperidine derivatives for use as substrates in the modified Mannich reaction are also commercially available (e.g. 4,4′-ethylenedipiperidine) and these should lead to new longer linkers suitable for the synthesis of metal bisphosphonates.

To increase the range of applications for which the known porous networks are suitable, the structures might be functionalised. This would be achieved by functionalising the ligand prior to synthesis. Alternatively, a variety of functionalised piperazines are commercially available (e.g. glycine anhydride — 2,5-piperazinedione). Provided these molecules are stable under the conditions of the modified Mannich reaction, the new ligands might lead to new structures. The ketone functional group is also itself synthetically interesting and this may allow post-synthetic modification of metal phosphonates.

Epilogue 8

Zeolitic Imidazolate Frameworks

In parallel with the studies of porous phosphonate materials, the porous properties of a series of zeolitic imidazolate frameworks (ZIFs) were investigated in collaboration with D. Fairén-Jiménez (University of Edinburgh, Edinburgh, UK). The intention of this work was to prepare a series of ZIFs with the same sodalite topology and to compare their porosities to N_2 at 77 K and CO_2 at both 196 K and 273 K. Steps in the isotherms were identified and their nature investigated.

8.1 Introduction

Zeolitic Imidazolate Frameworks (ZIFs) are a subgroup of MOFs. To date, most ZIFs have been reported with either Zn^{2+} or Co^{2+} cations in a tetrahedral coordination, using imidazole-based linkers.[117] Deprotonating the imidazole forms the imidazolate anion (IM) which is aromatic and therefore planar. IM coordinates metal cations through the N atoms in the ring, with an angle of $\sim 145°$. This angle is very similar to the O-Si-O angle found in many zeolite networks (*Fig. 8.1*).

A range of zeolite networks have been prepared with ZIFs.[205] The structure obtained from a given synthesis is determined by both the type and positions of

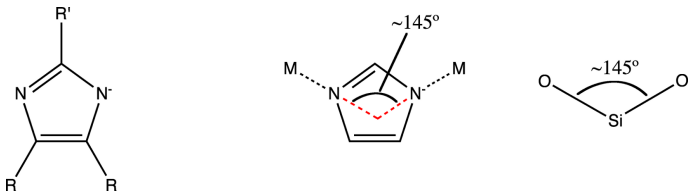

Figure 8.1: *Left:* The planar imidazolate anion (IM). ZIFs have been prepared with functionalised IM linkers, which act to direct the structure (R groups indicate sites which may be functionalised). *Right:* Comparison of the O-Si-O and M-N$\cdots$N-M angles in zeolites and ZIFs respectively.

the functional groups on the IM linker.[206] Of particular interest in the current work are imidazoles functionalised at the 2-position (R′ in *Fig. 8.1*): ZIF-8 (Zn^{2+} and 2-methylimidazole — 2-Me-IM),[117] 4 (Co^{2+} and 2-nitroimidazole — 5),[205] ZIF-67 (Co^{2+} and 2-Me-IM)[205] and ZIF-90 (Zn^{2+} and imidazole-2-carboxaldehyde — 2-CHO-IM)[207] all exhibit the sodalite structure.

In collaboration with D. Fairén-Jiménez (University of Edinburgh, Edinburgh, UK) a series of ZIFs with the sodalite structure (ZIF-8, ZIF-65(Co), ZIF-65(Zn) and ZIF-90) were synthesised. Phase purity of the samples and characterisation of the materials were performed as described for phosphonate frameworks (*Section 2*). Adsorption isotherms were collected for N_2 at 77 K, using a volumetric Micromeritics 2020, and for CO_2 at both 196 K and 273 K, using a gravimetric Hiden Isochema IGA.

8.2 Synthesis

8.2.1 ZIF-8

Park *et al.* report the solvothermal synthesis of ZIF-8 on a milligram scale.[117] Huang *et al.* reported a stirred, room temperature synthesis of ZIF-8,[208] which was susbequently improved and scaled by Pérez-Pellitero *et al.*.[209] Following this latter method, 2-Me-IM (6.44 g, 0.08 mol) was dissolved in MeOH (100 ml). $Zn(OH)_2$ (see *Appendix, SectionA.1* for details of preparation) was dissolved in ammonium hydroxide solution (35 %, 360 ml) and diluted with distilled water (140 ml). The $Zn(OH)_2$ solution was then added dropwise to the solution of 2-Me-IM with constant stirring at room temperature over two hours. The solution was stirred at room temperature overnight. A fine white precipitate was obtained from the reaction. The solid was separated by vacuum filtration, washed with distilled water (2×100 ml) and dried at 40°C.

8.2.2 ZIF-65(Co), ZIF-65(Zn), ZIF-67 & ZIF-90

Banerjee *et al.* report the synthesis of ZIF-65(Co),[205] whilst Morris *et al.* report a similar synthesis for ZIF-90.[207] Literature syntheses were repeated on a 15 ml scale using 30 ml Nalgene bottles. Reactions were all heated at 100°C for 18–96 hours. ZIF-67 and ZIF-90 were obtained in good purity and reactions were optimised. Using $Co(AcO)_2{\cdot}4H_2O$ in place of $Co(NO_3)_3{\cdot}6H_2O$ in a gel of composition 3.10 : 4.65 : 400 ($Co(AcO)_2$: 2-Me-IM : DMF) yielded a very fine powder of ZIF-67 (0.024 g). The addition of a small amount of MeOH, to give a gel composition

of 3.10 : 4.65 : 370 : 30 ($Co(AcO)_2$: 2-Me-IM : DMF : MeOH), increased the yield of ZIF-67 dramatically (0.1464 g).For ZIF-90, an initial gel composition of 1.32 : 4.65 : 400 ($Zn(AcO)_2$: 2-CHO-IM : DMF) was found to yield a phase pure crystalline powder of the material.

Synthesis of ZIF-65(Co) was unsuccessful. An unidentified Co containing phase was obtained from all syntheses. Using $Zn(NO_3)_3 \cdot 6H_2O$ instead of $Co(NO_3)_3 \cdot 6H_2O$ in a gel of composition of 2.0 : 5.0 : 400 ($Zn(NO_3)_3$: 2-NO2-IM : DMF) yielded cubic orange crystals of a new phase, labelled ZIF-65(Zn), were obtained. A second unidentified lighter coloured phase was also co-crystallised with ZIF-65(Zn). Using $Zn(AcO)_2 \cdot H_2O$ in place of $Zn(NO_3)_3 \cdot 6H_2O$ yielded only an unidentified lighter coloured phase.

8.3 Characterisation

Samples of each of the ZIF materials were analysed by TGA, SEM and powder X-ray diffraction. Samples of ZIF-65(Zn), ZIF-67 and ZIF-90 were also characterised by elemental analysis.

TGA analysis of each of the materials show the high thermal stability of ZIF-8, with framework collapse beginning at approximately 350°C. ZIF-67 and ZIF-90 are less thermally stable, with structure collapse beginning at approximately 240–260°C (*Fig. 8.2*). Both ZIF-67 and ZIF-90 also show weight loss events below 100°C (2.95 wt.% and 13.92 wt.% respectively) attributed to the loss of solvent occluded in the pores of the material. TGA of ZIF-65(Zn) also shows a weight loss due to loss of solvent from the structure (25–49°C: 2.14 wt.%). ZIF-65(Zn) shows a second weight loss at higher temperature (203–255°C: 6.2745 wt.%), the origin of which is unclear. This might be due to the narrow pore windows trapping solvent within the structure (*Section 8.3.1*) or could be the early stages of structure collapse (e.g. loss of NO_2). Further analysis is necessary to determine the exact cause.

Comparison of simulated and experimental powder X-ray diffraction patterns of the synthesised ZIFs shows reasonably good agreement. Models for simulated patterns of ZIF-8, ZIF-67 and ZIF-90 were taken from the literature,[117, 205, 207] whilst the model for ZIF-65(Zn) was taken from structure obtained from single crystal X-ray diffraction (*Section 8.3.1*) No additional peaks are present in the patterns, though some of the experimental peak intensities differ from the simulated values (*Fig. 8.3*). This is due to differences in the amount and type of solvent in the pores of the experimental samples and the literature models.

SEM micrographs of ZIF-65(Zn) show the material crystallises as large, often

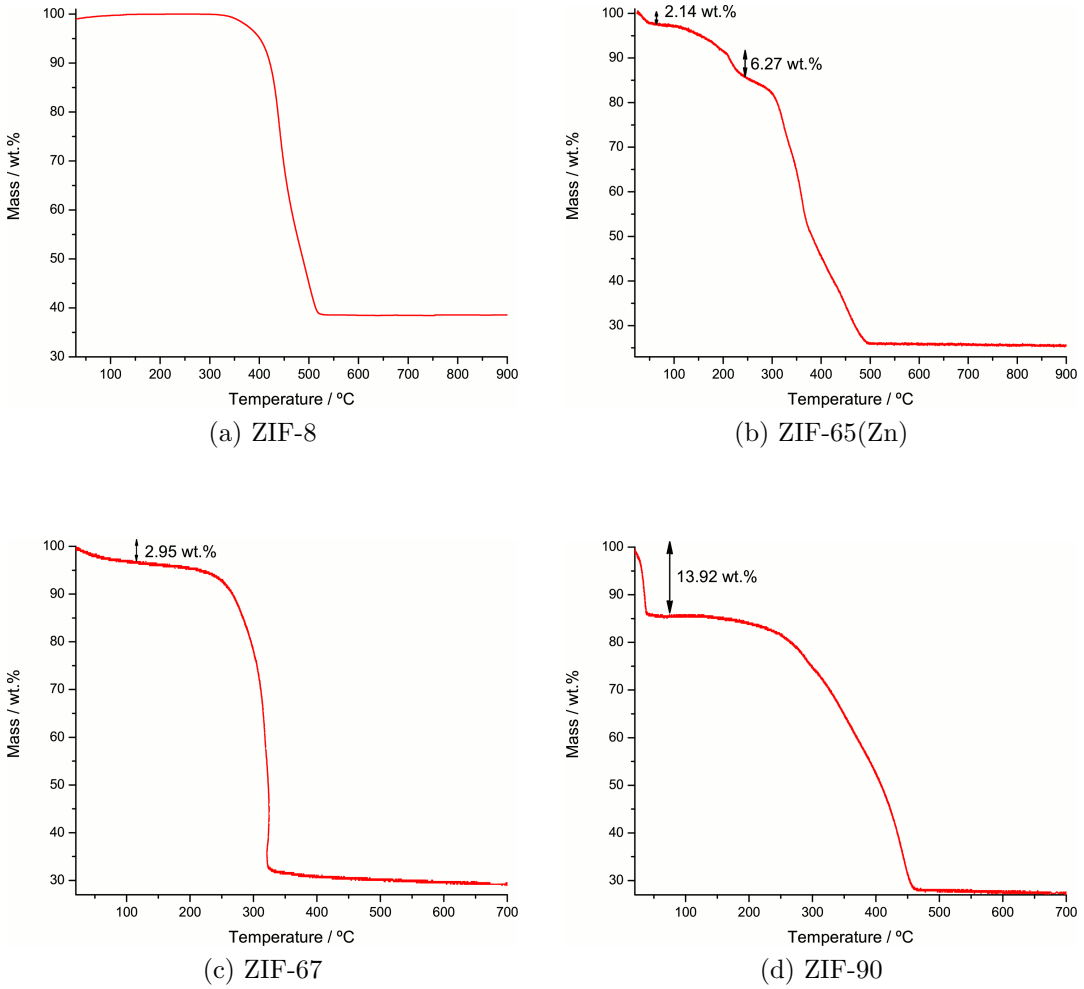

(a) ZIF-8 (b) ZIF-65(Zn)

(c) ZIF-67 (d) ZIF-90

Figure 8.2: TGA plots of the four ZIFs synthesised in this work over the ranges 20–900°C (ZIF-8 & ZIF-65(Zn)) or 20–700°C (ZIF-67 & ZIF-90). Principal weight losses due to solvent occluded in the pores are indicated. ZIF-8 is the most thermally stable, with framework collapse beginning above *ca.* 350°C.

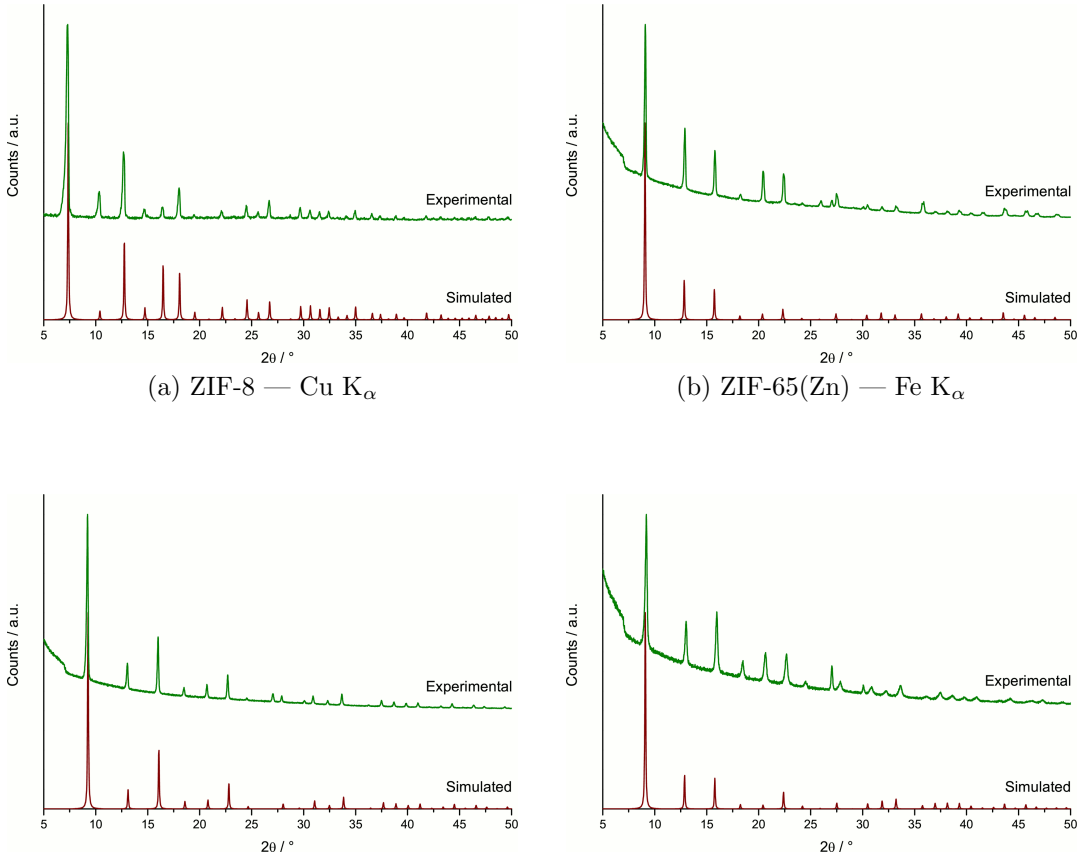

(a) ZIF-8 — Cu K_α

(b) ZIF-65(Zn) — Fe K_α

(c) ZIF-67 — Fe K_α

(d) ZIF-90 — Fe K_α

Figure 8.3: Powder X-ray diffraction patterns of the four ZIFs synthesised in this work, comparing the experimental diffraction patterns (green) with simulated patterns calculated using literature structures (red). The measurement X-ray wavelength is given for each pattern; all patterns show the range 5–50° 2θ regardless of X-ray wavelength.

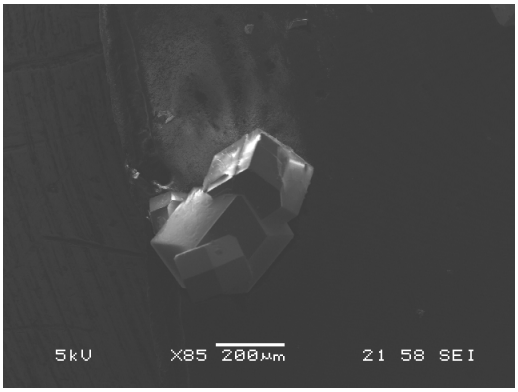

Figure 8.4: SEM micrograph showing ~ 200 μm cubic crystals of ZIF-65(Zn).

Phase	Composition	C / %		H / %		N / %	
ZIF-65(Zn)	$Zn(C_3H_2N_3O_2)_2$	22.59	(24.89)	2.68	(1.39)	23.64	(29.03)
ZIF-67	$Co(C_4H_5N_2)_2$	42.64	(43.45)	4.35	(4.56)	23.39	(25.34)
ZIF-90	$Zn(C_4H_3N_2O)_2$	36.67	(37.60)	2.97	(2.37)	18.87	(21.92)

Table 8.1: Elemental analysis results for three ZIF materials prepared by new method. Values in parentheses are expected values for the given composition.

intergrown, cubic crystals (~ 200 μm cubes — *Fig. 8.4*). ZIF-8, ZIF-67 and ZIF-90 were all obtained as microcrystalline powders, in which particle habit could not be clearly identified.

Elemental analysis results show good agreement for ZIF-67 and ZIF-90. Discrepancies in the observed values are due to the presence of DMF in the structures which is not accounted for in the given compositions. Elemental analysis results for ZIF-65(Zn) show a greater difference than for the other ZIFs. Crystals for this sample were separated manually from the solid obtained from the reaction and there may be some contamination with the unidentified light coloured phase which was co-crystallised with ZIF-65(Zn) (*Section 8.2.2*).

8.3.1 Structure of ZIF-65(Zn)

The structure of ZIF-65(Zn) was determined by S. Moggach (University of Edinburgh, Edinburgh, UK) from single crystal diffraction measurements. ZIF-65(Zn) has a sodalite topology (*Fig. 8.6*), with Zn^{2+} cations tetrahedrally coordinated by four 2-NO2-IM units (Zn-N: 2.025 Å). Each 2-NO2-IM linker coordinates two Zn^{2+} cations. The NO_2 functional groups project into the small $[Zn_4IM_4]$ windows of the sodalite cages, leaving an aperture of less than 2.5 Å for gas molecules to pass through in order to access the pore space within the cage (*Fig. 8.5*). Sodalite cages have a free diameter of $\sim$ 12 Å.

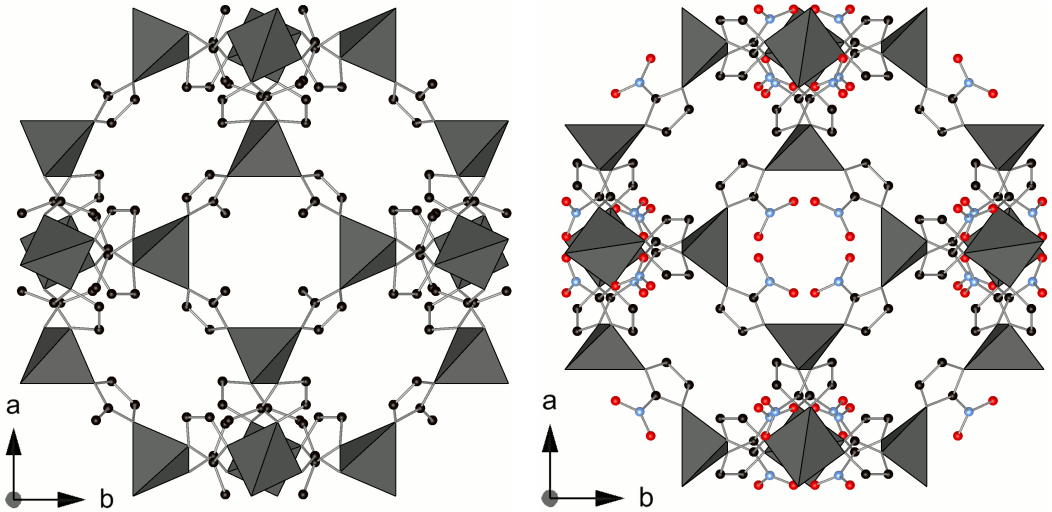

(a) (b)

Figure 8.5: Comparison of the sodalite cages of ZIF-8 (*left*) and ZIF-65(Zn) (*right*). The greater steric bulk of the NO_2 groups in ZIF-65(Zn) means that windows into the sodalite cages are blocked more efficiently than by the Me groups of ZIF-8.

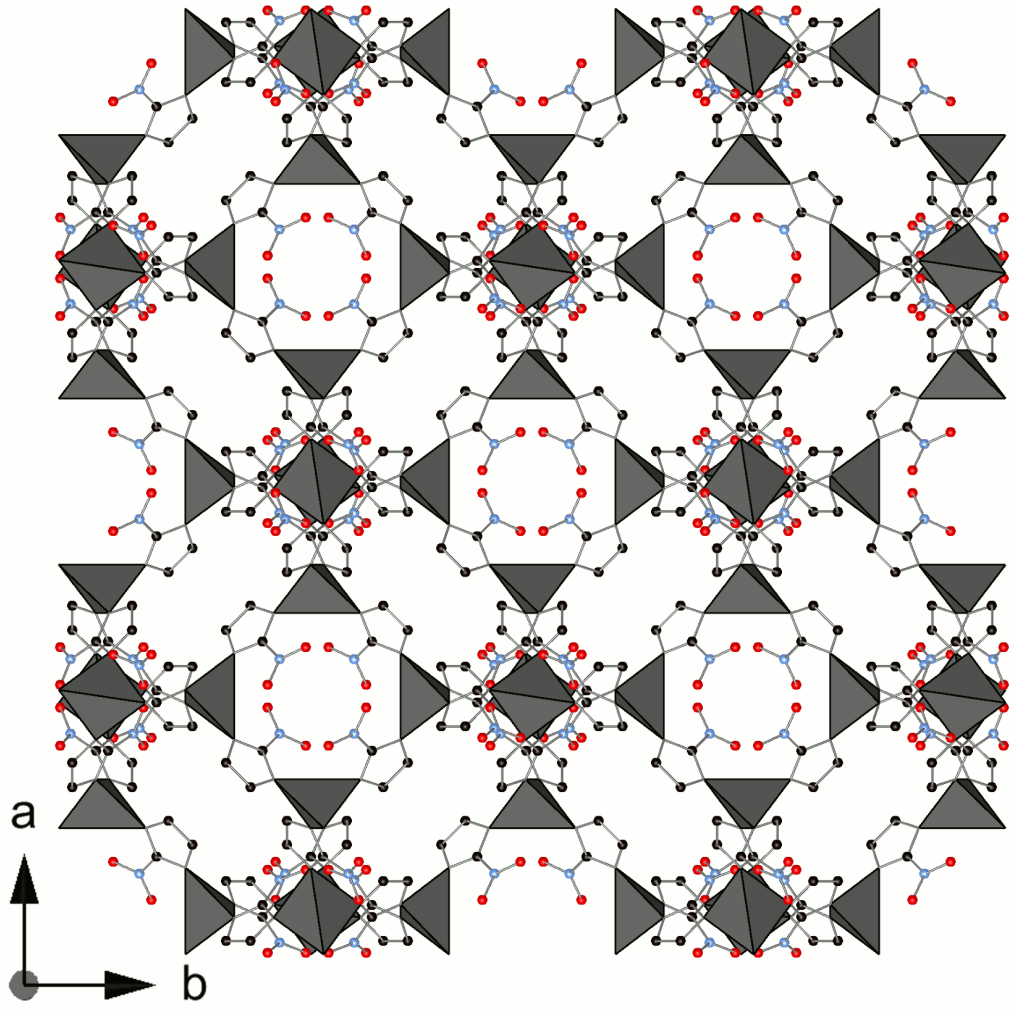

Figure 8.6: Structure of ZIF-65(Zn) viewed along the *c*-direction, showing the stacking of four sodalite cages (each representing one unit cell) in three dimensions.

8.4 Porosity

The porosity of ZIF-8 ZIF-65(Zn), ZIF-67 and ZIF-90 to N_2 at 77 K was investigated using a volumetric apparatus. The porosity of these materials to CO_2 at 196 K and 273 K was investigated using a gravimetric apparatus. Samples were pre-treated by first washing with MeOH for 24 hours to exchange DMF trapped in the cages of the structure. Samples were activated by heating to 200°C for three hours under vacuum (1×10^{-4} Torr). All ZIF materials were found to be porous to both N_2 and CO_2.

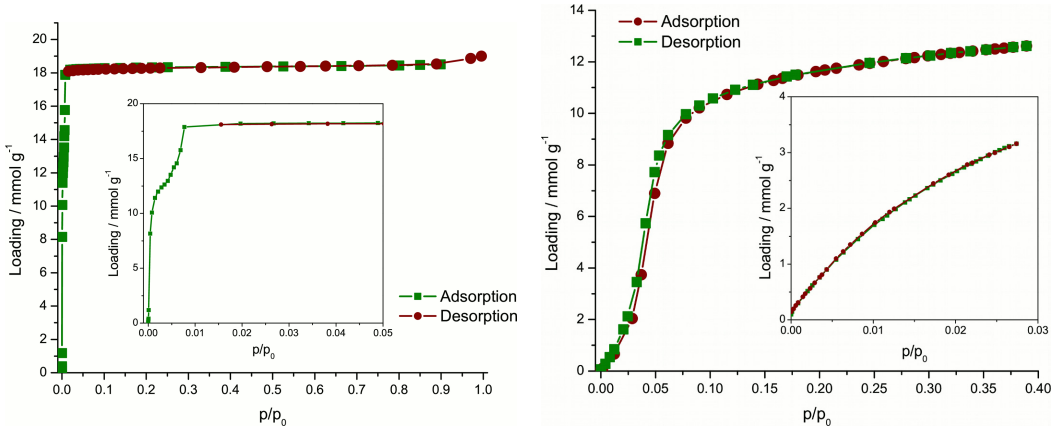

(a) N_2 isotherm at 77 K (b) CO_2 isotherm at 196 K

Figure 8.7: N_2 isotherm at 77 K (*left*; inset — detail of low pressure region, showing step in isotherm) and CO_2 isotherm (*right*: 196 K isotherm; inset shows 273 K isotherm) for adsorption by ZIF-8. Both adsorption (green, filled squares) and desorption (red, filled circles) are shown.

ZIF-8, ZIF-65(Zn) and ZIF-67 all show steps in their isotherms. Molecular simulations of adsorption isotherms, performed by D. Fairén-Jiménez (University of Edinburgh, Edinburgh, UK), and high-pressure crystallographic studies, performed by S. Moggach (University of Edinburgh, Edinburgh, UK), have indicated, in the case of ZIF-8, that these steps are caused by a *gate opening process*. In the as synthesised, activated material, the functional groups in the 2-positions of the IM linkers block the small $[Zn_4IM_4]$ windows between the sodalite cages. At a given pressure, the IM linkers swing to move the functional groups away from the centre of the window, opening up the structure. Such a structure is adopted by ZIF-8 at very high-pressure (1.47 GPa).[210] Interactions between the adsorbate molecules and the framework are thought to favour gate opening at the much lower pressures that the step in the adsorption isotherm is observed at. Steps in the isotherms of ZIF-65(Zn) and ZIF-67 are also attributed to gate opening effects. Work is continuing on these

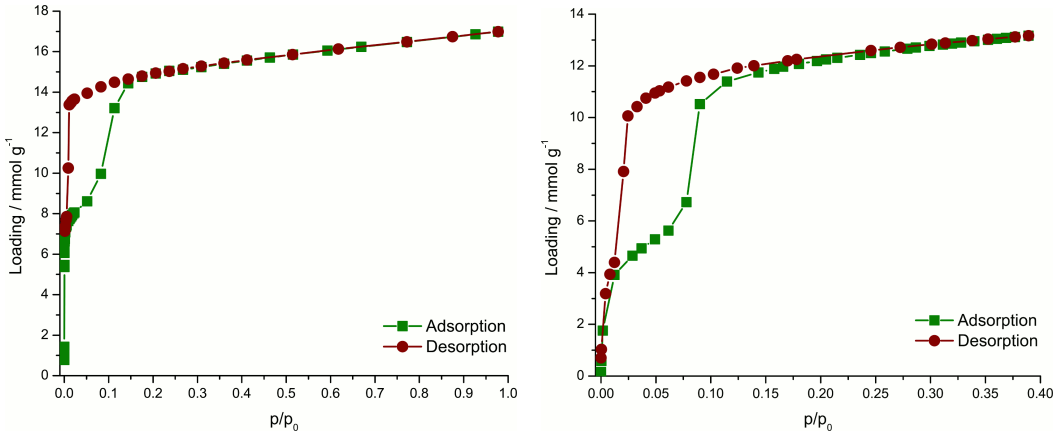

(a) N_2 isotherm at 77 K (b) CO_2 isotherm at 196 K

Figure 8.8: N_2 isotherm at 77 K (*left*) and CO_2 isotherm (*right*: 196 K isotherm) for adsorption by ZIF-65(Zn). Both adsorption (green, filled squares) and desorption (red, filled circles) are shown.

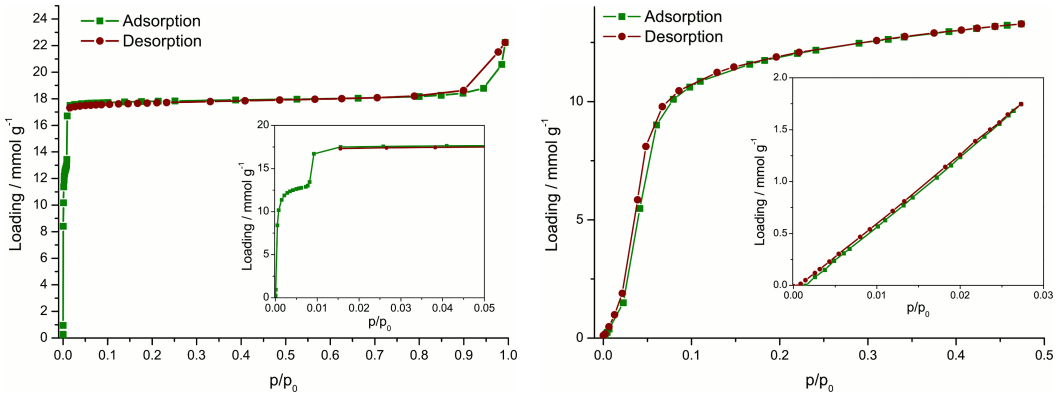

(a) N_2 isotherm at 77 K (b) CO_2 isotherm at 196 K

Figure 8.9: N_2 isotherm at 77 K (*left*; inset — detail of low pressure region, showing step in isotherm) and CO_2 isotherm (*right*: 196 K isotherm; inset shows 273 K isotherm) for adsorption by ZIF-67. Both adsorption (green, filled squares) and desorption (red, filled circles) are shown.

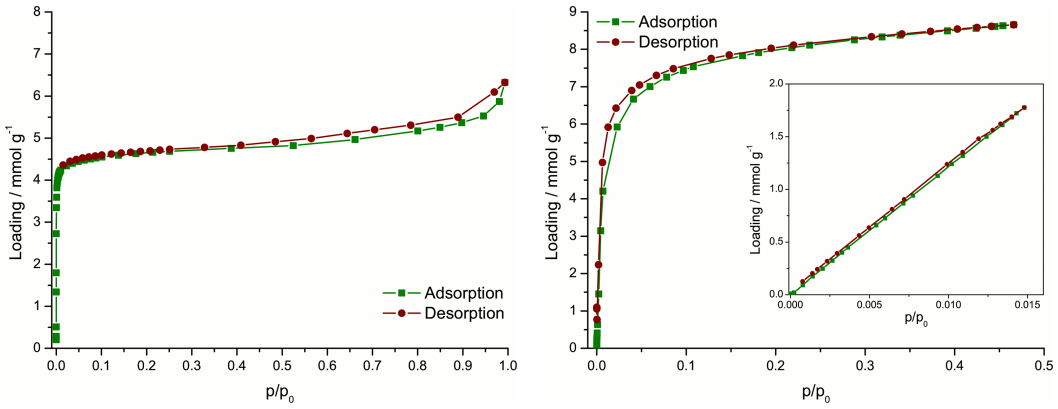

(a) N_2 isotherm at 77 K (b) CO_2 isotherm at 196 K

Figure 8.10: N_2 isotherm at 77 K (*left*) and CO_2 isotherm (*right*: 196 K isotherm; inset shows 273 K isotherm) for adsorption by ZIF-90. Both adsorption (green, filled squares) and desorption (red, filled circles) are shown.

materials to determine their high-pressure structures and to determine details of the interactions between adsorbates and framework (through molecule simulation).

8.5 Summary

A series of ZIF materials with structures exhibiting the sodalite topology have been prepared on larger scales than previously reported. In addition, ZIF-65(Zn) has been reported for the first time, a material isostructural with the previously reported ZIF-65(Co). Synthesis of ZIF-65(Co), by scaling up the reported high-throughput synthesis, has not been successful. ZIF-67 and ZIF-90 were prepared as phase pure powders. Adsorption isotherms using N_2 at 77 K and CO_2 at 196 K and 273 K show the prepared ZIFs are porous, and show a step at relatively low pressure in their isotherms. This is attributed to a gate opening process, in which the functional groups in the 2-position of the IM linker swing away from the narrow pore window allowing adsorbates better access to the large pore space within the sodalite cages.

Appendix A

Preparation of Non-Commercially Available Metal Sources

A.1 Preparation of $Zn(OH)_2$

$ZnCl_2$ (15.44 g, 0.15 mol) was dissolved in distilled H_2O (300 ml). The $ZnCl_2$ solution was stirred and aqueous NaOH solution (0.5 M) was added slowly. A very fine white precipitate of $Zn(OH)_2$ was observed. NaOH solution was added until the reaction had a pH of 7. The solid was separated by gravity filtration and dried overnight in a 40°C oven.

A.2 Preparation of $ScCl_3$

Insoluble Sc_2O_3 (10.0 g, 0.0725 mol) was mixed with distilled H_2O (20 ml) with stirring. The reaction was refluxed. Aqueous HCl solution (36 wt.%, 41 ml, 0.486 mol) was added dropwise to the reaction until the cloudy suspension of Sc_2O_3 had dissolved and the solution became clear. The reaction was cooled to leave a colurless solution ($ScCl_3$ — 1.45 mol dm^{-3}), which could be used in solvothermal reactions.

To obtain solid $ScCl_3$, water was removed *in vacuo*. Toluene was added to lower the boiling point of the solution. $ScCl_3$ was obtained as a deliquescent off-white solid.

A.3 Preparation of $Sc(piv)_3$

Insoluble pivalic acid (14.1 g, 0.138 mol) was mixed with distilled H_2O (20 ml). Solid sodium hydrogen carbonate (11.6 g, 0.138 mol) was dissolved in H_2O (40 ml) and added to the pivalic acid mixture. Once all pivalic acid was dissolved, $ScCl_3$ solution (1.45 mol dm^3, 31 ml, 0.045 mol) was added dropwise to the stirred pivalate solution. A white solid immediately precipitates. The solid was separated by vacuum filtration and dried overnight at 40°C. Without further purification, the fine solid gave elemental composition consistent with that of $Sc(piv)_3$ ($Sc(C_5H_9O_2)$: expected — C 51.7 %, H 7.8 %, N 0 %; found — C 48.9 %, H 7.43 %, N 0 %.

Appendix B

Unknown Phases in the $Y(AcO)_3$-H_4L System

Four phases have been identified in addition to structure $Y_2(\mathbf{L}H_2)_3$ in the $Y(AcO)_3$-$H_4\mathbf{L}$ system, of which only two, Y-H_4**L**U1 and Y-H_4**L**U4 have been obtained to any degree of phase purity (see *Section 4.3*, *Table 4.1*). Diffraction patterns of the best samples of each of the unknown phases have been collected (*Fig. B.1*).

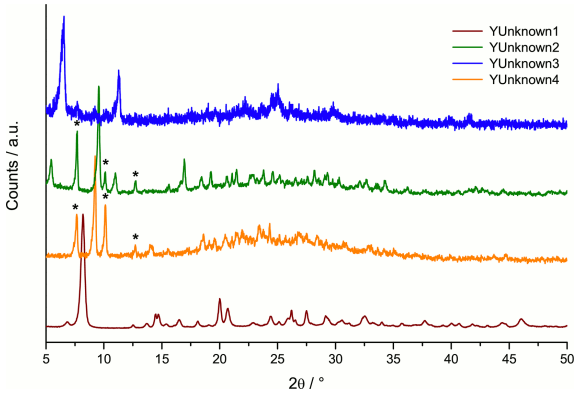

Figure B.1: Laboratory powder X-ray diffraction patterns (Cu K_α) of unknown phases in the $Y(AcO)_3$-$H_4\mathbf{L}$ system: Y-H_4**L**U1 (maroon); Y-H_4**L**U2 (orange); Y-H_4**L**U3 (dark green); Y-H_4**L**U4 (blue). Asterisks indicate peaks due to co-crystallised structure $Y_2(\mathbf{L}H_2)_3$.

B.1 Y-H$_4$LU1

Y-H$_4$**L**U1 has been analysed by TGA and EDX analyses. TGA data were collected over the range 30–900°C in flowing air. The TGA data may be divided into two principal weight loss events, occurring from 30–160°C (12.2 wt.%), assigned to the dehydration of the material, and a second starting at 325°C continuing to approximately 900°C, attributed to the collapse of the framework. Dehydration proceeds in a two step process, the first from 30–120°C (9.51 wt.%, 1.79 H_2O — assuming final solid is Y_2O_3) and the second from 120–160°C (2.31 wt.%, 0.5 H_2O), possibly indicating the presence of both chemisorbed and physisorbed water in the structure. EDX spectra show a mean Y:P ratio of 1.0 : 1.71, leading to ambiguity in the metal to ligand ratio. For a metal to ligand ratio of 4:3, the expected Y : P ratio is 1.0 : 1.5 (two P atoms per ligand), whereas for a M : L of 1:1 a ratio of 1.0 : 2.0 would be expected. The initial reaction conditions used a ratio of 2 : 1.5, consistent with the 4 : 3 ratio and therefore a composition of $Y_4\mathbf{L}_3 \cdot 4.6H_2O$ is proposed for Y-H$_4$**L**U1.

Diffraction data for Y-H$_4$**L**U1 have been successfully indexed from laboratory powder X-ray diffraction data (Cu K_α). Data were collected on a sample of the material mounted in a 0.7 mm glass capillary tube mounted in a Debye-Scherrer geometry at 298 K. The data were indexed using the TREOR routine of the EXPO2009 package[153, 148] with a triclinic cell (F.O.M. $M_{20} = 14$)[154] which was then fitted using the Le Bail routines of the GSAS suite of programs.[155, 156, 157] The final fit for a triclinic cell with parameters $a = 13.6023(15)$ Å, $b = 11.4426(11)$ Å, $c = 7.3659(5)$ Å, $\alpha = 91.349(7)°$, $\beta = 97.355(9)°$, $\gamma = 70.028(6)°$, V = 1068.41(16) Å^3 was $R_{wp} = 0.0627$ (*Fig. B.4*).

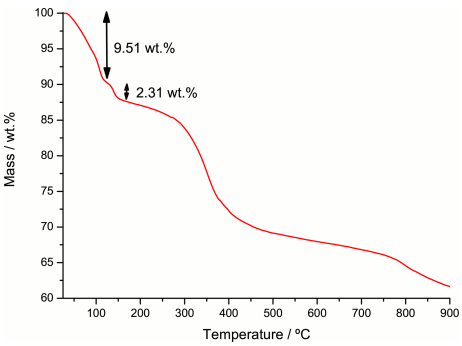

Figure B.2: TGA of Y-H$_4$**L**U1 from 25–900°C under dry air showing principal weight loss events.

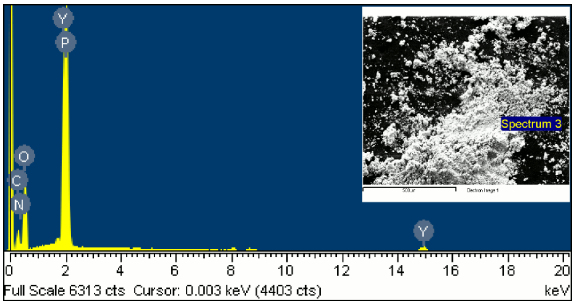

Figure B.3: EDX spectrum of Y-H$_4$**L**U1 indicating elements found. Y : P ratio of 1.0 : 1.71. Inset shows the area analysed.

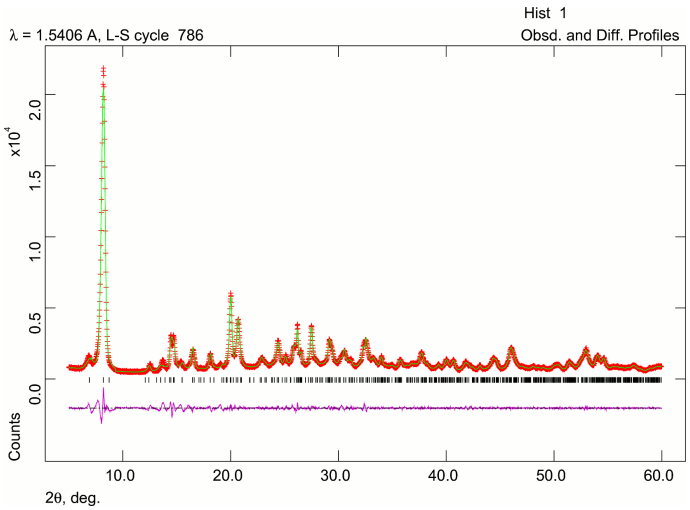

Figure B.4: Final Le Bail fit of Y-H$_4$**L**U1 with R_{wp} = 0.0627

B.2 Y-H$_4$LU4

Y-H$_4$**L**U4 was characterised by TGA and EDX analysis. TGA data were collected over the range 20–900°C in flowing air. TGA data show one weight loss (20–120°C — 8.80 wt.%) which corresponds to the loss of half a molecule of water per yttrium cation (assuming final solid is Y_2O_3 — *Fig. B.5*). Above 280°C a second weight loss begins, marking the onset of structural collapse. The EDX spectrum for Y-H$_4$**L**U4 gave an average Y : P ratio of 1.0 : 2.75, whilst Br was also found to be present in an average Y : Br ration of 1.0 : 0.2 (*Fig. B.6*). The Y : P ratio is intermediate between that expected for a metal:ligand ratio of 1 : 2 and 2 : 3. For charge balancing a metal:ligand ratio of 2 : 3 is expected and on this basis a composition of $Y_2(\mathbf{L}H_2)_3{\cdot}H_2O$ is proposed. The observation of Br in the EDX spectrum may, however, indicate a more complex situation.

Structural characterisation of Y-H$_4$**L**U4 was not possible as samples so far obtained have not been of sufficient crystallinity to permit the collection of suitable powder X-ray diffraction data.

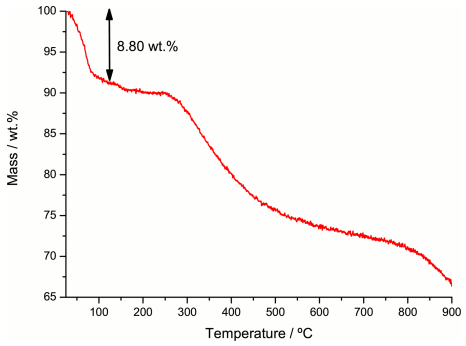

Figure B.5: TGA of Y-H$_4$**L**U4 from 20–900°C under dry air showing principal weight loss events.

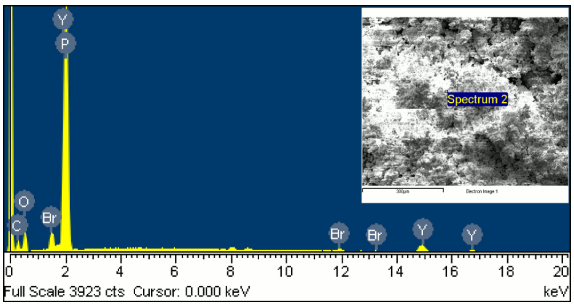

Figure B.6: EDX spectrum of Y-H$_4$**L**U4 indicating elements found. Y : P ratio of 1.0 : 2.75. Inset shows the area analysed.

Appendix C

Phases Formed with Divalent Cations and H_4LL

C.1 Reactions of $Mg^{(II)}$ with H_4LL

A series of High-Throughput (HT) reactions were performed using $Mg(AcO)_2$ as the metal source in reactions of the Mg/H_4**LL**/KOH system, with water as the solvent. Only one phase was observed, referred to as structure Mg-**LL**U1 of this work. Mg-**LL**U1 was obtained from gels with metal:ligand ratios of both 1 : 1 and 2 : 1 and with high KOH concentrations (two equivalents for gels with 1 : 1 metal:ligand ratios and four equivalents with 2 : 1 ratios) (*Fig. C.1*). With lower concentrations of base, either amorphous products or recrystallised ligand are obtained depending on the overall concentration of the reaction — at higher dilutions (1500 equivalents of water) amorphous products are obtained.

Sufficient amount of phase pure Mg-**LL**U1 was obtained from the HT reactions to

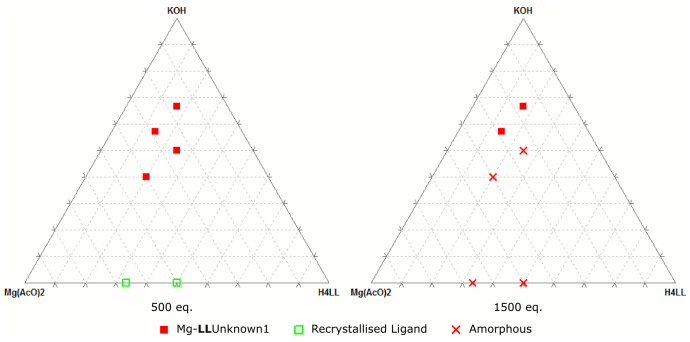

Figure C.1: Triplots summarising HT reactions investigating phases formed in the $Mg(AcO)_2$/H_4**LL**/KOH system. The number of equivalents of water used in each series is given below the each plot. All reactions were performed at 190°C for 24 hours.

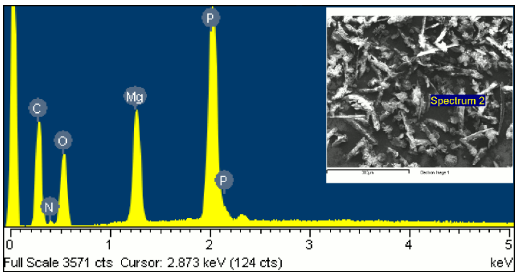

Figure C.2: EDX spectrum of Mg-**LL**U1, with Mg : P ratio of 1.0 : 1.17. All elements identified are labelled in the spectrum. Inset shows area analysed.

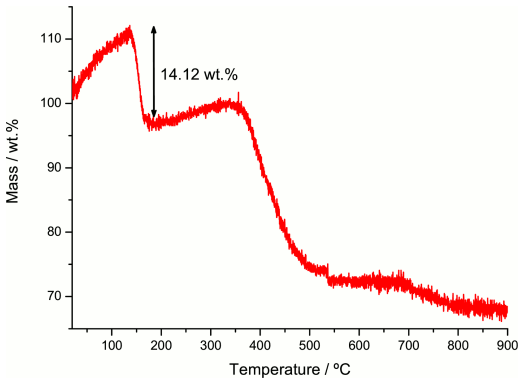

Figure C.3: TGA plot for Mg-**LL**U1 over the range 20–900°C, showing principal weight losses attributed to loss of water from the structure.

permit characterisation of the material by EDX and TGA. EDX spectra indicated a Mg : P ratio of 1.0 : 1.17 which corresponds well with a metal:ligand ratio of 2 : 1 (*Fig. C.2*). TGA of Mg-**LL**U1 shows a weight gain on heating from 20–139°C (10.81 wt.%). This result has been reproduced twice with the different samples. Such a weight gain could indicate the adsorption by the sample of gas from the carrier gas in the TGA apparatus or it may be an artifact due to the TGA. Further investigation is necessary to determine the cause. From 139–179°C the sample loses mass again (14.12 wt.%) assigned to the loss of physisorbed water or other adsorbates from the structure. This weight loss would be consistent with the loss of 0.5 molecules H_2O per Mg^{2+} cation (assuming final solid is MgO). Above 360°C, the material undergoes a series of weight loss events indicating the collapse of the framework.

Powder X-ray diffraction data were collected on a sample of Mg-**LL**U1 and indexed using the TREOR routine of EXPO2009.[153, 148] Fresh Mg-**LL**U1 was loaded into a 0.5 mm glass capillary tube. Data were collected using a Stoe Stadi P diffractometer (Cu K_α) over the range 5–90°2θ. Data above 50°were found to be of low intensity and discarded. The structure was indexed with a monoclinic unit cell, a = 14.989(7) Å, b = 6.276(6) Å, c = 11.456(8) Å, β = 106.71(6)°, V = 1032(18) Å^3 (M_{19} = 11).[154] Refinement of the unit cell was not attempted. Due to the limited amount of material obtained from HT synthesis, further characterisation has not been possible. Work on scaling up the synthesis of this material is being undertaken by the group of N. Stock (Christian-Albrechts-Universität zu Kiel, Kiel, Germany).

C.2 Reactions of $Fe^{(II)}$ with H_4LL

Using $Fe(AcO)_2$ as the metal source, two phases have been observed, labelled Fe-**LL**U1 and Fe-**LL**U2 in this work. Fe-**LL**U1 was obtained from reactions with four or fewer equivalents of KOH at metal:ligand ratio of both 1 : 1 and 2 : 1. Using a gel compostion of 2 : 1 : 3, Fe-**LL**U2 is co-crystallised with Fe-**LL**U1. It has so far not been possible to prepare Fe-**LL**U2 as a phase pure compound. Scaling up the reaction to a 7 ml scale, Fe-**LL**U1 was prepared with sufficient phase purity to characterise its composition by EDX. EDX spectra gave an Fe : P ratio of 1.0 : 2.39, indicating a metal:ligand ratio of 1 : 1 (*Fig. C.4*).

Although prepared phase pure, only the first peak of the diffraction pattern of Fe-**LL**U1 is well defined (*Fig. C.5*); higher angle peaks are broad and consequently overlapping, also having significantly lower intensity than the first peak. As a result it has not been possible to analyse the structure of Fe-**LL**U1 further.

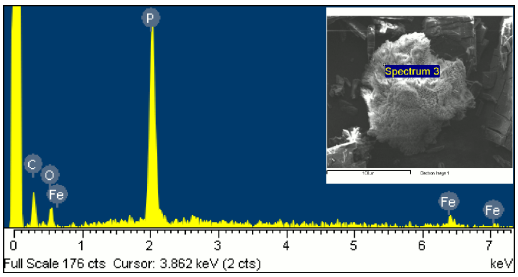

Figure C.4: EDX spectrum of Fe-**LL**U1, with principal elements present labelled. Fe : P ratio of 1.0 : 2.39. Inset shows area analysed.

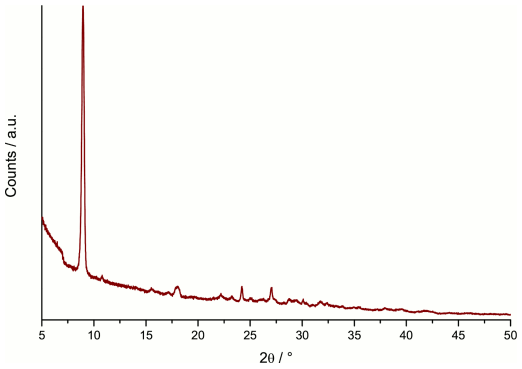

Figure C.5: Laboratory powder X-ray diffraction pattern of Fe-**LL**U1 (Fe K_α) over the range 5–90° 2θ.

C.3 Reactions of $Cu^{(II)}$ with H_4LL

HT reactions of $Cu(AcO)_2$ gave only one phase over a range of gel compositions. Structure Cu-**LL**U1 forms at $Cu(AcO)_2$: H_4**LL** ratios of both 1 : 1 and 2 : 1. High base concentrations (four equivalents per ligand equivalent) lead to either amorphous products or recrystallised ligand. The most crystalline samples of Cu-**LL**U1 were obtained with one equivalent of base, though in all cases Cu-**LL**U1 co-crystallised with ligand (*Fig. C.6*). From the HT reactions, the two conditions forming the most crystalline Cu-**LL**U1 (1 : 1 : 1 and 2 : 1 : 1 both with 800 equivalents of water) were scaled up to a 7 ml scale and found also to prepare Cu-**LL**U1, though again co-crystallised with unreacted H_4**LL**. It was possible to separate Cu-**LL**U1 by sonication and a complete characterisation was performed.

Cu-**LL**U1 was characterised by EDX. EDX analysis gave a Cu : P ratio of 1.0 : 2.39 (*Fig. C.7*), suggesting a metal:ligand ratio in the final solid of 1 : 1. TGA data for Cu-**LL**U1 show a weight loss 24–122°C (3.19 wt.%) assigned to dehydration of the sample. This weight loss is consistent with the structure losing $\sim$ 0.2 molecules of H_2O per Cu^{2+} cation. Such a low number of water molecules may indicate that the weight loss is due to the loss of water from the surface of crystals rather than a structural feature. Only determination of the crystal structure would provide more information on the nature of H_2O molecules within this structure. From EDX and TGA, a composition for the material of Cu(**LL**H_2)·0.2H_2O is proposed.

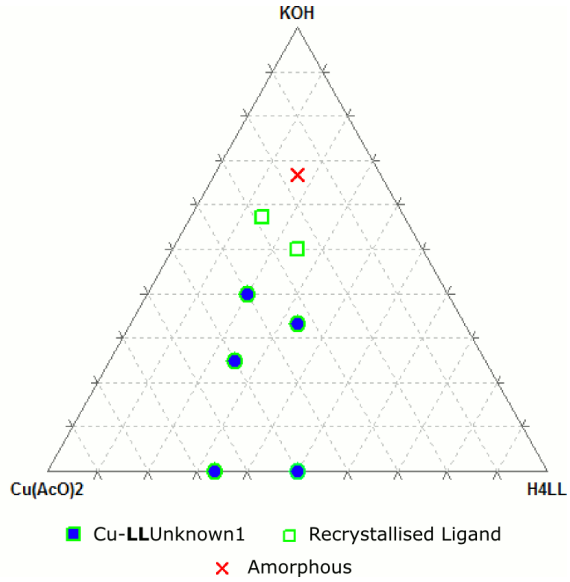

Figure C.6: Triplots summarising HT reactions investigating phases formed in the $Cu(AcO)_2$/H_4**LL**/KOH system. 800 equivalents of water were used in all reactions and reactions were reacted at 190°C for 24 hours.

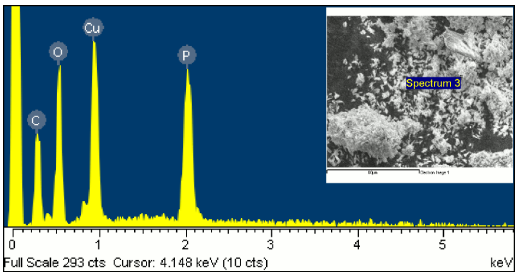

Figure C.7: EDX spectrum of Cu-**LL**U1 showing the principal elements present. Cu : P ratio of 1.0 : 2.39. Inset shows area analysed.

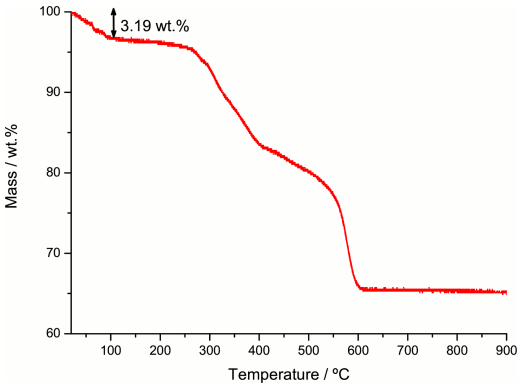

Figure C.8: TGA plot for Cu-**LL**U1 showing weightlosses attributed to the loss of water from the structure.

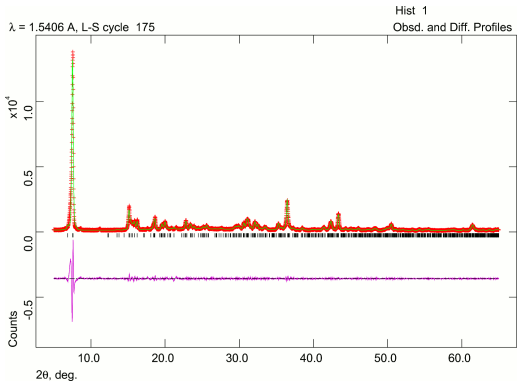

Figure C.9: Final Le Bail fit of the powder X-ray diffraction pattern (Cu K_α) of Cu-**LL**U1 (R_{wp} = 0.1722).

Laboratory powder diffraction data for Cu-**LL**U1 was also analysed. Data were collected on a Stoe Stadi P diffractometer fitted with a Cu K_α source in a Debye-Scherrer geometry over the range 5–90° 2θ at 298 K. Data were indexed using the TREOR routine of EXPO2009[153, 148] in a triclinic space group and analysed by Le Bail fitting.[155] The data fit the proposed cell at high angle, but the large asymmetry in the first peak proved difficult to fit (*Fig. C.9*). The final fit gave a unit cell with parameters a = 14.3331(13) Å, b = 13.1830(14) Å, c = 6.1555(5) Å, α = 97.888(10)°, β = 92.031(7)°, γ = 63.256(5)°, V = 1028.40(11) Å^3 (R_{wp} = 0.1722, R_p = 0.1105).

C.4 Reactions of $Zn^{(II)}$ with H_4LL

Reactions of $Zn(AcO)_2$ with H_4**LL** and KOH have been investigated by HT methods. Two phases were observed in the course of these reactions, labelled Zn-**LL**U1 and Zn_2**LL**. Zn_2**LL** has previously been obtained by Mowat and the structure reported as Zn_2**LL**·$2H_2O$; Zn-**LL**U1 is previously unknown. Zn-**LL**U1 was obtained from one reaction, with a gel composition of 1 : 1 : 4 ($Zn(AcO)_2$: H_4**LL** : KOH, 800 equivalents of water). Other reactions with metal:ligand ratio 1 : 1 yielded recrystallised ligand, in the absence of KOH, or amorphous products, with either one or two equivalents of KOH. At a metal:ligand ratio of 2 : 1 with two or more equivalents of base Zn_2**LL** was obtained. With less base however a mixture of unknowns or an amorphous product was obtained. Scaling up the gel preparing Zn-**LL**U1 to a 7 ml scale, a fine microcrystalline powder of Zn-**LL**U1 was obtained. It has not been possible to characterise the structure of this phase further due to peak broadening. Structure Zn_2**LL** was also observed in scaled up (7 ml) reactions, however it was co-crystallised with other phases. Diffraction patterns of both phases are given (*Fig. C.11*).

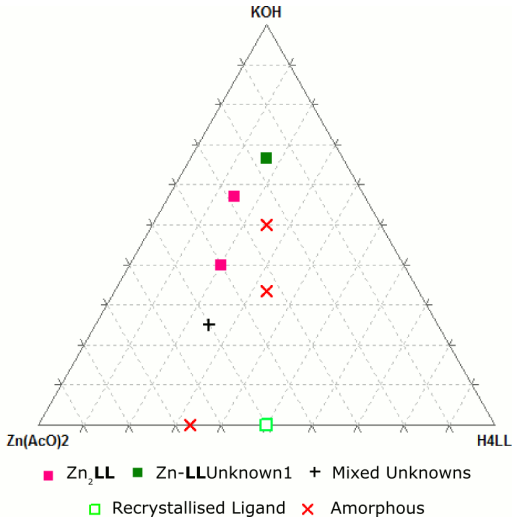

Figure C.10: Triplots summarising HT reactions investigating phases formed in the $Zn(AcO)_2$/H_4**LL**/KOH system. 800 equivalents of water were used in all reactions and reactions were reacted at 190°C for 24 hours.

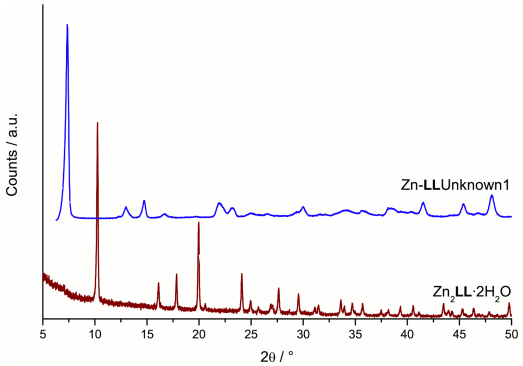

Figure C.11: Powder X-ray diffraction patterns of Zn-**LL**U1 and Zn_2**LL** (Fe K_α) over the range 5–50° 2θ.

C.5 Summary of Crystallographic Results

	Mg-**LL**U1	Cu-**LL**U1
Space Group	$P\,1c1$	$P\,1$
a / Å	14.989(7)	14.3331(13)
b / Å	6.276(6)	13.1830(14)
c / Å	11.456(8)	6.1555(5)
α / °		97.888(10)
β / °	106.71(6)	92.031(7)
γ / °		63.256(5)
V / Å^3	1032(18)	1028.40(11)
Diffractometer	Lab/Stoe Stadi P	Lab/Stoe Stadi P
Temperature / K	298	298
λ / Å	1.54056	1.54056
No. Reflections	-	738
R_{wp}	-	0.1722
R_p	-	0.1105
χ^2	-	9.722

Table C.1: Crystallographic data from the unit cells of Mg-**LL**U1 and Cu-**LL**U1. Mg-**LL**U1 data were obtained from indexing diffraction data; space group represents the extinction group, not the actual space group of the structure. Data for Cu-**LL**U1 were obtained from Le Bail analysis.

Appendix D

Phases Formed with Trivalent Cations and H_4**LL**

D.1 Reactions of $Al^{(III)}$ with H_4**LL**

Two metal sources were chosen for investigation of the Al^{3+}/H_4**LL**/KOH system in water: $AlCl_3$ and $Al(OH)(AcO)_2$. HT discovery arrays using the $Al(OH)(AcO)_2$ yielded only one phase, phase Al-**LL**U1 of this work, whilst a further two phases were obtained from reactions using $AlCl_3$ as the metal source, materials Al-**LL**U2 and Al-**LL**U3. Characteristic X-ray powder diffraction patterns from HT syntheses for each phase are given (*Fig. D.1*).

Using $Al(OH)(AcO)_2$, metal:ligand ratios of 1 : 1.5, 1.5 : 1.5 and 2 : 1.5 were investigated, using 800 equivalents of water and with synthesis performed at 190°C for 24 hours. The effect of increasing KOH concentration (0–6 equivalents) and consequently pH (3–9) was investigated (*Fig. D.2*). Al-**LL**U1 forms over the entire range of conditions investigated except the highest KOH concentration, when amorphous products were otained. With increasing KOH the crystallinity of Al-**LL**U1 samples decreases. The most crystalline samples were obtained in the pH range 5–7 (Al : H_4**LL**1.5 : 1.5, 4.5–5.5 equivalents KOH). At high ligand concentrations, Al-**LL**U1 crystallises with H_4**LL**.

A similar protocol was used to investigate reactions of $AlCl_3$ with H_4**LL**. The lower pH of $AlCl_3$ solution compared to $Al(OH)(AcO)_2$ allowed a different pH range to be investigated (1–9 for $AlCl_3$, vs 3–9 for $Al(OH)(AcO)_2$). Also the greater solubility of $AlCl_3$ made for more homogenous reaction gels. Under low KOH concentration (low pH) recrystallised ligand or amorphous products were obtained (*Fig. D.2*). Al-**LL**U1 was again obtained across a wide range of gel compositions, though synthesis was favoured by higher metal concentrations and reaction pH values

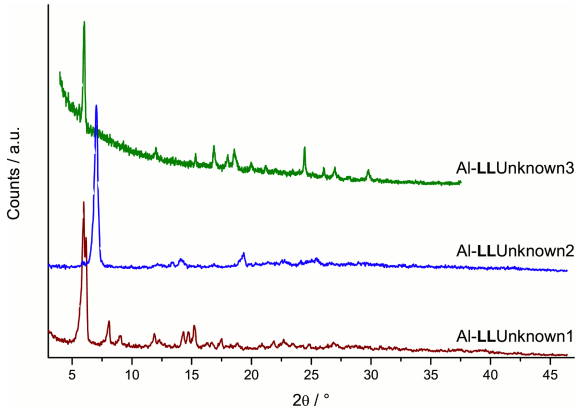

Figure D.1: Characterisitic laboratory powder X-ray diffraction patterns (Cu K_α) of phases Al-**LL**U1, Al-**LL**U2 and Al-**LL**U3 collected from HT reactions. Al-**LL**U3 data collected from a 7 ml scale reaction.

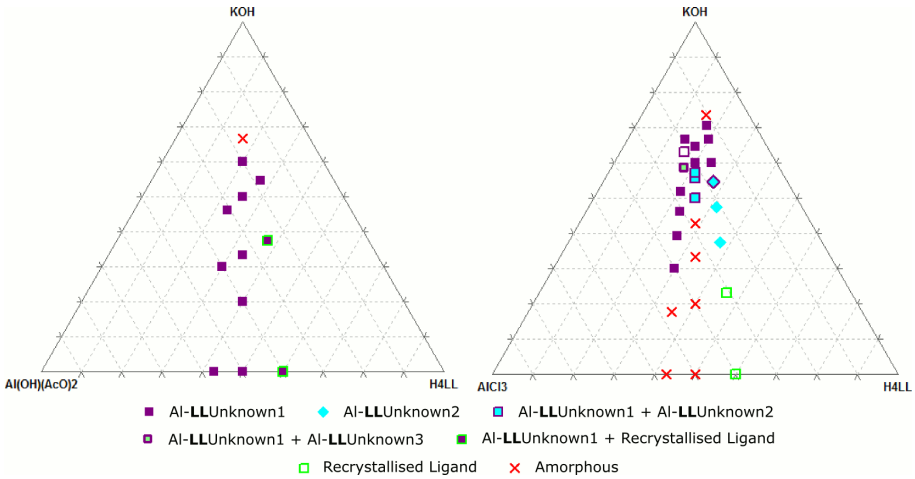

Figure D.2: HT reactions used to investigate the $Al^{(III)}$:H_4**LL**:KOH system. Reactions used water as the solvent (800 eq.) and were heated at 190°C for 24 hours. $Al(OH)(AcO)_2$ (*left*) and $AlCl_3$ (*right*) were used as metal sources.

of 5–6 (*c.f.* Al(OH)$(AcO)_2$ syntheses). In gels with lower pH and higher ligand concentration (M : **LL** 1 : 1.5, 1.5–2.0 equivalents of KOH; pH 2–4) Al-**LL**U2 was obtained. Al-**LL**U3 was obtained only as a secondary phase from a gel composition of 2.0 : 1.5 : 5.0:800 (Al : H_4**LL** : KOH : H_2O), though subsequent larger scale (7 ml) reactions have indicated that this phase may be obtained over a wider range of gel compositions than those indicated by HT methods).

D.2 Reactions of $Y^{(III)}$ with H_4LL

The materials formed by the crystallisation of $Y^{(III)}$ with H_4**LL** were investigated using $Y(AcO)_3$ and $Y(NO_3)_3$ as metal sources. HT discovery arrays used $Y(AcO)_3$ as the metal source to investigate metal:ligand ratios of 1.0 : 1.5, 1.5 : 1.5 and 2.0 : 1.5 with 800 equivalents of H_2O as the solvent (*Fig. D.4*). The amount of base was varied over the range 0–3.75 equivalents. Reactions were heated at 190°C for 24 hours. Two principal phases were identified, with the phase obtained most strongly dependent on the $Y(AcO)_3$: H_4**LL** ratio. Using a ratio of 1.0 : 1.5, Y-**LL**U2 was obtained, whilst with ratios of 1.5 : 1.5 and 2.0 : 1.5 a mixture of Y-**LL**U1 and Y-**LL**U2 were obtained — powder diffraction patterns of these two phases are given (*Fig.D.3*). At the higher $Y(AcO)_3$ concentration, the product contained a a greater proportion of Y-**LL**U1. Hints of a further two phases (Y-**LL**U3 and Y-**LL**U4) were also observed from the discovery array.

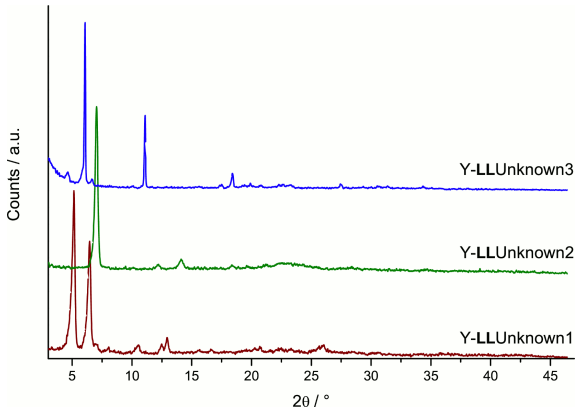

Figure D.3: Powder X-ray diffraction patterns (Cu K_α) of three $Y^{(III)}$-H_4**LL** phases prepared phase pure.

Using higher concentrations of $Y(AcO)_3$ (2.5 : 1.5 and 3.0 : 1.5) phase pure samples of Y-**LL**U1 were obtained (*Fig. D.4*). Using more dilute reaction conditions (1600 equivalents of H_2O) at a metal:ligand ratio of 1.0 : 1.5 gave Y-**LL**U2 and hints of Y-**LL**U3 at the lowest base concentrations.

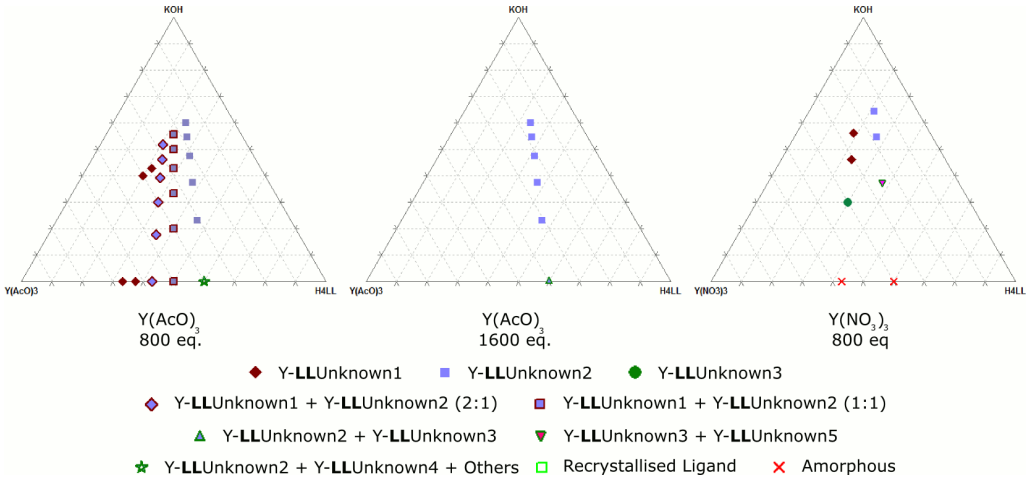

Figure D.4: HT reactions used to investigate the $Y^{(III)}$:H_4**LL**:KOH system. Reactions used water as the solvent (800 or 1600 eq.) and were heated at 190°C for 24 hours. $Y(AcO)_3$ (*left*: 800 eq. H_2O; *center*: 1600 eq. H_2O) and $Y(NO_3)_3$ (*right*: 800 eq. H_2O) were used as metal sources.

Using $Y(NO_3)_3$ as the metal source, Y-**LL**U1 and Y-**LL**U2 were obtained from reactions with metal:ligand ratios of 2.0 : 1.5 and 1.0 : 1.5 respectively provided KOH solution was added to raise the pH of the reaction to pH 4 or higher (*Fig. D.4*). Without pH modification, amorphous products were obtained. It was also possible to obtain Y-**LL**U3 phase pure from a reaction with a composition of 2.0 : 1.5 : 1.5 : 800 ($Y(NO_3)_3$: H_4**LL** : KOH : H_2O). A fifth Y-H_4**LL** phase was also observed in the $Y(NO_3)_3$-H_4**LL** system, though it has not been prepared phase pure.

From HT syntheses, crystallisation of Y-**LL**U1 is favoured for $Y^{(III)}$: H_4**LL** ratios of 2.5 : 1.5 whereas lower $Y^{(III)}$ concentrations favour the crystallisation of Y-**LL**U2. To crystallise either phase, weakly acidic conditions are necessary, hence using $Y(AcO)_3$ as the metal source favours their crystallisation. Under more acidic conditions, which may be achieved by the use of $Y(NO_3)_3$ as the metal source, Y-**LL**U3 is obtained. With $Y(NO_3)_3$ base must be added to raise the initial pH otherwise amorphous products are formed.

D.3 Reactions of $Yb^{(III)}$ with H_4LL

The chemistry of the $Yb^{(III)}$-H_4**LL** system is very similar to the $Y^{(III)}$-H_4**LL** system. Three phases have been identified from a HT discovery array. $Yb(AcO)_3$ was used as the metal source. Reactions used 800 equivalents of H_2O as the solvent and were heated at 190°C for 24 hours. Using a $Yb(AcO)_3$: H_4**LL** ratio of 1 : 1.5 Yb-**LL**U2 was crystallised. The powder X-ray diffraction pattern of Yb-**LL**U2 suggests it is an analogue of Y-**LL**U2. Yb-**LL**U1 and Yb-**LL**U3 were obtained at $Yb^{(III)}$: H_4**LL** ratios of both 1.5 : 1.5 and 2.0 : 1.5, though only as one component of a mixture of phases. Powder diffraction suggests these are analogues of the phases Y-**LL**U1 and Y-**LL**U3 respectively. The conditions to prepare these materials as pure phases have not yet been determined.

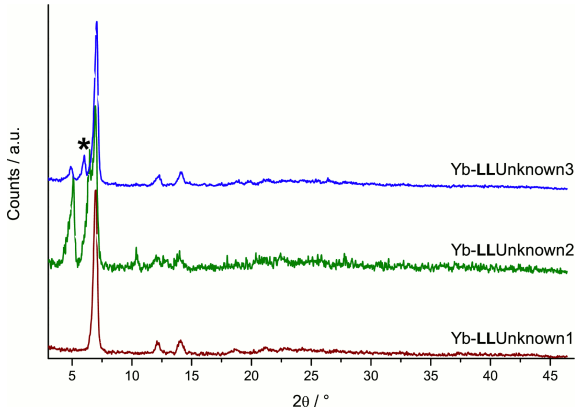

Figure D.5: Powder X-ray diffraction patterns (Cu K_α) of three $Yb^{(III)}$-H_4**LL** phases prepared phase pure. In Yb-**LL**U3 pattern, peak marked * is Yb-**LL**U3.

References

[1] Sircar, S. *Ind. Eng. Chem. Res.* **41**(6), 1389–1392 (2002).

[2] Jacoby, M. *Chem. Eng. News* **86**(4), 67–70 (2008).

[3] Chalmers, H. and Gibbins, J. *Proc. Inst. Mech. Eng. C J. Mech. Eng. Sci.* **224**(3), 505 –518 (2010).

[4] Rouquerol, J., Avnir, D., Fairbridge, C. W., Everett, D. H., Haynes, J. M., Pernicone, N., Ramsay, J. D. F., Sing, K. S. W., and Unger, K. K. *Pure Appl. Chem.* **66**(8), 1739–1758 (1994).

[5] Morris, R. and Wheatley, P. *Angew. Chem. Int. Ed.* **47**(27), 4966–4981 (2008).

[6] Parlett, C. M. A., Bruce, D. W., Hondow, N. S., Lee, A. F., and Wilson, K. *ACS Catal.* **1**(6), 636–640 (2011).

[7] Wheatley, P. S., Butler, A. R., Crane, M. S., Fox, S., Xiao, B., Rossi, A. G., Megson, I. L., and Morris, R. E. *J. Am. Chem. Soc.* **128**(2), 502–509 (2005).

[8] Férey, G. *Chem. Soc. Rev.* **37**(1), 191–214 (2008).

[9] Czaja, A. U., Trukhan, N., and Muller, U. *Chem. Soc. Rev.* **38**(5), 1284–1293 (2009).

[10] Wright, P. A. *Microporous Framework Solids.* RSC Materials Monographs. The Royal Society of Chemistry, (2008).

[11] Cronstedt, A. F. *Akad. Handl. Stockholm* **18**, 120–123 (1756).

[12] van Bekkum, H., Flanigen, E. M., Jacobs, P. A., and Jansen, J. C., editors. *Introduction to Zeolite Science and Practice.* Number 137 in Studies in Surface Science and Catalysis. Elsevier, 1st edition, (2001).

[13] Barrer, R. M. *J. Chem. Soc.* , 2158–2163 (1948).

[14] Barrer, R. M. *Discuss. Faraday Soc.* **7**, 135–141 (1949).

[15] Barrer, R. M. *Nature* **158**, 508 (1947).

[16] Breck, D. W., Eversole, W. G., and Milton, R. M. *J. Am. Chem. Soc.* **78**(10), 2338–2339 (1956).

[17] Breck, D. W., Eversole, W. G., Milton, R. M., Reed, T. B., and Thomas, T. L. *J. Am. Chem. Soc.* **78**(23), 5963–5972 (1956).

[18] Reed, T. B. and Breck, D. W. *J. Am. Chem. Soc.* **78**(23), 5972–5977 (1956).

[19] Breck, D. W. Patent, (1964).

[20] *Chem. Eng. News* **40**(17), 59–63 (1962).

[21] Kerr, G. T. and Kokotailo, G. T. *J. Am. Chem. Soc.* **83**(22), 4675 (1961).

[22] Barrer, R. M. and Denny, P. J. *J. Chem. Soc.* , 971–982 (1961).

[23] Baerlocher, C. and McCusker, L. B. http://www.iza-structure.org/databases/, September (2011).

[24] Colella, C. and Alberti, A. http://www.iza-online.org/natural/index.htm, September (2011).

[25] Foster, M. D. and Treacy, M. M. J. http://www.hypotheticalzeolites.net/, September (2011).

[26] Wilson, S. T., Lok, B. M., Messina, C. A., Cannan, T. R., and Flanigen, E. M. *J. Am. Chem. Soc.* **104**(4), 1146–1147 (1982).

[27] Flanigen, E. M., Lok, B. M., Patton, R. L., and Wilson, S. T. *Pure Appl. Chem.* **58**, 1351–1358 (1986).

[28] Lok, B. M., Messina, C. A., Patton, R. L., Gajek, R. T., Cannan, T. R., and Flanigen, E. M. *J. Am. Chem. Soc.* **106**(20), 6092–6093 (1984).

[29] Wilson, S. T. and Flanigen, E. M. In *Zeolite Synthesis*, volume 398 of *ACS Symposium Series*, 329–345. American Chemical Society (1989).

[30] Corma, A., Garcia, H., and Llabres i Xamena, F. X. *Chem. Rev.* **110**(8), 4606–4655 (2010).

[31] Ohrström, L. R., Batten, S. R., Champness, N. R., Chen, X., Garcia-Martinez, J., Kitagawa, S., O'Keeffe, M., Reedijk, J., and Suh, M. P. IUPAC Project: Coordination polymers and metal organic frameworks: terminology and nomenclature guidelines — http://www.iupac.org/web/ins/2009-012-2-200, August (2009).

[32] Kinoshita, Y., Matsubara, I., Higuchi, T., and Saito, Y. *Bull. Chem. Soc. Jpn.* **32**(11), 1221–1226 (1959).

[33] Allison, S. A. and Barrer, R. M. *J. Chem. Soc. A* **1969**, 1717–1723 (1969).

[34] Hoskins, B. F. and Robson, R. *J. Am. Chem. Soc.* **112**(4), 1546–1554 (1990).

[35] Li, H., Eddaoudi, M., Groy, T. L., and Yaghi, O. M. *J. Am. Chem. Soc.* **120**(33), 8571–8572 (1998).

[36] Chui, S. S., Lo, S. M., Charmant, J. P. H., Orpen, A. G., and Williams, I. D. *Science* **283**(5405), 1148–1150 (1999).

[37] Li, H., Eddaoudi, M., O'Keeffe, M., and Yaghi, O. M. *Nature* **402**(6759), 276–279 (1999).

[38] Eddaoudi, M., Kim, J., Rosi, N., Vodak, D., Wachter, J., O'Keeffe, M., and Yaghi, O. M. *Science* **295**(5554), 469–472 (2002).

[39] Yaghi, O. M., O'Keeffe, M., Ockwig, N. W., Chae, H. K., Eddaoudi, M., and Kim, J. *Nature* **423**(6941), 705–714 June (2003).

[40] O'Keeffe, M., Peskov, M. A., Ramsden, S. J., and Yaghi, O. M. *Acc. Chem. Res.* **41**(12), 1782–1789 (2008).

[41] Morris, W. and Yaghi, O. M. In *10th International Conference on Materials Chemistry (MC10)*, CS_O02 (The Royal Society of Chemistry, University of Manchester, Manchester, UK, 2011).

[42] Férey, G. *J. Solid State Chem.* **152**(1), 37–48 June (2000).

[43] Férey, G., Mellot-Draznieks, C., and Loiseau, T. *Solid State Sci.* **5**(1), 79–94 January (2003).

[44] Serre, C., Millange, F., Surblé, S., and Férey, G. *Angew. Chem. Int. Ed.* **43**(46), 6285–6289 (2004).

[45] Surblé, S., Serre, C., Mellot-Draznieks, C., Millange, F., and Férey, G. *Chem. Commun.* (3), 284–286 (2006).

[46] Serre, C., Mellot-Draznieks, C., Surblé, S., Audebrand, N., Filinchuk, Y., and Férey, G. *Science* **315**(5820), 1828 –1831 (2007).

[47] Serre, C., Surblé, S., Mellot-Draznieks, C., Filinchuk, Y., and Férey, G. *Dalton Trans.* (40), 5462–5464 (2008).

[48] Serre, C., Millange, F., Thouvenot, C., Nogus, M., Marsolier, G., Lour, D., and Frey, G. *J. Am. Chem. Soc.* **124**(45), 13519–13526 November (2002).

[49] Férey, G., Mellot-Draznieks, C., Serre, C., Millange, F., Dutour, J., Surblé, S., and Margiolaki, I. *Science* **309**(5743), 2040–2042 (2005).

[50] Férey, G., Serre, C., Mellot-Draznieks, C., Millange, F., Surblé, S., Dutour, J., and Margiolaki, I. *Angew. Chem. Int. Ed.* **43**(46), 6296–6301 (2004).

[51] Loiseau, T., Serre, C., Huguenard, C., Fink, G., Taulelle, F., Henry, M., Bataille, T., and Férey, G. *Chem. Eur. J.* **10**(6), 1373–1382 (2004).

[52] Mowat, J. P., Miller, S. R., Slawin, A. M., Seymour, V. R., Ashbrook, S. E., and Wright, P. A. *Micropor. Mesopor. Mater.* **142**(1), 322–333 (2011).

[53] Whitfield, T. R., Wang, X., Liu, L., and Jacobson, A. J. *Solid State Sci.* **7**(9), 1096–1103 (2005).

[54] Volkringer, C., Loiseau, T., Guillou, N., Ferey, G., Elkaim, E., and Vimont, A. *Dalton Trans.* (12), 2241–2249 (2009).

[55] Anokhina, E. V., Vougo-Zanda, M., Wang, X., and Jacobson, A. J. *J. Am. Chem. Soc.* **127**(43), 15000–15001 (2005).

[56] Bourrelly, S., Llewellyn, P. L., Serre, C., Millange, F., Loiseau, T., and Férey, G. *J. Am. Chem. Soc.* **127**(39), 13519–13521 (2005).

[57] Serre, C., Bourrelly, S., Vimont, A., Ramsahye, N. A., Maurin, G., Llewellyn, P. L., Daturi, M., Filinchuk, Y., Leynaud, O., Barnes, P., and Férey, G. *Adv. Mater.* **19**(17), 2246–2251 (2007).

[58] Llewellyn, P. L., Maurin, G., Devic, T., Loera-Serna, S., Rosenbach, N., Serre, C., Bourrelly, S., Horcajada, P., Filinchuk, Y., and Férey, G. *J. Am. Chem. Soc.* **130**(38), 12808–12814 (2008).

[59] Mellot-Draznieks, C., Girard, S., Férey, G., Schön, J. C., Cancarevic, Z., and Jansen, M. *Chem. Eur. J.* **8**(18), 4102–4113 (2002).

[60] Carter, V. J., Wright, P. A., Gale, J. D., Morris, R. E., Sastre, E., and Perez-Pariente, J. *J. Mater. Chem.* **7**(11), 2287–2292 (1997).

[61] Clearfield, A. and Smith, G. D. *Inorg. Chem.* **8**(3), 431–436 (1969).

[62] Poojary, D. M., Shpeizer, B., and Clearfield, A. *J. Chem. Soc., Dalton Trans.* (1), 111–113 (1995).

[63] Alberti, G., Costantino, U., Allulli, S., and Tomassini, N. *J. Inorg. Nucl. Chem.* **40**(6), 1113–1117 (1978).

[64] Dines, M. B. and DiGiacomo, P. M. *Inorg. Chem.* **20**(1), 92–97 (1981).

[65] Yamanaka, S. *Inorg. Chem.* **15**(11), 2811–2817 (1976).

[66] Yamanaka, S. and Hattori, M. *Inorg. Chem.* **20**(6), 1929–1931 (1981).

[67] Yamanaka, S., Matsunaga, M., and Hattori, M. *J. Inorg. Nucl. Chem.* **43**(6), 1343–1346 (1981).

[68] Alberti, G., Casciola, M., Vivani, R., and Biswas, R. K. *Inorg. Chem.* **32**(21), 4600–4604 (1993).

[69] Ortiz-Avila, C. Y. and Clearfield, A. *Inorg. Chem.* **24**(12), 1773–1778 (1985).

[70] Ortiz-Avila, C. Y., Bhardwaj, C., and Clearfield, A. *Inorg. Chem.* **33**(12), 2499–2500 (1994).

[71] Clearfield, A. *Curr. Opin. Solid State Mater. Sci.* **1**(2), 268–278 (1996).

[72] Poojary, M. D., Hu, H. L., Campbell, F. L., and Clearfield, A. *Acta Cryst. B* **49**(6), 996–1001 (1993).

[73] Dines, M. B., Cooksey, R. E., Griffith, P. C., and Lane, R. H. *Inorg. Chem.* **22**(6), 1003–1004 (1983).

[74] Alberti, G., Vivani, R., Marmottini, F., and Zappelli, P. *J. Porous Mater.* **5**(3), 205–220 (1998).

[75] Alberti, G., Costantino, U., Marmottini, F., Vivani, R., and Zappelli, P. *Angew. Chem. Int. Ed. Engl.* **32**(9), 1357–1359 (1993).

[76] Le Bideau, J., Payen, C., Palvadeau, P., and Bujoli, B. *Inorg. Chem.* **33**(22), 4885–4890 (1994).

[77] Maeda, K., Akimoto, J., Kiyozumi, Y., and Mizukami, F. *Angew. Chem. Int. Ed. Engl.* **34**(11), 1199–1201 (1995).

[78] Maeda, K., Kiyozumi, Y., and Mizukami, F. *Angew. Chem. Int. Ed. Engl.* **33**(22), 2335–2337 (1994).

[79] Maeda, K., Akimoto, J., Kiyozumi, Y., and Mizukami, F. *J. Chem. Soc., Chem. Commun.* (10), 1033–1034 (1995).

[80] Carter, V. J., Kujanpää, J. P., Riddell, F. G., Wright, P. A., Turner, J. F. C., Catlow, C. R. A., and Knight, K. S. *Chem. Phys. Lett.* **313**(3-4), 505–513 (1999).

[81] Maeda, K., Kiyozumi, Y., and Mizukami, F. *J. Phys Chem. B* **101**(22), 4402–4412 (1997).

[82] Gonzalez, J., Devi, R. N., Wright, P. A., Tunstall, D. P., and Cox, P. A. *J. Phys Chem. B* **109**(46), 21700–21709 (2005).

[83] Herdes, C., Valente, A., Lin, Z., Rocha, J., Coutinho, J. A. P., Medina, F., and Vega, L. F. *Langmuir* **23**(13), 7299–7305 June (2007).

[84] Lohse, D. L. and Sevov, S. C. *Angew. Chem. Int. Ed. Engl.* **36**(15), 1619–1621 (1997).

[85] Gao, Q., Guillou, N., Nogues, M., Cheetham, A. K., and Férey, G. *Chem. Mater.* **11**(10), 2937–2947 (1999).

[86] Barthelet, K., Merlier, C., Serre, C., Riou-Cavellec, M., Riou, D., and Férey, G. *J. Mater. Chem.* **12**(4), 1132–1137 (2002).

[87] Miller, S. R., Lear, E., Gonzalez, J., Slawin, A. M. Z., Wright, P. A., Guillou, N., and Férey, G. *Dalton Trans.* (20), 3319–3325 (2005).

[88] Harvey, H. G., Teat, S. J., and Attfield, M. P. *J. Mater. Chem.* **10**(12), 2632–2633 (2000).

[89] Harvey, H. G., Hu, J., and Attfield, M. P. *Chem. Mater.* **15**(1), 179–188 (2003).

[90] Maeda, K. *Micropor. Mesopor. Mater.* **73**(1–2), 47–55 (2004).

[91] Shimizu, G. K. H., Vaidhyanathan, R., and Taylor, J. M. *Chem. Soc. Rev.* **38**(5), 1430–1449 (2009).

[92] Vasylyev, M. V., Wachtel, E. J., Popovitz-Biro, R., and Neumann, R. *Chem. Eur. J.* **12**(13), 3507–3514 (2006).

[93] Vasylyev, M. and Neumann, R. *Chem. Mater.* **18**(12), 2781–2783 (2006).

[94] Taylor, J., Mahmoudkhani, A., and Shimizu, G. *Angew. Chem. Int. Ed.* **46**(5), 795–798 (2007).

[95] Liang, J. and Shimizu, G. K. H. *Inorg. Chem.* **46**(25), 10449–10451 (2007).

[96] Poojary, D. M., Zhang, B., Bellinghausen, P., and Clearfield, A. *Inorg. Chem.* **35**(18), 5254–5263 (1996).

[97] Plabst, M. and Bein, T. *Inorg. Chem.* **48**(10), 4331–4341 (2009).

[98] Plabst, M., McCusker, L. B., and Bein, T. *J. Am. Chem. Soc.* **131**(50), 18112–18118 (2009).

[99] Choi, N., Khan, I., Matthews, R. W., McPartlin, M., and Murphy, B. P. *Polyhedron* **13**(5), 847–850 (1994).

[100] Soghomonian, V., Diaz, R., Haushalter, R. C., O'Connor, C. J., and Zubieta, J. *Inorg. Chem.* **34**(17), 4460–4466 (1995).

[101] Taddei, M., Costantino, F., and Vivani, R. *Inorg. Chem.* **49**(20), 9664–9670 (2010).

[102] Zhang, N., Huang, C., Sun, Z., Zhang, J., Liu, L., Lu, X., Wang, W., and Tong, F. *Z. Anorg. Allg. Chem.* **636**(7), 1405–1409 (2010).

[103] LaDuca, R., Rose, D., DeBord, J. R. D., Haushalter, R. C., O'Connor, C. J., and Zubieta, J. *J. Solid State Chem.* **123**(2), 408–412 (1996).

[104] Groves, J. A., Wright, P. A., and Lightfoot, P. *Dalton Trans.* (11), 2007–2010 (2005).

[105] Groves, J. A., Miller, S. R., Warrender, S. J., Mellot-Draznieks, C., Lightfoot, P., and Wright, P. A. *Chem. Commun.* (31), 3305–3307 (2006).

[106] Wang, Y., Bao, S., Xu, W., Chen, J., Gao, S., and Zheng, L. *J. Solid State Chem.* **177**(4-5), 1297–1301 (2004).

[107] Zhang, J., Li, J., Sun, Z., Zhao, Y., Zhu, Y., Zhang, N., Liu, L., and Dalian, X. L. *Z. Anorg. Allg. Chem.* **634**(14), 2629–2633 (2008).

[108] Serre, C., Groves, J. A., Lightfoot, P., Slawin, A. M. Z., Wright, P. A., Stock, N., Bein, T., Haouas, M., Taulelle, F., and Férey, G. *Chem. Mater.* **18**(6), 1451–1457 (2006).

[109] Hawthorne, F. *Acta Cryst. B* **50**(5), 481–510 (1994).

[110] Groves, J. A., Wright, P. A., and Lightfoot, P. *Inorg. Chem.* **44**(6), 1736–1739 (2005).

[111] Mowat, J. P., Groves, J. A., Wharmby, M. T., Miller, S. R., Li, Y., Lightfoot, P., and Wright, P. A. *J. Solid State Chem.* **182**(10), 2769–2778 (2009).

[112] Groves, J. A., Stephens, N. F., Wright, P. A., and Lightfoot, P. *Solid State Sci.* **8**(3-4), 397–403 (2006).

[113] Pearce, G. M. *Synthesis, Adsorption and Catalysis of Large Pore Metal Phosphonates.* PhD thesis, University of St Andrews, (2009).

[114] Miller, S. R., Pearce, G. M., Wright, P. A., Bonino, F., Chavan, S., Bordiga, S., Margiolaki, I., Guillou, N., Férey, G., Bourrelly, S., and Llewellyn, P. L. *J. Am. Chem. Soc.* **130**(47), 15967–15981 November (2008).

[115] Du, Z., Xie, Y., and Wen, H. *Inorg. Chim. Acta* **362**(2), 351–354 (2009).

[116] Costantino, F., Gentili, P. L., and Audebrand, N. *Inorg. Chem. Commun.* **12**(5), 406–408 (2009).

[117] Park, K. S., Ni, Z., Ct, A. P., Choi, J. Y., Huang, R., Uribe-Romo, F. J., Chae, H. K., O'Keeffe, M., and Yaghi, O. M. *Proc. Natl. Acad. Sci.* **103**(27), 10186 –10191 (2006).

[118] Hao, X. P., Cui, D. L., Shi, G. X., Yin, Y. Q., Xu, X. G., Wang, J. Y., Jiang, M. H., Xu, X. W., Li, Y. P., and Sun, B. Q. *Chem. Mater.* **13**(8), 2457–2459 (2001).

[119] Wei, X., Xu, G., Ren, Z., Wang, Y., Shen, G., and Han, G. *J. Cryst. Growth* **310**(18), 4132–4137 (2008).

[120] Yang, X., Williams, I. D., Chen, J., Wang, J., Xu, H., Konishi, H., Pan, Y., Liang, C., and Wu, M. *J. Mater. Chem.* **18**(30), 3543–3546 (2008).

[121] Demazeau, G. *J. Mater. Sci.* **43**(7), 2104–2114 (2008).

[122] Modeshia, D. R. and Walton, R. I. *Chem. Soc. Rev.* **39**(11), 4303–4325 (2010).

[123] Laye, R. H. and McInnes, E. J. *Eur. J. inorg. Chem.* **2004**(14), 2811–2818 (2004).

[124] Meek, S. T., Greathouse, J. A., and Allendorf, M. D. *Adv. Mater.* **23**(2), 249–267 (2011).

[125] Rabenau, A. *Angew. Chem. Int. Ed. Engl.* **24**(12), 1026–1040 (1985).

[126] *Parr Acid Digestion Vessels: Operating Instruction Manual.* Moline, Illiois 61265, USA, (2011).

[127] DuPont. http://www2.dupont.com/Teflon_Industrial/en_US/tech_info/techinfo_compare.html, September (2011).

[128] Atkins, P. W. and De Paula, J. *Atkins' Physical Chemistry.* Oxford University Press, Oxford, UK, 7th edition, (2002).

[129] Cheetham, A. K. and Mellot, C. F. *Chem. Mater.* **9**(11), 2269–2279 (1997).

[130] Surblé, S., Millange, F., Serre, C., Férey, G., and Walton, R. I. *Chem. Commun.* (14), 1518–1520 (2006).

[131] Millange, F., Medina, M., Guillou, N., Férey, G., Golden, K., and Walton, R. *Angew. Chem. Int. Ed.* **49**(4), 763–766 (2010).

[132] Ahnfeldt, T., Moellmer, J., Guillerm, V., Staudt, R., Serre, C., and Stock, N. *Chem. Eur. J.* **17**(23), 6462–6468 (2011).

[133] Shoaee, M., Anderson, M., and Attfield, M. *Angew. Chem. Int. Ed.* **47**(44), 8525–8528 (2008).

[134] Moh, P. Y., Cubillas, P., Anderson, M. W., and Attfield, M. P. *J. Am. Chem. Soc.* **133**(34), 13304–13307 (2011).

[135] Stock, N. *Micropor. Mesopor. Mater.* **129**(3), 287–295 (2010).

[136] Maniam, P. and Stock, N. *Inorg. Chem.* **50**(11), 5085–5097 (2011).

[137] Clegg, W. *Crystal Structure Determination.* Number 60 in Oxford Chemistry Primers. Oxford University Press, Oxford, UK, (1998).

[138] Giacovazzo, C., Monaco, H. L., Viterbo, D., Scordari, F., Gilli, P., Zanotti, G., and Catti, M. *Fundamentals of Crystallography.* Number 2 in IUCR Texts on Crystallography. Oxford University Press, Oxford, UK, 1st edition, September (1992).

[139] Woolfson, M. M. *Introduction X-Ray Crystallography.* Cambridge University Press, Cambridge, UK, 2nd edition, (1978).

[140] Sheldrick, G. *Acta Cryst. A* **64**(1), 112–122 (2008).

[141] Burla, M. C., Caliandro, R., Camalli, M., Carrozzini, B., Cascarano, G. L., De Caro, L., Giacovazzo, C., Polidori, G., Siliqi, D., and Spagna, R. *J. Appl. Cryst.* **40**(3), 609–613 (2007).

[142] Burla, M. C., Caliandro, R., Camalli, M., Carrozzini, B., Cascarano, G. L., De Caro, L., Giacovazzo, C., Polidori, G., and Spagna, R. *J. Appl. Cryst.* **38**(2), 381–388 (2005).

[143] Altomare, A., Burla, M. C., Camalli, M., Cascarano, G. L., Giacovazzo, C., Guagliardi, A., Moliterni, A. G. G., Polidori, G., and Spagna, R. *J. Appl. Cryst.* **32**(1), 115–119 (1999).

[144] Fitch, A. N. *J. Res. Natl. Inst. Stand. Technol.* **109**(1), 133–142 (2004).

[145] Thompson, S. P., Parker, J. E., Potter, J., Hill, T. P., Birt, A., Cobb, T. M., Yuan, F., and Tang, C. C. *Rev. Sci. Instrum.* **80**(7), 075107–9 (2009).

[146] David, W. I. F., Shankland, K., McCusker, L. B., and Baerlocher, C., editors. *Structure Determination from Powder Diffraction Data.* Number 13 in IUCR Monographs on Crystallography. Oxford University Press, Oxford, UK, 1st edition, August (2006).

[147] Rietveld, H. M. *J. Appl. Cryst.* **2**(2), 65–71 June (1969).

[148] Altomare, A., Camalli, M., Cuocci, C., Giacovazzo, C., Moliterni, A., and Rizzi, R. *J. Appl. Cryst.* **42**(6), 1197–1202 (2009).

[149] Altomare, A., Caliandro, R., Camalli, M., Cuocci, C., Giacovazzo, C., Moliterni, A. G., and Rizzi, R. *J. Appl. Cryst.* **37**(6), 1025–1028 November (2004).

[150] Roisnel, T. and Rodrigues-Carvajal, J. In *Proceedings of the Seventh European Powder Diffraction Conference (EPDIC 7), Barcelona, Spain, May 20–23, 2000,* Delhez, R. and Mittelmeijer, E. J., editors, volume 378–381 of *Materials Science Forum*, 118–123. Trans Tech Publications Inc., (2001).

[151] Visser, J. *J. Appl. Cryst.* **2**(3), 89–95 (1969).

[152] Boultif, A. and Louer, D. *J. Appl. Cryst.* **37**(5), 724–731 (2004).

[153] Werner, P. E., Eriksson, L., and Westdahl, M. *J. Appl. Cryst.* **18**(5), 367–370 (1985).

[154] de Wolff, P. *J. Appl. Cryst.* **1**(2), 108–113 (1968).

[155] Le Bail, A. *Powder Diffr.* **20**(4), 316 (2005).

[156] Larson, A. C. and Von Dreele, R. B. *General Structure Analysis System (GSAS).* Los Alamos National Laboratory, USA, (1994).

[157] Toby, B. *J. Appl. Cryst.* **34**(2), 210–213 (2001).

[158] Horcajada, P., Serre, C., Vallet-Regí, M., Sebban, M., Taulelle, F., and Férey, G. *Angew. Chem. Int. Ed.* **45**(36), 5974–5978 (2006).

[159] Alaerts, L., Maes, M., Giebeler, L., Jacobs, P. A., Martens, J. A., Denayer, J. F. M., Kirschhock, C. E. A., and De Vos, D. E. *J. Am. Chem. Soc.* **130**(43), 14170–14178 (2008).

[160] Sabo, M., Henschel, A., Frode, H., Klemm, E., and Kaskel, S. *J. Mater. Chem.* **17**(36), 3827–3832 (2007).

[161] Attard, G. and Barnes, C. *Surfaces*. Number 59 in Oxford Chemistry Primers. Oxford University Press, Oxford, UK, (1998).

[162] Brunauer, S., Emmett, P. H., and Teller, E. *J. Am. Chem. Soc.* **60**(2), 309–319 (1938).

[163] Rouquerol, F., Rouquerol, J., and Sing, K. S. W. *Adsorption by Powders and Porous Solids: Principles, Methodology and Applications*. Academic Press, (1998).

[164] Yun, J., Düren, T., Keil, F. J., and Seaton, N. A. *Langmuir* **18**(7), 2693–2701 (2002).

[165] Keskin, S., Liu, J., Rankin, R. B., Johnson, J. K., and Sholl, D. S. *Ind. Eng. Chem. Res.* **48**(5), 2355–2371 (2008).

[166] Düren, T., Bae, Y., and Snurr, R. Q. *Chem. Soc. Rev.* **38**(5), 1237–1247 (2009).

[167] Rappe, A. K., Casewit, C. J., Colwell, K. S., Goddard, W. A., and Skiff, W. M. *J. Am. Chem. Soc.* **114**(25), 10024–10035 (1992).

[168] Mayo, S. L., Olafson, B. D., and Goddard, W. A. *J. Phys. Chem.* **94**(26), 8897–8909 (1990).

[169] Jorgensen, W. L., Maxwell, D. S., and Tirado-Rives, J. *J. Am. Chem. Soc.* **118**(45), 11225–11236 (1996).

[170] Martin, M. G. and Siepmann, J. I. *J. Phys. Chem. B* **102**(14), 2569–2577 (1998).

[171] Gupta, A., Chempath, S., Sanborn, M. J., Clark, L. A., and Snurr, R. Q. *Molec. Simul.* **29**(1), 29–46 (2003).

[172] Turner, M. J., McKinnon, J. J., Jayatilaka, D., and Spackman, M. A. *CrystEngComm* **13**(6), 1804–1813 (2011).

[173] Düren, T., Millange, F., Férey, G., Walton, K. S., and Snurr, R. Q. *J. Phys. Chem. C* **111**(42), 15350–15356 (2007).

[174] Walton, K. S. and Snurr, R. Q. *J. Am. Chem. Soc.* **129**(27), 8552–8556 (2007).

[175] Bae, Y., Yazaydın, A. Ö., and Snurr, R. Q. *Langmuir* **26**(8), 5475–5483 (2010).

[176] Rouquerol, J., Llewellyn, P. L., and Rouquerol, F. In *Characterization of Porous Solids VII Proceedings of the 7th International Symposium on the Characterization of Porous Solids (COPS-VII), Aix-en-Provence, France, 26–28 May 2005,* Llewellyn, P. L., Rodriquez-Reinoso, F., Rouquerol, J., and Seaton, N. A., editors, volume 160 of *Studies in Surface Science and Catalysis*, 49–56. Elsevier, (2007).

[177] Everett, D. H. *Pure Appl. Chem.* **31**, 577–638 (1972).

[178] Xu, L., Sahimi, M., and Tsotsis, T. T. *Phys. Rev. E* **62**(5), 6942–6948 (2000).

[179] Düren, T., Jakobtorweihen, S., Keil, F. J., and Seaton, N. A. *Phys. Chem. Chem. Phys.* **5**(2), 369–375 (2003).

[180] Zoń, J., Garczarek, P., and Białek, M. *Metal Phosphonate Chemistry: From Synthesis to Applications*, chapter Chapter 6: Synthesis of Phosphonic Acids and Their Esters as Possible Substrates for Reticular Chemistry, 170–191. The Royal Society of Chemistry (2012).

[181] Moedritzer, K. and Irani, R. R. *J. Org. Chem.* **31**(5), 1603–1607 (1966).

[182] Mowat, J. P. S. Honours Report, University of St Andrews, St Andrews, (2007).

[183] Stock, N., Karaghiosoff, K., and Bein, T. *Z. Anorg. Allg. Chem.* **630**(13-14), 2535–2540 (2004).

[184] Miller, S. R. *Scandium-Bearing Open Framework Materials*. PhD thesis, University of St Andrews, St Andrews, (2008).

[185] Accelrys, San Diego, USA and Cambridge UK. *Cerius2 Program Suite*.

[186] Shannon, R. D. *Acta Cryst. A* **32**(5), 751–767 September (1976).

[187] Orgel, L. E. *Nature* **187**(4736), 504–505 (1960).

[188] Figgis, B. N. and Robertson, G. B. *Nature* **205**(4972), 694–695 February (1965).

[189] Kongshaug, K. O., Fjellvåg, H., and Lillerud, K. P. *Solid State Sci.* **2**(2), 205–214 (2000).

[190] Spek, A. *J. Appl. Cryst.* **36**(1), 7–13 (2003).

[191] Bonelli, B., Civalleri, B., Fubini, B., Ugliengo, P., Areán, C. O., and Garrone, E. *J. Phys. Chem. B* **104**(47), 10978–10988 November (2000).

[192] Valenzano, L., Civalleri, B., Chavan, S., Palomino, G. T., Arean, C. O., and Bordiga, S. *J. Phys. Chem. C* **114**(25), 11185–11191 July (2010).

[193] Dietzel, P. D. C., Morita, Y., Blom, R., and Fjellvåg, H. *Angew. Chem. Int. Ed.* **44**(39), 6354–6358 (2005).

[194] Sonnauer, A., Hoffmann, F., Fröba, M., Kienle, L., Duppel, V., Thommes, M., Serre, C., Férey, G., and Stock, N. *Angew. Chem. Int. Ed.* **48**(21), 3791–3794 (2009).

[195] Martínez-Tapia, H. S., Cabeza, A., Bruque, S., Pertierra, P., García-Granda, S., and Aranda, M. A. G. *J. Solid State Chem.* **151**(1), 122–129 April (2000).

[196] Tarazona, P. *Phys. Rev. A* **31**(4), 26722679 (1985).

[197] Tarazona, P. *Phys. Rev. A* **32**(5), 3148 (1985).

[198] Tarazona, P., Marconi, U. M. B., and Evans, R. *Mol. Phys.* **60**(3), 573 – 595 (1987).

[199] Zecchina, A., Otero Arean, C., Turnes Palomino, G., Geobaldo, F., Lamberti, C., Spoto, G., and Bordiga, S. *Phys. Chem. Chem. Phys.* **1**(7), 1649–1657 (1999).

[200] Fischer, K. F. and Schramm, V. In *Molecular Sieve Zeolites-I*, volume 101 of *Advances in Chemistry*, 250–258. American Chemical Society (1974).

[201] Yuan, H., Chen, J., Zhu, G., Li, J., Yu, J., Yang, G., and Xu, R. *Inorg. Chem.* **39**(7), 1476–1479 (2000).

[202] Britt, D., Furukawa, H., Wang, B., Glover, T. G., and Yaghi, O. M. *Proc. Natl. Acad. Sci.* **106**(49), 20637 –20640 (2009).

[203] Bloch, E. D., Murray, L. J., Queen, W. L., Chavan, S., Maximoff, S. N., Bigi, J. P., Krishna, R., Peterson, V. K., Grandjean, F., Long, G. J., Smit, B., Bordiga, S., Brown, C. M., and Long, J. R. *J. Am. Chem. Soc.* **133**(37), 14814–14822 (2011).

[204] Mitchell, L. Unpublished Result: Successful doping of Mn^{2+} into STA-16(Co), December (2011).

[205] Banerjee, R., Phan, A., Wang, B., Knobler, C., Furukawa, H., O'Keeffe, M., and Yaghi, O. M. *Science* **319**(5865), 939 –943 (2008).

[206] Hayashi, H., Cote, A. P., Furukawa, H., O'Keeffe, M., and Yaghi, O. M. *Nature Materials* **6**(7), 501–506 (2007).

[207] Morris, W., Doonan, C. J., Furukawa, H., Banerjee, R., and Yaghi, O. M. *J. Am. Chem. Soc.* **130**(38), 12626–12627 (2008).

[208] Huang, X., Lin, Y., Zhang, J., and Chen, X. *Angew. Chem.* **118**(10), 1587–1589 (2006).

[209] Pérez-Pellitero, J., Amrouche, H., Siperstein, F., Pirngruber, G., Nieto-Draghi, C., Chaplais, G., Simon-Masseron, A., Bazer-Bachi, D., Peralta, D., and Bats, N. *Chem. Eur. J.* **16**(5), 1560–1571 (2010).

[210] Moggach, S., Bennett, T., and Cheetham, A. *Angew. Chem. Int. Ed.* **48**(38), 7087–7089 (2009).